Engineering a modular virus-like particle platform for enhanced vaccine assembly



Hung-Jen Wu

Department of Biochemistry
Worcester College
University of Oxford

Michaelmas 2022

This thesis is submitted in partial fulfilment of the requirements for the degree of Doctor of Philosophy.

Abstract

Virus-like particles (VLPs) are assemblies that resemble viruses in their size, shape, and multivalent display of protein subunits, but lack the genetic material to infect cells. VLP-displayed antigens are more immunogenic than in their uncoupled form. SpyCatcher003 is a protein engineered from a fibronectin-binding protein of *Streptococcus pyogenes* that rapidly forms an irreversible isopeptide bond with its peptide partner, SpyTag. This thesis presents SpyCatcher003-mi3 VLPs, which I generated by fusing SpyCatcher003 to the mi3 scaffold, a modified version of the computationally-designed i301 nanocage. I demonstrate that SpyCatcher003-mi3 can be solubly expressed in *Escherichia coli*, can be purified via ammonium sulfate precipitation to high yields, and remains stable at temperatures between 25 ºC and 95 ºC. This VLP can accommodate antigens of diverse sizes and symmetries. Assembly on SpyCatcher003-mi3 elicits high levels of neutralizing antibodies against influenza haemagglutinin and neuraminidase, as well as the receptor-binding domain (RBD) of SARS-CoV-2 and select betacoronavirus variants. I demonstrated that SpyCatcher003-mi3 can be expressed solubly in a mammalian cell-line. Then I engineered N-linked glycosylation sequons on flexible hydrophilic loops on the VLP with the goal of shielding antibody binding to the mi3 scaffold and SpyCatcher003, to focus antibody responses on the displayed antigen. I found no significant change in the level of antibody titers that bound specifically to the mi3 scaffold and the SpyCatcher003:SpyTag003 moiety, relative to that of the displayed antigen (SARS-CoV-2 RBD). Fusion of SpyCatcher003-mi3 with the albumin-binding sequence, ABD035, was also insufficient to change the relative induction of antibodies specific to SARS-CoV-2 RBD, the SpyCatcher003:SpyTag003 moiety and the mi3 scaffold. Further analysis and combination of blocking components will be required to maximize glycan and

albumin-dependent antibody shielding. Nonetheless, the high stability, simple purification, and easy functionalization of the existing SpyCatcher003-mi3 platform can potentially accelerate the vaccine development process against many infectious diseases.

Authorship Declaration

I declare that this thesis is entirely my own work, with the following exceptions:

Chapter 1:

Figure 1.1: SpyTag/SpyCatcher split domain rendering was made by Theodora Bruun

Figure 1.3: Graph with VLP yields and DLS measurements between SpyCatcher-mi3 and SpyCatcher-i301 were adopted from images in Bruun et al., 2018

Figure 1.4 B: SpyCatcher003 and SpyCatcher product formation data and graph were modified from Keeble et al., 2019.

Figure 1.5: Influenza HA trimer (PDB ID: 5UGY) and antibody figures are modified from images in Bajic et al., 2019.

Figure 1.6: Side view of Influenza (A/California/04/2009(H1N1)) HA trimer (PDB ID: 4JTV) is modified from image in Guthmiller et al., 2021

Chapter 3:

Figure 3.1: SpyCatcher003:SpyTag003 isopeptide bond formation schematic adopted from figure in Rahikainen et al., 2021; VLP capsid image adopted from figure in Brune et al., 2016.

Figure 3.2: i301 nanocage originated from Hsia et al., 2016. SpyCatcher003 parent domain rendering was made by Irsyad Khairil Anuar.

SpyCatcher-mi3+C165A+C203A was cloned by Anne-Marie Anderson

Figure 3.9/10/15: Data and images were adopted from figures in Rahikainen et al., 2021

Figure 3.11/12: Data and images were adopted from figures in Tan et al., 2021

Figure 3.13/14: Data and images were adopted from figures in Cohen et al., 2021b

Chapter 4:

Figure 4.2: SpyCatcher003 parent domain rendering was made by Irsyad Khairil Anuar.

Figure 4.10: TEM images of glycosylated VLPs taken by Niels Wicke

SUMO-SpyTag003 was expressed by Irsyad Khairil Anuar

Figure 4.13: Glycan mass spectrometry data was generated by Dr. Joel Allen.

SpyCatcher003:SpyTag003 was expressed by Rolle Rahikainen

RBD-His_6 expression, mice immunizations and serum harvesting were performed by Tiong Tan

Expression and biophysical characterization of albumin-binding SpyCatcher003-mi3 variant VLPs were performed by David Schramm

This thesis has not been submitted for any other degree or to another other institution.

Publications so far from my graduate studies:

Cohen, A.A., Gnanapragasam, P.N.P., Lee, Y.E., Hoffman, P.R., Ou, S., Kakutani, L.M., Keeffe, J.R., **Wu, H.-J**., Howarth, M., West, A.P., et al. (2021b). Mosaic nanoparticles elicit cross-reactive immune responses to zoonotic coronaviruses in mice. Science *371*, 735–741.

Rahikainen, R., Rijal, P., Tan, T.K., **Wu, H**., Andersson, A.C., Barrett, J.R., Bowden, T.A., Draper, S.J., Townsend, A.R., and Howarth, M. (2021). Overcoming symmetry mismatch in vaccine nanoassembly through spontaneous amidation. Angewandte Chemie International Edition *60*, 321–330.

Acknowledgements

I cannot help but smile, to this day, whenever I remember how a Skype call that I had scheduled with Professor Mark Howarth simply to ask about “a molecular superglue” became a formal DPhil interview five minutes before it took place, after he asked for my CV. I want to thank him for accepting me into his lab and guiding me through the ups-and-downs of this research journey. His mentorship has enabled me to become a more meticulous and independent experimentalist these past three years, but I know there is still plenty of room for me to grow. I would also like to thank my co-supervisor, Professor Alain Townsend for providing me with invaluable feedback on my experimental work and with insights pertaining to VLP immunology and immunizations.

I would like to thank my fellow lab mates in the Howarth laboratory for all the experimental guidance, patience, and being good sounding boards for me during my time in this lab. The present team, at the time of this writing, exemplifies what a great team should look like, and I hope this collaborative culture persists well after my departure. I’m grateful to postdocs Anne-Marie, Rolle, James, Anthony, Anusuya, and Henry, who have helped me find my footing at various parts of my training. I would like to extend a special thank you to Sheryl, Rory, Lasya, and Claudia for being my confidants, great neighbors/chefs, and company outside of lab. It’s been an extraordinary pleasure meeting you and I hope our paths will cross again (in America) someday.

Outside of my lab, I’m grateful to Dr. Tiong Tan for performing my mice immunizations like clockwork, Dr. Joel Allen for help with performing and troubleshooting glycan mass spectrometry, and members of Professor Pamela Bjorkman’s lab for spearheading work on SpyCatcher003-mi3 mosaic nanoparticle vaccines. I also appreciate my thesis committee members and assessors, Professors Petros Ligoxygakis, John

Vakonakis, Mark Wormald, Omer Dushek, and Oliver Bannard, for taking the time to critique my project at different stages. I would like to thank Professors Matthew Whitby and Grant Ritchie for their advice and moral support.

I would like to extend my gratitude across the Atlantic, firstly to all my beloved professors and friends at The George Washington University for providing me with an excellent environment to discover myself, what I can be, and instilling in me a sense of direction. Secondly, I would like to also extend my gratitude to all my dear friends from Georgetown University and Professors Cynthia Rosenthal, Dean Rosenthal, Amrita Cheema, You-Shin Chen, and Dr. Anirudh Gaur, for introducing me to the exciting wonders of biochemistry research, and providing the positive experiences that motivated me to pursue this degree, despite my having a non-traditional academic background. Recalling all these wonderful memories have helped me stay the course during the most challenging times of my DPhil.

Most importantly I want to thank my mother, Su-Chen Chen for being the strongest pillar of unconditional love and support in my life. Regardless of the geographic distance between us, she has always been “in the arena” with me, facing challenges and sharing joys together. Although she was initially discouraged from studying science and math in university due to her gender, she sacrificed a great deal for me to truly discover my passion and study the things that she never had a chance to do herself. I aspire to someday create new opportunities for others, as she has done for me. I hope that my doctoral training will represent the start of this endeavor.

Table of Contents

Abstract **2**
Authorship Declaration **4**
Acknowledgements **6**
Dedication **11**
Abbreviations **12**
List of Figures **17**
Chapter 1: Introduction **20**
1.1 Immunology of vaccines 21
1.1.1. Historical background of vaccines 21
1.1.2 Virus-like particle vaccines 22
1.1.2.1 VLP immunology 23
1.1.2.2. Prior work on SpyCatcher VLPs 24
1.1.3 Existing methods of amplifying and targeting antibody responses 29
1.1.3.1 Removing undesirable epitopes 29
1.1.3.2 Shielding undesirable epitopes 30
1.1.3.3 Stabilizing prefusion conformation of viral proteins 33
1.1.3.4 Unmasking occluded epitopes 34
1.1.3.5 Epitope resurfacing 35
1.1.3.6 Heterologous antigen display 36
1.1.4 Thesis objectives 38
Chapter 2: Materials and Methods **40**
2.1 Cloning 41
2.1.1 Polymerase chain reaction 41
2.1.2 Gibson assembly 42
2.1.3 Bacterial culture media preparation 43
2.1.4 Transforming competent *E. coli* 43
2.1.5 Miniprep of plasmid DNA 44
2.1.6 Maxiprep of plasmid DNA 44
2.1.7 Sanger sequencing 45
2.2 Expression and purification of VLPs 45
2.2.1 *E. coli* protein expression and incubation conditions 45
2.2.2 Mammalian cell culture maintenance 46

2.2.3 Gel filtration chromatography of VLPs 46
2.2.4 C-tag affinity purification of VLPs and antigens 47
2.2.5 His_6Tag affinity purification of proteins 47
2.2.6 Mammalian cell expression and purification of VLPs 48
2.2.7 Ammonium sulfate precipitation of VLPs 49
2.2.8 Spy & Go affinity purification of SpyTag-RBD 50
2.2.9 Endotoxin removal and quantification 51
2.2.10 Residual nucleic acid quantification 51
2.3 Glycan analysis and characterization of VLPs 52
2.3.1 PNGase F digestion 52
2.3.2 Endo H_f digestion 52
2.3.3 VLP sample preparation for LC-MS-ESI quantification 53
2.3.4 LC-MS-ESI quantification of VLP glycan composition 53
2.3.5 Data analysis of LC-MS-ESI results 53
2.4 Characterization of VLP solubility, stability and reactivity 54
2.4.1 Dynamic light scattering 55
2.4.2 Temperature-dependent solubility assay 56
2.4.3 Model SpyTag-Antigen reaction time course 56
2.4.4. Transmission electron microscopy (TEM) 57
2.5 Assessing immunogenicity of nanoparticles 57
2.5.1 VLP preparation for vaccination 57
2.5.2 Mice immunization and blood sampling 58
2.5.3 Endpoint ELISA 58
2.5.4 IgG subtyping 59
2.5.5 Statistical analysis of ELISA 60
2.6 Structure visualization 60
Chapter 3: Development of the SpyCatcher003-mi3 VLP Scaffold 61
3.1 Expression and characterization of particles linked to SpyCatcher or SpyCatcher003 66
3.1.1 Bacterial expression and affinity purification of particles 66
3.1.2 Heat stability of particles 69
3.1.3 Ammonium sulfate precipitation of SpyCatcher003-mi3 75
3.1.4 Residual nucleic acid measurements for SpyCatcher003-mi3 preps 78
3.2 Reactivity of VLPs with antigens of varying symmetries and valencies 79

3.3 Immunogenicity of SpyCatcher003-mi3 vaccine candidates 85
3.3.1 Immunogenicity of SARS-CoV-2 RBD-coupled VLPs 85
3.3.2 Immunogenicity of influenza hemagglutinin and neuraminidase-coupled VLPs 97
3.4 Discussion 100
Chapter 4: Development of a Shielded SpyCatcher003-mi3 Scaffold 103
4.1. Design of glycosylated SpyCatcher003-mi3 particles 108
4.1.1. Expression of SpyCatcher003-mi3 in HEK293 cells 108
4.1.2. Specific flexible loop Insertion of N-linked glycans 109
4.1.3 Expression and affinity purification of glycosylated particles 116
4.1.4 Confirmation of VLP glycosylation status 123
4.1.5 Assessing particle uniformity of glycosylated VLPs 125
4.1.6 Heat stability of glycosylated particles 128
4.1.7 Time course reactivity of glycosylated particles 131
4.1.8 N-linked glycan composition and occupancy analysis 134
4.2 Immunogenicity of SARS-CoV-2 RBD-decorated glycosylated SpyCatcher003-mi3 VLPs 136
4.2.1 Assessing extent of RBD-focused antibody responses 136
4.2.2 IgG subtyping of glycosylated VLP immune response 140
4.3 Design of albumin-binding SpyCatcher003-mi3 particles 143
4.3.1 Expression of SpyCatcher003-mi3 with albumin-binding domain 143
4.3.2 Assessing role of albumin-binding domains against antibody binding 147
4.4 Immunogenicity of SARS-CoV-2 RBD-decorated albumin-binding SpyCatcher003-mi3 VLPs 151
4.4.1 Assessing the extent of RBD-focused antibody responses 151
4.5. Discussion 154
Chapter 5: Summary and Discussion 164
Bibliography 169

謹獻給我摯愛的母親，陳淑貞女士，我的祖母，陳許凱女女士，
以及我的祖父，陳拱照先生。

Abbreviations

A_{280}	Absorbance at 280 nm
A_{652}	Absorbance at 652 nm
ABD035	Albumin-binding domain 35 (Jonsson et al, 2008)
ACE2	Angiotensin converting enzyme 2
APC	Antigen-presenting cell
AS	Ammonium sulfate
BCA	Bicinchoninic acid
BCR	B-cell receptor
bp	Base-pair
CD4	Cluster of differentiation 4
CHO	Chinese hamster ovary
CL	Cleared Lysate
COVID-19	Coronavirus disease 2019
Cp3	Coat protein 3
CpG	5’-C-phosphate-G-3’
CyRPA	Cysteine-rich protective antigen
DC	Dendritic cell
DEAE	Diethylaminoethyl
DLS	Dynamic light scattering
DMSO	Dimethyl sulfoxide
dNTP	Deoxynucleoside triphosphate
dsDNA	Double-stranded DNA
DTT	Dithiothreitol

E(1-5)	Elution (1-5)
EDTA	Ethylenediaminetetraacetic acid
ELISA	Enzyme-linked immunosorbent assay
Endo H	Endoglycosidase H
Env	Envelope (protein)
Env CD4bs	Envelope CD4 binding site
EU	Endotoxin unit
FcγR	Fc-gamma receptor
FDA	U.S. Food and Drug Administration
FT	Flowthrough
GFP	Green fluorescent protein
GGS	Glycine-glycine-serine (linker)
Glyc	Glycosylated
h	Hour
HA	Hemagglutinin
HBsAg	Hepatitis B surface antigen
HEK	Human embryonic kidney
HIV	Human immunodeficiency virus
HPLC	High-performance liquid chromatography
HRP	Horseradish peroxidase
HSA	Human serum albumin
IC50	half-maximal inhibitory concentration
IgG	Immunoglobulin G
IL	Interleukin

IPTG	Isopropyl-β-D-thiogalactopyranoside
kb	kilobase
kDa	kilodalton
Kif	Kifunensine
KPDG	2-keto-deoxy-phosphogluconate
LAL	Limulus amebocyte lysate
LB	Luria Bertani broth
LC	Liquid chromatography
LC-ESI-MS	Liquid chromatography in combination with electrospray ionization-mass spectrometry
m/z	Mass-to-charge ratio
mAb	Monoclonal antibody
MHC	Major histocompatibility complex
min	Minute
MS	Mass spectrometry
MWCO	Molecular weight cutoff
n.s.	Not statistically significant
NA	Neuraminidase
NAD^+	Nicotinamide adenine dinucleotide
NDV	Newcastle disease virus
NiNTA	Nickel nitrilotriacetic acid
ODN	Oligo-deoxynucleotide
OspC	Outer surface protein C
PBS	Phosphate-buffered saline
PCR	Polymerase chain reaction

PDB	Protein data bank
PEG	Polyethylene Glycol
PI	Protein inhibitors
PMSF	Phenylmethylsulfonylfluoride
PNGase-F	Peptide-N-Glycosidase F
ppm	Parts-per-million
RBD	Receptor-binding domain
RBS	Receptor-binding site
R_h	Hydrodynamic radius
rpm	Revolutions per minute
RSV	Respiratory syncytial virus
s	Second
S-FLU	Single-cycle influenza viruses
s.d.	Standard deviation(s)
SARS-CoV	Severe Acute Respiratory Syndrome Coronavirus 1
SARS-CoV-2	Severe Acute Respiratory Syndrome Coronavirus 2
SC003/-mi3	SpyCatcher003/-mi3
SDS-PAGE	Sodium dodecyl sulfate–polyacrylamide gel electrophoresis
SEC	Size exclusion chromatography
SN	Supernatant
SOC	Super optimal broth with catabolite repression
ssRNA	Single-stranded RNA
ST003	SpyTag003
TAE	Tris-acetate-EDTA

TEM	Transmission Electron Microscopy
Th1/2	T-helper cells type 1/2
TL	Total lysate
TLR	Toll-like receptors
TMB	3,3',5,5'-Tetramethylbenzidine
TNF	Tumor necrosis factor
V	Volt
VLP	Virus-like particles
W	Wash
WHO	World Health Organization

Unique VLP Construct Nomenclature:

SpyCatcher003-mi3: SC003-mi3/WT
SpyCatcher003-ABD035-mi3: Mid. ABD035/ABD035-M
SpyCatcher003-mi3-ABD035: C Term. ABD035/ABD035-CT
SpyCatcher003-SA21-mi3: SA21-M
SpyCatcher003-Alb8-mi3: Alb8-M
SpyCatcher003-mi3-SA21: SA21-CT
SpyCatcher003-mi3-Alb8: Alb8-CT
“:” : coupled to (an antigen of interest)

List of Figures

Chapter 1:

Figure 1.1. Splitting the CnaB2 domain yields the protein-peptide partners, SpyCatcher and SpyTag 25

Figure 1.2. Design principle of mi3 scaffold 26

Figure 1.3. Affinity purification yield and particle uniformity comparison between SpyCatcher-mi3 and VLP predecessors 27

Figure 1.4. Comparison of SpyCatcher and SpyCatcher003 sequences and reaction rates 28

Figure 1.5. Shielding undesirable epitopes with glycans and antibodies 32

Figure 1.6. Epitope grafting procedure 36

Figure 1.7. Heterologous antigen display strategy on VLPs to focus response on conserved regions 38

Chapter 3:

Figure 3.1. Design principle of the SpyCatcher VLP Platform 63

Figure 3.2. Mutation sites and C-tag purification gels of SpyCatcher-mi3 and SpyCatcher003-mi3 variants 68

Figure 3.3. Yields of SpyCatcher-mi3 and SpyCatcher003-mi3 variants 69

Figure 3.4. Temperature-dependent solubility of SpyCatcher-mi3 and SpyCatcher003-mi3 variants 72

Figure 3.5. Particle uniformity of SpyCatcher-mi3 and SpyCatcher003-mi3 variants subjected to temperatures between 25 ^{o}C and 95 ^{o}C 74

Figure 3.6. Ammonium sulfate precipitation of SpyCatcher003-mi3 76

Figure 3.7. Size-excluded chromatogram of 25% and 30% (w/v) ammonium sulfate precipitated SpyCatcher003-mi3. 78

Figure 3.8. Residual DNA quantification of SpyCatcher003-mi3 preparations 79

Figure 3.9. SpyCatcher003 can efficiently couple antigens of different sizes and symmetries 82

Figure 3.10. Antigen-coupled SpyCatcher003-mi3 forms uniform-sized particles 84

Figure 3.11. RBD-coupled SpyCatcher003-mi3 elicit strong antibody responses against RBD, which block ACE2. 87

Figure 3.12. RBD-coupled SpyCatcher003-mi3 is stable at different temperatures, against freeze-thaw and lyophilization 89

Figure 3.13. Human/bat-derived sarbecovirus RBD-coupled SpyCatcher003-mi3 elicits strong cross-reactive responses against displayed RBD 94

Figure 3.14. RBD-coupled SpyCatcher003-mi3 elicit strong cross-reactive responses against non-displayed RBDs 96

Figure 3.15. H3 Vic HA and N1-coupled SpyCatcher003-mi3 elicit high neutralization antibody titers 99

Chapter 4:

Figure 4.1. C-tag affinity purification gel of HEK293-expressed SpyCatcher003-mi3 and comparison with bacterial-expressed SpyCatcher003-mi3 109

Figure 4.2. Selected N-glycan sequon loop insertion sites on SpyCatcher003 and mi3. . 112

Figure 4.3. Expression studies of N-linked glycan sequons inserted in flexible SpyCatcher003 and mi3 loops 114

Figure 4.4. Size-exclusion chromatography of glycosylated VLP variants. 116

Figure 4.5. C-tag affinity purification gel results of S50 Glyc. SpyCatcher003-mi3 and SpyCatcher003-G124 Glyc. mi3 VLPs 119

Figure 4.6. C-tag affinity purification gel and SEC of CHO-expressed S50 Glyc. SpyCatcher003-mi3 and SpyCatcher003-G124 Glyc. mi3 120

Figure 4.7. C-tag affinity purification gel and SEC of S50 Glyc. SpyCatcher003-G124 Glyc. mi3 candidate VLP 122

Figure 4.8. PNGase-F digestion of glycosylated VLPs 124

Figure 4.9. Endo H digestion of S50 Glyc. SpyCatcher003-mi3 expressed with Kifunensine 125

Figure 4.10. SEC chromatogram, dynamic light scattering, and negative stained images of glycosylated VLPs 127

Figure 4.11. Temperature-dependent solubility assays of glycosylated SpyCatcher003-mi3 compared to bacterial-expressed SpyCatcher003-mi3 VLPs 130

Figure 4.12. Coupling efficiency of bacterial-expressed SpyCatcher003-mi3 and glycosylated SpyCatcher003-mi3 133

Figure 4.13. Mass spectrometry glycan analysis of S50 Glyc. SpyCatcher003-mi3 and S50 Glyc. SpyCatcher003-mi3+Kifunensine 135

Figure 4.14. Gel analysis of proteins used for testing ELISA serum binding 137

Figure 4.15. SARS-CoV-2 RBD-, mi3-, and SpyCatcher003:SpyTag003-specific antibody responses. 140

Figure 4.16. IgG1 and IgG2a subtyping of glycosylated VLPs. 142

Figure 4.17. Linear construct schematics and DLS measurements of ABD035 SpyCatcher003-mi3 VLP variants 147

Figure 4.18. Measuring changes in SpyCatcher003-mi3:HA-Vic serum binding against albumin-bound SpyCatcher003-mi3 VLPs. 150

Figure 4.19. Coupling of SARS-CoV-2 RBD on ABD035 SpyCatcher003-mi3 VLPs 152

Figure 4.20. SARS-CoV-2 RBD-, mi3-, and SpyCatcher003:SpyTag003-specific antibody responses 153

Chapter 1: Introduction

Chapter 1: Introduction

1.1 Immunology of vaccines

1.1.1. Historical background of vaccines

Along with clean water and sanitation, vaccines are one of the most effective public health interventions (Rappuoli et al., 2014). Between 1924 and 2014, vaccines have prevented over 103 million cases of childhood disease across the globe (Greenwood, 2014; Rappuoli et al., 2014; van Panhuis et al., 2013). In the 20th century, vaccines have helped increase the average human life-span by 30 years (Cooper et al., 2002). The very fact that the economies of countries with greater access to efficacious vaccines are projected to recover sooner from the COVID-19 pandemic than those that lack access underscores the importance of this technology in everyone's lives (World Health Organization, 2021).

The first recorded attempt of human vaccination dates back to the 16th century when individuals were immunized against smallpox virus in China and India by variolation, a process in which individuals were inoculated with the live virus itself (Boylston, 2012). While variolation reduced mortality rates, it was still risky because variolated individuals were still able to spread smallpox to naïve individuals and create outbreaks with normal mortality rates (Bachmann and Jennings, 2010). In the eighteenth century, Edward Jenner observed that milkmaids who developed a pox-like infection were immune from smallpox infection. He introduced the concept of vaccination by infecting his servant's son with material from cowpox. The boy proved to be immune to smallpox and this vaccination approach was consequently practiced through Europe (Bachmann and Jennings, 2010).

In the 1880s, Louis Pasteur and his colleagues pioneered the idea of attenuation, which involved weakening the virulence of pathogen, via serial cultivation, before injecting into patients (Plotkin, 2014). Pasteur and his colleagues developed the first human rabies

vaccine in 1885 and showed that it could also protect against non-attenuated rabies strains (Plotkin, 2014). Towards the end of the nineteenth century, vaccines against typhoid, plague, cholera, diphtheria, and pertussis were made from heat and chemical treatment of the pathogens (Plotkin, 2014). In 1980, smallpox was eradicated due to a successful WHO-coordinated global vaccination campaign. Vaccines based on attenuated pathogens, however, run the risk of inducing serious side effects in some patients and may revert to a virulent state (Huang et al., 2004). Expressing recombinant subunit vaccines can overcome this safety issue and can be mass-produced at low cost (Nascimento and Leite, 2012; Pollet et al., 2021). Unlike attenuated vaccines, recombinant subunit proteins on their own are poorly immunogenic and require an adjuvant to achieve reasonable immunogenicity (Delany et al., 2014; Pérez et al., 2012).

1.1.2 Virus-like particle vaccines

Virus-like particles (VLPs) are supramolecular protein structures that resemble viruses in appearance, but lack the viral genetic material, therefore rendering them non-infectious (Nooraei et al., 2021). VLPs can offer the immunogenicity of attenuated vaccines along with the safety and low production cost of recombinant subunit vaccines (Nooraei et al., 2021). The inability of VLPs to recombine, replicate or revert to a virulent state makes them safer to use for elderly or immunocompromised individuals (Jennings and Bachmann, 2008). VLPs were first discovered in 1968 in the sera of patients with leukemia, Down's syndrome, and hepatitis (Bayer et al., 1968; Nooraei et al., 2021).The cavity present in VLPs enable these particles to also serve as targeted delivery vehicles of genes, peptides, immunomodulators and drugs (Chung et al., 2020; Nooraei et al., 2021; Steinmetz, 2010). VLPs can be expressed recombinantly in plant, mammalian, yeast, bacterial and insect cell systems (Bahar et al., 2021; Balke and Zeltins, 2020; Joe et al.,

2020; Nooraei et al., 2021; Saraswat et al., 2016; Tariq et al., 2021). Chimeric VLPs can also be formed from assembling distinct viral proteins (Syomin and Ilyin, 2019).

In 1986 the Hepatitis B virus vaccine, based on the protein antigen S (HBsAg), was the first VLP vaccine to be licensed (Spice et al., 2020). As of 2021, there are commercially available VLP vaccines targeting Human Papilloma Virus (Gardasil, Gardasil9, Cervarix), Hepatitis B Virus (Sci-B-Vac), Hepatitis E Virus (Hecolin) and *Plasmodium falciparum* (Mosquirix), with others in various phases of clinical trials (Jennings and Bachmann, 2008; Nooraei et al., 2021). In 2022, NVX-CoV2373 (Nuvaxovid) became the first protein nanoparticle vaccine to receive emergency-use authorization from the U.S. Food and Drug Administration for immunization against COVID-19 (U.S. Food and Drug Administration, 2022).

1.1.2.1 VLP immunology

One advantageous application of VLPs lies in vaccination, due to their ability to stimulate cellular responses and magnify an overall humoral response (McFall-Boegeman and Huang, 2022). The immunogenicity of a VLP is attributed mainly to its size, repetitive structure, and ability to stimulate innate immune cells, which can in turn activate an adaptive immune response. The 20-200 nm diameter of VLPs (Bachmann and Jennings, 2010) enables their efficient drainage directly into lymph nodes from the site of injection or VLPs can be taken up by dendritic cells and transported to draining lymph nodes for subsequent presentation to antigen-presenting cells (Jennings and Bachmann, 2008). VLPs are recognized by antigen-presenting cells (APC), such as dendritic cells, via pattern recognition receptors, such as toll-like receptors (TLR) and C-type lectin receptors (Nooraei et al., 2021). Following recognition, APCs facilitate VLP transfer to secondary lymphoid organs. VLPs can help dendritic cells mature, which results in the secretion of pro-inflammatory cytokines TNF-α and IL-1β (Fiebiger et al., 2001). Proteolysis of the VLP

in the dendritic cells (DC) leads to the display of VLP peptide fragments on the DC surface via the major histocompatibility complex (MHC) (Banchereau and Steinman, 1998). Co-stimulatory molecules and the peptide-bound MHC class II can then activate CD4+ T-helper cells that induce B and T cell propagation and differentiation (Morón et al., 2003; Parker, 1993; Syomin and Ilyin, 2019). The VLP's ability to display antigens on its surface in a repetitive organized manner enables the VLP to interact directly via B-cell receptor cross-linking (Bachmann and Jennings, 2010). Sometimes B cells can detect VLPs and activate a humoral response independent of T-helper cell involvement or the innate immune system (López-Macías, 2012; Nooraei et al., 2021; Yao et al., 2004).

Besides displaying antigens on their surface, VLPs can also stimulate innate immune cells, via pathogen-associated molecular pattern receptor recognition, by packaging Toll-like Receptor (TLR) ligands such as single-stranded RNA (ssRNA) and CpG (non-methylated CG nucleotide motifs) oligo-deoxynucleotides (CpG-ODNs) within its cavity. The inclusion of CpG-ODNs, a TLR 9 ligand, or ssRNA, a TLR 7 ligand, can stimulate B-cells and induce isotype switching (Jegerlehner et al., 2007; Krieg, 2006).

1.1.2.2. Prior work on SpyCatcher VLPs

The Howarth laboratory pioneered the SpyCatcher-SpyTag system (Zakeri et al., 2012) and used it for covalently coupling antigens onto a VLP scaffold (Fig 1.1). This plug and display technology works by mixing a split domain of *Streptococcus pyogenes* FbaB fused to a nanoparticle with a peptide tag fused to an antigen of interest (Zakeri et al., 2012). Previously an N-terminal truncated SpyCatcher was conjugated to cp3 coat protein from bacteriophage AP205 to form the SpyCatcher-AP205 VLP (Brune et al., 2016). When SpyCatcher-AP205 was conjugated to the recombinant malarial antigen Pfs25-SpyTag, it elicited better quality antibodies relative to Pfs25-SpyTag displayed on the IMX313 and Qβ multimerization platforms (Leneghan et al., 2017). SpyCatcher-AP205 also generated high

antibody titers against cancer antigens and allergy-related cytokines (Palladini et al., 2018; Thrane et al., 2016). Despite SpyCatcher-AP205's ability to generate relevant antibodies, its low yield and instability are problems that prevent its development as a vaccine (Bruun et al., 2018).

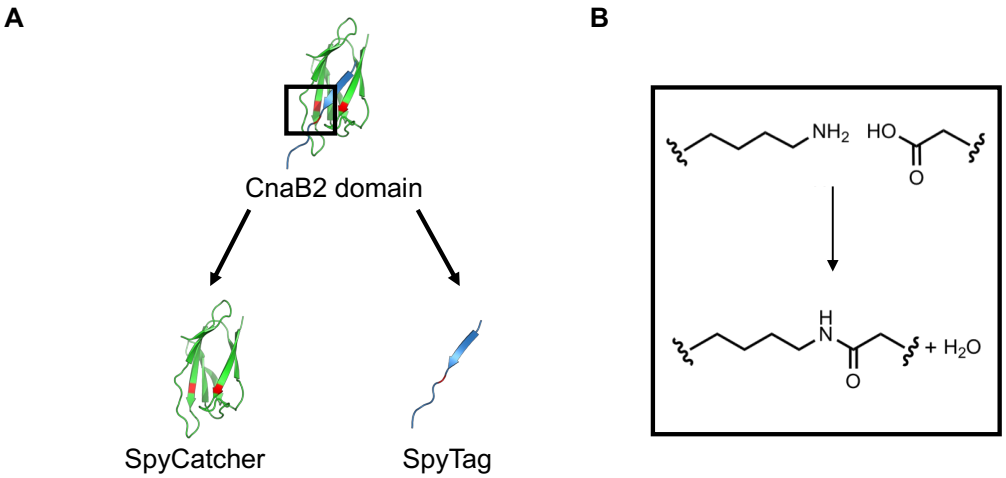


Figure 1.1. Splitting the CnaB2 domain yields the protein-peptide partners, SpyCatcher and SpyTag: *(*A) PyMOL cartoon representation of CnaB2 (PDB:4MLS), with SpyCatcher (green), its catalytic Glu and reactive Lys (red), as well as SpyTag (blue) with its reactive Asp shown in red. Boxed region shows relative location of spontaneous isopeptide bond formation between Lys and Asp; (B) Molecular representation of the amidation reaction occurring between SpyCatcher and SpyTag. Figures adopted from image by Theodora Bruun.

Computationally-designed nanocages of viral and non-viral origin have garnered significant interest in developing vaccines (Cristie-David et al., 2018). David Baker and colleagues designed one such nanocage, dubbed "i301", derived from the 2-keto-deoxy-phosphogluconate (KPDG) aldolase of the thermophilic bacterium *Thermotoga maritima* (Hsia et al., 2016). Introducing five interface mutations to the wild-type trimer produced a self-assembling 60-mer particle that remains stable in high concentrations of denaturant

and temperatures of 25-80 ^{o}C; each trimer of i301 was also able to display two copies of superfolder GFP (Hsia et al., 2016). Realizing the potential of i301 to resolve the instability of SpyCatcher-AP205, two former members of the Howarth laboratory genetically fused SpyCatcher to the N-terminus of i301 and engineered two surface cysteine-to-alanine mutations (Fig 1.2) on i301 to decrease disulfide bond-mediated aggregation between particles (Bruun et al., 2018).

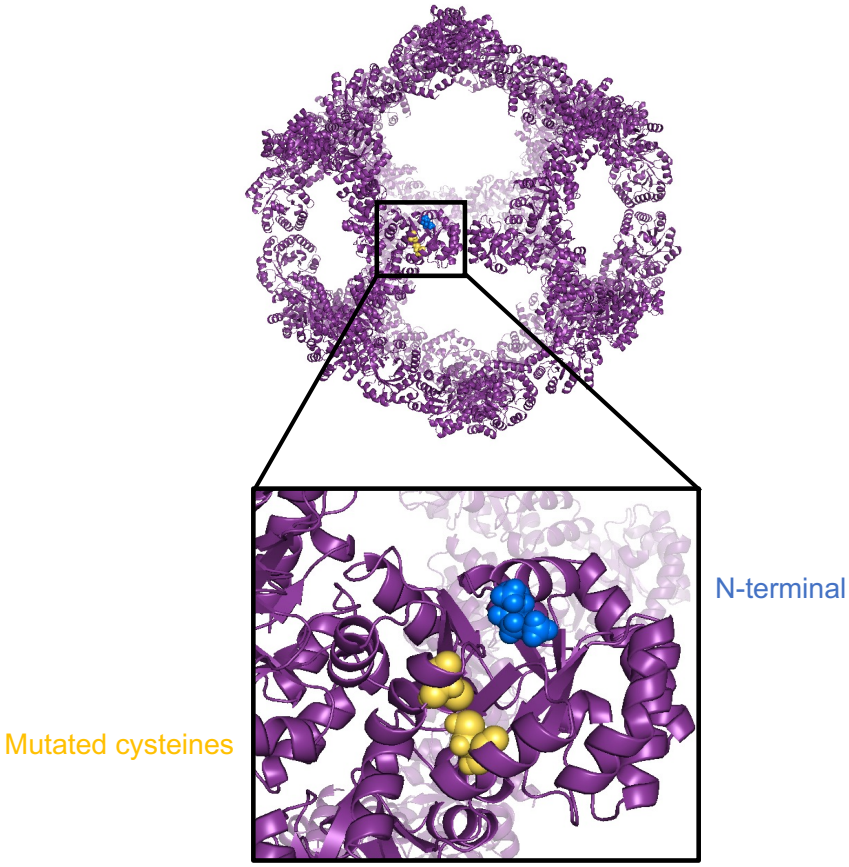


Figure 1.2. Design principle of mi3 scaffold: Zoomed-in view (lower box) of surface-based cysteines, C76 and C100 (both in gold), mutated to alanines on the i301 particle (purple) to generate mi3. The N-terminus of the i301 monomer is illustrated in blue. Computational rendering adapted from Hsia et al., 2016.

This particle, dubbed “SpyCatcher-mi3”, expressed a 20-fold greater yield than SpyCatcher-AP205 and demonstrated enhanced particle stability than SpyCatcher fused to i301 (Bruun et al., 2018) (Fig 1.3). SpyCatcher-mi3 also showed 95% coupling efficiency (in 16 hours) with different malarial antigens and generated high antibody titers specific to the malarial antigen, CyRPA (Bruun et al., 2018).

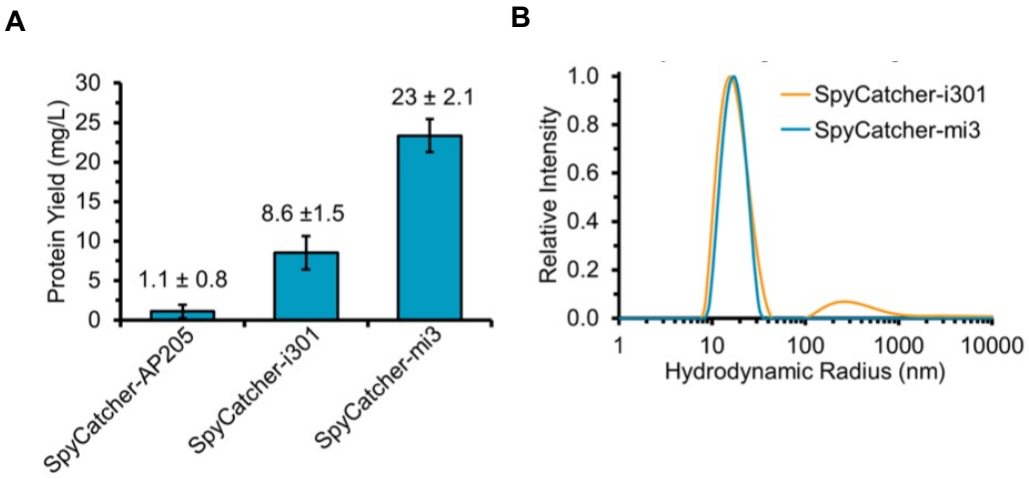
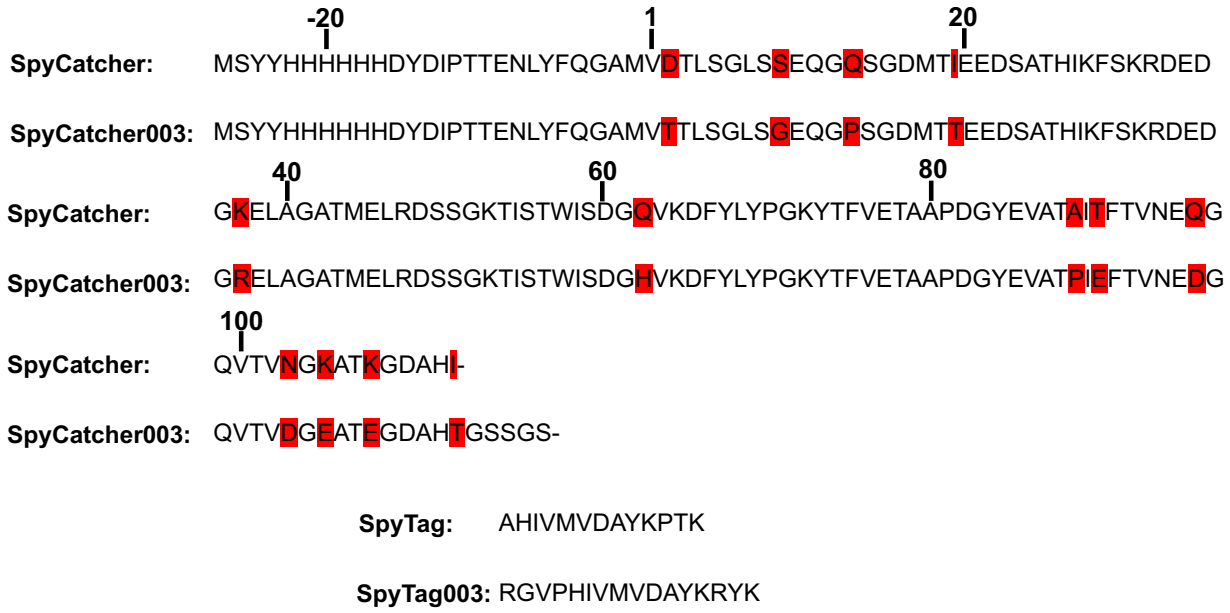


Figure 1.3. Affinity purification yield and particle uniformity comparison between SpyCatcher-mi3 and VLP predecessors: (A) fusing SpyCatcher to mi3 enhances yield, compared to SpyCatcher-AP205 and SpyCatcher-i301; all yields are expressed as mean ±1 s.d., n = 3; (B) DLS measurements show that SpyCatcher-mi3 maintains greater particle uniformity than SpyCatcher-i301 and is less prone to aggregation. Both VLPs were stored for 5 weeks at 4 ^{o}C. Credit: Data/image credit: Bruun et al., 2018.

The version of SpyCatcher used to study the AP205 and mi3 particles has the problem of self-reactivity and reacting slowly with its SpyTag-protein partner (Keeble et al., 2017). SpyCatcher003 was developed after thirteen additional mutations were rationally designed into SpyCatcher (Fig 1.4 A), in an effort to improve its stability and charge complementarity to its Tag partner (Keeble et al., 2017, 2019).The second-order rate constant for SpyTag003/SpyCatcher003 was 5.5 ±0.6 × 10^{5} $M^{-1}s^{-1}$ (mean ± 1 s.d., n=3),

which is 400-fold faster than 1.4 ×10^3 $M^{-1}s^{-1}$ shown for SpyTag/SpyCatcher (Keeble et al., 2019). Seeing how this comparatively rapid reaction rate (Fig 1.4 B) would be helpful for modular assembly of mi3 VLPs with a SpyTag-antigen, I decided to make a VLP using SpyCatcher003 and mi3.

A



B

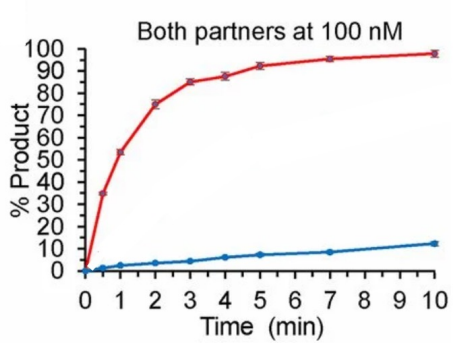


Figure 1.4. Comparison of SpyCatcher and SpyCatcher003 sequences and reaction rates: (A) Aligned sequences of SpyCatcher (top row) and SpyCatcher003 (bottom row) with mutated residues highlighted in red; (B) Reaction rate plot of 100 nM SpyCatcher003 (red) or 100 nM SpyCatcher (blue) reacting at 25 °C with 100 nM SpyTag003-sfGFP or

SpyTag-sfGFP, respectively. Product formation is presented as mean ± 1 s.d., n=3. Figure 1.4 (B) modified from Keeble et al., 2019.

However, one major drawback of the SpyCatcher VLP is that the scaffold and the SpyCatcher:SpyTag moiety introduces new epitopes (Caradonna and Schmidt, 2021). This can potentially increase interclonal B cell competition and dilute the antibody response specific to the antigen of interest (Caradonna and Schmidt, 2021). It may also be possible that the SpyCatcher003-mi3 VLP provide MHC II epitopes for helper T cells to aid B cells in recognizing haptenic determinants on the attached antigen. So while it is clear that SpyCatcher VLPs can magnify humoral responses, there is still reason to investigate different ways of amplifying on-target and restrict off-target responses on this SpyCatcher VLP.

1.1.3 Existing methods of amplifying and targeting antibody responses

1.1.3.1 Removing undesirable epitopes

Complex protein antigens, with multiple epitopes, can bind a diverse range of B cells (Finney et al., 2018; Kuraoka et al., 2016). This results in interclonal B cell competition that binds both the epitope of interest and irrelevant epitopes (Caradonna and Schmidt, 2021). One way of reducing the pool of competing B cell clones is to eliminate the undesirable epitopes from an immunogen. Previously HIV Env, Influenza hemagglutinin (HA), and Respiratory syncytial virus (RSV) F proteins have been expressed in a truncated form to minimize antibody exposure to irrelevant epitopes, while retaining conformation of the target epitope (Caradonna and Schmidt, 2021). This resulted in the creation of trimeric HA stem, RSV head fusion, and engineered outer domain HIV Env trimers (Boyington et al., 2016; Corbett et al., 2019; Jardine et al., 2013; H. Wang et al., 2018).

1.1.3.2 Shielding undesirable epitopes

An alternative method of reducing the pool of competing B cell clones that bind to non-target epitopes (Fig 1.5 A) would be to occlude these intact regions. One way of doing this is to sterically occlude epitopes by binding antibodies to them, forming immune complexes (Fig 1.5 B). This approach has been attempted on HIV glycoproteins, flavivirus and influenza antigens, confirming a decrease in antibody response to the occluded epitopes (Caradonna and Schmidt, 2021; Tang et al., 2021; Tsouchnikas et al., 2015; Zarnitsyna et al., 2015). However, producing immune complexes may be challenging because it relies on the availability of high affinity monoclonal antibodies for different antigen strains and whether or not an antigen can remain stable with antibodies bound to it. When antibodies bind to a target epitope, this can affect protein conformation in other parts of the antigen and introduce new epitopes (Tsouchnikas et al., 2015). Immune complex vaccine candidates also pose a risk of triggering immune dysregulation in the form of prolonged FcγR signaling and inflammatory responses in chronic infectious and autoimmune diseases (Tang et al., 2021; Wang and Ravetch, 2015).

Another way of restricting off-target epitope responses is by introducing N-linked glycan sequons to sterically shield nearby epitopes (Fig 1.5 C). In their natural state, glycans are indispensable in nearly every aspect of a virus' life cycle. Glycans may mediate infection by helping viruses recognize host cells and interacting with molecules on the host cell surface (Li et al., 2021b). After infecting the host cell with its genome, most viruses rely on the endoplasmic reticulum to synthesize N-glycans and the Golgi apparatus to modify existing N-glycans and add O-glycans (Li et al., 2021b). As viral proteins are processed in the ER, immature glycans ($Glc_1Man_9GlcNAc_2$) serve as ligands for chaperones like calnexin and calreticulin to ensure that the protein is correctly folded (Li et al., 2021b). The absence of glycans limits the transport of proteins from the ER to the

Golgi (Dash et al., 1994; Luo et al., 2015), the release of viral progeny from host cells (Altgärde et al., 2015; Hanna et al., 2005), and ultimately the virus' transmissibility (Li et al., 2020; Mathys and Balzarini, 2015). Differences in glycan composition on viruses like HIV affect the binding of the virus to dendritic cell and macrophage surface receptors, which in turn influences the immune response that is generated against the virus (Li et al., 2021b; Lin et al., 2003; Willey et al., 1996)

Some antigens, like the SARS CoV-2 spike trimer and the HIV envelope protein, exploit their high density of glycans to block antibody recognition of surface epitopes (Casalino et al., 2020; Crispin et al., 2018; Wei et al., 2003). The presence of glycosylation on nanoparticle vaccine candidates can stimulate effective T cell and B cell dependent immune responses to displayed antigens (Alam et al., 2021; Hyakumura et al., 2015; Tokatlian et al., 2019; Zhang et al., 2020). The strategic placement of glycans on non-target regions of influenza HA and HIV Env proteins has enabled enhanced antibody responses to target previously subdominant epitopes like the HA head, the HA stem and the envelope CD4 binding site (Env CD4bs) (Bajic et al., 2019; Boyoglu-Barnum et al., 2020; Caradonna and Schmidt, 2021; Duan et al., 2018). At the same time, there are some instances in which the presence of glycans may not significantly increase serum binding, nor can it guarantee enhanced binding to a subdominant target epitope (Bajic et al., 2019; Caradonna and Schmidt, 2021; Duan et al., 2018; Thornlow et al., 2021).

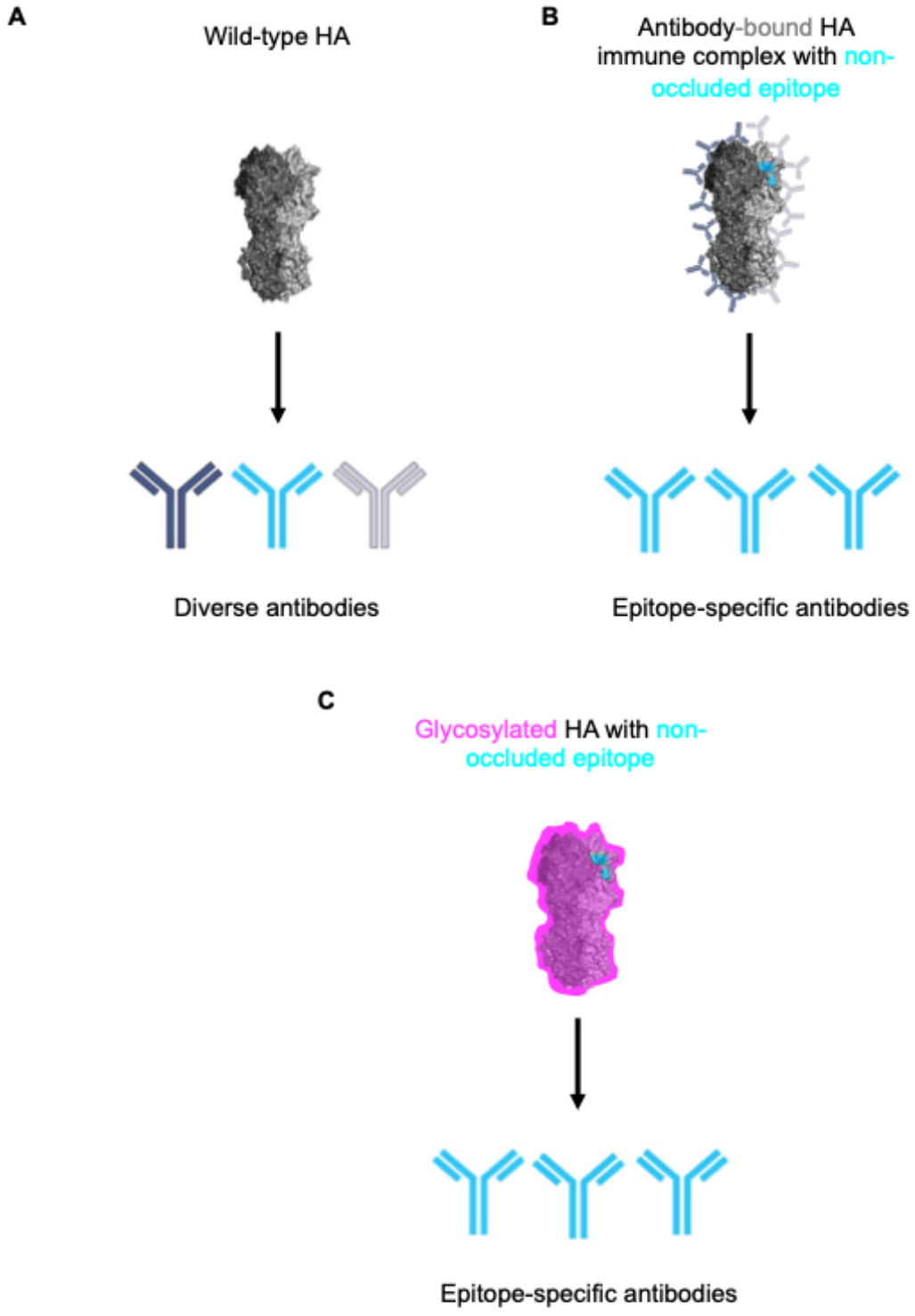


Figure 1. 5. Shielding undesirable epitopes with glycans and antibodies: **(**A) Wild-type HA elicits a range of antibodies (dark blue, light blue, gray) that bind to its epitopes;

(B) High affinity antibodies (dark blue and gray) can occlude epitopes in wild-type HA, as part of an immune complex, while focusing antibody response against an exposed epitope of interest (light blue); (C) Glycosylation (pink) on HA can occlude epitopes on wild-type HA, while focusing antibodies against a non-occluded epitope of interest (light blue). PyMOL rendering of influenza HA Trimer is based on PDB ID: 5UGY. Figure modified from images in Bajic et al., 2019.

1.1.3.3 Stabilizing prefusion conformation of viral proteins

After viruses attach to host cell receptors, stable viral envelope proteins transition to a metastable state in the acidic environment of endosomal vesicles to facilitate the fusion of the viral and endosomal membranes along with the delivery of viral genome to host cells (Pallesen et al., 2017). For some vaccines to work, the immune system must raise antibodies that prevent this fusion. Therefore, mutations stabilizing the prefusion conformation of viral envelope proteins in vaccines can lead to more effective antibody responses (Caradonna and Schmidt, 2021).

One way of stabilizing viral proteins is by introducing prolines, which have rigid backbone dihedral angles, to loops integral for transitioning the protein to a post-fusion state. For instance, stabilized versions of both MERS (Pallesen et al., 2017) and SARS-CoV-2 spikes (Hsieh et al., 2020) were generated by introducing two prolines in a loop, located on top of the trimer, effectively preventing human-viral membrane fusion. Prolines were also introduced to stabilize a hinge loop of RSV-F protein to prevent assembly of a long coiled-coil and subsequent transition into a postfusion conformation (Krarup et al., 2015).

Another way of stabilizing viral proteins is by engineering disulfide bonds between adjacent protein domains. Stabilized Lassa virus glycoprotein C (GPC) was made by introducing cysteines to covalently bind GP1 and GP2 together, to prevent GP2 from

forming a postfusion six-helical bundle configuration (Hastie et al., 2017). Similarly, stabilized HIV Env trimers were partly generated by engineering cysteine mutations to bind glycoproteins gp120 and gp41 together (Sanders and Moore, 2017). Along with an α-helix-breaking proline insertion, these mutations prevent gp41 from transitioning into a postfusion configuration (Sanders and Moore, 2017)

Stabilized prefusion HIV Env antigens have been deployed in clinical trials (Caradonna and Schmidt, 2021; Sanders et al., 2015; Sanders and Moore, 2017) and stabilized SARS-CoV-2 spike trimers are used in current COVID-19 vaccines (Caradonna and Schmidt, 2021; Hsieh et al., 2020; Tian et al., 2021).

1.1.3.4 Unmasking occluded epitopes

The enzymatic removal of glycans from the surface of hyperglycosylated antigens can help to expose some proximal epitopes to antibody recognition (Caradonna and Schmidt, 2021). This approach has previously succeeded in increasing the breadth of antibodies elicited against CD4bs on HIV Env (Dubrovskaya et al., 2019) and the stem of HA trimer (Liu et al., 2016). Removing glycans from the mutation-prone SARS-CoV-2 S protein elicits a robust and protective response in mice against the alpha, gamma, and delta variants of concern (Huang et al., 2022). At the same time, the removal of glycans that do not directly occlude an epitope can impact antibody binding to adjacent epitopes (Boyoglu-Barnum et al., 2020; Caradonna and Schmidt, 2021; Y. Huang et al., 2020b). Un-masking might not always ensure elicitation of broad antibody responses against glycan-occluded epitopes (Caradonna and Schmidt, 2021; Ringe et al., 2019). This technique may be limited in its applicability to generating VLP vaccine candidates because the removal of glycans can impact an antigen's ability to maintain its correct conformation.

1.1.3.5 Epitope resurfacing

One way of magnifying antibody responses to epitopes with subdominant responses is to graft epitope(s) of interest onto the surface of an antigenically distinct scaffold protein (Caradonna and Schmidt, 2021) (Fig 1.6). For instance, scientists have grafted non-circulating HA head strains onto the stem to focus antibody response towards the stem (Hai et al., 2012). Phase I clinical studies demonstrated that this chimeric protein was capable of eliciting cross-reactive antibodies against the HA stem (Bernstein et al., 2020; Caradonna and Schmidt, 2021). When the H1 HA receptor-binding site (RBS) epitope was grafted onto scaffolds consisting of non-circulating H4 and H14 HA strains, mice that were primed with H1 HA saw an increase in breadth of RBS-specific B cells following boost (Bajic et al., 2020; Caradonna and Schmidt, 2021). Beyond influenza antigen targets, grafting neutralizing epitopes of RSV-F protein onto orthogonal protein scaffolds also helped increase antibody titers against these select epitopes relative to their initial conformation and positions on the RSV-F protein (Caradonna and Schmidt, 2021; Sesterhenn et al., 2019, 2020). A disadvantage of epitope resurfacing lies in the possibility of new epitopes being introduced to the protein because of the grafting (Caradonna and Schmidt, 2021). To the best of my knowledge, there are no epitope-resurfaced vaccine candidates that are commercially available.

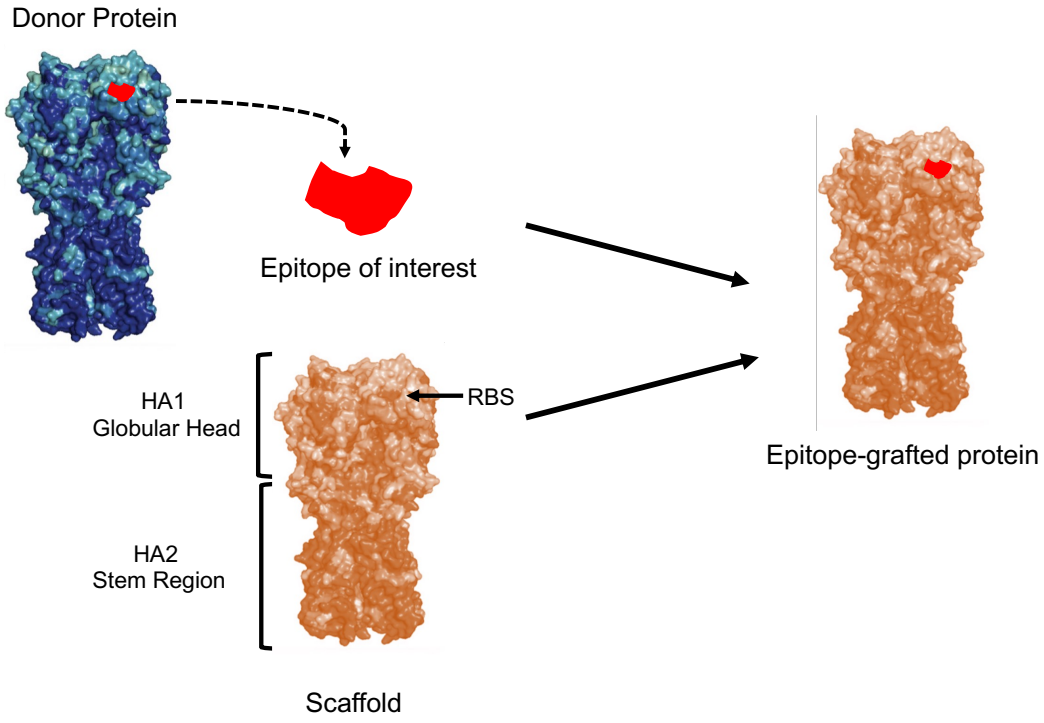


Figure 1.6. Epitope grafting procedure: The sequence from an epitope of interest (red) from a donor protein (light and dark blue) is inserted into the sequence of a distinct protein scaffold (orange) and expressed, resulting in an epitope-grafted protein (orange scaffold with red epitope of interest). Positions of HA1, HA2, and RBS (receptor binding site) are annotated on the HA trimer. PyMOL rendering of influenza HA trimer is based on PDB ID: 4JTV. Figure adapted from image in (Guthmiller et al., 2021).

1.1.3.6 Heterologous antigen display

The simultaneous display of multiple antigens on an immunogen can be configured to focus antibody responses to conserved epitopes by increasing the frequency each epitope is presented and ensuring all other non-target epitopes are presented only once (Caradonna and Schmidt, 2021) (Fig 1.7). It is believed this display format could help select for B cells with higher avidity for the conserved target epitope (Caradonna and Schmidt, 2021). Nanoparticles that simultaneously displayed HA variants elicited broadly protective antibodies that targeted the subdominant and conserved stem region of HA

(Boyoglu-Barnum et al., 2021). Additionally, co-displaying the RBDs of influenza HA variants on a nanoparticle raised neutralizing antibodies against an epitope centered on a conserved patch of the hypervariable HA head domain (Kanekiyo et al., 2019). In one case, immunizing with a heterologous HA trimer-displayed particle was not significantly different, in terms of induced cross-reactive B-cells, than immunizing with a mixture of corresponding homotypic HA trimer particles (Cohen et al., 2021a). This suggests that the advantages of heterologous antigen-displayed VLPs may be limited by the type of antigens displayed on the particles (Cohen et al., 2021a) . While the displayed HA trimer consists of both a head and a stem domain, it is possible that the conserved epitopes of the stem domain might be sterically occluded from BCR binding (Cohen et al., 2021a) . Furthermore, the HA trimers used in this study originated from group 1 and 2 influenza strains, while previous heterologous antigen-displayed particles displayed HA head domains from one subfamily (Cohen et al., 2021a; Kanekiyo et al., 2019).

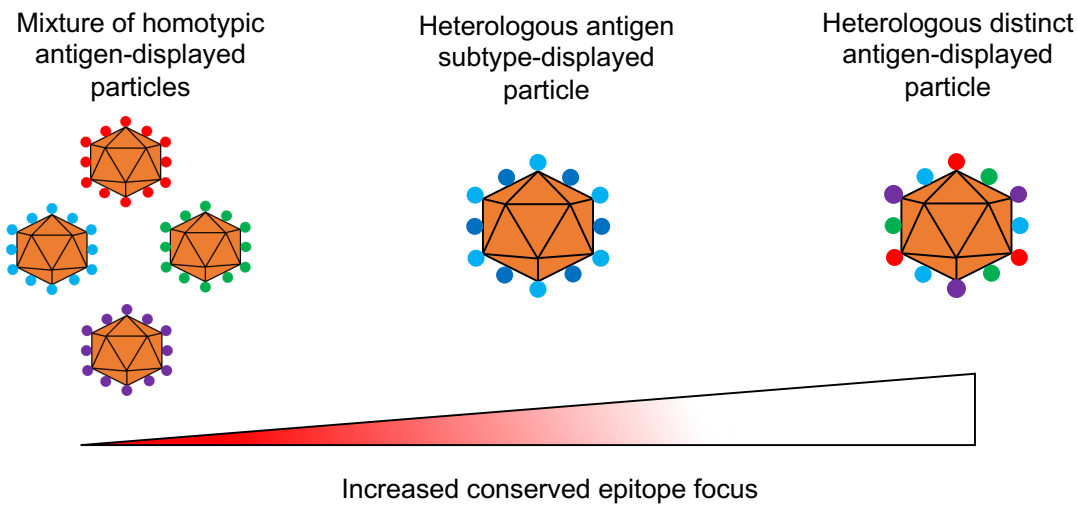


Figure 1.7. Heterologous antigen display strategy on VLPs to focus response on conserved regions*:* Heterologous distinct antigen-displayed particles offer enhanced antibody responses to conserved epitopes, more so than homotypic antigen-displayed VLPs and heterologous display of antigens within a subtype. Distinct antigens are represented by circles (red, green, light blue, and purple), displayed on an icosahedral VLP (orange). Dark blue circles represent an antigen subtype of light blue circles. Increased response to conserved epitopes is shown in a gradient from red to white (least to greatest).

1.1.4 Thesis objectives

The broad goal of my thesis is to investigate and rationally incorporate select immunomodulation strategies into a new modular VLP platform. The first goal was to incorporate the SpyCatcher003 protein onto the mi3 VLP scaffold with the aim of enhancing coupling to antigens, as well as improving stability and solubility. I also aimed to establish a purification method independent of affinity chromatography. I further conducted expression studies on SpyCatcher003-mi3 in mammalian cell-lines, to enable mammalian-type glycosylation. Considering the advantages and drawbacks of different antibody focusing techniques listed previously, I decided to examine the extent that SpyCatcher003-

mi3 can accommodate antibody shielding functions using N-glycosylation sequons and albumin binding sequences. For N-glycosylation, I aimed to provide a rational approach to engineer sequons on flexible loops of the VLP, before characterizing VLP stability and solubility. For albumin-binding, I start by discussing David Schramm's work on engineering soluble and stable VLP variants that show binding to serum albumin in plate assays. For both N-glycosylated and albumin-binding SpyCatcher003-mi3 VLPs, I evaluated the extent of antibody shielding by comparing the serum binding levels of the mi3 scaffold, the displayed RBD antigen, and the SpyCatcher003:SpyTag003 moiety between SpyCatcher003-mi3 and each VLP variant. I conclude by discussing each antibody shielding strategy and proposing future experiments that can characterize the surface area coverage of albumin or N-glycosylation on these VLPs or ways to expand the coverage.

Chapter 2: Materials and Methods

Chapter 2: Materials and Methods

2.1 Cloning

2.1.1 Polymerase chain reaction

Polymerase chain reactions (PCR) were performed using the Q5 High Fidelity DNA 2X Master Mix (New England BioLabs) in C1000 thermal cyclers (Bio-Rad). All single-stranded oligonucleotides and double-stranded gBlocks were ordered from Integrated DNA Technologies (IDT) in desiccated and desalted forms without additional purification.

Unless mentioned otherwise, all PCR reactions were conducted in a 25 µL volume with 10 ng template plasmid. The cycling conditions used in PCR were: initial denaturation for 3 min at 98 ^{o}C followed by 30 cycles of (98 ^{o}C denaturing for 30 s; 60-70 ^{o}C annealing for 30 s/kb and 72 ^{o}C extension for 2 min). The protocol ends with a final extension of 72 ^{o}C for 5 min before samples are cooled at 12 ^{o}C. PCR samples were kept at -20 ^{o}C, if not immediately used.

PCR products were analyzed by loading 25 µL of the reaction on a 1% (w/v) agarose gel containing 0.01% (v/v) SYBR Safe (Sigma-Aldrich) and run for 40 min at 180 V in TAE buffer (40 mM Tris, 20 mM acetic acid, 1 mM EDTA, pH 8.0) at 25 ^{o} C. Images of gels were taken using a Gel Imager Universal Hood II (Bio-Rad) and subsequently analyzed with Image Lab 6.0 Software (Bio-Rad).

Gel excision was performed on bands with amplicons of appropriate size determined by the 1 kb Plus dsDNA Ladder (New England BioLabs). Excision was performed on a XcitaBlue Conversion Screen and Filter (Bio-Rad) to protect the amplicons against possible UV damage. The gel-extracted fragments were purified using the QIAquick Gel Extraction Kit (Qiagen) and eluted in 30 µL volumes. 20 µL of the extracted

DNA was subjected to digestion with 2 µL DpnI (New England BioLabs; R0176S), mixed thoroughly and incubated at 37 ^{o}C for 4 h.

2.1.2 Gibson assembly

Gibson assembly was performed using a custom-made Gibson mix. This custom mix involves first making a 5X ISO Buffer by combining the following ingredients in a 15 mL Falcon tube (3 mL 1 M Tris-HCl, pH 7.25 at 25 ^{o}C; 1.5 g PEG-8000; 150 µL 2 M $MgCl_2$, 300 µL 1 M DTT (Dithiothreitol); 240 µL of 100 mM dNTP mix (25 mM each of dGTP, dCTP, dATP, dTTP; ThermoFisher 10297018); 300 µL of 100 mM NAD^+ (Nicotinamide adenine dinucleotide). MilliQ water was added to a final volume of 6 ml. A 320 µL aliquot of the 5X ISO buffer was then added to 454 µL of MilliQ H_2O, combined with 6.4 µL of 1U/ µL T5 Exonuclease (New England BioLabs; M0363S), and 160 µL of 40U/ µL Taq DNA Ligase (New England BioLabs; M0208L). All these ingredients were mixed properly before being poured into a plastic reservoir. A multichannel pipette was then used to transfer 10 µL aliquots into a strip of 8 Endotoxin-free PCR tubes. 10 µL aliquots of custom-made Gibson mix were stored at -20 ^{o}C. Unless specified otherwise, fragments of DpnI-digested plasmid backbone amplicons were mixed in molar ratios based on the length of fragment and the DNA concentration measured by Nanodrop (ThermoFisher Scientific). 0.48-0.50 pmol of combined plasmid amplicons were prepared as a 10 µL solution, with MilliQ water added to compensate for volume. This 10 µL mixture of plasmid amplicons was mixed via gentle pipetting on ice with the 10 µL aliquot of the prepared 2X Gibson mix previously described. This 20 µL mixture was then incubated at 48 ^{o}C in a C1000 thermal cycler (Bio-Rad) for 12-16 h.

2.1.3 Bacterial culture media preparation

All media used for bacterial culture was obtained following preparation by the Media Glassware Sterilization Laboratory of the Department of Biochemistry in the following manner:

SOC Medium (1 L Volume)

20 g Tryptone, 5 g Yeast Extract, 0.59 g NaCl, 0.186 g KCl, 2.03 g $MgCl_2.6H_2O$ and 2.46 g $MgSO_4.7H_2O$ were dissolved together in 820 mL of MilliQ water and autoclaved. 180 mL pre-sterilized 20% (w/v) Glucose was then added to the mixture.

LB Broth Low Salt (1 L Volume)

10 g Tryptone, 5 g Yeast Extract and 5 g NaCl were dissolved in 1 L of MilliQ water and its pH was adjusted to 7.0 at 25 ^oC. The mixture was then autoclaved for 20 min at 121 ^oC

Antibiotic concentrations were adopted as follows:

Ampicillin: 100 µg/mL

Kanamycin: 50 µg/mL

2.1.4 Transforming competent *E. coli*

Unless mentioned otherwise, all *E. coli* strains were transformed with expression plasmids in a similar manner. A 100 µL vial of *E. coli* was mixed with 0.5 ng of plasmid DNA. After two minutes on ice, the tube with *E. coli* and plasmid was immersed in a 42 ^oC water bath for 45 s. Immediately, the vial was set on ice for 5 minutes. This mixture was put into a 15 mL Falcon tube with 250 µL of SOC media then shaken for 1 h at 37 ^{o} C, 5% (v/v) CO_2 and 200 rpm to allow for the expression of the antibiotic resistance gene.

After 1 h, the 350 µL *E. coli* and SOC media mixture was spread thoroughly on 180 mm agar plates made with the appropriate antibiotic. Once the surface has dried, the plate was turned upside down and allowed to grow for 16-18 h at 37 ^oC.

2.1.5 Miniprep of plasmid DNA

A colony was picked from an LB agar plate and grown in 10 mL LB Low Salt media. This was contained in a 50 mL Falcon tube, supplemented with 1% (v/v) of appropriate antibiotic. This culture was incubated at 37 ^{o}C and shaken at 200 rpm for 16-18 h. The 10 mL culture was then spun down for 10 min in a centrifuge at 4000 x g. The resulting supernatant was discarded and Miniprep was performed via the GeneJet Plasmid MiniPrep Kit (ThermoFisher Scientific). The remaining pellet was resuspended in 500 µL of provided Resuspension Buffer with RNAse, and pipetted into a 2 mL Falcon tube with 500 µL of provided Lysis Buffer. This mixture was inverted 5 times until a clear solution formed. 700 µL of provided Neutralization Buffer was then added, resulting in a milk-like mixture. This mixture was then centrifuged for 10 min at 16,000 x g and added to a spin column provided by the manufacturer. Following a wash with 700 µL of Wash Buffer, the spin column was centrifuged for 2 min to get rid of residual ethanol. 30 µL of MilliQ H_2O was added to the column to elute the purified DNA. The concentration and purity of the DNA was then measured via 280 nm absorbance on Nanodrop (ThermoFisher Scientific).

2.1.6 Maxiprep of plasmid DNA

A colony was picked from an LB agar plate and grown in 200 mL LB Low Salt media. This was contained in a sterilized 500 mL glass Erlenmeyer flask, supplemented with 1% (v/v) of appropriate antibiotic. The resulting supernatant was discarded and Maxiprep was performed via the ZymoPURE II Plasmid Maxiprep Kit (Zymo Research; D4203). The bacterial cell pellet was first suspended in 14 mL of ZymoPURE P1 reagent and 14 mL of the provided ZymoPURE P2 reagent until the solution turned purple and viscous. Following the addition of 14 mL ZymoPURE P3 reagent, the lysate was loaded into a syringe filter and pushed through. The 33-35 mL of cleared lysate was mixed with 14 mL ZymoPURE Binding Buffer by inverting the 50 mL Falcon tube five times. The lysate-

binding buffer mixture was poured into the V-P (Vacuum Pump) Column Assembly and allowed to flow through completely. With the vacuum off, 5 mL ZymoPURE Wash 1 was added to the V-P Column assembly and allowed to pass through. 5 mL ZymoPURE Wash 2 was added and allowed to pass through, two times. The lower unit of the assembly was then attached to a 1.5 mL microcentrifuge tube and centrifuged for 1 min at 11,000 x g to get rid of residual wash buffer. The plasmid DNA was eluted with 400 µL ZymoPURE Elution buffer. The quality and concentration of DNA was assessed via 280 nm readings on Nanodrop (ThermoFisher Scientific).

2.1.7 Sanger sequencing

All expression constructs produced were verified in their region of interest or in an open reading frame. All Sanger sequencing was performed by Source Biosciences (Cambridge, UK).

2.2 Expression and purification of VLPs

2.2.1 *E. coli* protein expression and incubation conditions

VLPs were expressed in competent *E. coli* BL21 (DE3)-RIPL cells (Agilent). After transformation of expression plasmids and incubation for 16-18 h, a single colony was selected on 50 µg/mL kanamycin-supplemented LB agar plates. Single colonies were inoculated into a 10 mL culture of LB Low Salt media with 50 µg/mL kanamycin, grown up for 16-18 h at 37 ^{o}C and shaken at 200 rpm. 10 mL starter cultures were diluted in 1 L of pre-warmed LB Low Salt media with 50 µg/mL kanamycin. This mixture was incubated at 37 ^{o}C and 200 rpm until an A_{600} reading of 0.8 was reached. This culture was then induced with 0.5 mM of isopropyl β-D-1-thiogalactopyranoside (IPTG) and allowed to incubate at 22 ^{o}C and shaken at 200 rpm for 18-20 h.

2.2.2 Mammalian cell culture maintenance

Both Expi293-F and ExpiCHO cells (Thermo Fisher Scientific) were grown in 250 mL volume Erlenmeyer flasks with vent caps (Corning, Cat. No. 431144). Flasks held either 25 mL of Expi293-F Expression Medium (Thermo Fisher Scientific) or 30 mL of ExpiCHO Expression Medium (Thermo Fisher Scientific), supplemented with 50 U/mL of Penicillin, 50 µL/mL Streptomycin (Sigma Aldrich Cat. No. P4333), unless stated otherwise. The cell cultures were incubated in 37 ^{o}C and 5% (v/v) CO_2 until they reached 5 x 10^6 cells/mL, upon which they were subcultured.

2.2.3 Gel filtration chromatography of VLPs

Size exclusion chromatography was performed on the ÄKTA Pure 25 (GE Healthcare) system at 4^{o} C. All columns used were calibrated against a commercially-available molecular weight standard (BioRad, Cat. No. 151-1901). The following columns were used for the proteins of corresponding molecular weights: HiPrep 16/60 Sephacryl S400 HR column (GE Healthcare) for 20-8,000 kDa globular proteins; Superose 6 Increase 10/300 GL column (GE Healthcare) for 5-5000 kDa globular proteins; 10/300 HiLoad 16/600 Superdex 75 pg column (GE Healthcare) for 3-70 kDa proteins and HiLoad 16/600 Superdex 200 pg column (GE Healthcare) for 60-600 kDa proteins. All these columns were subjected to a 1 mL/min flow rate. Unless described otherwise, the primary mobile phase used was 25 mM Tris-HCl, 150 mM NaCl, pH 8.5 at 4 ^{o}C. Fractions of VLPs were identified based on SDS PAGE and collected, unless described otherwise. Protein concentration was determined using the Pierce bicinchoninic acid (BCA) Assay Kit (Thermo Fisher Scientific).

2.2.4 C-tag affinity purification of VLPs and antigens

One pellet derived from a 250 mL culture was suspended in 10 mL of lysis buffer, consisting of 25 mM Tris-HCl, 150 mM NaCl, pH 8.5 at 4 °C, 0.1 mg/mL lysozyme, 1 mg/mL cOmplete mini EDTA-free protease inhibitor (Sigma-Aldrich), and 1 mM phenylmethanesulfonyl fluoride (Sigma Aldrich). This mixture was then rotated for 1 h at 4 °C. The cell lysate was sonicated on ice for 5 min (10 s on and 10 s off), before it was centrifuged at 17,000 x g for 30 min at 4 °C. 2.5 mL of Capture Select C-tag Affinity Matrix (Thermo Fisher Scientific) was equilibrated to 25 mM Tris-HCl, 150 mM NaCl, pH 8.5 at 4 °C. The cleared lysate was divided into two falcon tubes, mixed with equal amounts of equilibrated resin, and rotated 1 h at 4 °C. The mixture was then poured into separate PolyPrep columns and washed with 25 mL of 25 mM Tris-HCl, 150 mM NaCl, pH 8.5 at 4 °C in each. Five fractions of proteins were eluted using buffer consisting of 20 mM Tris-HCl, 2 M MgCl2, pH 7.4 at 4 °C. Before each elution, there was a 5 minute incubation period with the buffer. The five eluted fractions were then diluted with a 10 × stock of 250 mM Tris-HCl, 1.5 M NaCl, pH 8.5 at 4 °C. Protein concentration was monitored via A280 readings on a Nanodrop (Thermo Fisher Scientific). The selected eluants were pooled then dialyzed in 300 kDa molecular weight cutoff cellulose ester dialysis tubing (SpectrumLabs) against 25 mM Tris-HCl, 150 mM NaCl, pH 8.5 for removal of $MgCl_2$ for 20 h at 4 °C. The dialyzed product was then concentrated in a 5 mL 30 kDa MWCO Vivaspin centrifugation unit (Sartorius) to 0.5 mL volume, before gel filtration chromatography.

2.2.5 His_6Tag affinity purification of proteins

Unless otherwise mentioned, 1 mL of Ni-NTA resin (Qiagen) equilibrated in a suitable buffer was added to cleared lysate for every 1 L of bacterial culture or 25 mL of Expi293/ExpiCHO culture. This mixture was incubated at 4 °C on a rolling incubator for 1 h. The resin-lysate mixture was then poured into Polyprep columns (Bio-Rad) and

permitted to flow through via gravity. The resin in the polyprep column was then washed with 10 × resin volume of Ni-NTA binding buffer (50 mM Tris-HCl, 300 mM NaCl, pH 7.8 at 4 °C) with 10 mM imidazole. After the buffer flowed through with gravity, the resin was then washed twice with 10 × resin volume Ni-NTA binding buffer with 30 mM imidazole. Proteins were eluted from binding Ni-NTA beads after the resin was incubated with the 1× resin volume of elution buffer, consisting of Ni-NTA binding buffer with 200 mM imidazole, for 5 minutes. Subsequent elution samples were taken while 280 nm absorbance reads were monitored on Nanodrop. The collected protein fractions were then monitored on an SDS protein gel. Relevant fractions were then pooled, dialyzed in an appropriate buffer to remove imidazole and concentrated in a Vivaspin centrifugation unit of appropriate MWCO, before being subjected to gel filtration chromatography.

2.2.6 Mammalian cell expression and purification of VLPs

Cryo-preserved vials of Expi293-F cells were subcultured twice and allowed to grow to $3 \times 10^6 – 5 \times 10^6$ cells/mL. ExpiCHO cells were subcultured twice and allowed to grow to $6 \times 10^6 – 8 \times 10^6$ cells/mL. Unless specified otherwise, mammalian cells were cultured in 250 mL flasks (Corning). One day before transfecting the cells, Expi293-F cells and ExpiCHO cells were adjusted to 3×10^6 - 4×10^6 cells/mL and were allowed to grow for 17-20 h. Samples were taken from each culture and Trypan Blue staining (Thermo Fisher Scientific; 15250061) was performed to validate 95-99% viability. Expi293-F cells were diluted to a final density of 3×10^6 viable cells/mL and ExpiCHO cells were diluted to a density of 3×10^6 viable cells/mL. The adjusted cultures were then resuspended in 50 mL of 0.22 μm filtered, 37 °C warmed media. Unless specified otherwise, 60 μg of plasmid DNA was used for transfecting each 50 mL culture volume. For expression in Expi293-F cultures, 3 mL of pre-warmed media was mixed with the 160 μL of Expifectamine 293 reagent, which was then incubated with 3 mL of warmed media mixed with 160 μg of

plasmid DNA for 20 min. The 6 mL mixture was then slowly added to the 250 mL flask and allowed to incubate in a 37 °C , 7% (v/v) CO_2 shaking incubator for 18-22 h. Subsequently 300 µL of Expi293 Enhancer 1 and 3 mL of Expi293 Enhancer 2 were added to the flask. In an attempt to express a mannose-dense S50 Glyc. SpyCatcher003-mi3 VLP, I then added kifunensine to the culture flask equivalent to a 5 nM concentration.

For expression in Expi-CHO cultures, 2 mL of 37 °C pre-warmed media was mixed with the 160 µL of Expifectamine CHO reagent, which was then incubated with 2 mL of warmed media mixed with 160 µg of plasmid DNA for 5 minutes. This 4 mL mixture was then slowly added to the 250 mL flask and allowed to incubate in a 37 °C , 7% (v/v) CO_2 shaking incubator for 18-22 h. Subsequently 300 µL of ExpiCHO Enhancer and 12 mL of ExpiCHO Feed were added to the flask.

Expi293-F cells were harvested after 5 days and ExpiCHO cells after 10 days. Upon harvest, cultures were centrifuged at 4,000 x g for 10 min and the cleared lysate was pushed through a 0.22 µm filter. The filtered lysate from one 30 mL culture was suspended with 2 mL of CaptureSelect™ C-tag XL (ThermoFisher Scientific) resin or CaptureSelect™ C-tag affinity matrix (ThermoFisher Scientific) resin and incubated on a roller for at least 2 h in 4 °C. The same wash, elution, and dialysis procedures mentioned in Section 2.2.4 were followed for purification of mammalian cell-expressed VLPs.

2.2.7 Ammonium sulfate precipitation of VLPs

The amount of 99% Pure Laboratory Grade Ammonium Sulfate (Thermo Fisher Scientific) required for 15% (w/v) to 30% (w/v) precipitations was weighed out based on an online calculator provided by Encor Biotechnology (https://www.encorbio.com/protocols/AM-SO4.htm). 25 mL of 0.22 µm filtered cleared lysate from bacterial or mammalian cultures was then aliquoted into 50 mL Falcon tubes. The designated amount of ammonium sulfate was poured into the tube gradually and set

on a roller to dissolve particulates before the rest of the ammonium sulfate was added. A magnetic stir bar was then put into the 50 mL Falcon tube. The 50 mL Falcon tube was then turned upside down and allowed to stir at 200 rpm for 1 h at 4 °C. The incubated sample was centrifuged for 30 min at 30,000 x g at 4 °C and remaining pellet was resuspended in 5-7.5 mL of 25 mM Tris-HCl, 150 mM NaCl, pH 8.5 at 4 °C. The ammonium sulfate precipitated product was then dialyzed twice against 25 mM Tris-HCl, 150 mM NaCl, pH 8.5 at 4 °C for 12 h each at a 150-fold excess and for another 12 h at a 200-fold excess. The sample was subsequently filtered with a 0.22 µm syringe filter and 1 to 1.5 mL of sample was used run on an equilibrated HiPrep 16/60 Sephacryl S-400 HR (GE Healthcare) column for gel filtration chromatography, using the mobile phase buffer of 25 mM Tris-HCl, 150 mM NaCl, pH 8.5 at 4 °C. These elutions between the 45-65 mL range were concentrated using a 30 kDa spin column and measured for concentration using a Pierce bicinchoninic acid (BCA) assay (Thermo Fisher Scientific).

2.2.8 Spy & Go affinity purification of SpyTag-RBD

Harvested Expi293-F cell lysate is diluted such that one-third of its final volume is TP buffer (25 mM orthophosphoric acid and adjusted to pH 7.0 at 22 °C with Tris-base). TP buffer-equilibrated pre-made Spy&Go resin (Khairil Anuar et al., 2019) is then mixed with the diluted supernatant and incubated on a roller at 4 °C for 1 h. Upon pouring the resin-lysate mixture into a Polyprep column, the buffer is allowed to flow through via gravity. The set resin is then washed twice with ten column volumes of TP buffer. One column volume of 2.5 M Imidazole in TP buffer, pH 7.0 at 25 °C is added to the resin mixture and incubated for 5 minutes before elutions are collected. Five elutions are collected before these fractions are run on SDS-PAGE and stained with Coomassie. Relevant fractions are then pooled and dialyzed against a buffer consisting of 10 mM Tris-HCl, 200 mM NaCl, pH 8.0 at 4 °C. The dialyzed fractions are then concentrated using the

10 kDa MWCO Vivaspin centrifugal unit and purified via SEC using the Superdex 75pg 16-600 column, run at 1 mL/min flow rate with the dialysis buffer used as its mobile phase.

2.2.9 Endotoxin removal and quantification

Potential sources of endotoxin were removed from purified protein preps using Triton X-114 phase separation. Preps were put into endotoxin-free 1.5 mL microcentrifuge tubes (StarLab, cat. no. E1415−1510) and adjusted so that 1% (v/v) Triton X-114 (Sigma Aldrich) was added to each prep. The samples were placed on ice and gently mixed by pipetting until all the Triton X-114 was dissolved. Following dissolution, the samples underwent 37 ^{o}C incubation for 5 min and centrifugation for 1 min at 16,900 x g at 37 ^{o}C. The top phase was was carefully pipetted off, placed into an unused endotoxin-free 1.5 mL microcentrifuge tube, and this same procedure was repeated on the collected top phase twice. Endotoxin concentration was then quantified using the Limulus amebocyte lysate (LAL) Endotoxin Quantification Kit (Thermo Fisher Scientific). For all immunized VLPs, the endotoxin level was maintained below the recommended 20 endotoxin units/mL (EU/mL) for administration of recombinant protein vaccines (Brito and Singh, 2011).

2.2.10 Residual nucleic acid quantification

C-tag affinity purified SpyCatcher003-mi3 and 20% (w/v) ammonium sulfate precipitated SpyCatcher003-mi3 was adjusted to 0.125 mg/mL. Standard protocol in the Quant-iT PicoGreen dsDNA kit (Invitrogen; P11496) was followed to prepare reagents, standard, and to measure sample fluorescence. This experiment was carried out on a 96-well microplate for fluorescent plate assays (Invitrogen; M33089) covered with aluminum foil and performed in a 25 ^{o}C dark room.

2.3 Glycan analysis and characterization of VLPs

2.3.1 PNGase F digestion

Digestion with PNGase F (Peptide-N-Glycosidase F) (New England BioLabs; P0704S) was used to assess the presence of N-linked glycans on proteins. PNGase-F is an amidase that specifically cleaves the glycosidic bond between the first N-acetylglucosamine precursor and asparagine residue of hybrid, high mannose, and complex N-linked oligosaccharides. 2 µg of protein was combined 1 µL of provided 10X Glycoprotein Denaturing Buffer and MilliQ water to make a 10 µL total reaction volume. After heating this mixture at 100 ^{o}C for 10 min in a C1000 Thermal Cycler, the denatured glycoprotein was set on ice and centrifuged for 10 s. This volume was then combined with 2 µL of provided 10X GlycoBuffer 2, 2 µL of provided 10% (v/v) NP-40 and 6 µL MilliQ water to make a 10 µL total reaction volume. 1 µL of PNGaseF was added to the 20 µL mixture (consisting of protein, Glycoprotein Denaturing Buffer, MilliQ water, GlycoBuffer2 and 10% (v/v) NP-40) and incubated at 37 ^{o}C for 1 h. 10 µL volumes of both a control and the digested proteins were run simultaneously on a 16% (w/v) non-reducing SDS-PAGE and visualized by Coomassie staining for the presence of a downward shift.

2.3.2 Endo H_f digestion

Digestion with Endo H_f (protein fusion of Endoglycosidase H and maltose binding protein) (New England BioLabs; P0703S) was used to assess the presence of mannose-dense glycans on proteins. Endo H_f specifically cleaves the diacetylchitobiose core, between the first and second N-acetylglucosamines closest to asparagine, of mannose-rich N-linked oligosaccharides (Maley et al., 1989). 1 µg of protein was combined with 1 µL of provided 10X Glycoprotein Denaturing Buffer and sufficient MilliQ water to make a 10 µL reaction volume. This sample was heated at 100 ^{o}C for 10 min in a C1000 Thermal Cycler.

2 µL of provided 10X GlycoBuffer 3, 1 µL of Endo H_f, and enough MilliQ water to make a total 20 µL reaction volume was combined with the denatured protein for incubation on a C1000 Thermal Cycler for 1 h at 37 ^oC. 10 µL of both a control and the digested proteins were run simultaneously on 16% (w/v) non-reducing SDS-PAGE and visualized by Coomassie staining for the presence of a downward shift.

2.3.3 VLP sample preparation for LC-MS-ESI quantification

This procedure was performed by Dr. Joel Allen from Prof. Max Crispin's group at the University of Southampton. 0.17 mg of S50 Glyc. SpyCatcher003-mi3, 0.2 mg SpyCatcher003-G124 Glyc. mi3, and 0.2 mg S50 Glyc. SpyCatcher003-mi3 with Kifunensine VLPs were denatured, in triplicates, for 1 h in a solution of 50 mM Tris-HCl (pH 8.0 at 25 ^oC) with 6 M urea and 5 mM dithiothreitol (DTT). The VLPs were then reduced and alkylated with 20 mM iodoacetamide (IAA), incubated in the dark for 1 h and further incubated for 1 h in 20 mM DTT to remove residual IAA. The alkylated glycosylated VLP proteins were then buffer exchanged into 50 mM Tris-HCl (pH 8.0 at 25 ^oC) using a 3 kDa MWCO Vivaspin ultrafiltration unit (Sartorius) and two of the triplicate samples were digested overnight with trypsin, chymotrypsin (Mass Spectrometry grade, Promega), and alpha-lytic protease (Sigma Aldrich) at a 1:30 (w/w) ratio. The digested peptides were dried and extracted with the C18 Zip-tip (Merck Millipore). Dr. Joel Allen adopted this protocol from his lab's prior work (Eldrid et al., 2021).

2.3.4 LC-MS-ESI quantification of VLP glycan composition

This procedure was performed by Dr. Joel Allen from Prof. Max Crispin's group at the University of Southampton. The extracted peptides were dried and resuspended in 0.1% formic acid. This was "analyzed by nano-scale liquid chromatography in combination with electrospray ionization-mass spectrometry (nanoLC-ESI-MS), with an Ultimate 3000

high-performance liquid chromatography (HPLC) [system] (Thermo Fisher Scientific) and an Orbitrap Eclipse mass spectrometer (Thermo Fisher Scientific), [utilizing] electron-transfer high-energy collision dissociation fragmentation" (Eldrid et al., 2021). The fragmented peptides were separated via an EasySpray PepMap RSLC C18 analytical column (dimensions: 75 µm × 75 cm). A PepMap 100 C18 column (3 µm × 75 µm × 2 cm) was used as a trapping column prior to the analytical column. The LC conditions employed to ensure all the sample was eluted from column were: a "280 min linear gradient with 4-32% (v/v) acetonitirile in 0.1 % (v/v) formic acid over 260 min followed by 20 min of alternating 76% (v/v) acetonitrile in 0.1% (v/v) formic acid and 4% (v/v) acetonitrile in 0.1% (v/v) formic acid" (Eldrid et al., 2021). The system's flow rate was set to 300 nL/min, spray voltage maintained at 2.7 kV, and the capillary set to 40 ^{o}C. The temperature of the ion transfer tube was maintained at 275 ^{o}C and scan range set to 375-1500 m/z. The reaction kinetics of electron-transfer high-energy collision dissociation was determined via "prior calibration using PierceFlexMix and supplemental higher energy collision dissociation set to 15%" (Eldrid et al., 2021) The Orbitrap resolution set for precursor and fragment detection was MS1=120,000 and MS2=30,000. The MS1 AGC target "was set to standard and injection time was set to auto" (Eldrid et al., 2021). Dr. Joel Allen adopted this protocol from his lab's prior work (Eldrid et al., 2021).

2.3.5 Data analysis of LC-MS-ESI results

This procedure was performed by Dr. Joel Allen from Prof. Max Crispin's group at the University of Southampton. Byos (Version 3.5; Protein Metrics Inc.) was used to extract fragmentation data from the raw file. Peptides with scores above 100 were accepted and evaluated as a true positive if "the correct combination of a-, b-, c-, x-, y-, z- fragment ions were observed with oxonium ions" for each N-linked glycan (Eldrid et al., 2021). Protein Metrics 305 N-linked glycan library, with manually added sulfated glycans, was used to

identify MS data of peptides. The relative site occupancy of each glycan and the unoccupied portion was determined by chromatography peak areas for peptides with an identical amino acid sequence. “The precursor mass tolerance was set at 4 to 10 ppm for fragments” with a 1% false discovery rate permitted (Eldrid et al., 2021). The quantity of each glycan type per N-linked sequon and the unoccupied portions were based on extracted ion chromatographic areas for peptides with identical amino acid sequence. Possible O-linked glycans were determined for each peptide using extracted ion chromatographic areas and its occupancy was quantified across multiple repeats. Dr. Joel Allen adopted this protocol from his lab’s prior work (Eldrid et al., 2021).

2.4 Characterization of VLP solubility, stability and reactivity

2.4.1 Dynamic light scattering

When analyzing heated VLPs, these samples were subjected to temperatures of 25 ^{o}C, 37 ^{o}C, 55 ^{o}C, 75 ^{o}C, or 95 ^{o}C for 1 h and cooled at 4 ^{o}C for 10 min using a C1000 thermal cycler (Bio-Rad). These heated samples were centrifuged for 30 min at 16,900 x g to remove aggregates, then adjusted to 0.125 mg/mL using 0.22 µm filtered buffer consisting of 25 mM Tris-HCl, 150 mM NaCl, pH 8.5 at 4 ^{o}C. Otherwise, VLP samples were adjusted to 0.1 mg/mL using 0.22 µm filtered buffer consisting of 25 mM Tris-HCl, 150 mM NaCl, pH 8.5 at 4 ^{o}C and centrifuged for 30 min at 16,900 x g to remove aggregates. 20 µL of the sample was loaded into a re-usable cuvette and each sample was measured at 20 ^{o}C using an Omnisizer (Viscotek) with 10 scans of 10 s each. The intensity distribution of triplicate samples were plotted and its average/standard deviations tabulated in Excel.

2.4.2 Temperature-dependent solubility assay

Unless otherwise specified, 50 µL of SpyCatcher-mi3 or SpyCatcher003-mi3 variants at 30 µM concentration in 25 mM Tris-HCl, 150 mM NaCl, pH 8.5 at 4 ^{o}C were incubated at 25 ^{o}C, 37 ^{o}C, 55 ^{o}C, 75 ^{o}C, or 95 ^{o}C for 1 h and cooled at 4 ^{o}C for 10 min using a C1000 thermal cycler (Bio-Rad). Following incubation, these samples were centrifuged for 30 min at 16,900 x g to remove aggregates. The supernatant was run on 16% (w/v) SDS PAGE and its band intensity after Coomassie staining was analyzed using Image Lab 6.0 software (Bio-Rad). The 25 ^{o}C sample was defined to be 100% soluble. The band intensity of each temperature was plotted in triplicates and its average/standard deviations tabulated in Excel.

2.4.3 Model SpyTag-Antigen reaction time course

200 µL of 1 µM of each VLP variant subunits buffered in 25 mM Tris-HCl, 150 mM NaCl, pH 8.5 at 4 ^{o}C was reacted with 200 µL of 3 µM of affinity-purified SUMO-SpyTag003, buffered in 1X PBS pH 7.4. Each sample was thoroughly mixed in a 1.5 mL tube and set to react at 25 ^{o}C for 0.5 min , 1 min, 3 min, 5 min, 10 min time points. Each reaction was stopped by mixing 1X SDS Loading Buffer and incubated at 99 ^{o}C. This reaction was performed in triplicates. 10 µL of reacted samples between 0.5 min and 10 min were run alongside unreacted VLPs and SUMO-SpyTag003 proteins on 16% (w/v) SDS-PAGE with Coomassie staining. The band intensities of unreacted and reacted VLP subunits were analyzed using Image Lab 6.0 software (Bio-Rad). The percentage of reacted product = 100 × [1-(VLP subunits band post-SUMO incubation)/(un-reacted VLP subunits band)]. The percentage of reacted product was plotted as a function of time in triplicates, with averages and standard deviations in Excel.

2.4.4. Transmission electron microscopy (TEM)

This procedure was performed by Niels Wicke. 0.3 mL of 0.1 mg/mL VLPs in 25 mM Tris-HCl, 150 mM NaCl, pH 8.5 at 4 ^{o}C was centrifuged for 30 min at 16,900 x g. These samples were applied onto carbon 200 mesh copper grids for 2 min, blotted with filter paper, stained with 2% (w/v) uranyl acetate for 10 s, and blotted again before being air-dried. A FEI Tecnai T12 transmission electron microscope was used to image grids at 120 kV on a Gatan US1000 CCD camera.

2.5 Assessing immunogenicity of nanoparticles

2.5.1 VLP preparation for vaccination

Unless mentioned otherwise, 250 µL of 2 µM Expi293-F expressed VLP subunits were reacted with 250 µL of 12 µM SpyTag-RBD for 24 h at 4 ^{o}C. These RBD-coupled VLPs were dialyzed 1:2000 into endotoxin-free 25 mM Tris-HCl, 150 mM NaCl, pH 8.5 at 4 ^{o}C for 24 h in a 1 MDa MWCO membrane (Spectrum Laboratories). The dialyzed product was then spun down at 16,900 x g for 30 min. 10 µL of the RBD-coupled and un-coupled VLPs were run on 16% (w/v) SDS-PAGE with Coomassie staining. The band intensities of reacted and unreacted VLP subunits were measured using Image Lab 6.0 software (Bio-Rad) to estimate the percentage of VLP subunits coupled with RBD. The same Coomassie-stained SDS gel was also monitored to ensure dialysis efficiency and that uncoupled RBDs were absent in the samples used for mice immunization. LAL Chromogenic Endotoxin Quantitation Kit (Thermo Fisher Scientific) was used to measure endotoxins. All samples used for immunization possessed <20 EU/mL endotoxin. BCA was used to measure the protein concentration of the RBD-coupled VLPs. All RBD-coupled VLP samples were prepared 2-3 days prior to immunization and stored at 4 ^{o}C.

2.5.2 Mice immunization and blood sampling

Dr. Tiong Tan from Prof. Alain Townsend's laboratory performed this procedure. The equivalent of 0.5 µg of RBD coupled to SpyCatcher003-mi3 VLPs or in unconjugated form were adjuvanted with Addavax (Invivogen) in a 1:1 ratio (adjusted to volumes of 25 µL VLP + 25 µL Addavax for one dose). Mice immunization was "performed according to UK Animals (Scientific Procedures) Act Project License (PBA43A2E4) and approved by the University of Oxford Local Ethical Review Body" (Tan et al., 2021). 5 week-old female C57BL/6 mice (Envigo) were housed in compliance "with the UK Home Office ethical and welfare guidelines and fed standard chow and water *ad libitum*" (Tan et al., 2021). Unless mentioned otherwise, six mice were immunized intramuscularly with 0.5 µg/dose of RBD each on day 0 and 14 and monitored at least twice weekly by observation and weighing. On day 42, cardiac puncture was performed to humanely sacrifice the mice and collect sera samples. These whole blood samples were collected in Microtainer SST tubes (BD) and permitted to clot at 22 ^{o}C for 1-2 h before being centrifuged at 10,000 x g for 10 min. The clarified sera were then transported to fresh tubes and heat inactivated at 56 ^{o}C for 30 minutes before they were stored at -20 ^{o}C.

2.5.3 Endpoint ELISA

96 well MaxiSorp microtiter plates (Thermo Fisher) were coated for 24 h at 4 ^{o}C with 50 µL of recombinant RBD antigen, mi3-C-tag, or SpyCatcher003:SpyTag003 at 2 µg/mL concentration in 1X PBS, pH 7.4. Plates were then washed three times with 200 µL PBS/T (1X PBS, pH7.4 with 0.5% (v/v) Tween-20) per well. Each well on the plate was then blocked with PBS/T with 10% (w/v) skim milk for 1 h at 25 ^{o}C. These plates were washed another three times with 200 µL PBS/T per well. Unless otherwise mentioned, each well was incubated with 50 µL of two-fold serially diluted duplicate serum samples for 1 h at 25 ^{o}C. For glycosylated SpyCatcher003-mi3 VLPs, my serum dilutions in PBS/T with

10% (w/v) skim milk ranged between 1:50 and 1:102,400. For albumin-binding SpyCatcher003-mi3 VLPs, my serum dilutions in PBS/T with 10% (w/v) skim milk ranged between 1:100 and 1:12,800. Plates were washed a further three times with 200 µL PBS/T per well and 50 µL of HRP-conjugated goat anti-mouse total IgG (Sigma-Aldrich) diluted 1:1,500 in PBS/T with 10% (w/v) skim milk was added to each well and incubated for 1 h at 25 ^{o}C. Following another three washes with PBS/T, 50 µL of 1-Step Ultra TMB ELISA Substrate Solution (ThermoFisher, 34028) was added to develop each well. Absorbance measurements at 652 nm after 5 minutes incubation for the glycosylated VLPs and after 1 minute incubation for the albumin-binding VLPs, were obtained using a FLUOstar Omega plate reader (BMG Labtech). The endpoint titer is defined as the x-axis intercept of the dilution curve at a mean 652 nm absorbance reading of eight antigen-coated wells not incubated with serum, plus ten standard deviations.

2.5.4 IgG subtyping

96 well MaxiSorp microtiter plates (Thermo Fisher) were coated for 24 h at 4 ^{o}C with 50 µL of recombinant RBD antigen at 2 µg/mL concentration in 1X PBS, pH 7.4. Plates were then washed three times with 200 µL PBS/T (1X PBS, pH7.4 with 0.5% (v/v) Tween-20) per well. Each well on the plate was then blocked with PBS/T with 10% (w/v) skim milk for 1 h at 25 ^{o}C. Plates were washed another three times with 200 µL PBS/T and each well was incubated with 50 µL of four-fold serially diluted duplicate serum samples, ranging from 1:50 to 1:52,428,800, for 1 h at 25 ^{o}C. Plates were washed a further three times with 200 µL PBS/T per well. 50 µL of HRP-conjugated goat anti-mouse IgG1 (Bethyl Laboratories) diluted 1:1,500 in PBS/T with 10% (w/v) skim milk was added to each well to measure Th2 response. 50 µL of HRP-conjugated goat anti-mouse IgG2a/c (Bethyl Laboratories) diluted 1:1,500 in PBS/T with 10% (w/v) skim milk was added to each well to measure Th1 response. These plates were then incubated for 1 h at 25 ^{o}C. Following

another three washes with PBS/T, 50 µL of 1-Step Ultra TMB ELISA Substrate Solution (ThermoFisher, 34028) was added to develop each well. Absorbance measurements at 652 nm after 5 minutes incubation, unless otherwise mentioned, were obtained using a FLUOstar Omega plate reader (BMG Labtech). The definition of endpoint titers used here was similar to that described in section 2.5.3.

2.5.5 Statistical analysis of ELISA

Statistical analysis was performed for all endpoint ELISAs in this study using GraphPad Prism 7.0. Unless otherwise mentioned, significance between different immunization groups were performed on $\log_{10}$-transformed data using one-way ANOVA with Bonferroni correction. In all statistical tests, $p<0.05$ were reported as significant; $p>0.05$ were reported as non-significant (n.s.).

2.6 Structure visualization

PyMOL version 2.2.2 was used to visualize all protein structures. The models visualized here include the parent domain of SpyCatcher003 based on PDB: 2X5P and SpyTag based on PDB: 4MLI. A design model of the i301 nanocage, constructed from twenty copies of the Class I KDPG aldolase trimer (PDB: 1WA3) with E26K, E33L, K61M, D187V, and R190A mutations arranged in icosahedral symmetry, was used in this study as a close representation of the mi3 scaffold (Hsia et al., 2016). B-factors between 0 and 20 were represented on each subunit of the computationally-designed i301 nanocage by a gradient transitioning from red to blue, respectively. B-factors between 0 and 30 were represented on structures of the SpyCatcher003 parent domain and SpyTag by a gradient transitioning from red to blue, respectively.

Chapter 3: Development of the SpyCatcher003-mi3 VLP Scaffold

Chapter 3: Development of the SpyCatcher003-mi3 VLP Scaffold

VLP vaccines safely deliver antigens to the immune system through multimerization on an immunogenic scaffold, by promoting lymph node drainage and uptake by antigen presenting cells (Bachmann and Jennings, 2010). The dense, repetitive display of antigens on the VLP surface promotes B-cell receptor cross-linking and activation (Bachmann et al., 1993; Schiller and Lowy, 2018).

There are different methods available for generating VLPs. Immunogenic VLPs for some arenaviruses (Strecker et al., 2003), paramyxoviruses (McGinnes et al., 2011; Walpita et al., 2011) and bunyaviruses (Habjan et al., 2009; Överby et al., 2006; Shi et al., 2006) can form solely due to the presence of expressed viral matrix, capsid, and fusion glycoproteins. Recombinant antigens can be conjugated to VLP scaffolds via chemical conjugation, genetic fusion, bio-orthogonal chemistry using unnatural amino acids (Brune and Howarth, 2018; Patel and Swartz, 2011; Smith et al., 2013), or two-component assembly (Bale et al., 2016; Brouwer et al., 2019; Walls et al., 2020). Genetic fusion can be problematic because of the possibility that the folding of complex antigens may interfere with particle assembly (Brune and Howarth, 2018; Bruun et al., 2018; Smith et al., 2013). Chemical conjugation results in non-uniform coverage of antigens on the VLP surface (Brune and Howarth, 2018; Bruun et al., 2018). An alternative conjugation strategy is to separately optimize the antigen and scaffold production and later assemble both components together. This would be possible using the SpyCatcher-SpyTag protein-peptide pairing via an isopeptide bond (Fig 3.1 A) formed between Lys and Asp (Zakeri et al., 2012). In the context of a VLP, this means that SpyCatcher-scaffold and SpyTag-antigen expression can be optimized separately (Fig 3.1B).

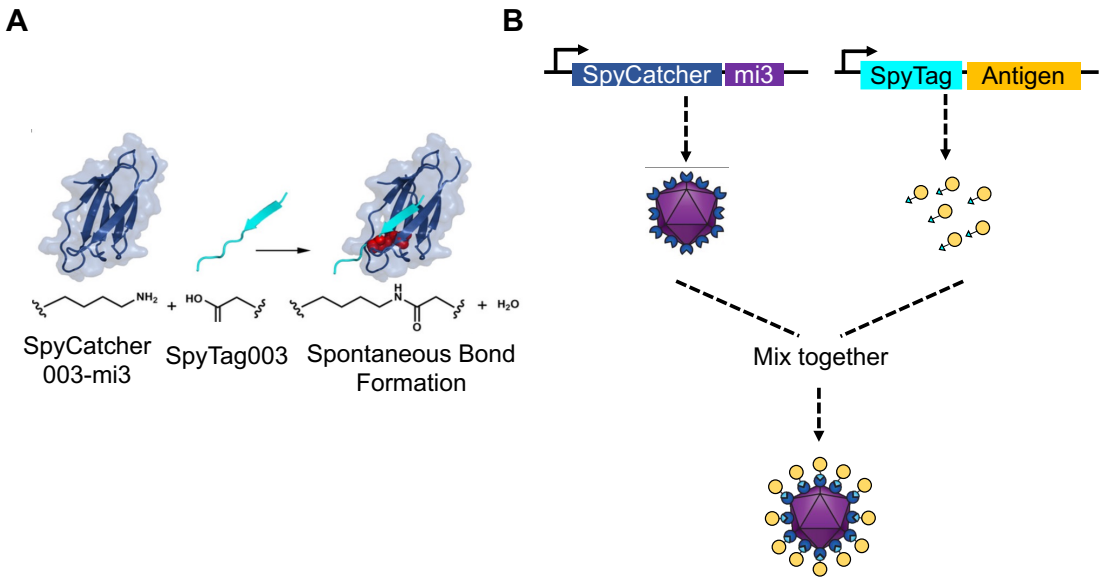


Figure 3.1. Design principle of the SpyCatcher VLP platform: (A) SpyCatcher and SpyTag proteins are derived from splitting of the CnaB2 domain, forming an irreversible isopeptide bond upon mixing. Image adapted from Rahikainen et al., 2021. (B) SpyCatcher-mi3 and SpyTag-antigens can be expressed separately and form a decorated VLP by mixing both components. Image adapted from Brune et al., 2016.

Karl Brune, a former DPhil student from the Howarth laboratory, designed the SpyCatcher-AP205 VLP by conjugating an N-terminal truncated SpyCatcher to the cp3 coat protein from bacteriophage AP205 (Brune et al., 2016). SpyCatcher-AP205, conjugated to the recombinant malarial antigen Pfs25-SpyTag, elicited higher quality antibodies for malaria transmission-blocking than Pfs25 conjugated to the IMX313 and Qβ assembly platforms (Leneghan et al., 2017). SpyCatcher-AP205 also generated high specific-antibody titers against cancer antigens and allergy-related cytokines (Palladini et al., 2018; Thrane et al., 2016). In spite of SpyCatcher-AP205's ability to generate relevant antibodies, SpyCatcher-AP205's low expression yield and low stability are problems that

hinder its development as a practical vaccine (Bruun et al., 2018). The adaptVAC-developed ABNCoV2 SARS-CoV-2 VLP vaccine also uses AP205 as a scaffold but relies on a different Tag/Catcher system for SARS-CoV-2 receptor-binding domain (RBD) attachment (Fougeroux et al., 2021; Tan et al., 2016). At the time of this writing, this vaccine candidate is currently undergoing Phase III clinical trials (Clinical trial identifier: NCT05329220).

Computationally-designed nanocages of viral and non-viral origin have garnered significant interest in the development of vaccines. David Baker and colleagues designed one such nanocage, dubbed “i301”, derived from the 2-keto-deoxy-phosphogluconate (KPDG) aldolase of the hyperthermophilic bacterium *Thermotoga maritima* (Hsia et al., 2016). Introducing five interface mutations to the wild-type trimer produced a self-assembling 60-mer particle that remains stable in high concentrations of denaturant and temperatures of 25-80 ^{o}C. Each trimer of i301 was also able to display two copies of superfolder GFP (Hsia et al., 2016). Realizing the potential of i301 to resolve the instability of SpyCatcher-AP205, Theodora Bruun and Dr. Anne-Marie Anderson of the Howarth lab genetically fused SpyCatcher to the N-terminus of i301 and engineered two surface cysteine-to-alanine mutations (C76A and C100A) on i301 (Fig 1.2) , to decrease disulfide bond-mediated aggregation between particles (Fig 1.3 B) (Bruun et al., 2018). This particle, dubbed “SpyCatcher-mi3”, gave a 20-fold greater expression yield than that of SpyCatcher-AP205 and demonstrated higher temperature stability between 25 ^{o}C and 95 ^{o}C (Fig 1.3 A) (Bruun et al., 2018). SpyCatcher-mi3 also showed 95% coupling efficiency (in 16 hours) with different malarial antigens and generated high avidity antibody titers specific to a malarial antigen, CyRPA-SpyTag (Bruun et al., 2018). The version of SpyCatcher used to study the AP205 and mi3 particles has the problem of self- reactivity and reacting slowly with its SpyTag-protein partner (Keeble et al., 2017). Dr. Anthony

Keeble, of the Howarth lab, used phage display to select for a faster-reacting SpyCatcher002 that can react with SpyTag002 10-fold faster than the parental pair (Keeble et al., 2017). Subsequently he developed SpyCatcher003 after five additional mutations were rationally designed into SpyCatcher002, to improve its charge complementarity with the peptide partner. The melting temperature (T_m) of SpyTag003/SpyCatcher003 is 95.2 ºC and its second-order rate constant for reaction with SpyTag003 is 5.5 ±0.6 × 10^5 $M^{-1}s^{-1}$ (mean ± 1 s.d., n=3). This is 400-fold faster than SpyTag/SpyCatcher, which had a second-order rate constant of 1.4 × 10^3 M^{-1} s^{-1} (Keeble et al., 2019; Zakeri et al., 2012). Dr. Rolle Rahikainen found that sera from 52 healthy UK adults had 5.4-fold lower median antibody titers against SpyCatcher003:SpyTag003 than SpyCatcher:SpyTag (Rahikainen et al., 2021). Seeing how fast reaction rate, high melting temperature and low sero-reactivity would be helpful for modular assembly of mi3 VLPs with a SpyTag-antigen, I decided to make and characterize SpyCatcher003-mi3.

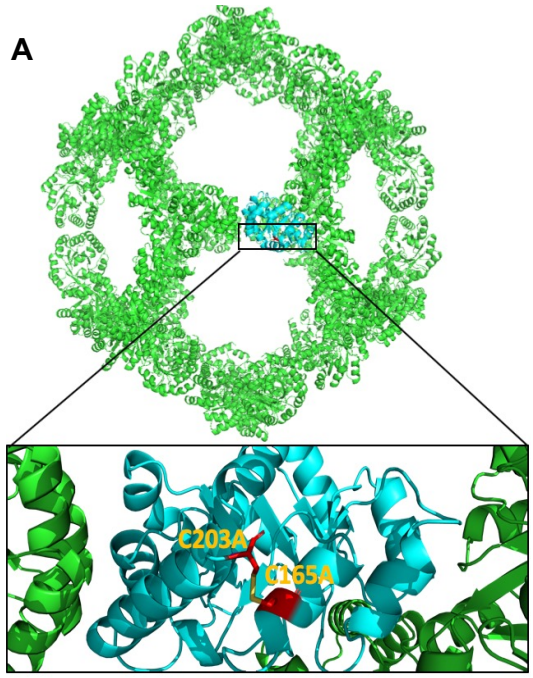
In this chapter, I show the results of experiments I have performed to enhance the stability and solubility of SpyCatcher003-mi3. I established the possibility of scaling up production of SpyCatcher003-mi3 for plug-and-display VLP assembly without affinity purification, thereby eliminating the dependence of the VLP's yield on resin capacity and cost. This approach is also beneficial, given that an affinity tag may interfere with protein-protein interactions (Zhao et al., 2013). I demonstrate that the system is rapidly reactive to SpyTag-antigens at 25 ºC and show evidence of the platform's versatility in coupling antigens with different symmetries and valencies. Finally I provide evidence showing that SpyCatcher003-mi3 multimerized with select influenza and severe acute respiratory syndrome coronavirus 2 (SARS-CoV-2) antigens elicits high, and sometimes neutralizing antibody titers, thereby confirming its immunogenic potency.

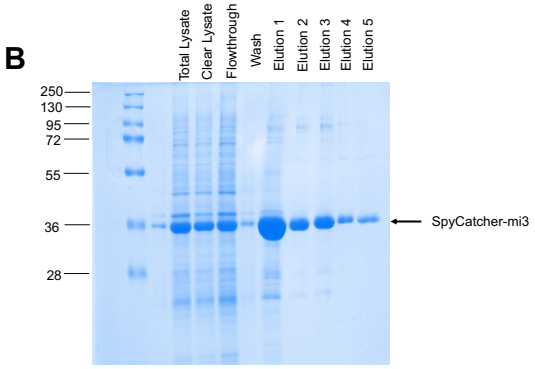
3.1 Expression and characterization of particles linked to SpyCatcher or SpyCatcher003

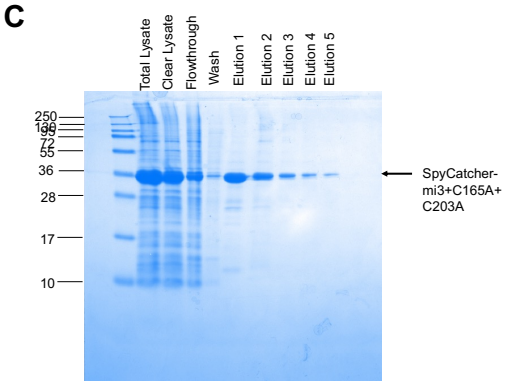
3.1.1 Bacterial expression and affinity purification of particles

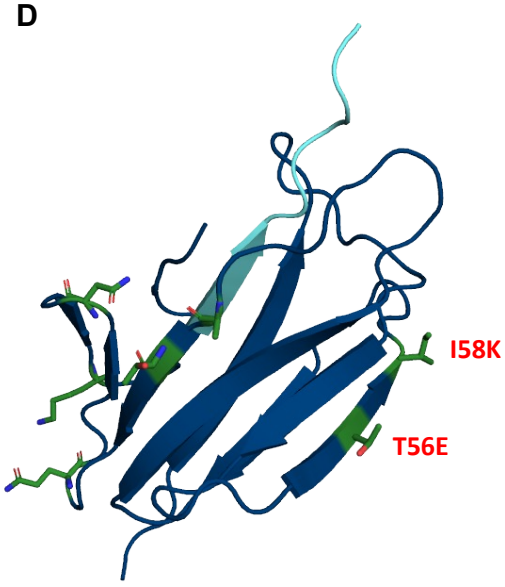
My first goal was to see if SpyCatcher-mi3 could be further modified to improve its solubility and heat stability. Theodora Bruun introduced surface cysteine to alanine mutations at residues 76 and 100 of i301 (Fig 1.2) to generate the mi3 nanoscaffold (Bruun et al., 2018). I mutated the two remaining surface cysteines at residues 165 and 203 to alanines (Fig 3.2 A) to eliminate possible interchain disulfide bonding formation that might have affected the abnormal increase in hydrodynamic radius when SpyCatcher-mi3 was heated to 55 ^{o}C for 1 h (Bruun et al., 2018). I decided to mutate C165 and C203 residues on mi3 to alanines because I believe its side chains would not introduce any steric or electrostatic effects that could perturb the main chain's conformation. To improve solubility, glycine can be an alternative mutation because its side chain offers conformational flexibility. Serine could also be a suitable mutation for the two surface cysteines, given its compact size and polar nature. The oxygen in its hydroxyl side chain can form hydrogen bonds with nearby portions of the protein backbone

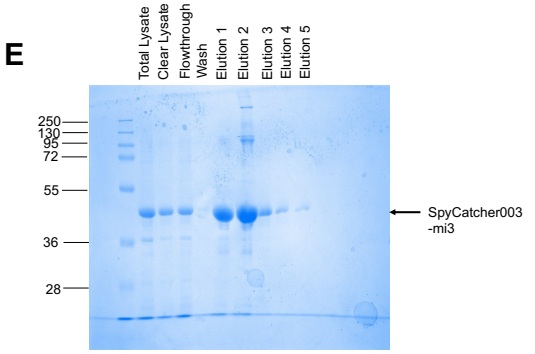
C-tag affinity purification of SpyCatcher-mi3 (Fig 3.2 B) from *E. coli* expression yielded 11 ± 3.6 mg/L (mean ± 1 s.d., n=3), while C-tag affinity purification of SpyCatcher-mi3 with C165A and C203A mutations (SpyCatcher-mi3+C165A+C203A) (Fig 3.2 C) yielded 12 ± 1.5 mg/L (mean ± 1 s.d., n=3) product.


A
C203A
C165A


B
Total Lysate
Clear Lysate
Flowthrough
Wash
Elution 1
Elution 2
Elution 3
Elution 4
Elution 5
250
130
95
72
55
36
28
SpyCatcher-mi3


C
Total Lysate
Clear Lysate
Flowthrough
Wash
Elution 1
Elution 2
Elution 3
Elution 4
Elution 5
250
72
55
36
28
17
10
SpyCatcher-
mi3+C165A+
C203A


D
I58K
T56E


E
Total Lysate
Clear Lysate
Flowthrough
Wash
Elution 1
Elution 2
Elution 3
Elution 4
Elution 5
250
130
95
72
55
36
28
SpyCatcher003
-mi3

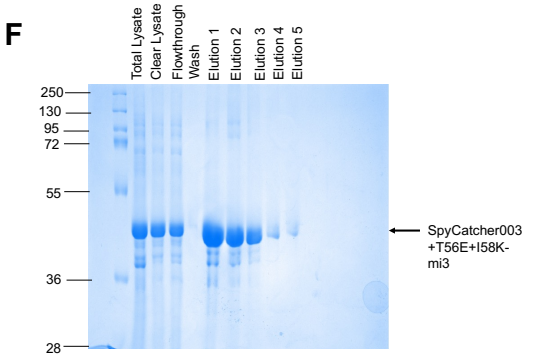

F
Total Lysate
Clear Lysate
Flowthrough
Wash
Elution 1
Elution 2
Elution 3
Elution 4
Elution 5
250
130
95
72
55
36
28
SpyCatcher003
+T56E+I58K-
mi3

Figure 3. 2. Mutation sites and C-tag purification gels of SpyCatcher-mi3 and SpyCatcher003-mi3 variants: (A) Rendering of i301 nanocage (computational model from Hsia et al., 2016, coded in lime-green) with mapped positions of C165A and C203A mutations (red) relative to one monomer unit (aquamarine); (B) Affinity purification gel showing soluble product of SpyCatcher-mi3; (C) Affinity purification gel showing soluble product of SpyCatcher-mi3 with C165A and C203A mutations; (D) PyMOL rendering of the parent domain of SpyCatcher003 based on PDB: 2X5P (dark blue) and 4MLI (SpyTag displayed in aquamarine) (image credit: Irsyad Khairil Anuar), with mapped SpyCatcher003 mutation sites (dark green); (E) Affinity purification gel showing soluble product of SpyCatcher003-mi3; (F) Affinity purification gel showing soluble product of SpyCatcher003-mi3 with T56E and I58K mutations. Non-reducing 16% (w/v) SDS gels (Fig 3.2 B, C, E, F) were stained with Coomassie.

My second goal was to examine whether replacing SpyCatcher with SpyCatcher003 would still allow for the formation of a soluble and reactive VLP. Prior lab members found that fusing other proteins (which reacted rapidly with peptide tags) such as: SpyCatcher002 (Keeble et al., 2017), DogCatcher (Keeble et al., 2022), and SnoopCatcher (Veggiani et al., 2016), to the N-terminus of mi3 did not result in intact VLPs (unpublished data). SpyCatcher003-mi3 formed a soluble product (Fig 3.2 E) with an affinity-purified yield of 13 ± 3.1 mg/L (mean ± 1 s.d., n=3). In the development of SpyCatcher003, Dr. Anthony Keeble found, via CamSol analysis, that mutating the threonine at residue 56 to glutamate and isoleucine at residue 58 (Fig 3.2 D) to lysine can form a salt bridge that may enhance SpyCatcher003's solubility (Keeble, 2018; unpublished). Incorporating these mutations (mutant VLP dubbed SpyCatcher003+T56E+I58K-mi3) allowed expression of a soluble product (Fig 3.2 F) with a purified yield of 16 ± 2.0 mg/L (mean ± 1 s.d., n=3) product. There was no substantial difference in yield between the four particles (Fig 3.3).

I optimized bacterial expression yields of VLPs by inducing with 0.5 mM IPTG (Isopropyl β-D-1-thiogalactopyranoside) at A_{600} (absorbance at 600 nm) of 0.5 and 0.8, varying the time that cell lysate binds with affinity resin, and performing size exclusion with equilibrated Superose 6 Increase 10/300 and HiPrep 16/60 Sephacryl S-400 columns. I also tried heating the cell lysate to induce crashing of non-specific protein contaminants (Wu, 2019; unpublished).

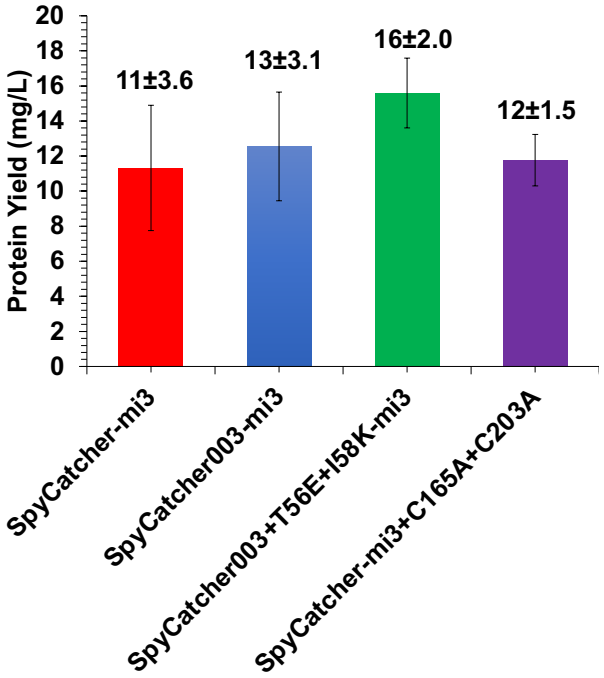
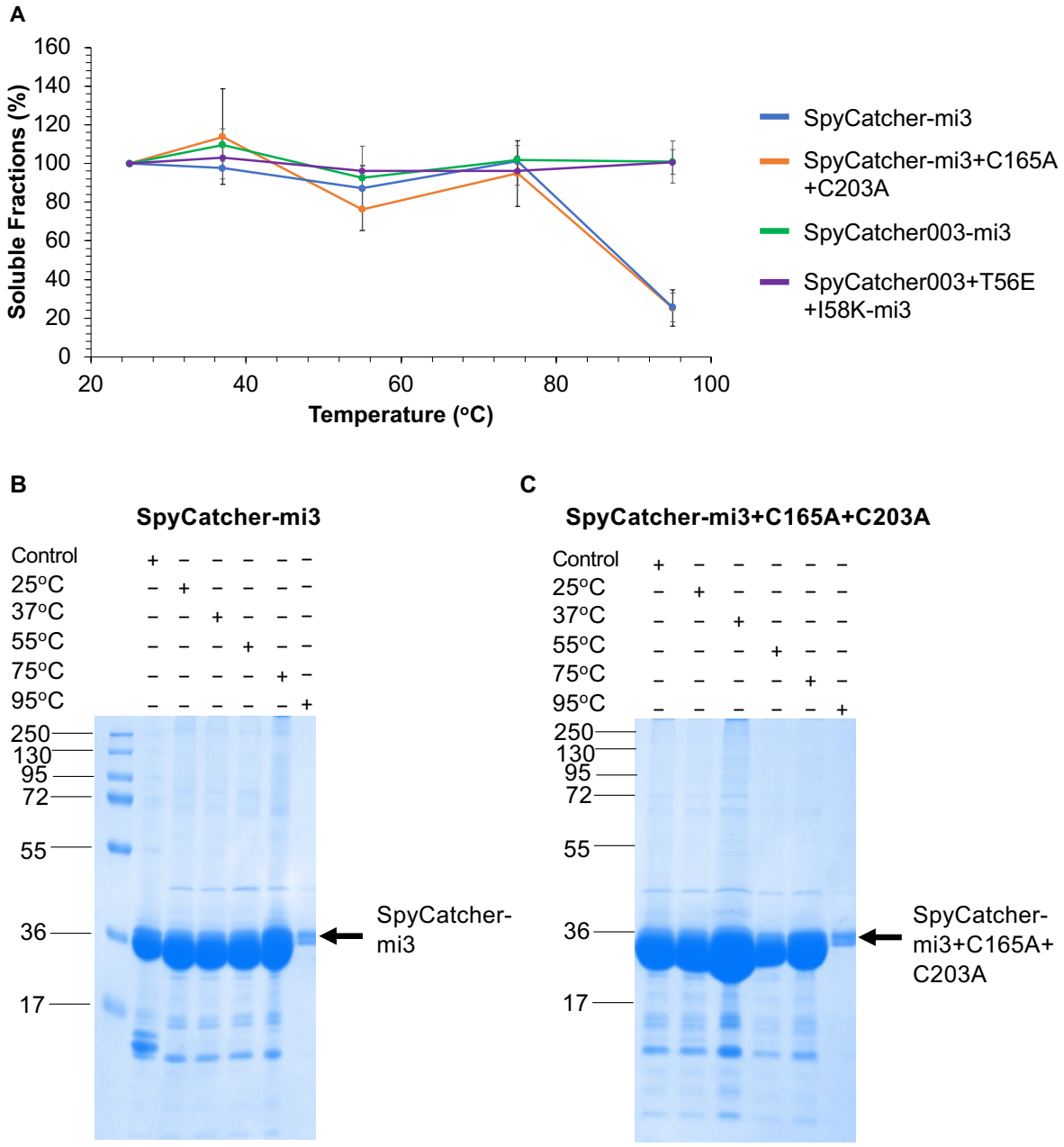


Figure 3. 3. Yields of SpyCatcher-mi3 and SpyCatcher003-mi3 variants: Yields of VLPs purified from affinity C-tag chromatography (mean±1 s.d., n=3) were compared for SpyCatcher-mi3, SpyCatcher003-mi3, SpyCatcher003+T56E+I58K-mi3 and SpyCatcher-mi3+C165A+C203A.

3.1.2 Heat stability of particles

Vaccines are often needed in regions of the world that lack reliable cold-chains. Heat stability of this scaffold could help ensure the efficacy of vaccine candidates that rely on this platform. To characterize the resilience of my VLPs, I heated samples to

temperatures between 25 ºC and 95 ºC for 1 h, before cooling them at 4 ºC for 10 min. Gel densitometry analysis reveals that SpyCatcher-mi3 and SpyCatcher-mi3 with C165A and C203A mutations crash out at 55 ºC and 95 ºC while SpyCatcher003-mi3 and SpyCatcher003-mi3 with T56E and I58K mutations retain between 90-100% solubility between 55 ºC and 95 ºC (Fig 3.4).


A
Soluble Fractions (%)
160
140
120
100
80
60
40
20
0
20
40
60
80
100
Temperature (°C)
SpyCatcher-mi3
SpyCatcher-mi3+C165A
+C203A
SpyCatcher003-mi3
SpyCatcher003+T56E
+I58K-mi3
B
SpyCatcher-mi3
Control
25°C
37°C
55°C
75°C
95°C
250
130
95
72
55
36
17
SpyCatcher-
mi3
C
SpyCatcher-mi3+C165A+C203A
Control
25°C
37°C
55°C
75°C
95°C
250
130
95
72
55
36
17
SpyCatcher-
mi3+C165A+
C203A

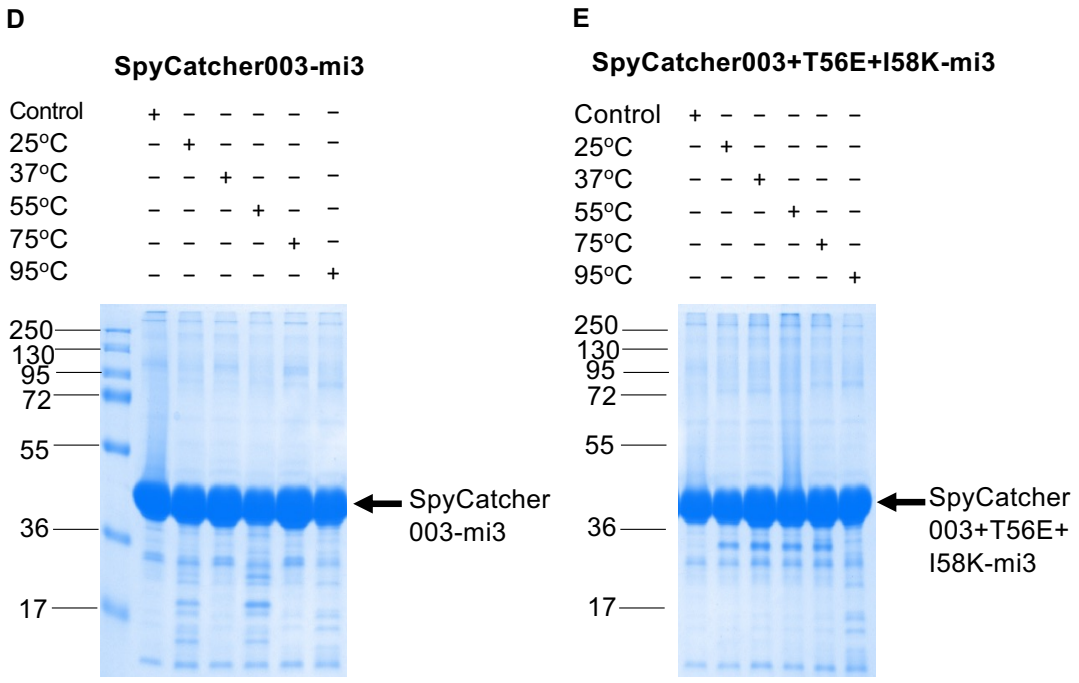


Figure 3. 4. Temperature-dependent solubility of SpyCatcher-mi3 and SpyCatcher003-mi3 variants: A) Graph of solubility, determined by band densitometry, of SpyCatcher003-mi3, SpyCatcher003+T56E+I58K-mi3, SpyCatcher-mi3 and SpyCatcher-mi3+C165A+C203A particles after being heated to 25-95 °C for 1 h and cooled at 4 °C for 10 min (mean ± 1 s.d., n=3). Sample SDS gels of B) SpyCatcher-mi3, C) SpyCatcher-mi3+C165A+C203A, D) SpyCatcher003-mi3, E) SpyCatcher003+T56E+I58K-mi3 samples, all heated to 25-95 °C for a 1 h and cooled at 4 °C at 10 min. Non-reducing 16% (w/v) SDS gels (3.4 B-E) were stained with Coomassie

I then utilized dynamic light scattering (DLS) to observe how particle uniformity changes with temperatures between 25 °C and 95 °C for 1 h, before cooling the particles at 4 °C for 10 min. The increased standard deviation of the SpyCatcher-based VLPs' hydrodynamic radii to 6 nm at 55 °C suggests this may be caused by particle aggregation. (Fig 3.5 A-C). The particle uniformity of SpyCatcher003-mi3 and its variant with T56E and I58K mutations remains consistent in the same temperature range (Fig 3.5 D-F).

Altogether, this suggests that including the SpyCatcher003 moiety on the mi3 scaffold contributes to enhanced temperature-dependent solubility over SpyCatcher. It also does not appear that the additional C165A and C203A mutations mitigate temperature-dependent solubility or particle uniformity issues observed in SpyCatcher-mi3. From this point on, no VLPs bearing the original SpyCatcher will be considered for further analysis.

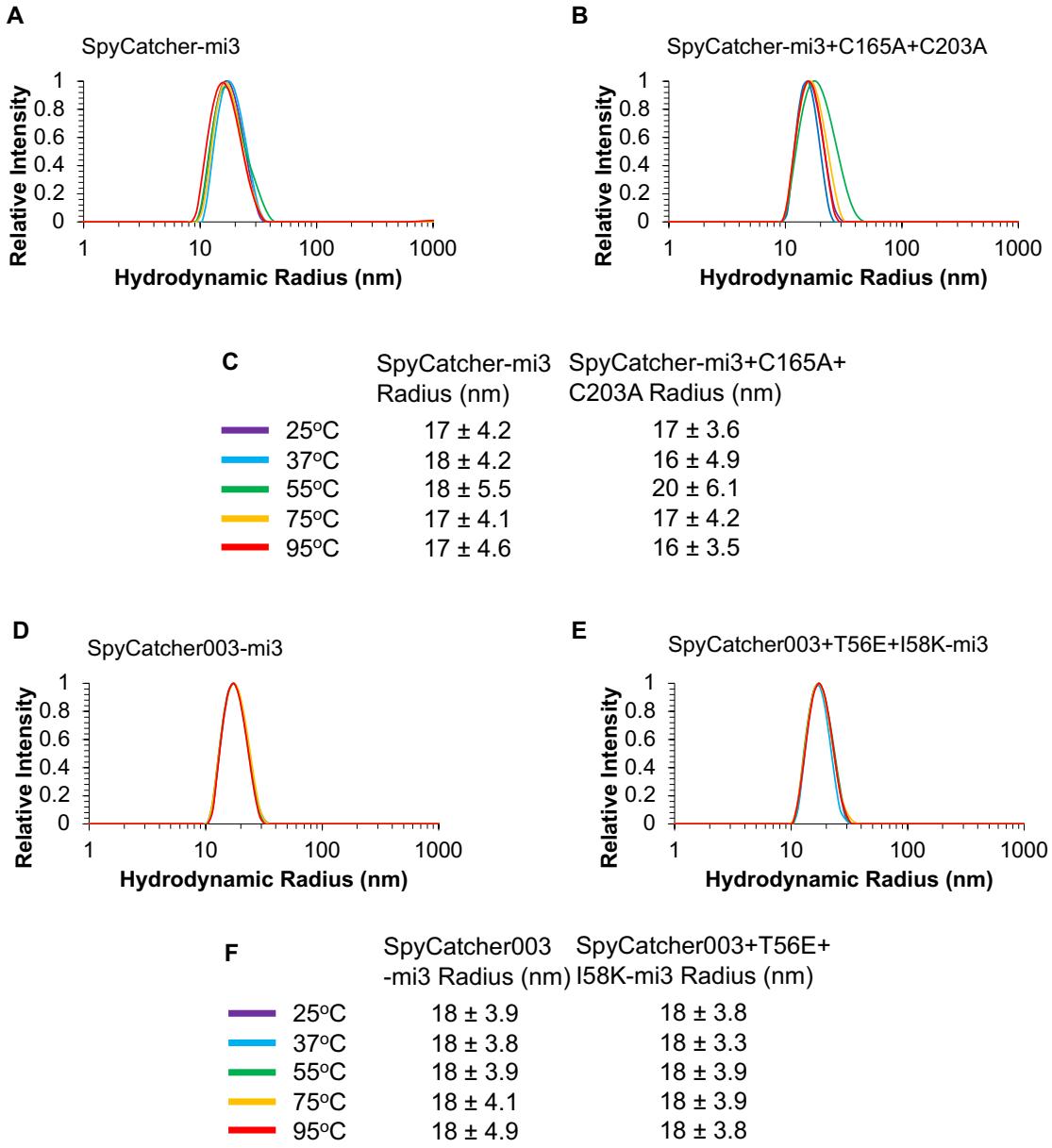


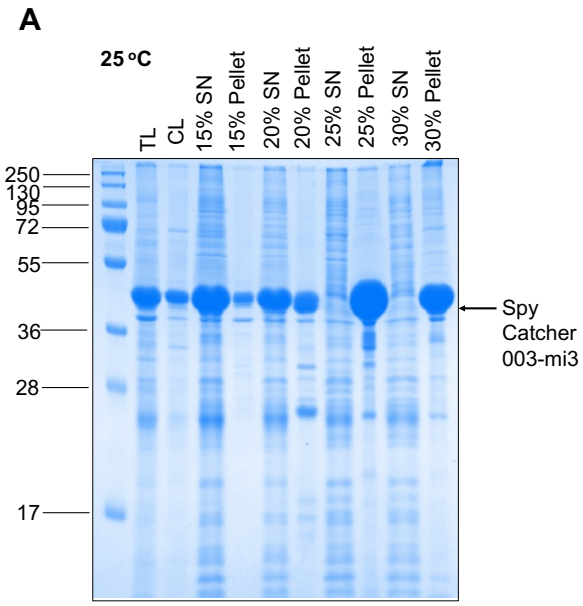
Figure 3. 5. Particle uniformity of SpyCatcher-mi3 and SpyCatcher003-mi3 variants subjected to temperatures between 25 ºC and 95 ºC: DLS measurement spectra of (A) SpyCatcher-mi3 and (B) SpyCatcher-mi3+C165A+C203A particles; (C) average hydrodynamic radii measurements of SpyCatcher-mi3 and SpyCatcher-mi3+C165A+C203A particles (mean±1 s.d., n=3). DLS measurement spectra of (D) SpyCatcher003-mi3 and (E) SpyCatcher003+T56E+I58K-mi3; (F) average hydrodynamic radii measurements of SpyCatcher003-mi3 and SpyCatcher003+T56E+I58K-mi3 particles (mean±1 s.d., n=3).

3.1.3 Ammonium sulfate precipitation of SpyCatcher003-mi3

Having determined the stability of SpyCatcher003-mi3, I examined the possibility for SpyCatcher003-mi3 particle purification to be scaled-up via ammonium sulfate precipitation. Affinity purification is costly and difficult to scale up (Lichty et al., 2005; M. Zhao et al., 2019).

i301 was also initially purified using ammonium sulfate precipitation and heating to eliminate non-target proteins (Hsia et al., 2016). Since the efficiency of this process depends on the concentration of ammonium sulfate and the temperature in which the cell lysate is incubated (Hebert et al., 1973; Wingfield, 2001), I chose to examine these two parameters and determine how they affect SpyCatcher003-mi3 yield.

I saturated bacterial cell lysate with 15-30% (w/v) of ammonium sulfate and mixed the solution in 4 ^{o}C and 25 ^{o}C. At both temperatures, adding 25% and 30% (w/v) ammonium sulfate salts out the most VLPs, as determined by band density. Following gel filtration chromatography, the cell lysate mixed at 25 ^{o}C and saturated with 25% (w/v) and 30% (w/v) ammonium sulfate yielded 52.7 mg/L and 37.6 mg/L of SpyCatcher003-mi3, respectively (Fig 3.6 A). Following gel filtration chromatography, SpyCatcher003-mi3 cell lysate mixed at 4 ^{o}C and saturated with 25% (w/v) and 30% (w/v) ammonium sulfate yielded 83.2 mg/L and 95.5 mg/L of SpyCatcher003-mi3, respectively (Fig 3.6 B).

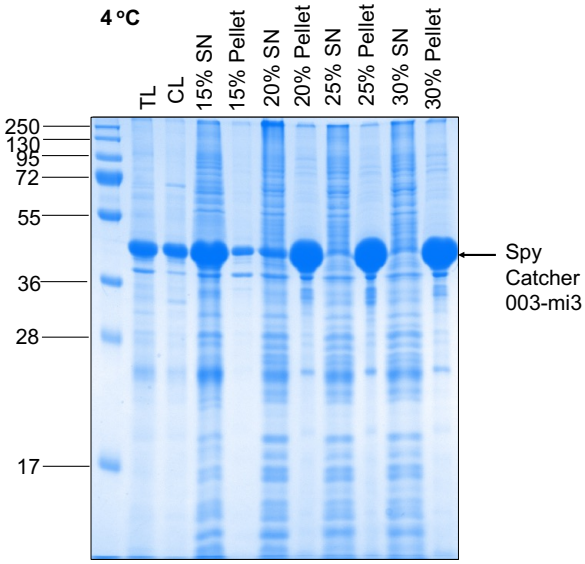


25% AS Precipitation

Step	Vol. (ml)	Total protein (mg)	Total Target Protein (mg)	Yield (%)	Purity of Target Protein (%)	Est. Yield of Target Protein per L culture (mg/L)
Cleared Lysate	10	71.5	54.2	100	76	217
25% Ammonium Sulfate Precipitation	7.5	25.5	22.2	41	87	88.8
Pooled Peak from S400 16/600 Column	5	4.7	4.4	8	93	52.7

30% AS Precipitation

Step	Vol. (ml)	Total protein (mg)	Total Target Protein (mg)	Yield (%)	Purity of Target Protein (%)	Est. Yield of Target Protein per L culture (mg/L)
Cleared Lysate	10	71.5	54.2	100	76	217
30% Ammonium Sulfate Precipitation	7.5	22.5	20.3	38	90	81.2
Pooled Peak from S400 16/600 Column	5	3.3	3.17	6	96	37.6



25% AS Precipitation

Step	Vol. (ml)	Total protein (mg)	Total Target Protein (mg)	Yield (%)	Purity of Target Protein (%)	Est. Yield of Target Protein per L culture (mg/L)
Cleared Lysate	10	71.5	58.5	100	81.8	234
25% Ammonium Sulfate Precipitation	7.5	29.25	26.6	40.4	91	106
Pooled Peak from S400 16/600 Column	5	7.2	6.9	10.5	96	83.2

30% AS Precipitation

Step	Vol. (ml)	Total protein (mg)	Total Target Protein (mg)	Yield (%)	Purity of Target Protein (%)	Est. Yield of Target Protein per L culture (mg/L)
Cleared Lysate	10	71.5	58.5	100	81.8	234
30% Ammonium Sulfate Precipitation	7.5	25.5	24	36.5	93	96
Pooled Peak from S400 16/600 Column	5	8.25	7.9	12	96.3	95.5

Figure 3. 6. Ammonium sulfate precipitation of SpyCatcher003-mi3: (A) SDS gel results displaying ammonium sulfate (AS) precipitation of SpyCatcher003-mi3 ranging from 15% to 30% (w/v) saturation of SpyCatcher003-mi3 lysate at 25 °C (left) and stepwise purification tables of 25% and 30% (w/v) precipitation at 25 °C (right). (B) SDS gel results displaying AS precipitation of SpyCatcher003-mi3 ranging from 15% to 30% (w/v) saturation of SpyCatcher003-mi3 at 4 °C. (left) and stepwise purification tables of 25% and 30% (w/v) precipitation at 4 °C. (right) Gel-loaded samples include total lysate (TL),

cleared lysate (CL), supernatant (SN) and resuspended pellet (Pellet). Non-reducing 16% (w/v) SDS gels (3.6 A, B) were stained with Coomassie.

SpyCatcher003-mi3 saturated with 25% (w/v) and 30% (w/v) ammonium sulfate were able to assemble into particles, as confirmed via SEC (Fig 3.7). This suggests that ammonium sulfate precipitation at 4 °C is more conducive to producing a higher SpyCatcher003-mi3 yield than at 25 °C. Furthermore, I showed here that it is feasible to efficiently purify a much higher yield of SpyCatcher003-mi3 with ammonium sulfate precipitation than with affinity resin. Precipitating SpyCatcher003-mi3 with 25% (w/v) or 30% (w/v) ammonium sulfate at 4 °C produces VLPs of 96% purity. This aligns with the WHO recommendation of at least 95% protein purity for the RTS,S/AS01 VLP malaria vaccine (World Health Organization, 2014). Scientists at Merck Research Laboratories reported a 98% protein purity, assessed by SDS gel densitometry, in their work to develop a downstream processing procedure for recombinant HPV L1 capsid protein VLPs (Cook et al., 1999).

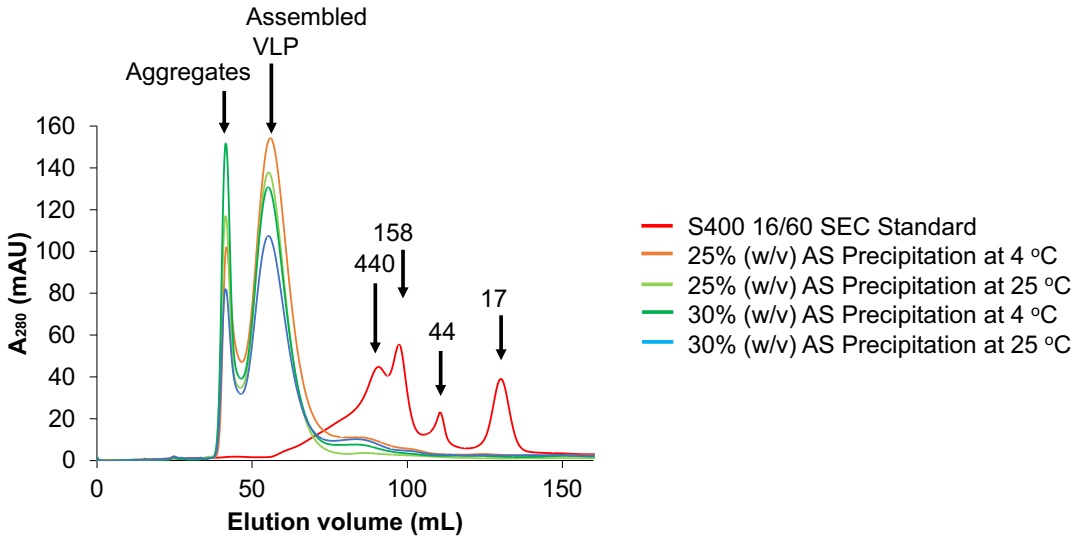


Figure 3. 7. Size-excluded chromatogram of 25% and 30% (w/v) ammonium sulfate precipitated SpyCatcher003-mi3: Size-excluded VLPs precipitated at 25% (w/v) saturation in 4 ^{o}C and 25 ^{o}C are marked in orange and light green, respectively. Size-excluded VLPs precipitated at 30% (w/v) saturation in 4 ^{o}C and 25 ^{o}C are marked in dark green and blue, respectively. Standard is marked in red and the labeled molecular weights are denominated in kDa.

3.1.4 Residual nucleic acid measurements for SpyCatcher003-mi3 preps

The presence of host cell-derived nucleic acid is a recurring problem in batch vaccine production. Residual nucleic acids pose a risk in vaccines preps because of their immunostimulatory potential and the possibility that genomes of infectious viruses may be present (Shin et al., 2007). The World Health Organization (WHO) and the U.S. Food and Drug Administration (FDA) guidelines mandate all vaccines to have no more than 10 ng/dose of double-stranded DNA, less than 200 base-pairs in length (Food and Drug Administration, 2010; Shin et al., 2007). I measured nucleic acid levels using a fluorescent double-stranded DNA (dsDNA) quantitation assay and found that SpyCatcher003-mi3, purified via the C-tag affinity chromatography column, contains approximately 3.8 ± 0.1 ng/mL of dsDNA (Fig 3.8). SpyCatcher003-mi3, derived from 20% (w/v) ammonium sulfate precipitation contains 4.7 ± 0.1 ng/mL of dsDNA (Fig 3.8). These low values indicate that my current downstream processing protocol can produce SpyCatcher003-mi3 with limited residual nucleic acids.

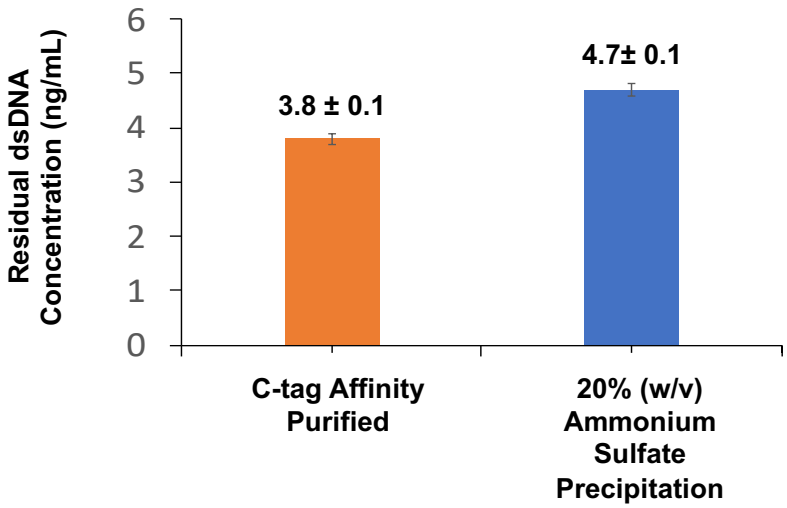


Figure 3. 8. Residual DNA quantification of SpyCatcher003-mi3 preparations: A comparison of residual dsDNA concentrations measured in both C-tag affinity purified (orange) and 20% (w/v) ammonium sulfate precipitated (blue) preparations. Concentrations were measured using the Quant-IT Picogreen dsDNA assay and assessed against a Lambda DNA standard calibration curve (mean±1 s.d., n=3).

3.2 Reactivity of VLPs with antigens of varying symmetries and valencies

To investigate how well antigens of different sizes and symmetries couple to SpyCatcher003-mi3 subunits, Dr. Rolle Rahikainen expressed a panel of selected monomeric to tetrameric SpyTag and SpyTag003-fused antigens, coupled them to SpyCatcher003-mi3 subunits, and assessed coupling efficiencies at different molar ratios (Rahikainen et al., 2021). He also assessed possible crashing-out on SDS-PAGE.

The SARS-CoV-2 spike receptor-binding domain (RBD) was expressed with an N-terminal SpyTag, representing a monomeric protein. A N-terminally truncated fragment of Outer surface protein C (OspC) from the Lyme Disease-causing bacterium, *Borrelia burgdorferi*, was fused to an N-terminal SpyTag003 as a representative parallel dimeric protein (denoted as C2 symmetry, parallel). An N-terminal truncated fragment of Newcastle Disease Virus (NDV) hemagglutinin-neuraminidase (HN) fused to a C-terminal

SpyTag003 is a representative anti-parallel dimeric protein (denoted as C2 symmetry, antiparallel). Since Influenza antigens possess diversity between strains (Iuliano et al., 2018), Hemagglutinin H3 from Victoria/361/2011 (H3 Vic) was utilized as a representative trimeric protein (denoted as C3 symmetry). Neuraminidase (N2) from A/Victoria/361/2011 was included as a representative tetrameric protein (C4 symmetry). The additional two representative tetramers (denoted as D2 symmetry) of divergent size used for coupling were the 60 kDa streptavidin from *Streptomyces avidinii* and the 483 kDa *E.coli* β-galactosidase (Fig 3.9 A).

Dr. Rahikainen found that, apart from β-galactosidase, all the other selected antigens were able to couple efficiently with equimolar quantities of SpyCatcher003-mi3 subunits (Fig 3.9 B, C). Near-complete coupling was possible, suggesting that potential steric hindrance of antigens coupled to the scaffold did not affect SpyCatcher003 reactivity (Rahikainen et al., 2021). However, the size of the antigen and the orientation of its subunits with SpyTag/SpyTag003 determines the extent of its coupling efficiency with SpyCatcher003-mi3 subunits (Rahikainen et al., 2021). Both dimeric OspC and trimeric H3 Vic HA were able to efficiently couple via its subunits at 1:1 and 1:1.5 VLP subunit to antigen ratio, with sparse amounts of unreacted antigens remaining (Fig 3.9 B) (Rahikainen et al., 2021). This confirms OspC's ability to couple via its two SpyTags, as well as H3 Vic HA coupling through its three SpyTags (Rahikainen et al., 2021). When SpyCatcher003-mi3 subunits were reacted with three times molar excess of anti-parallel dimeric NDV-HN, there was still considerable excess of unreacted antigen; this confirms covalent coupling through only one SpyTag (Rahikainen et al., 2021) (Fig 3.9 B). The dihedral Streptavidin tetramer coupled efficiently to the VLP subunits at a 1.5:1 ratio, but β-galactosidase was unable to couple efficiently at the ratios provided (Rahikainen et al., 2021). This observed difference suggests that antigen size is one factor that may limit

covalent coupling. Another limiting factor for covalent coupling may be the positioning of SpyTags on different faces of a large protein, like β-galactosidase. It is possible that any uncoupled SpyTags remaining following VLP-antigen coupling may covalently bind SpyCatcher003 from other VLP subunits and collectively induce aggregation between VLPs. (Fig 3.9 B) (Rahikainen et al., 2021).

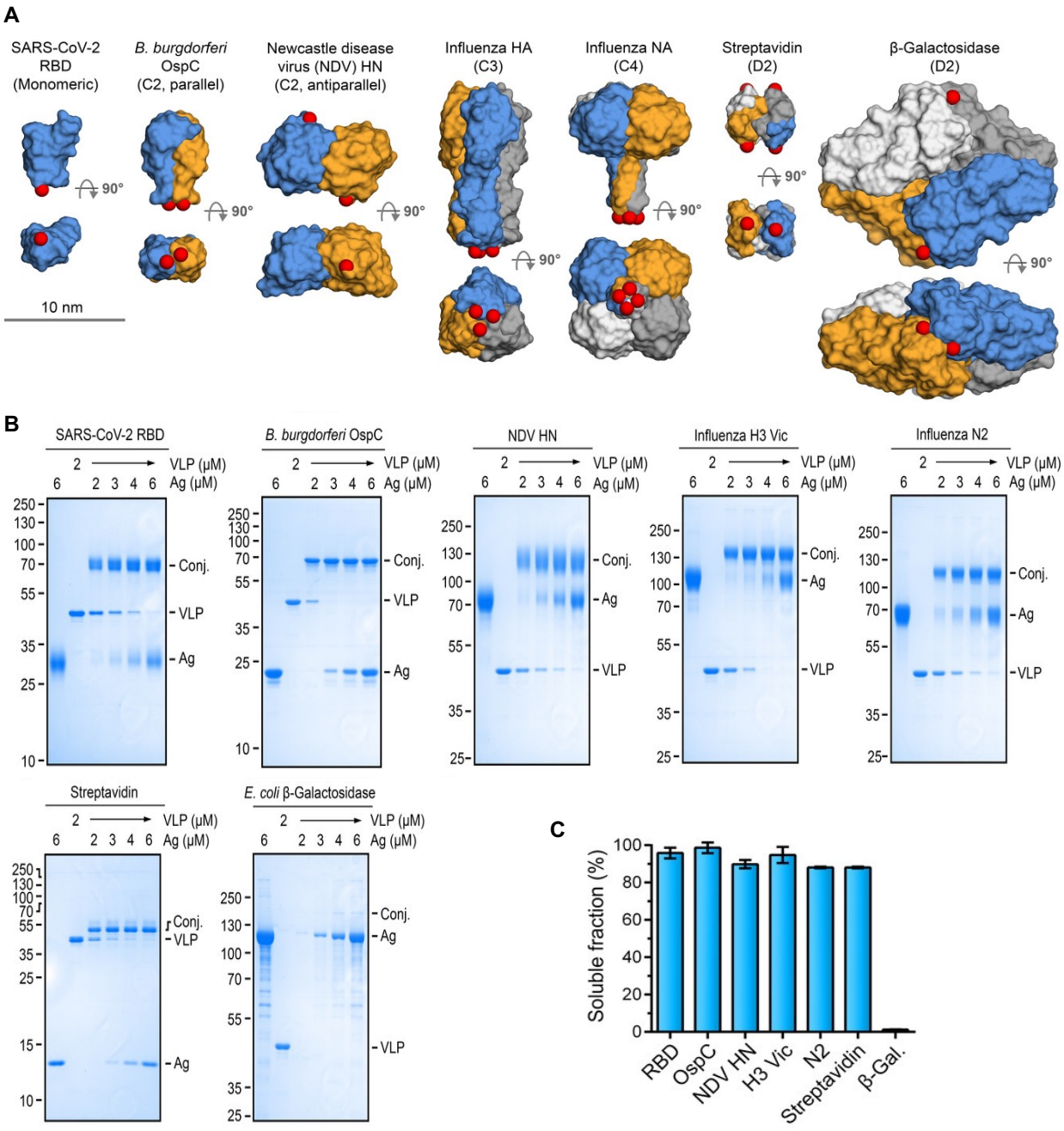
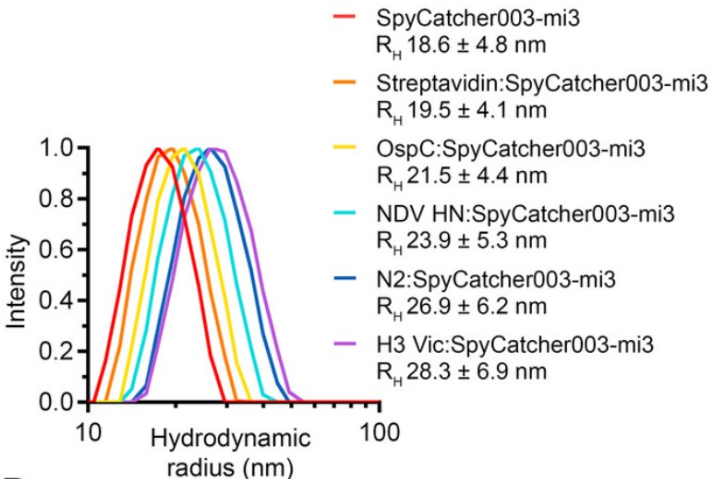


Figure 3. 9. SpyCatcher003 can efficiently couple antigens of different sizes and symmetries: (A) Space-filling models of each antigen of different symmetry are colored for different chains (in blue, orange, white, and gray) and shown in two orientations; the position of either SpyTag or SpyTag003 is colored in red. The antigens are constructed according to the following PDB IDs: RBD: 6W41, OspC: 1G5Z, NDV HN: 3T1E, HA: 4UO0, NA: 2HTY (modified with tetramerization domain: 1USE), streptavidin: 1SWB, β-

galactosidase: 6DRV. (B) Reducing SDS-PAGE with Coomassie staining display centrifuged supernatant of antigens reacted with VLPs, for 16 h at 4 ^{o}C, in select molar ratios. (C) SDS-PAGE densitometry measurements of soluble antigen-coupled fractions at 1:1 molar ratio (mean ± s.d., n=3). Data/image credit: adopted from Rahikainen et al., 2021.

DLS measurements and TEM images of negatively stained VLPs coupled to OspC, NDV HN and H3 Vic HA further confirmed uniform particle size (Fig 3.10 A, B). This experiment underscores the ability of SpyCatcher003-mi3 to couple to antigens of diverse multimeric structures and sizes without compromising solubility, while remaining monodisperse (Rahikainen et al., 2021). However, the insoluble nature of β-galactosidase-coupled particles suggests that a possible limitation of this platform is the display of large tetrameric antigens with dihedral symmetry (Rahikainen et al., 2021).

A



B

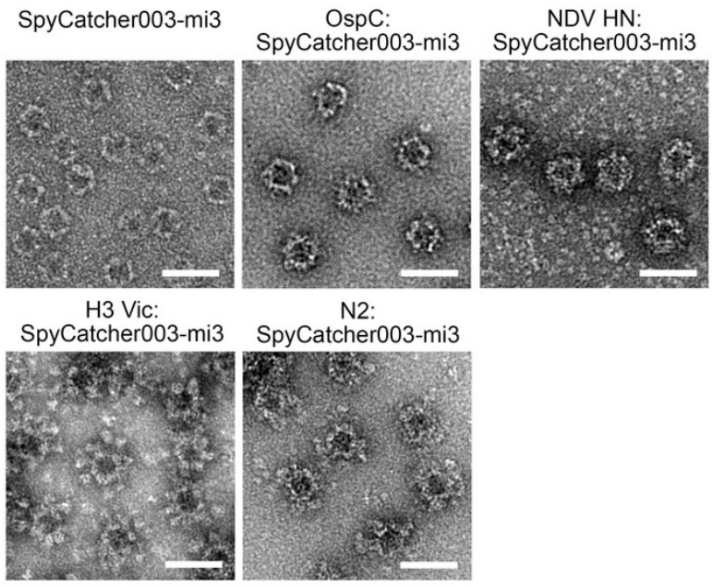


Figure 3. 10. Antigen-coupled SpyCatcher003-mi3 forms uniform-sized particles: (A) DLS-measured hydrodynamic radii (mean ± s.d., n=3) of SpyCatcher003-mi3 (red) and VLP decorated with Streptavidin (orange), OspC (yellow), NDV HN (aquamarine), N2 (blue), or H3 (purple). (B) Negative-stained TEM images of SpyCatcher003-mi3, VLP decorated with OspC, NDV HN, H3 Vic, and N2. Scale bar (white) represents 50 nm in length. Data/image credit: Rahikainen et al., 2021.

3.3 Immunogenicity of SpyCatcher003-mi3 vaccine candidates

3.3.1 Immunogenicity of SARS-CoV-2 RBD-coupled VLPs

In the two decades before the COVID-19 pandemic in 2020, two zoonotic betacoronaviruses, severe acute respiratory syndrome coronavirus 1 (SARS-CoV) and Middle East respiratory syndrome coronavirus (MERS-CoV) had also caused outbreaks on a smaller scale (Wu et al., 2020). These two viruses had intermediary animal host species before finally leading to human outbreaks (de Wit et al., 2016). The animal source and intermediate host(s) of SARS-CoV-2 are not currently known (Lytras et al., 2021). All this suggests that coronaviruses will remain an ongoing health threat and underscores the need for a coronavirus vaccine that could protect against future outbreaks.

The key SARS-CoV-2 vaccine target is the spike (S) protein trimer, which is responsible for mediating viral attachment, fusion, and entry. Previously, SARS-CoV and MERS-CoV receptor-binding domains (RBD) have been shown to be immunogenic and capable of eliciting neutralizing antibodies in different animals (Jiang et al., 2012; Zhou et al., 2018). SARS-CoV-2 RBD is also capable of inducing neutralizing antibody responses (Quinlan et al., 2020; Yang et al., 2020) and most of the potent neutralizing antibodies recovered from infected patients are bound to RBD (Ju et al., 2020; Rogers et al., 2020). Dr. Tiong Tan, from Alain Townsend's laboratory at Oxford, decorated SpyCatcher003-mi3 with RBD to study its enhanced immunogenicity on a VLP (Tan et al., 2021). For the immunization studies, female C57BL/6 mice were selected for their immunocompetency and reliability in prior studies for dosing with SpyCatcher003-mi3 (Rahikainen et al., 2021). Female BALB/c mice were then used, as a second mouse strain, to confirm the immunogenicity observed in C57BL/6 mice under the same dosage regimen (Tan et al., 2021).

Dr. Tan's experiments showed that immunizing BALB/c or C57BL/6 mice with a 0.1 or 0.5 μg antigen dose of SpyCatcher003-mi3:RBD VLPs (Fig 3.11 A) can generate significantly higher RBD-specific antibody titers than the uncoupled VLP on its own (Fig 3.11 B). For both mice strains, immunization with SpyCatcher003-mi3:RBD also generates more antibodies to RBD than the quantity present in the plasma of critical/severe convalescent patients with natural infection (Fig 3.11 B).

Dr. Tan also assessed how well immunized mice sera blocked recombinant ACE2 from binding to RBD coated on a plate (Fig 3.11 C). For both mice strains immunized with the same antigen doses, immunizing with SpyCatcher003-mi3:RBD VLPs increased RBD-specific titers by 5-10 fold and ACE2 blocking by 10-50 fold relative to the plasma of convalescent patients (Fig 3.11 C) (Tan et al., 2021). Given that the level of ACE2 blocking antibodies are low in both mild and critical/severe convalescent patients, immunizing with SpyCatcher003-mi3:RBD VLPs may offer protective antibodies against SARS-CoV-2 (Tan et al., 2021) .

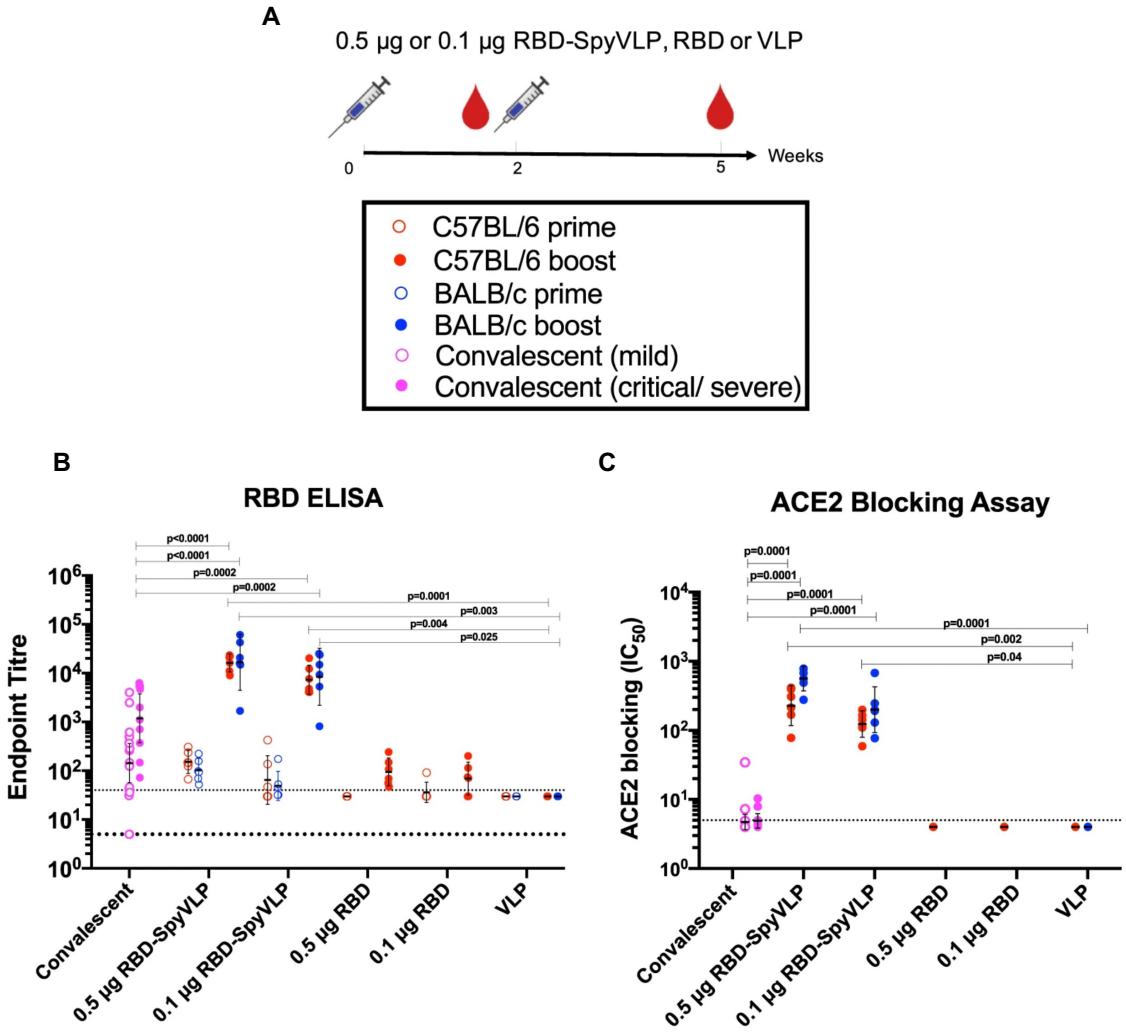


Figure 3. 11. RBD-coupled SpyCatcher003-mi3 elicit strong antibody responses against RBD, which block ACE2: (A) C57BL/6 mice (red) and BALB/c mice (blue) were injected with 0.1 or 0.5 µg RBD, the same antigen dose of RBD coupled to SpyCatcher003-mi3 (RBD-SpyVLP), or SpyCatcher003-mi3 (VLP) alone, adjuvanted with Addavax. Mice were bled two weeks after priming and three weeks after boosting with RBD, VLP or RBD-SpyVLP samples. (B) Sera were analyzed in an ELISA against RBD; (C) Sera were analyzed in an ACE2 blocking assay. This consisted of first incubating sera from immunized mice in wells coated with RBD-SpyVLPs. Recombinant biotinylated ACE2-Fc was then added before the plates were developed with a secondary streptavidin-HRP. The maximum signal (Max) was obtained by incubating biotinylated ACE2-Fc without mice sera or plasma to the RBD-SpyVLP-coated well. The minimum signal (Min) was

obtained by incubating PBS or BSA buffer to the RBD-SpyVLP coated well. The percentage binding of biotinylated ACE2-Fc to RBD was defined as (X−Min)/(Max−Min)*100, where X is the measurement of serum or plasma; IC_{50} was then determined upon plotting on a graph. Graphs (B) and (C) display endpoint titer and IC50 measurements from C57BL/6 mice sera following prime (open red circle) and boost (closed red circle); from BALB/c mice sera following prime (open blue circle) and boost (closed circle); from convalescent sera of humans with mild symptoms (open pink circle) and critical/severe symptoms (closed pink circle). Data presented consist of group geometric means ± 95% confidence intervals. Dotted line represents the value of the lowest mouse serum dilution tested. Bold dotted line represents the value of the lowest human serum dilution tested. Kruskall-Wallis test and Dunn's multiple comparison test were used to evaluated differences between two dosing groups. Two-tailed Mann–Whitney U test was used compare immunized groups against convalescent human sera. Data/image credit: Tan et al., 2021.

Dr. Tan also confirmed that the SpyCatcher003-mi3:RBD complex was resilient to freezing (Fig 3.12 A), resistant to five freeze-thaw cycles (Fig 3.12 B), and its reconstitution after lyophilization did not affect the binding of select mAbs, derived from convalescent patients, to non-overlapping epitopes of RBD (Tan et al., 2021) (Fig 3.12 C, D). Binding to these structurally defined footprints was evaluated using conformational-sensitive antibody CR3022 (footprint PDB: 6W41), dimeric ACE2-Fc (footprint PDB: 6M0J), FI3-A (footprint PDB: 6YZ5), FD-11A (footprint PDB: 6WPT), FM-7B (footprint PDB: 6WPT), and a negative control Influenza mAb (Tan et al., 2021). These results support that SpyCatcher003-mi3, decorated with solely SARS-CoV-2 RBD, is likely to induce neutralizing antibodies against SARS-CoV-2 and simultaneously address logistical challenges for vaccine deployment (Tan et al., 2021).

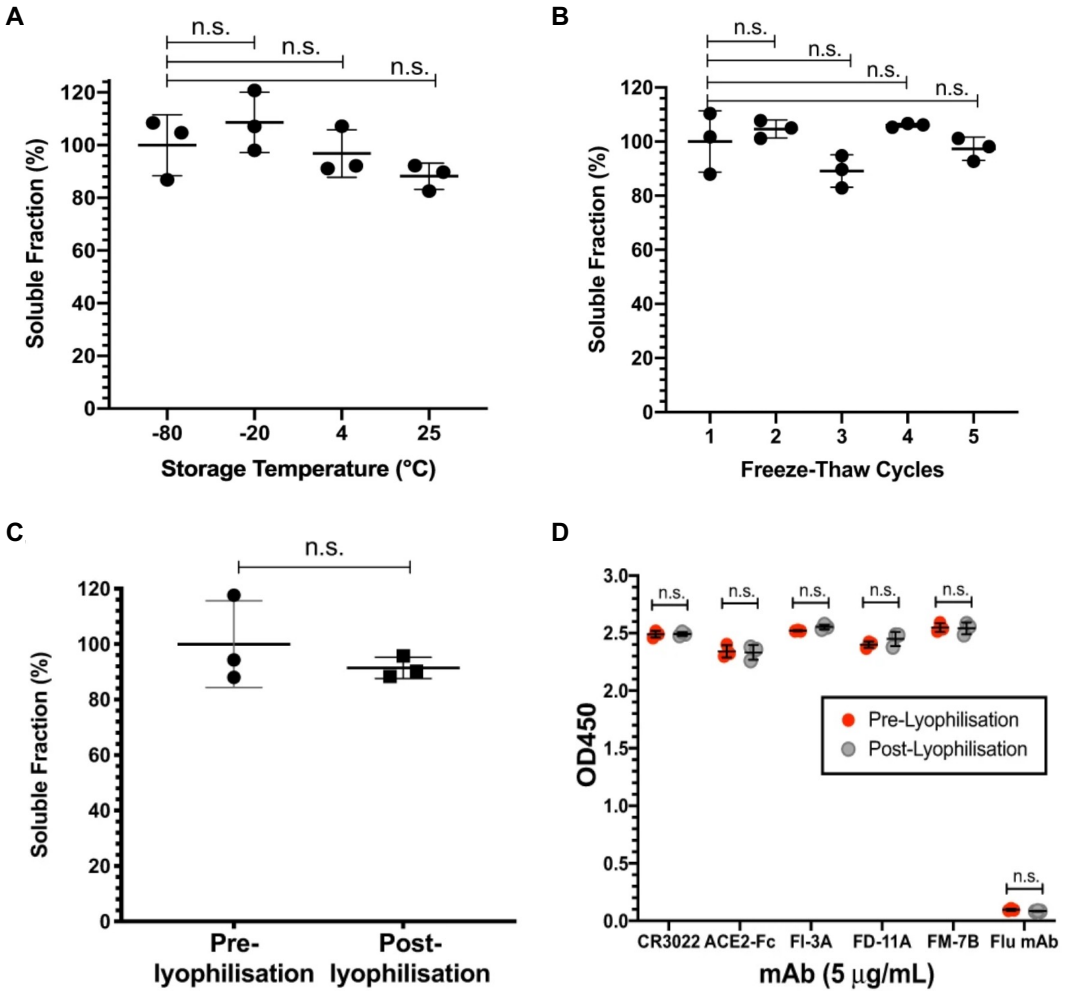


Figure 3. 12. RBD-coupled SpyCatcher003-mi3 is stable at different temperatures, against freeze-thaw and lyophilization: (A) Solubility fraction of RBD:SpyCatcher003-mi3 after two weeks of storage at specific temperatures. (B) Solubility fraction of RBD:SpyCatcher003-mi3 after 1 to 5 rounds of freeze-thaw. (C) Solubility fraction of RBD:SpyCatcher003-mi3 pre- and post-lyophilization (black circle and square, respectively) after reconstitution in the same buffer volume. (D) mAbs binding to non-overlapping RBD epitopes was measured pre- and post-lyophilization. Statistical differences in (A) and (B) were measured using the Kruskal-Wallis test and Dunn's multiple comparison test. Statistical difference in (C) and (D) was determined using Mann–Whitney U test. Two-tailed non-significance is abbreviated as "n.s.". Data/image credit: Tan et al., 2021.

The existence of coronavirus reservoirs in bats (Menachery et al., 2015, 2016) and concerning serological surveillance data of individuals who live near bat habitats (Wang et al., 2018) support the possibility of coronavirus transmission to humans in the future. Coronaviruses are also prone to mutate during replication and by RNA recombination if a human is infected with multiple strains (Pollett et al., 2021). Therefore, there is a desire for vaccines that can give broad protection against coronaviruses (Morens et al., 2022; Poland et al., 2021). One strategy is to simultaneously display heterologous antigens on an immunogenic scaffold. This approach has been reported to, in previous instances, focus antibody responses on conserved epitopes by enhancing cross-reactive B-cell avidity (Boyoglu-Barnum et al., 2021; Kanekiyo et al., 2019). Using the SpyCatcher003-mi3 VLP platform that I had developed earlier, we collaborated with Pamela Bjorkman's laboratory at Caltech to realize a VLP that displays heterologous antigens. Her group multimerized animal- and human-derived coronavirus RBD variants with SpyCatcher003-mi3 to evaluate its ability to generate cross-reactive antibody responses (Cohen et al., 2021b).

Building on a study that assessed the tropism of sarbecovirus RBD variants (Letko et al., 2020), the Bjorkman group selected for the particles eight different human- and animal-derived RBDs, classified into distinct clades (1, 2, 1/2, and 3) (Cohen et al., 2021b) . RBD from SARS-CoV-2 (clade 1/2) was derived from a human coronavirus, while RBDs from WIV1 and SHC014 (clade 1) or RmYN02, Rs4081 and Rf1 (clade 2) all originated from bat coronaviruses in China (Cohen et al., 2021b) . Bat-derived WIV1 and SHC014 are considered a danger for human transmission (Menachery et al., 2015, 2016). The RBD from RaTG13 (clade 1/2) was selected as the bat coronavirus most closely related to SARS-CoV-2 (Andersen et al., 2020; Cohen et al., 2021b). The RBD from Pang17 (clade 1/2) was derived from pangolins (Lam et al., 2020). The Bjorkman group then made four distinct RBD particles (Fig 3.13 A) (Cohen et al., 2021b) . The first particle,

mosaic-4a, multimerized RBDs from SARS-CoV-2, RaTG13, SHC014, and Rs4081. The second particle, mosaic-4b, multimerized RBDs from pang17, RmYN02, Rf1 and WIV1. The particle, mosaic-8, consists of all RBDs present in mosaic-4a and mosaic-4b. A final homotypic particle was decorated with SARS-CoV-2 RBDs. When aligned together, each of the VLP-displayed RBDs share 68-95% sequence similarity, with most of the variability localized to the ACE2 receptor binding motif (Cohen et al., 2021b) .

Mice immunization with these VLPs generated antibodies with detectable binding to all the RBDs (Cohen et al., 2021b) . The homotypic SARS-CoV-2 RBD:VLP provided enhanced response to the heterologous RBDs relative to the SARS-CoV-2 S trimer (SARS-2 S) itself (Fig 3.13 C-E) (Cohen et al., 2021b) . There was also no significant difference in SARS-2-specific IgG and neutralization response between the homotypic RBD particle and the three mosaic particles (Fig 3.13 D) (Cohen et al., 2021b) . This study also compared serum responses on “matched RBDs” (when RBD(s) displayed on a particle are the same as those used in measuring serum binding; coded in gray on the X-axis of histograms in Fig 3.13) and “mismatched RBDs” (when RBD(s) absent on a particle are the same as those used to measure serum binding; coded in red on the X-axis of histograms in Fig 3.13) (Cohen et al., 2021b) . Although the mosaic-4b particle lacked display of SARS-CoV-2 RBD (SARS-2 RBD), its corresponding IgG titer level was not substantially different from that of particles including SARS-2 RBD such as, mosaic-4a, mosaic-8 and the homotypic SARS-2 RBD particle (Fig 3.13 D) (Cohen et al., 2021b) . Serum from mice boosted with mosaic-4b was also able to neutralize the SARS-2 pseudovirus (Fig 3.13 D) (Cohen et al., 2021b) . Boost sera from all decorated VLPs neutralized SHC014 and WIV1, even though some VLPs used for immunization did not display either (Fig 3.13 E) (Cohen et al., 2021b) .

IgG from mice immunized with mosaic-4a and mosaic-8 particles bound SHC014 RBD more than the homotypic SARS-2 RBD particle after priming (Fig 3.13 E) (Cohen et al., 2021b) . Sera from mice boosted with mosaic-4a and mosaic-8 particle immunization were also able to neutralize SHC014 pseudovirus more than boosted sera from the homotypic SARS-2 RBD particle (Fig 3.13 E) (Cohen et al., 2021b) . The same sera from mosaic-4a and mosaic-8 immunized mice also displayed high IgG binding and neutralizing activity against Rs4081 and RaTG13 (Fig 3.13 F) (Cohen et al., 2021b) . Hence, these data suggest that displaying four or eight different RBDs together on SpyCatcher003-mi3 does not impede the immune response towards any one of the RBDs (Cohen et al., 2021b) .

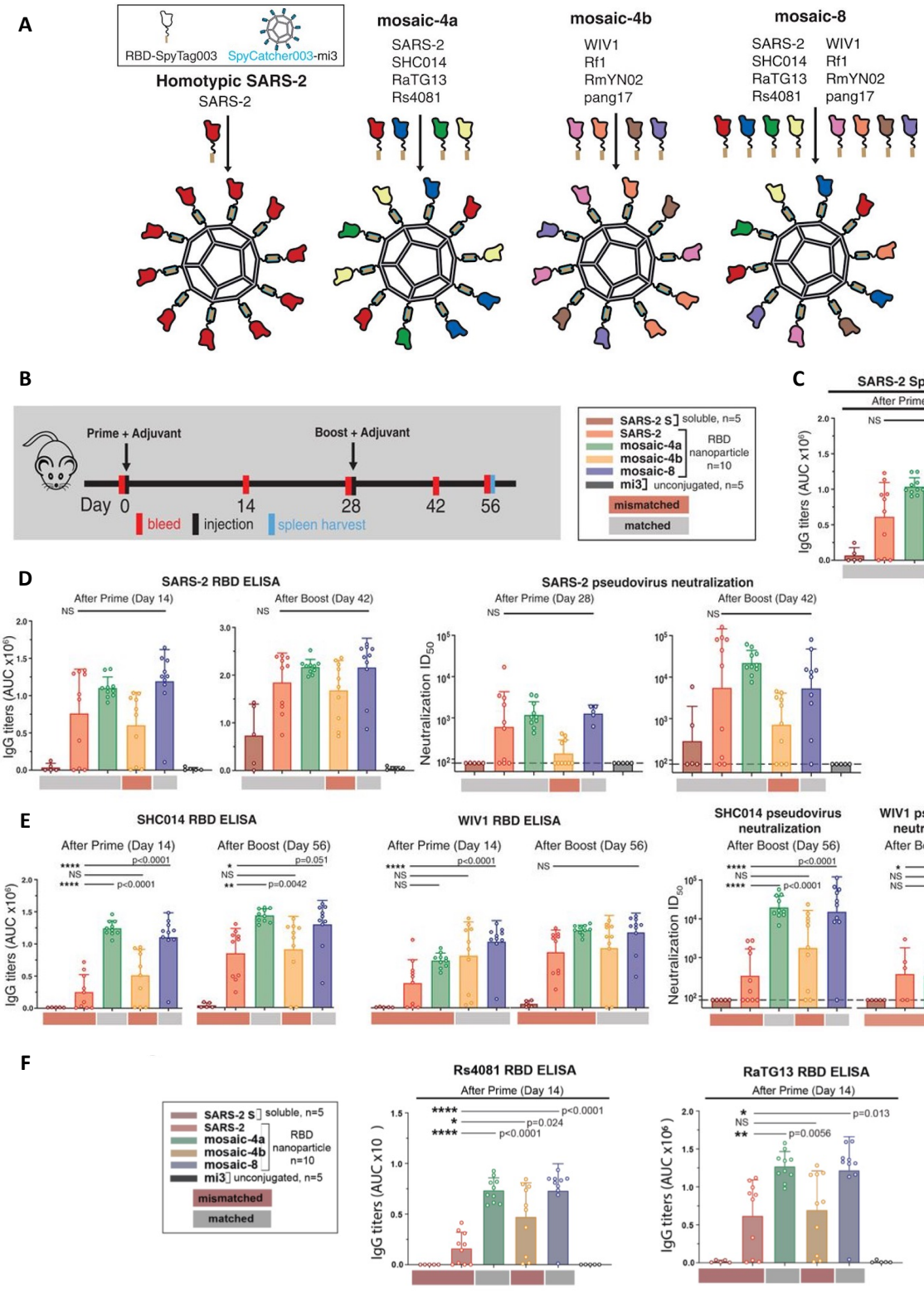

A
RBD-SpyTag003
SpyCatcher003-mi3
Homotypic SARS-2
SARS-2
mosaic-4a
SARS-2
SHC014
RaTG13
Rs4081
mosaic-4b
WIV1
Rf1
RmYN02
pang17
mosaic-8
SARS-2
SHC014
RaTG13
Rs4081
WIV1
Rf1
RmYN02
pang17
B
Prime + Adjuvant
Boost + Adjuvant
Day 0
14
28
42
56
bleed
injection
spleen harvest
SARS-2 S] soluble, n=5
SARS-2
mosaic-4a
mosaic-4b
mosaic-8
mi3] unconjugated, n=5
RBD nanoparticle n=10
mismatched
matched
C
SARS-2 Spike ELISA
After Prime (Day 14)
NS
IgG titers (AUC x10⁶)
D
SARS-2 RBD ELISA
After Prime (Day 14)
After Boost (Day 42)
NS
IgG titers (AUC x10⁶)
SARS-2 pseudovirus neutralization
After Prime (Day 28)
After Boost (Day 42)
NS
Neutralization ID50
E
SHC014 RBD ELISA
After Prime (Day 14)
After Boost (Day 56)
p<0.0001
NS
p<0.0001
p=0.051
p=0.0042
IgG titers (AUC x10⁶)
WIV1 RBD ELISA
After Prime (Day 14)
After Boost (Day 56)
p<0.0001
NS
NS
NS
SHC014 pseudovirus neutralization
After Boost (Day 56)
p<0.0001
NS
p<0.0001
Neutralization ID50
WIV1 pseudovirus neutralization
After Boost (Day 56)
p=0.028
NS
NS
F
SARS-2 S] soluble, n=5
SARS-2
mosaic-4a
mosaic-4b
mosaic-8
mi3] unconjugated, n=5
RBD nanoparticle n=10
mismatched
matched
Rs4081 RBD ELISA
After Prime (Day 14)
p<0.0001
p=0.024
p<0.0001
IgG titers (AUC x10)
RaTG13 RBD ELISA
After Prime (Day 14)
p=0.013
NS
p=0.0056
IgG titers (AUC x10⁶)

Figure 3. 13. Human/bat-derived sarbecovirus RBD-coupled SpyCatcher003-mi3 elicits strong cross-reactive responses against displayed RBD: (A) Different combination of RBDs expressed with SpyTag are used to form a homotypic particle and three different mosaic particles, as indicated. (B) Mice were dosed, boosted and bled according the following schedule; (C) ELISA IgG titer measurement against SARS-CoV-2 spike trimer (SARS-2 Spike); (D) ELISA IgG titer measurement against SARS-2 RBD (post-prime and boost) (left), SARS-2 pseudovirus neutralization levels (post-prime and boost) (right); (E) ELISA IgG titer measurement: against SHC014 RBD (post-prime and boost) (left), against WIV1 RBD (post-prime and boost) (center), SHC014 and WIV1 pseudovirus neutralization levels (post-boost) (right); (F) ELISA IgG titer measurement against Rs4081 RBD and RaTG13 RBD (post-prime) (left and right, respectively). Colors representing VLPs and their matched/mismatched status are specified in the key. All ELISA IgG titers are measured as area-under-the curve (AUC). Neutralization levels are represented as half-maximal inhibitory dilutions (ID_{50}) against pseudovirus of the respective coronavirus. Each dot is representative of an immunized mouse with means and standard deviations drawn in the form of rectangular bars and horizontal lines. Significant values between different groups are represented by horizontal lines and asterisks with p-values. Non-significant is denoted as “n.s.” Data/image credit: Cohen et al., 2021b.

An additional four RBD variants were not coupled to any particles and were used to evaluate sera from RBD nanoparticle immunizations for cross-reactive responses. Of these, Yunnan2011 (Yun11) (clade 2), BM-4831 (clade 3), and BtKY72 (clade 3) were derived from bat viruses in China, Bulgaria, and Kenya, respectively (Cohen et al., 2021b; Tao and Tong, 2019). The human coronavirus-derived RBDs originated from SARS-CoV, MERS-CoV, a SARS-CoV-2 variant with the Y453F mutation and another variant with Q493K/Q498K/P499T mutations (Cohen et al., 2021b) .

Priming with the mosaic-8 particle elicited significantly higher IgG titer binding relative to the homotypic SARS-2 particle, against Yun 11, BM4831, and BtKY72 RBDs

(Fig 3.14 A, B) (Cohen et al., 2021b) . IgG titers following immunization with the homotypic SARS-2 RBD particle failed to bind or neutralize the SARS-CoV RBD (Fig 3.14 A). However, priming with the mosaic-8 particle also elicited higher IgG titer binding and neutralization against the SARS-CoV RBD (Fig 3.14 A) (Cohen et al., 2021b) . This discrepancy in immune responses may be because the SARS-2 RBD only has 73% amino acid identity to SARS-RBD while the other included RBDs in mosaic-8a, such as SHC014 and WIV1 are 95% and 82% identical, respectively (Cohen et al., 2021b). After boosting with the homotypic SARS-2 RBD particle and mosaic-4a, there was some detectable pseudovirus neutralization, although this was still lower than that of mosaic-8 (Fig 3.14A) (Cohen et al., 2021b) . The level of IgG titers that bound to the SARS-2 RBD Y345P mutant and the Q493K/Q498K/P499T mutant, following boost immunization, were similar between the homotypic SARS-2 RBD particle and the mosaic particles (Fig 3.14 C) (Cohen et al., 2021b) . None of the homotypic or mosaic particles were able to elicit IgG titers against MERS RBD (Fig 3.14 D) (Cohen et al., 2021b) .

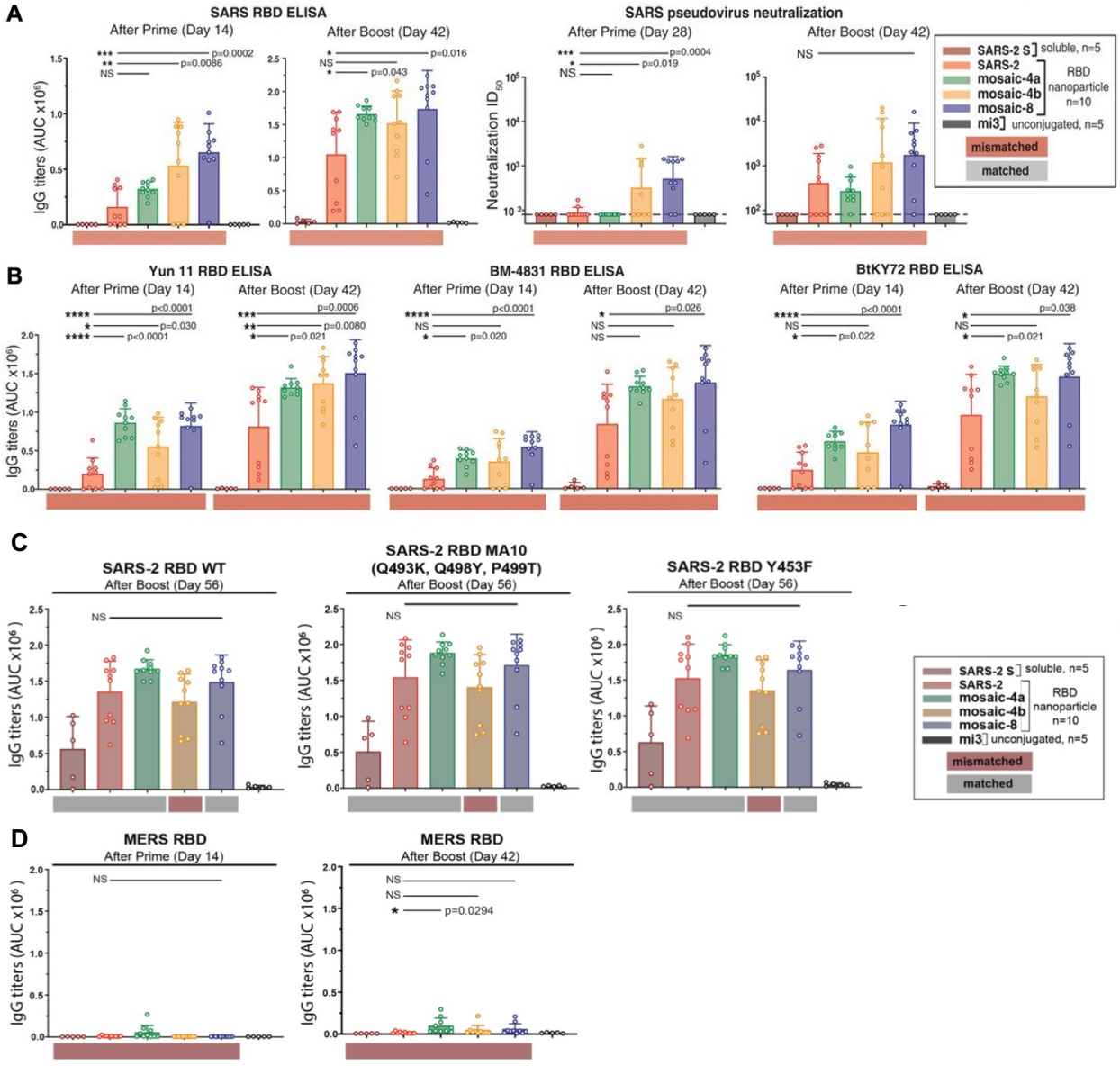


Figure 3. 14. RBD-coupled SpyCatcher003-mi3 elicit strong cross-reactive responses against non-displayed RBDs: (A) ELISA IgG titer measurement against SARS-RBD (post-prime and boost) (left), SARS pseudovirus neutralization levels (post-prime and boost) (right); (B) ELISA IgG titer measurement against: Yun11 RBD (post-prime and boost) (left), BM-4831 RBD (post-prime and boost) (center), BtKY72 RBD (post-prime and boost) (right); (C) ELISA IgG titer measurement against: SARS-2 RBD (post-boost) (left), SARS-2 RBD Q493K/Q498K/P499T mutant (post-boost) (center), SARS-2 RBD Y453F mutant (post-boost) (right); (D) ELISA IgG titer measurement against MERS

RBD (post-prime, left; boost, right). Colors representing VLPs and their matched/mismatched status are specified in the legends. All ELISA IgG titers are measured as area-under-curve (AUC). Neutralization levels are represented as half-maximal inhibitory dilutions (ID_{50}) against pseudovirus of the respective coronavirus. Each dot is representative of an immunized mouse with means and standard deviations drawn in the form of rectangular bars and horizontal lines. Significant values between different groups are represented by horizontal lines and asterisks with p-values. Non-significant is denoted as "n.s." Data/image credit: Cohen et al., 2021b.

3.3.2 Immunogenicity of influenza hemagglutinin and neuraminidase-coupled VLPs

Previously it was shown that SpyCatcher003-mi3 was able to stably couple trimeric and tetrameric antigens (Fig 3.9). To take advantage of this observation in the context of influenza, Dr. Rolle Rahikainen in the Howarth group coupled SpyCatcher003-mi3 to hemagglutinins (HA) H3 Vic and H3 Aichi, alongside neuraminidase (NA) N1, before intramuscularly immunizing mice with an 0.1 μg antigen dosage. The immunogens were adjuvanted with Addavax in a normal prime-boost scheme (Fig 3.15 A). Wild-type Victoria/361/2011 (Vic/361) and unconjugated H3 Vic were employed as controls for the H3 Vic:VLP immunization (Rahikainen et al., 2021). Single-cycle influenza viruses (S-FLU) pseudotyped with H3 Aichi and N1 were employed as controls for H3 Aichi:VLP and N1:VLP immunizations, respectively (Rahikainen et al., 2021). S-FLU is a suitable control because it is a virion that can only infect host cells but lacks the necessary gene to express more HA or NA (Powell et al., 2012). Antibody titers were assessed by incubating cells expressing surface H3 or N1 in the presence of boosted serum samples. It was observed that H3 Vic:VLPs elicited 7-fold higher median antibody titers than the same dose of unconjugated H3 Vic HA antigen (Fig 3.15 B) (Rahikainen et al., 2021). H3 Aichi:VLP only slightly increases the median antibody titer, although the difference was not significant (Fig 3.15 C) (Rahikainen et al., 2021). N1:VLP elicited 490-fold higher titers than

the same dose of unconjugated N1 and this level was similar to that of S-FLU-pseudotyped N1 (N1 S-FLU) (Fig 3.15 D) (Rahikainen et al., 2021).

A virus microneutralization assay was performed to study the efficacy of HA-specific antibodies (Fig 3.15 E). The H3 Vic:VLP generated 8.5-fold higher median neutralization titers relative to unconjugated H3 Vic and the Vic/361 virus control (Fig 3.15 F) (Rahikainen et al., 2021). The H3 Aichi:VLP generated 12-fold higher median neutralizing titers relative to unconjugated H3 Aichi and S-FLU pseudotyped with H3 Aichi (Fig 3.15 G) (Rahikainen et al., 2021). Separately, an enzyme-linked lectin assay (ELLA) was next performed to study the extent that NA-specific antibodies can inhibit sialic acid cleavage (Fig 3.15 H). While unconjugated N1 elicited no detectable response, N1:VLPs generated a potent N1 inhibition response not significantly different from that of N1-pseudotyped S-FLU (Fig 3.15 I) (Rahikainen et al., 2021). This data suggests that displaying these specific influenza hemagglutinin and neuraminidase molecules on SpyCatcher003-mi3 provides enhanced antibody titer and efficacy.

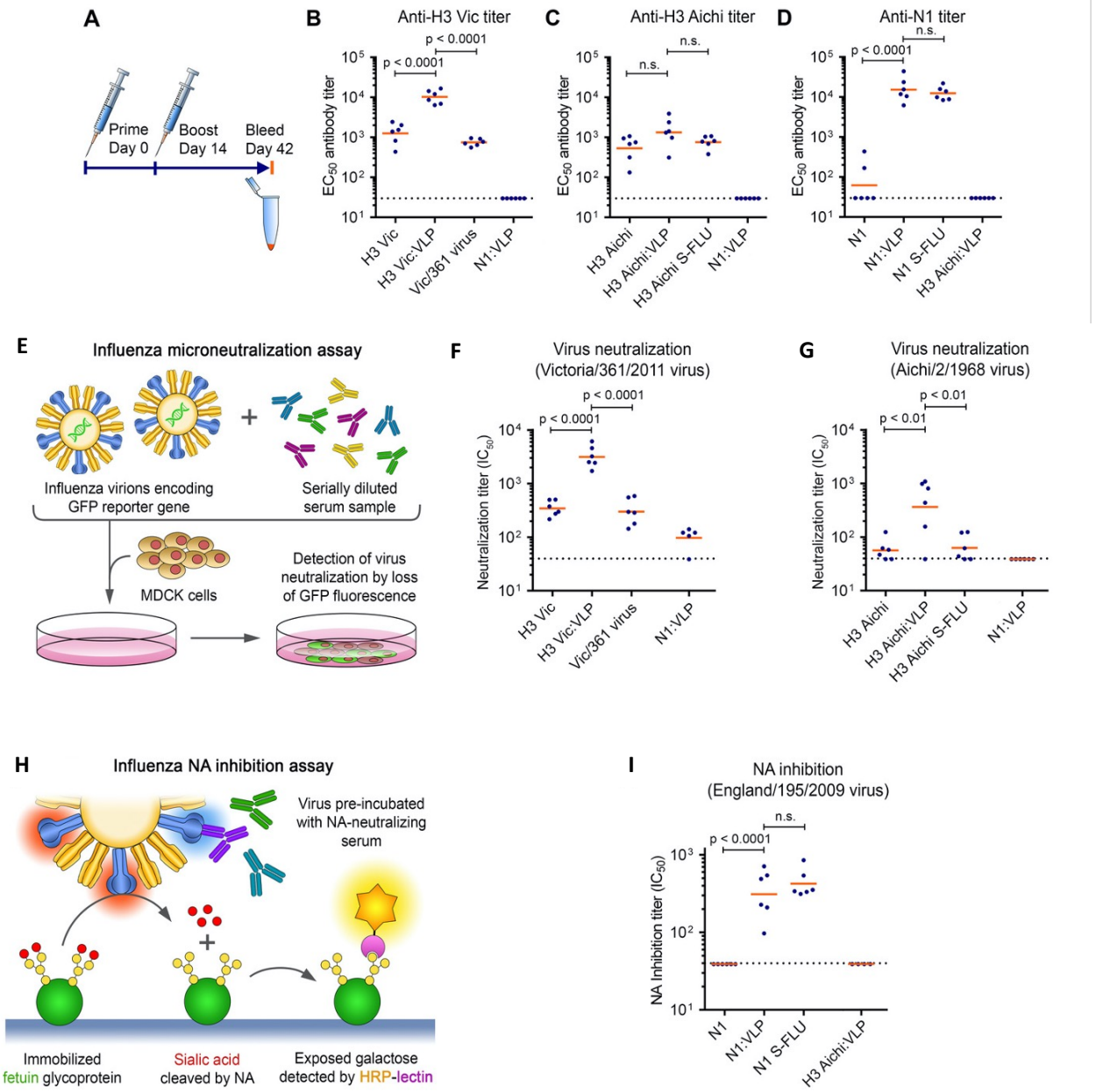


Figure 3. 15. H3 Vic HA and N1-coupled SpyCatcher003-mi3 elicit high neutralization antibody titers: (A) Immunization schedule; (B) Antibody titer measurement against H3 Vic HA, from mice primed/boosted with H3 Vic HA, H3 Vic HA:SpyCatcher003-mi3 (H3 Vic:VLP), Vic/361 virus and N1 NA:SpyCatcher003-mi3 (N1:VLP, negative control); (C) Antibody titer measurement against H3 Aichi HA, from mice primed and boosted with H3 Aichi HA, H3 Aichi HA:SpyCatcher003-mi3 (H3 Aichi:VLP), H3 Aichi S-FLU, and N1:VLP (negative control); (D) Antibody titer measurement against N1 NA, from mice primed and

boosted with: N1 NA, N1:VLP, N1 NA S-FLU (N1 S-FLU), H3 Aichi:VLP (negative control). (E) Schematic of microneutralization assay; neutralizing titer corresponds to a decrease in GFP fluorescence signal; (F) Microneutralization assay against Victoria/361/2011 virus, using sera from mice immunized with: H3 Vic HA, H3 Vic:VLP, Vic/361 virus and N1:VLP (negative control); (G) Microneutralization assay against Aichi/2/1968 virus, using sera from mice immunized with: H3 Aichi HA, H3 Aichi:VLP, H3 Aichi S-FLU and N1:VLP (negative control); (H) Schematic of NA inhibition assay; a decrease in HRP-lectin binding to fetuin is indicative of N1 NA inhibition. (I) Measurement of inhibition titer for mice immunized with N1 NA, N1:VLP, N1 NA:S-FLU (N1 S-FLU), or H3 Aichi:VLP. Each blue dot represents an immunized mouse and the mean is represented by an orange horizontal bar. Dashed line indicates limit of detection in assay (1:40 dilution). Statistical significance was determined using $\log_{10}$-transformed data and one-way ANOVA with Bonferroni correction. Not significant is denoted as “n.s.” Data/image credit: adopted from Rahikainen et al., 2021.

3.4 Discussion

Multiple factors must be considered in the design of an effective VLP platform. My laboratory previously observed SpyCatcher-mi3 aggregation upon heating (Bruun et. al, 2018). This concerning behavior was the reason for me to explore whether mutating the remaining surface cysteines of the mi3 monomer at residues 165 and 203, aimed to eliminate possible interchain disulfide bonding, might mitigate this problem. However, the issue persisted.

For a vaccine platform to be scalable, especially for use in developing countries, it must be both stable and possess low costs for production. I kept the mi3 component from SpyCatcher-mi3 because it was engineered from a thermophilic marine bacterium. I replaced SpyCatcher with SpyCatcher003 because of SpyCatcher003’s higher thermal stability, increased reactivity, and the fact that human sera tested showed five times less anti-SpyTag003:SpyCatcher003 antibodies compared to anti-SpyTag:SpyCatcher

antibodies. I showed that the resultant particle, SpyCatcher003-mi3, can be expressed solubly in *E. coli* and purified to high yields without an affinity tag, through ammonium sulfate precipitation in scalable volumes and SEC. I have also shown that including T56E and I58K mutations on SpyCatcher003 results in soluble VLP expression. My current yields demonstrate that there is still some room for optimizing growth and induction conditions; a higher yield should be possible through utilizing fermentation methods (Chen et al., 2016). Besides ammonium sulfate precipitation, PEG has also been used to successfully precipitate VLPs (Koho et al., 2012; Tsoka et al., 2000). Some examples of downstream techniques developed to purify large biomolecules include chromatography methods using polymethacrylate monolith resins with peptide ligands, polystyrene gigapore resins with DEAE groups, as well as ultracentrifugation, which is still widely used for VLP purification (Effio and Hubbuch, 2015).

SpyCatcher003-mi3 is also able to display antigens of diverse sizes and symmetries. DLS measurements confirm that particles decorated with select monomeric, dimeric, trimeric, and tetrameric antigens are monodisperse. Notably, both the antiparallel NDV HN dimer and the D2 symmetrical streptavidin were able to couple the VLP without compromising its solubility. However, when the particle is coupled with large, tetrameric β-galactosidase, the particles completely aggregated. These results suggest that one limitation of SpyCatcher003-mi3 may lie in its ability to couple large, dihedral antigens. The panel of displayed antigens used here did not include those with cubic (i.e. icosahedral capsid) (Gomes et al., 2017) or unbounded symmetry (i.e. helical filaments) (Marini et al., 2019) since they are sufficiently multivalent to produce an immune response without further multimerization (Rahikainen et al., 2021).

Hemagglutinins H3 Vic and H3 Aichi along with neuraminidase N1 were able to couple SpyCatcher003-mi3 while preserving VLP solubility. Immunization of decorated

SpyCatcher003-mi3 with H3 Vic and N1 elicited higher antibody titers compared to the same amount of unconjugated antigen due to multivalent display. These results show that HA and NA, displayed on SpyCatcher003-mi3, are highly immunogenic in mice. Previous attempts to create HA-based VLP vaccines include genetically fusing HA to protein scaffolds (Kanekiyo et al., 2013) and using SpyCatcher/SpyTag to co-display multiple HA variants and antigenic portions of the HA protein (Cohen et al., 2021a; Sharma et al., 2020; Thrane et al., 2020). The current seasonal influenza vaccines are designed to optimally generate antibodies to the HA head domain (Krammer, 2019). Some of these vaccines can also raise antibody responses against NA, even though the quantity and antigenicity of NA are not standardized (Giurgea et al., 2020; Sultana et al., 2014). Some studies show that antibodies against neuraminidase can be just as potent and protective (Creytens et al., 2021; Krammer et al., 2018). However, there are currently few research efforts dedicated to evaluating NA-decorated VLPs (Quan et al., 2012; Smith et al., 2017).

Chapter 4: Development of a Shielded SpyCatcher003-mi3 Scaffold

Chapter 4: Development of Shielded SpyCatcher003-mi3 Particles

After producing bacterial-expressed SpyCatcher003-mi3 and confirming its immunogenicity, I then proceeded to examine whether SpyCatcher003-mi3 could be expressed solubly in mammalian cells. Compared to bacterial cells, mammalian cells allow for proteins to undergo certain post-translational modifications and be secreted directly into cell media for harvesting and downstream processing. Two of the key mammalian cell-lines approved for recombinant protein expression include Chinese hamster ovary (CHO) cells and human embryonic kidney 293 (HEK293) cells (Dumont et al., 2016). CHO cells are favored for therapeutic protein production due to their ability to largely produce human-like glycans, high purification yield (in the range of g/L culture), the ability to be scaled up in serum-free media, and its safety track-record (Lai et al., 2013; Lalonde and Durocher, 2017). However, CHO cells are unable to produce certain human-like glycans such as the bisecting form of N-Acetylglucosamine and α(2,6)-linked sialic acid residues (Chin et al., 2019; Fliedl et al., 2015). CHO cells also produce non-human glycans such as N-glycolylneuraminic acid and galactose-α-1,3-galactose, which can induce immunogenicity against the protein (Fliedl et al., 2015). Being a human-derived cell line, HEK293 can produce human glycans and is capable of producing antibodies at yields of up to 600 mg/L culture (Spidel et al., 2016). Since HEK293 and CHO have been used to produce numerous commercially approved pharmaceuticals (Dumont et al., 2016; Walsh, 2014), I planned to test the feasibility of expressing SpyCatcher003-mi3 in these two cell-lines.

Many innate immune cells recognize glycans on the surface of antigens as a pathogen-associated molecular pattern, before initiating an immune response (Reily et al., 2019). Different laboratories have taken advantage of this principle to design nanoparticle vaccine candidates, which have been very effective at stimulating both B cell and T cell dependent immune responses to displayed antigens (Alam et al., 2021; Hyakumura et al.,

2015; Tokatlian et al., 2019; Zhang et al., 2020). For some antigens, like the HIV envelope protein and the SARS-CoV-2 spike trimer, a high density of glycans can also block antibody recognition of certain epitopes (Casalino et al., 2020; Crispin et al., 2018; Wei et al., 2003). Some research groups used glycans to shield certain regions of the antigen, thereby re-focusing antibody response to other unmasked epitope(s) (Frey et al., 2021; Shinnakasu et al., 2021). The presence of glycans on proteins can also enhance the stability of protein structures against proteolysis and in varying pH and temperature conditions (Shental-Bechor and Levy, 2008; Zhou and Qiu, 2019).

Previous engineering of SpyCatcher protein loops resulted in enhanced resilience and reactivity with SpyTag-proteins (Keeble et al., 2017, 2019). Rationally mutating SpyCatcher has also allowed SpyCatcher-SpyTag protein-peptide partners to be repurposed as a bacteriophage display strategy for optimizing the sequences of cell-penetrating peptides (Stone et al., 2016) and for affinity purification (Spy&Go) (Khairil Anuar et al., 2019). The previous success that my laboratory had in engineering SpyCatcher proteins gave me confidence that inserting N-linked glycosylation sites, consisting of only three amino acid modifications at most, is also feasible without compromising SpyCatcher functionality. To date, no published literature has examined the effects of loop modifications on the solubility and stability of the mi3 scaffold. These unique properties of glycans and their potential for enhanced immunogenicity when placed on a nanoparticle led me to believe that a glycosylated SpyCatcher003-mi3 VLP may offer similar advantages. It would be especially advantageous as a vaccine platform if the glycosylated particle could be produced as efficiently in mammalian cells and be as immunogenic as the bacterial-expressed SpyCatcher003-mi3.

With valuable insights gathered from engineering glycosylated SpyCatcher003-mi3 VLPs, I turned my attention back to my bacterial-expressed SpyCatcher003-mi3 VLPs. I

want to see if these VLPs can be engineered such that albumin could shield parts of the scaffold by binding to specific 18-53 residue-long albumin-binding sequences. If this bacterial-expressed SpyCatcher003-mi3 can bind albumin, while adequately displaying antigens and staying soluble, it could offer another means of occluding the scaffold with non-immunogenic material using a system that could be expressed in bacterial cells.

Serum albumin is present in the human blood at a relatively high concentration of 35-50 g/L and has a half-life of 19 days (Merlot et al., 2014). Serum albumin binds and transports fatty acids, ions, and hormones throughout the body and regulates the osmotic pressure of blood (Merlot et al., 2014). At the same time, some species of bacteria, like streptococci, possess membrane proteins that bind human serum albumin (HSA) with high affinity and specificity. This is a mechanism that helps to shield the bacteria from the immune system (Egesten et al., 2011; Kronvall et al., 1979). Human serum albumin had been previously used to construct nanoparticles due to their biocompatible and biodegradable nature (Elzoghby et al., 2012). Examples of clinically-approved applications include the ultrasound contrast reagent (Albunex^{TM}) and chemotherapy medication, nab-paclitaxel (Abraxane^{TM}) (Gradishar, 2006; Keller et al., 1989). Binding HSA with the paclitaxel drug helped decrease progression of metastatic breast cancer and increased patient survival (Gradishar, 2006; Gradishar et al., 2009; Guan et al., 2009). Several pre-clinical studies show that binding albumin to peptide vaccines enable the vaccine to drain/accumulate in the lymph node, enhance antigen presentation, and elicit cytotoxic T-cell responses (Gao et al., 2021; Rakhra et al., 2021; Wang et al., 2018c). Albumin-coated tobacco mosaic virus nanoparticles decreased antibody recognition and neutralization of the particle itself, increasing the nanoparticle's circulation time (Gulati et al., 2018; Pitek et al., 2016, 2018). Serum albumin's well-documented ability to be attached to proteins and elicit unique immune responses inspired a Part II student in our laboratory, David

Schramm, to explore engineering and validating serum albumin-bound SpyCatcher003-mi3 nanoparticles.

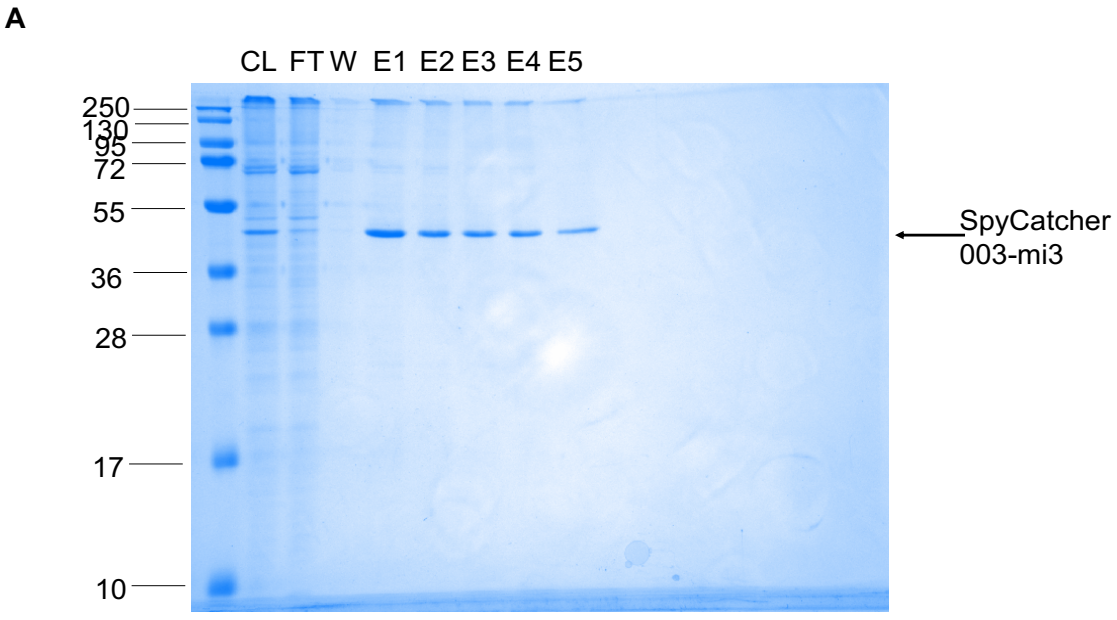
In the first part of this chapter, I explain my rationale and approach to engineering glycosylated SpyCatcher003-mi3 VLPs. Upon confirming their solubility, I characterize the particles' uniformity, geometry, heat resilience, reactivity, and glycosylation status. In addition to testing the particle's immunogenicity against SARS-CoV-2 RBD, I also test how well my inserted glycans occluded the mi3 scaffold and SpyCatcher003:SpyTag003 protein by measuring serum binding levels against each. I conclude by examining the IgG subtypes generated against RBD in boosted mice sera and provide an assessment of what this suggests for the application of glycosylated SpyCatcher003-mi3:RBD variants as a SARS-CoV-2 vaccine candidate.

In the second part of this chapter, I start by discussing the work of David Schramm on engineering and validating serum albumin-bound bacterial-expressed SpyCatcher003-mi3 nanoparticles. I then describe my work on measuring the antibody titers induced by particles coupled with SARS-CoV-2 RBD, with or without serum albumin-based shielding.

4.1. Design of glycosylated SpyCatcher003-mi3 particles

4.1.1. Expression of SpyCatcher003-mi3 in HEK293 cells

Before N-linked glycans could be engineered on SpyCatcher003-mi3, I first had to make sure that SpyCatcher003-mi3 could fold correctly and be secreted in mammalian cell culture. I cloned the sequence of bacterial-expressed SpyCatcher003-mi3 onto a pENTR4 mammalian expression plasmid backbone and transfected this plasmid into HEK293 culture. This sequence has no consensus N-linked glycosylation sequons of Asn-X-Ser/Thr, with X being any amino acid except Pro. After adding the kit-provided enhancers, the VLPs were harvested after seven days of cell incubation. Following affinity purification and SEC, a soluble protein product, with the same molecular weight as SpyCatcher003-mi3 (37 kDa), was observed on a 16% (w/v) SDS protein gel (Fig 4.1 A). The band of the HEK293-expressed SpyCatcher003-mi3 also resembles that of the bacterial-expressed SpyCatcher003-mi3 (Fig 4.1 B).



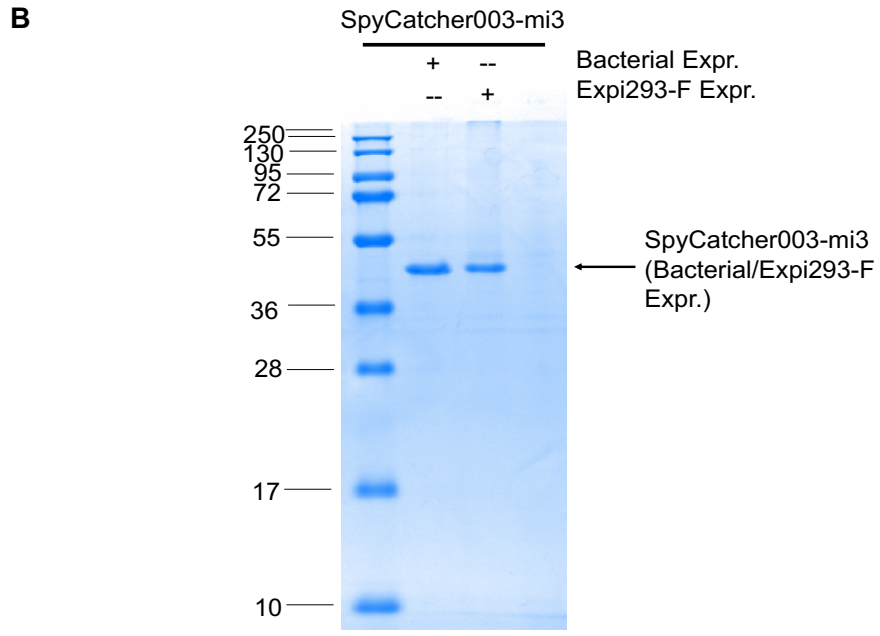


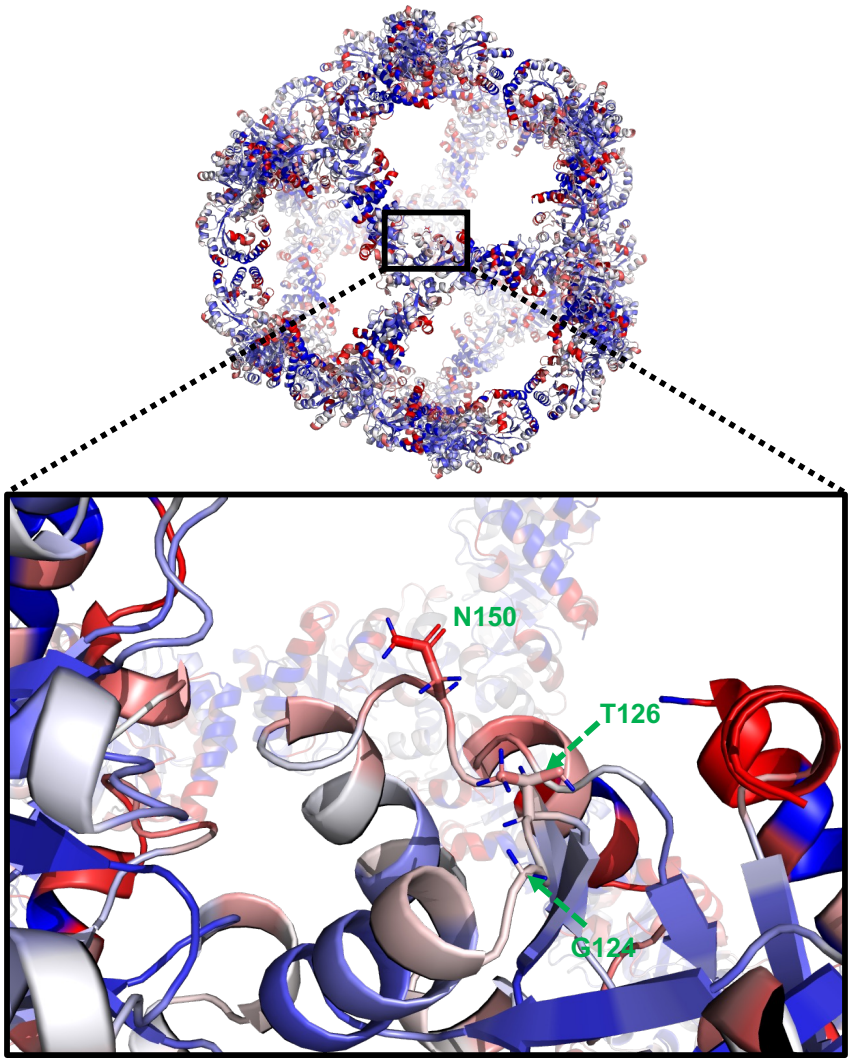
Figure 4.1. C-tag affinity purification gel of HEK293-expressed SpyCatcher003-mi3 and comparison with bacterial-expressed SpyCatcher003-mi3: (A) Affinity purification gel showing soluble expression of SpyCatcher003-mi3 from HEK293 culture; (B) Comparison of protein bands from bacterial-expressed and HEK293-expressed (Expi293-F Expr.) SpyCatcher003-mi3. The gel labels are abbreviated as follows: Cleared lysate (CL), flow-through (FT) , wash (W), Elutions (1-5) (E1-5). Both non-reducing 16% (w/v) gels were stained with Coomassie.

4.1.2. Specific flexible loop Insertion of N-linked glycans

I used published crystal structures to visualize the parent domain of SpyCatcher003 (PDB: 2X5P) and SpyTag (adapted from PDB: 4MLI). I visualized the mi3 scaffold using the i301 particle model, constructed from arranging twenty modified copies of the Class I KDPG adolase trimer crystal structure (PDB: 1WA3 with E26K, E33L, K61M, D187V, and R190A mutations) in a dodecahedral symmetry (Hsia et al., 2016). I then

designated three criteria to decide where I would insert the N-linked glycan sequons on the flexible loops of the SpyCatcher003 protein and the mi3 scaffold. First, I only selected loops that that were situated on the surface and faced outward relative to the nanocage. I next narrowed down my selection of candidate loops based on PyMOL visualization of its B-factors, which indicate the region of a molecule with the greatest level of observed mobility relative to the other atoms in the crystal structure. I recognize that taking this approach to select for candidate loops will not detect the intrinsically flexible loops stabilized by crystal-packing interactions. Lastly, I made sure that the N-linked glycan sequons were not located near monomer-monomer interfaces of the mi3 scaffold or the reactive site of SpyCatcher003 (Khairil Anuar et al., 2019). The resulting candidate insertion sites that met these criteria on mi3 were: N150, G124 and T126. The insertion sites that met these criteria on SpyCatcher003 were: S50, G61 and G83 (Fig 4.2 A and B).

A



N150	-GPFPNVKFVPT-	-GPFPNVSFVPT-
G124	-AMKLGHTILKL-	-AMKLNGSHTILKL-
T126	-KLGHTILKLFPG-	-KLGHNGTILKLFP-

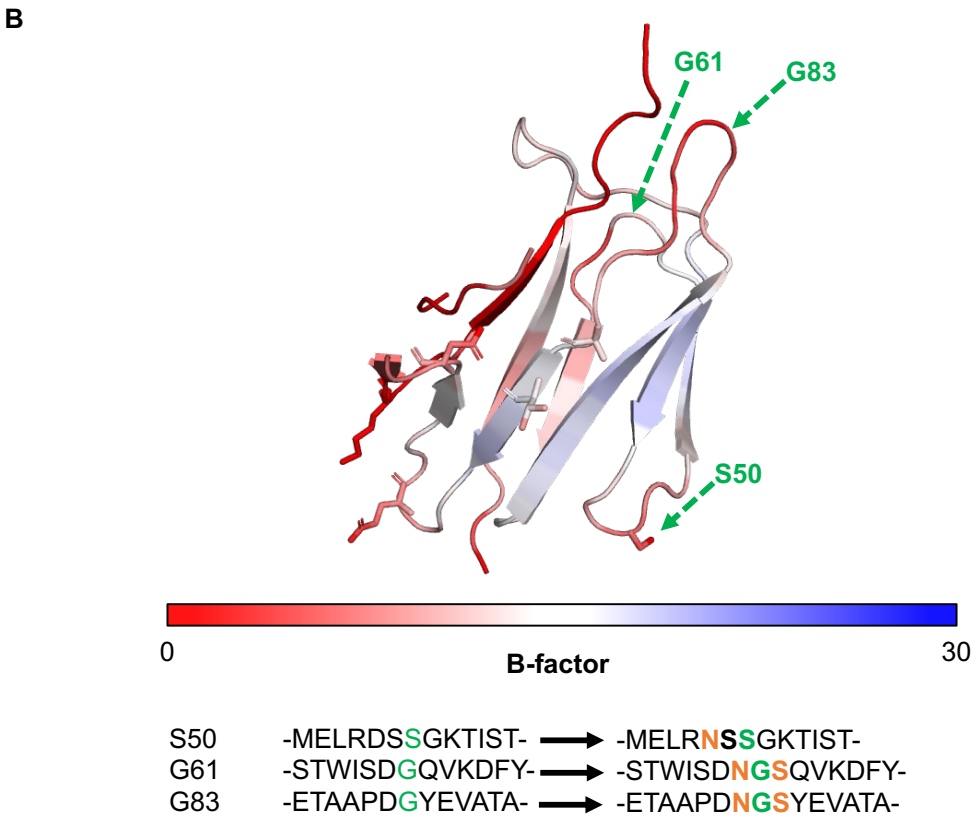
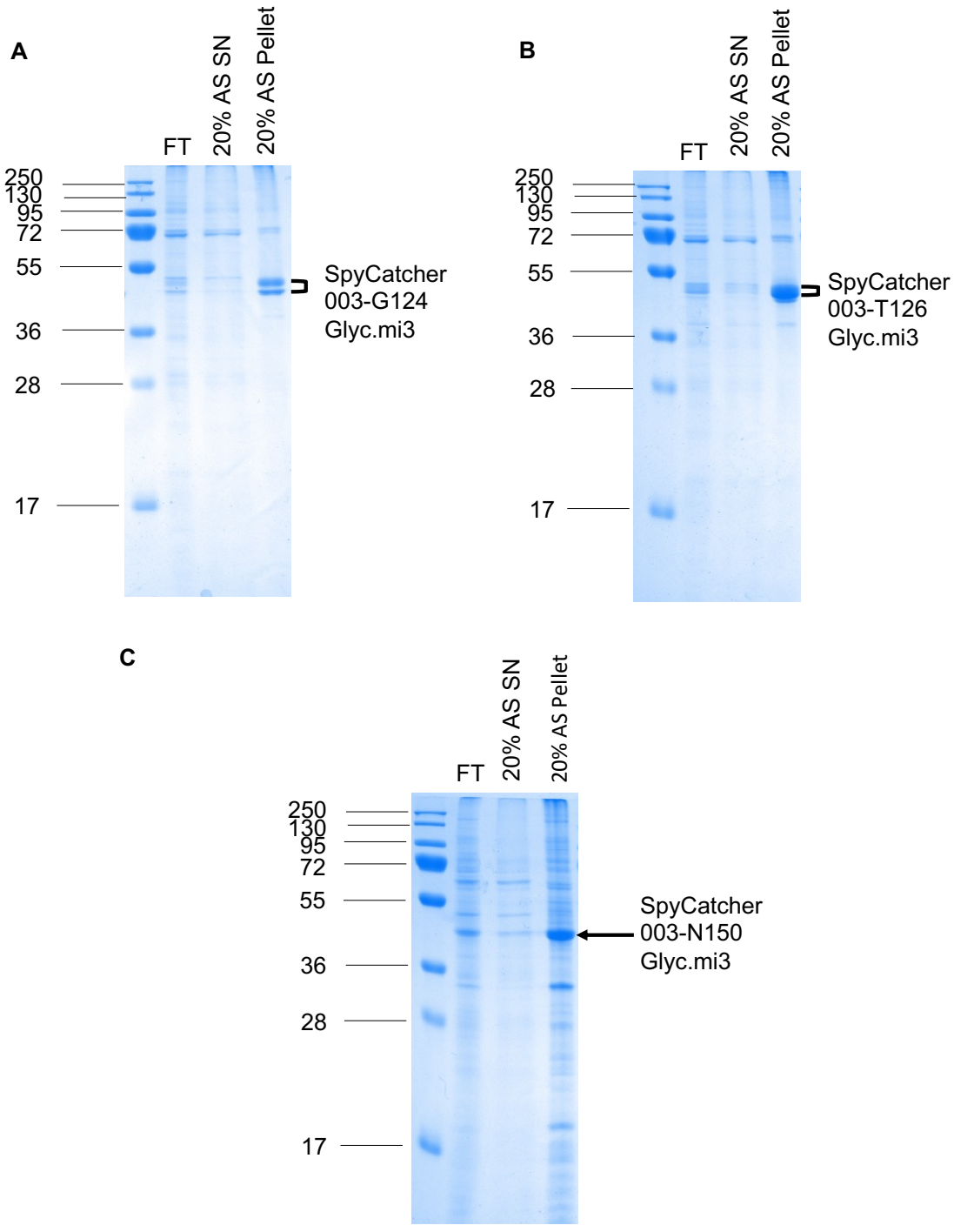


Figure 4. 2. Selected N-glycan sequon loop insertion sites on SpyCatcher003 and mi3: (A) PyMOL rendering of the i301 nanocage (Credit: Hsia et al., 2016) with colored B-factors from 0 (red) to 20 (blue) and loop insertion sites (green); (B) PyMOL rendering of SpyCatcher003 parent domain based on PDB 2X5P and 4MLI (only SpyTag displayed) (Image credit: Irsyad Khairil Anuar) with colored B-factors from 0 (red) to 30 (blue) and loop insertion sites (green). In both (A) and (B), orange colored residues represent the amino acids introduced to generate an N-glycosylation sequon.

I cloned the consensus N-glycosylation sequon peptide, Asn-X-Ser/Thr, into SpyCatcher003-mi3 while changing as little of the original VLP amino acid sequence as possible. I then expressed each of these constructs in 25 mL of HEK293 culture and performed ammonium sulfate precipitation and affinity purification to examine the extent of soluble protein expression. I observed that all my candidate VLPs with inserted N-linked glycan sequons expressed solubly (Fig 4.3).


A
FT
20% AS SN
20% AS Pellet
250
130
95
72
55
36
28
17
SpyCatcher
003-G124
Glyc.mi3
B
FT
20% AS SN
20% AS Pellet
250
130
95
72
55
36
28
17
SpyCatcher
003-T126
Glyc.mi3
C
FT
20% AS SN
20% AS Pellet
250
130
95
72
55
36
28
17
SpyCatcher
003-N150
Glyc.mi3

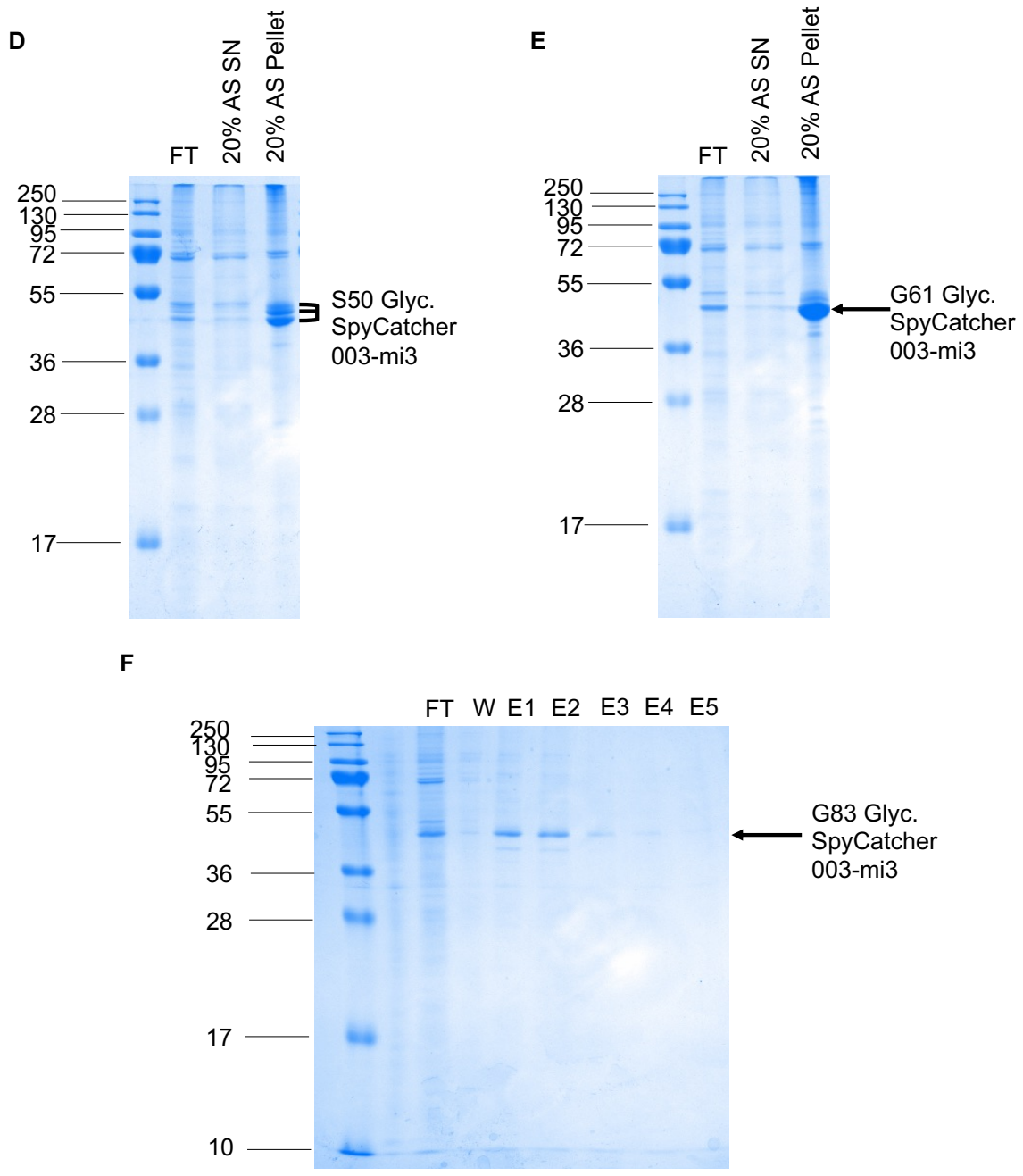


Figure 4. 3. Expression studies of N-linked glycan sequons inserted in flexible SpyCatcher003 and mi3 loops: 20% (w/v) ammonium sulfate precipitation gel results of: (A) SpyCatcher003-G124 Glyc. mi3; (B) SpyCatcher003-T126 Glyc. mi3; (C) SpyCatcher003-N150 Glyc. mi3; (D) S50 Glyc. SpyCatcher003-mi3; (E) G61 Glyc. SpyCatcher003- mi3. (F) C-tag XL affinity purification of G83 Glyc. SpyCatcher003-mi3. Gel labels were abbreviated as follows: Flow-through (FT); wash (W), Elutions 1-5 (E1-5),

ammonium sulfate supernatant (AS SN), ammonium sulfate resuspended pellet (AS Pellet). All gels (A-F) were run on non-reducing 16% (w/v) SDS-PAGE and stained with Coomassie. C-tag XL resin was used in Fig 4.3 F because there was a shortage of C-tag CaptureSelect resin at the time of this experiment.

However, not all these candidate VLPs assembled into particles of the correct size. SEC results (Fig 4.4) show that inserting the N-glycan sequon at residue T126 of mi3 did not result in formation of a particle. Inserting a N-glycan sequon at residue G83 of SpyCatcher003 and residue N150 of mi3 produced an excess of artifact products smaller in size than VLP monomers or larger than the bacterial-expressed SpyCatcher003-mi3 VLP itself. The particle with an N-glycan sequon inserted at residue G61 produced an assembled particle with the correct size, but in a small amount relative to other VLP variants. Particles with N-glycan sequons positioned at residue S50 of the SpyCatcher003 protein and residue G124 of the mi3 scaffold show up on SEC with a similar-sized product as bacterial-expressed SpyCatcher003-mi3. These two VLP variants also have minimal amounts of lower-mass protein artifacts. Both these VLP candidates also appear double-banded, which might suggest that the heavier band is the glycosylated portion of the particle and the lighter band is the unglycosylated portion (Fig. 4.3). Based on these observations I decided to characterize the HEK293-expressed SpyCatcher003-mi3 with N-linked glycan sequons inserted at residue S50 of SpyCatcher003 (S50 Glyc. SpyCatcher003-mi3) and another at residue G124 of mi3 (SpyCatcher003-G124 Glyc. mi3).

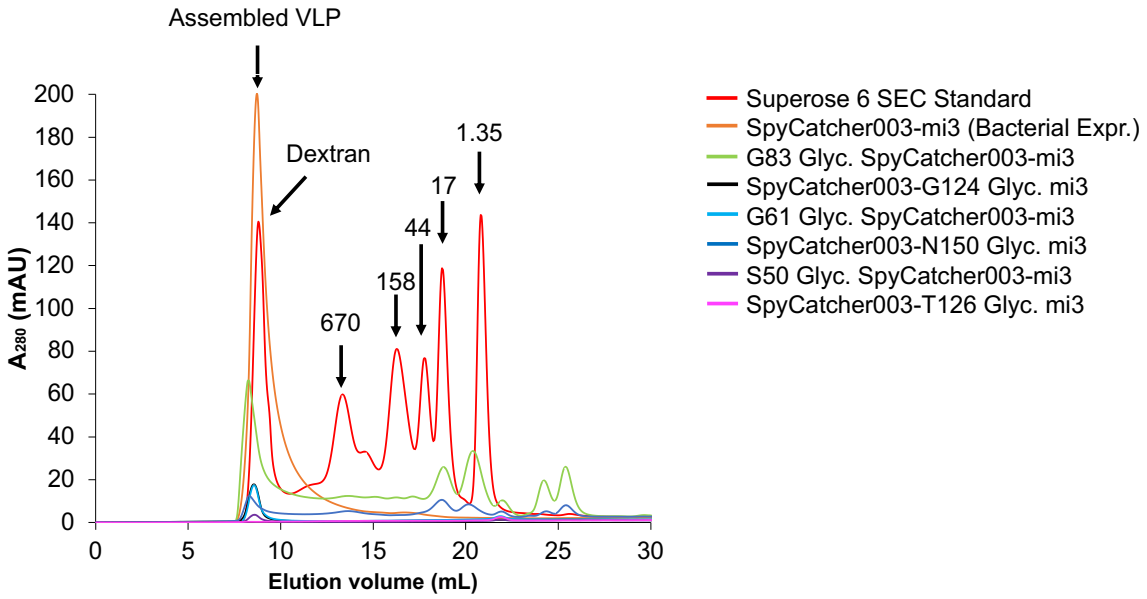


Figure 4. 4. Size-exclusion chromatography of glycosylated VLP variants: Bacterial-expressed SpyCatcher003-mi3 is marked in orange. The VLPs with N-glycan sequons inserted on SpyCatcher003 at residues: G83 (G83 Glyc. SpyCatcher003-mi3) is in light green, G61 (G61 Glyc. SpyCatcher003-mi3) is light blue, and S50 (S50 Glyc. SpyCatcher003-mi3) is in purple. The VLPs with N-glycan sequons inserted on mi3 at residues: G124 (SpyCatcher003-G124 Glyc. mi3) is in black, N150 (SpyCatcher003-N150 Glyc. mi3) is dark blue, and T126 (SpyCatcher003-T126 Glyc. mi3) is in pink. The standard is marked in red and the labeled molecular weights are denominated in kDa.

4.1.3 Expression and affinity purification of glycosylated particles

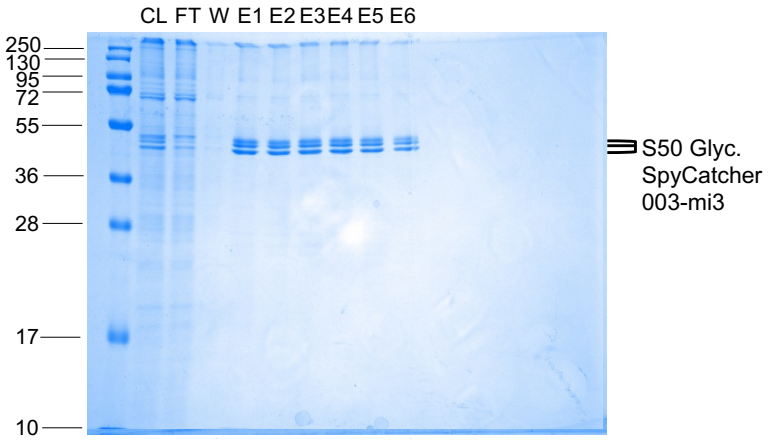
I had observed that ammonium sulfate precipitation, previously used for purifying large batches of bacterial-expressed SpyCatcher003-mi3, tends to lead to excessive crashing out of HEK293-expressed VLP variants. To avoid losing yield, I reverted to using C-tag CaptureSelect affinity resin to purify more S50 Glyc. SpyCatcher003-mi3 and SpyCatcher003-G124 Glyc. mi3 VLPs for characterization. To optimize VLP yield, I allowed the constructs to express for seven days after adding the kit-provided enhancers

to the culture. S50 Glyc. SpyCatcher003-mi3 and SpyCatcher003-G124 Glyc. mi3 produced soluble VLP products in line with their expected molecular weights of 37 kDa (Fig 4.5 A and B).

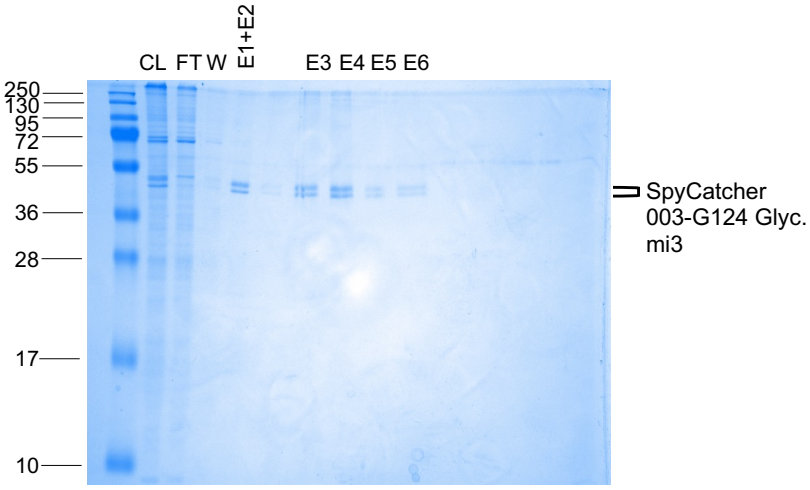
I also wanted to express a mannose-dense SpyCatcher003-mi3 variant in order to target delivery of the VLP to antigen-presenting cells and to raise robust T cell responses. Previously, the presence of high mannose-oligosaccharides has enabled nanoparticles to be trafficked to follicles in a mannose binding lectin-dependent manner (Read et al., 2022; Tokatlian et al., 2019), helped enhance dendritic cell maturation, and induced robust Th1 or Th2 cytokine responses (Alam et al., 2021; Sun et al., 2021). Creating this particle could provide insights into how the different glycan composition would impact stability and immunogenicity relative to the other glycoforms.

In an effort to generate a mannose-dense VLP variant, I expressed S50 Glyc. SpyCatcher003-mi3 with 5 nM Kifunensine (S50 Glyc. SpyCatcher003-mi3 + Kif), a selective class I α-mannosidase inhibitor (Elbein et al., 1990). By inhibiting the class I α-mannosidase in the ER, kifunensine prevents mannose cleavage, resulting in proteins with $Man_9GlcNAc_2$ glycan structures. This modification produced a soluble product identical in size (37 kDa) to S50 Glyc. SpyCatcher003-mi3, but deviates in that it has one heavy band as opposed to two stacked heavy bands (Fig 4.5 A and C). Previously I had attempted to express VLPs with 5 μM kifunensine, but it was low-yielding (<0.5 mg/L), could not form uniform-sized particles and was not stable at 25 ^{o}C. I initially believed that decreasing the concentration of kifunensine in culture could produce a partially-mannosylated particle, while retaining some non-mannose glycans that could help the particle to fold and assemble correctly.

A


CL FT W E1 E2 E3 E4 E5 E6
250
130
95
72
55
36
28
17
10
S50 Glyc.
SpyCatcher
003-mi3

B


CL FT W
E1+E2
E3 E4 E5 E6
250
130
95
72
55
36
28
17
10
SpyCatcher
003-G124 Glyc.
mi3

C

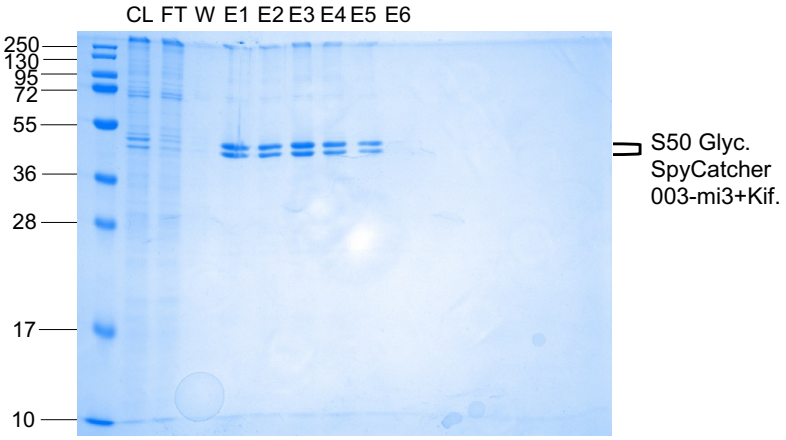

CL FT W E1 E2 E3 E4 E5 E6
250
130
95
72
55
36
28
17
10
S50 Glyc.
SpyCatcher
003-mi3+Kif.

Figure 4. 5. C-tag affinity purification gel results of S50 Glyc. SpyCatcher003-mi3 and SpyCatcher003-G124 Glyc. mi3 VLPs: (A) Purification gel of HEK293-expressed S50 Glyc. SpyCatcher003-mi3; (B) Purification gel of HEK293-expressed SpyCatcher003-G124 Glyc. mi3; (C) Purification gel of HEK293-expressed S50 Glyc. SpyCatcher003-mi3 with Kifunensine (S50 Glyc. SpyCatcher003-mi3+Kif). Samples loaded on each gel include: cleared lysate (CL), flow-through (FT), wash (W); Elutions 1-5 (E1-5). All non-reduced 16% (w/v) SDS gels were stained with Coomassie.

S50 Glyc. SpyCatcher003-mi3 and SpyCatcher003-G124 Glyc. mi3 VLPs were also expressed in the CHO cell line. Like HEK293 cells, the CHO cells expressed soluble monomers with similar size and band appearance. However, I observe that CHO cell expression also produces bands corresponding to protein forms of lower mass (Fig 4.6 A and B). Moreover, SEC results show that the soluble monomers were unable to assemble into a particle of the appropriate size (Fig 4.6 C). This may suggest that the specific composition or occupancy of N-linked glycans synthesized by CHO cells prevented adequate VLP assembly. These observations suggest that CHO cells may not be a suitable means of scaling up glycosylated SpyCatcher003-mi3 production.

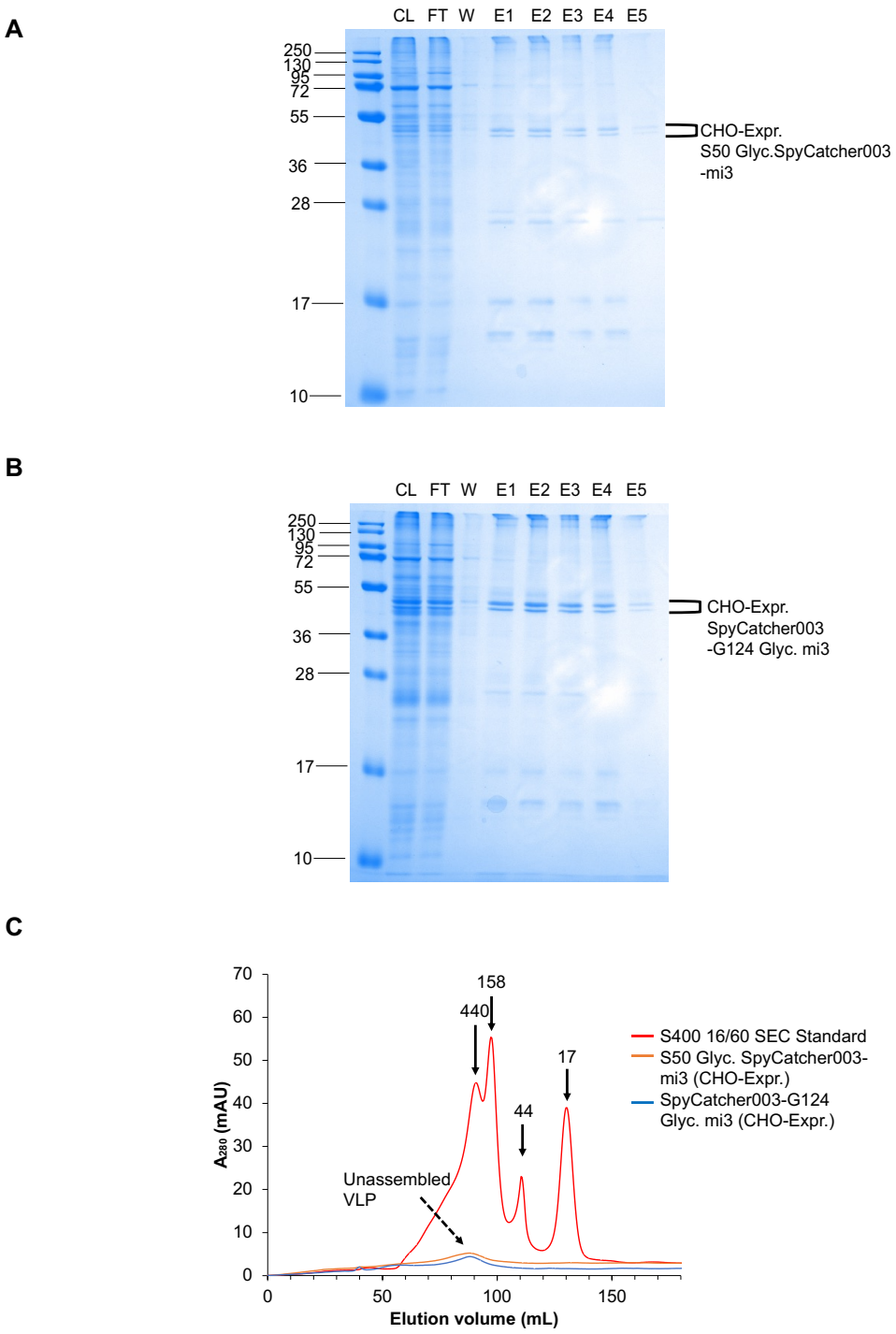


Figure 4. 6. C-tag affinity purification gel and SEC of CHO-expressed S50 Glyc. SpyCatcher003-mi3 and SpyCatcher003-G124 Glyc. mi3: (A) Purification gel of CHO-expressed S50 Glyc. SpyCatcher003-mi3; (B) Purification gel of CHO-expressed

SpyCatcher003-G124 Glyc. mi3. Samples loaded on each gel include: cleared lysate (CL), flow-through (FT), wash (W); Elutions 1-5 (E1-5). Both non-reduced 16% (w/v) SDS gels were stained with Coomassie. (C) SEC comparison of CHO-expressed VLPs. CHO-expressed S50 Glyc. SpyCatcher003-mi3 is marked in orange; CHO-expressed SpyCatcher003-G124 Glyc. mi3 is marked in blue. The standard is marked in red and the labeled molecular weights are denominated in kDa.

I had also attempted to make a glycosylated SpyCatcher003-mi3 with two glycosylation sites present at S50 and G124 simultaneously (S50 Glyc. SpyCatcher003-G124 Glyc. mi3). If realized, such particle with two N-linked glycosylation sequons could potentially have greater occupancy and shield more of the VLP's surface area. When expressed in HEK293 cells, the soluble product band was quite low (Fig 4.7 A). SEC results show a small amount of particle assembly, dwarfed by an even larger product peak corresponding to the mass of unassembled trimers (Fig 4.7 B). This observation suggests that the existence of both these N-linked glycans prevent adequate particle formation. For this reason, I did not characterize this particle further.

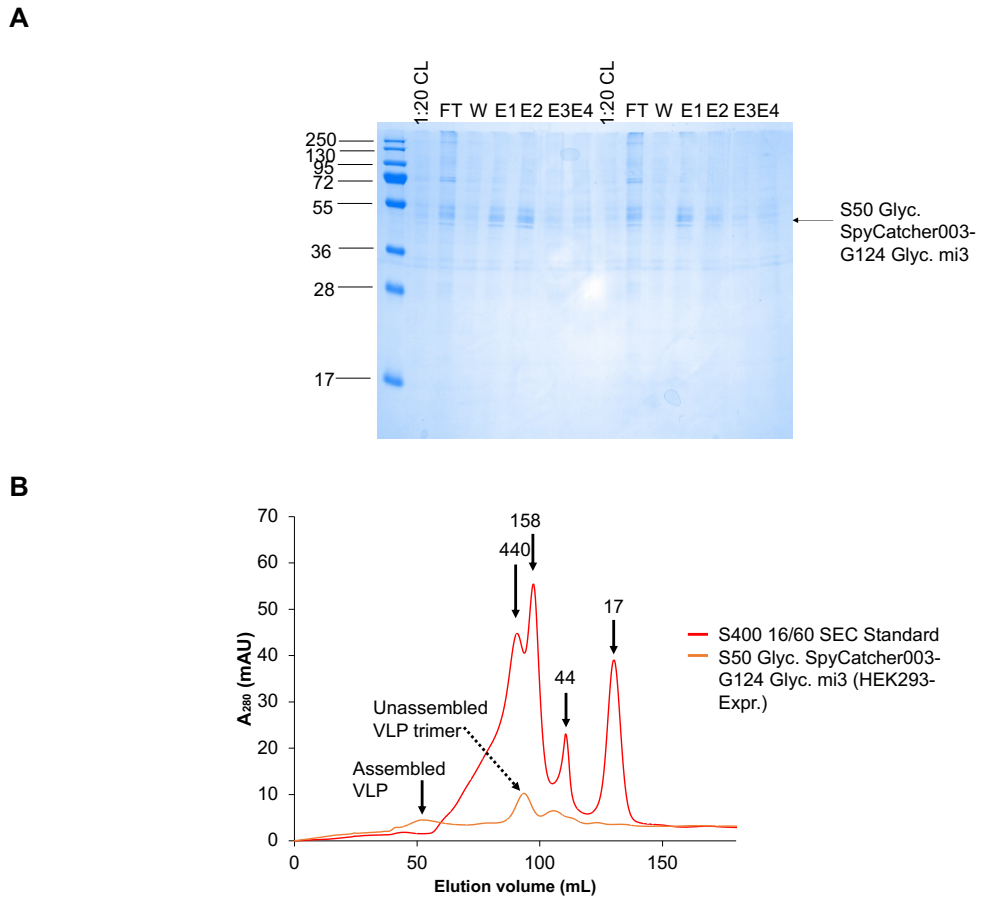


Figure 4. 7. C-tag affinity purification gel and SEC of S50 Glyc. SpyCatcher003-G124 Glyc. mi3 candidate VLP: (A) Purification gel of HEK293-expressed S50 Glyc. SpyCatcher003-G124 Glyc. mi3; (B) SEC of S50 Glyc. SpyCatcher003-G124 Glyc. mi3 is represented in orange, column standard is represented in red and the labeled molecular weights are denominated in kDa. 16% (w/v) non-reduced SDS gel was stained in Coomassie. The gel labels are abbreviated as follows: 1:20 diluted cleared lysate (1:20 CL), flowthrough (FT), wash (W), Elutions 1-5 (E1-5). This VLP was purified with C-tag XL resin because the lab had a shortage of C-tag CaptureSelect resin at the time of this experiment.

Compared to the bacterial-expressed SpyCatcher003-mi3, the size-excluded, C-tag affinity-purified yields of HEK293-expressed VLPs were low. HEK293-expressed

SpyCatcher003-mi3 has an estimated purification yield of only 1 mg/L culture. S50 Glyc. SpyCatcher003-mi3 has an estimated purification yield of 4 mg/L culture while SpyCatcher003-G124 Glyc. mi3 has a yield of 3.2 mg/L culture. S50 Glyc. SpyCatcher003-mi3 + Kif has a yield of 1.4 mg/L culture.

4.1.4 Confirmation of VLP glycosylation status

Before proceeding to further characterization and immunization, it is important to confirm that N-linked glycosylation is present on the each of the loop-based N-linked glycan sequons. I digested each soluble VLP in Peptide-N-Glycosidase F (PNGase-F), an amidase that specifically cleaves the glycosidic bond between the first N-acetylglucosamine precursor and asparagine residue of hybrid, high mannose, and complex N-linked oligosaccharides. A shift in VLP band position on SDS-PAGE would be indicative of N-linked glycan presence. Bands corresponding to S50 Glyc. SpyCatcher003-mi3, S50 Glyc. SpyCatcher003-mi3 + Kif, and SpyCatcher003-G124 Glyc. mi3 all displayed a shift after PNGase-F digestion (Fig 4.8 A and B). This confirms that its heavier band corresponds to glycosylated portions of the VLP, while the lighter band corresponds to the unglycosylated portion of the VLP. According to gel densitometry band analysis, S50 Glyc. SpyCatcher003-mi3 was 60% glycosylated, SpyCatcher003-G124 Glyc. mi3 was 61% glycosylated and S50 Glyc. SpyCatcher003-mi3 + Kif was 63% glycosylated. HEK293-expressed SpyCatcher003-mi3, which had no consensus N-linked glycosylation sequons, showed an absence of N-linked glycans (Fig 4.8 A).

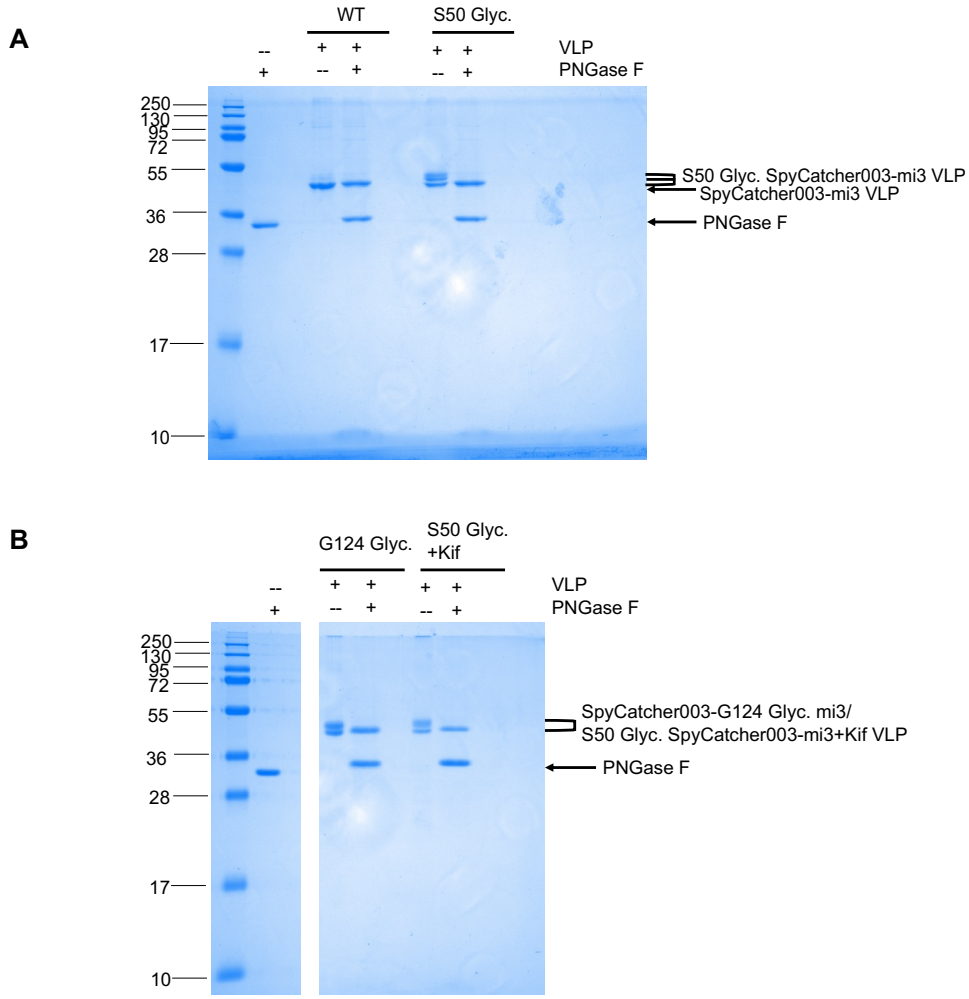


Figure 4. 8. PNGase-F digestion of glycosylated VLPs: (A) PNGase-F digestion of HEK293-expressed SpyCatcher003-mi3 (WT) and S50 Glyc. SpyCatcher003-mi3 (S50 Glyc.); (B) PNGase-F digestion of SpyCatcher003-G124 Glyc. mi3 (G124 Glyc.) and S50 Glyc. SpyCatcher003-mi3 expressed with 5 nM Kifunensine (S50 Glyc. + Kif). Both non-reduced 16% (w/v) SDS gels were stained with Coomassie.

Having confirmed that S50 Glyc. SpyCatcher003-mi3 + Kif had N-linked glycosylation, it is important to now confirm that the N-linked oligosaccharides on this VLP are mannose-dense. The S50 Glyc. SpyCatcher003-mi3 + Kif VLP was digested with Endoglycosidase H (Endo H), which specifically cleaves the diacetylchitobiose core,

between the first and second N-acetylglucosamine closest to asparagine, of mannose-rich N-linked oligosaccharides (Maley et al., 1989). A shift in VLP band position on SDS-PAGE would be indicative of high-mannose glycosylation. Following Endo H digestion, S50 Glyc. SpyCatcher003-mi3 + Kif showed only a slight band shift (Fig 4.9). While this particle is glycosylated, it appears to lack mannose-rich glycosylation. This may be because kifunensine is not effective at a concentration as low as 5 nM. Taken together, these results show that the specific sequons I inserted into flexible loops allow for soluble VLP expression and different amounts or perhaps types of N-linked glycan synthesis.

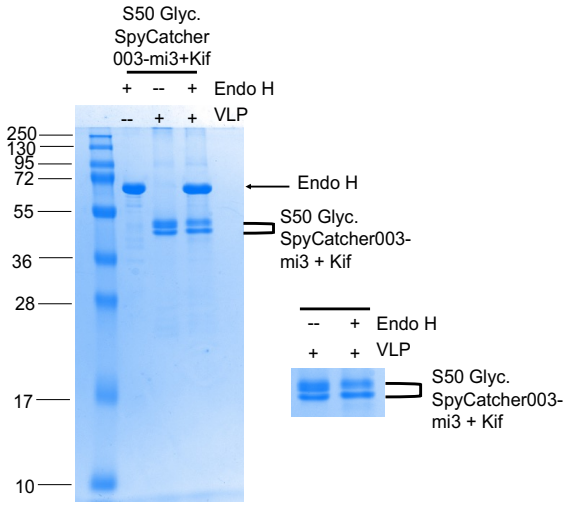


Figure 4. 9. Endo H digestion of S50 Glyc. SpyCatcher003-mi3 expressed with Kifunensine: Gel with zoomed-in view (right) showing slight shift in VLP band after Endo H digestion. This non-reduced 16% (w/v) SDS gel was stained with Coomassie.

4.1.5 Assessing particle uniformity of glycosylated VLPs

I performed SEC on all my HEK293-expressed VLPs and saw that they assembled into particles of their expected size (Fig 4.10 A). Checking the size uniformity of my glycosylated VLPs will help ensure their ability to display an optimal number of antigens on its surface. Using dynamic light scattering (Fig 4.10 B), I observe that HEK293-expressed SpyCatcher003-mi3 had a hydrodynamic radius of 23 ± 7.2 nm (mean±1 s.d., n=3). S50

Glyc. SpyCatcher003-mi3 had a hydrodynamic radius of 28 ± 11 nm, (mean±1 s.d., n=3). SpyCatcher003-G124 Glyc. mi3 had a hydrodynamic radius of 30 ± 13 nm, (mean±1 s.d., n=3). S50 Glyc. SpyCatcher003-mi3 + Kif had a hydrodynamic radius of 22 ± 6.3 nm, (mean±1 s.d., n=3). S50 Glyc. SpyCatcher003-mi3 and SpyCatcher003-G124 Glyc. mi3 have larger radii and standard deviations than SpyCatcher003-mi3, suggesting that a non-uniform distribution of glycans inserted in SpyCatcher003 or mi3 loops impacts the size of the particles. It is interesting that S50 Glyc. SpyCatcher003-mi3 with Kifunensine yields particles with decreased hydrodynamic radius standard deviations, since the VLP does not appear to be mannose-rich.

Negative stain transmission electron microscopy (TEM) images of HEK293-expressed SpyCatcher003-mi3, S50 Glyc. SpyCatcher003-mi3 or SpyCatcher003-G124 Glyc. mi3 displayed fully-formed particles identical to those seen in previous studies that used the mi3 scaffold fused to SpyCatcher or SpyCatcher003 (Bruun et al., 2018; Rahikainen et al., 2021) (Fig 4.10 C). All these data show that the presence of N-linked glycans on mi3 or SpyCatcher003 loops do not affect the geometry of particles, nor do the particles aggregate. However, I believe that expressing the VLPs in HEK293 and/or having N-linked glycans on these particles contribute to the larger variation in particle radii relative to the bacterial-expressed SpyCatcher003-mi3

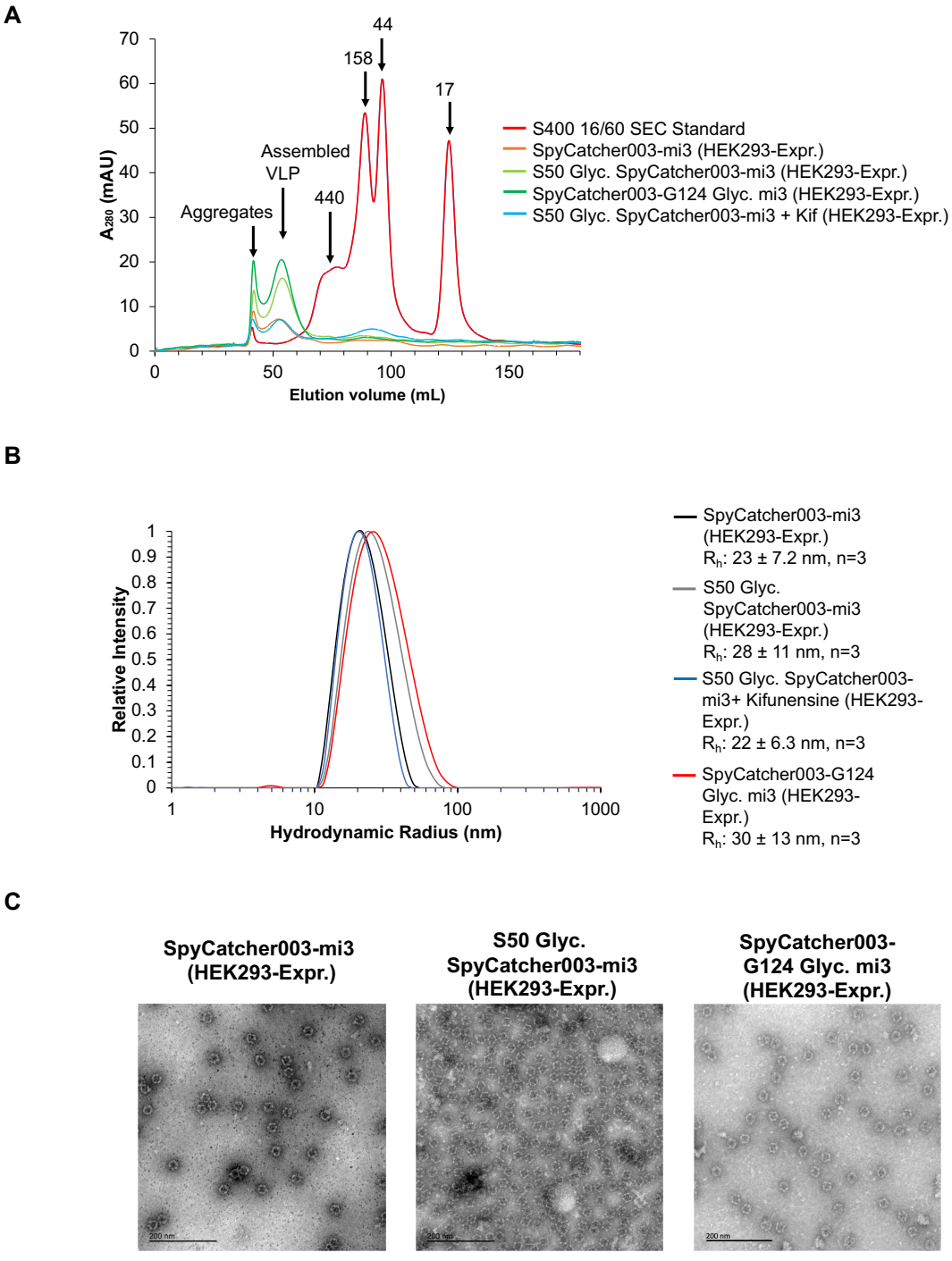


Figure 4. 10. SEC chromatogram, dynamic light scattering, and negative stained images of glycosylated VLPs: (A) SEC of glycosylated VLPs and HEK293-expressed SpyCatcher003-mi3. SpyCatcher003-mi3 is marked in orange; S50 Glyc. SpyCatcher003-mi3 is marked in light green; SpyCatcher003-G124 Glyc. mi3 is marked in dark green; S50

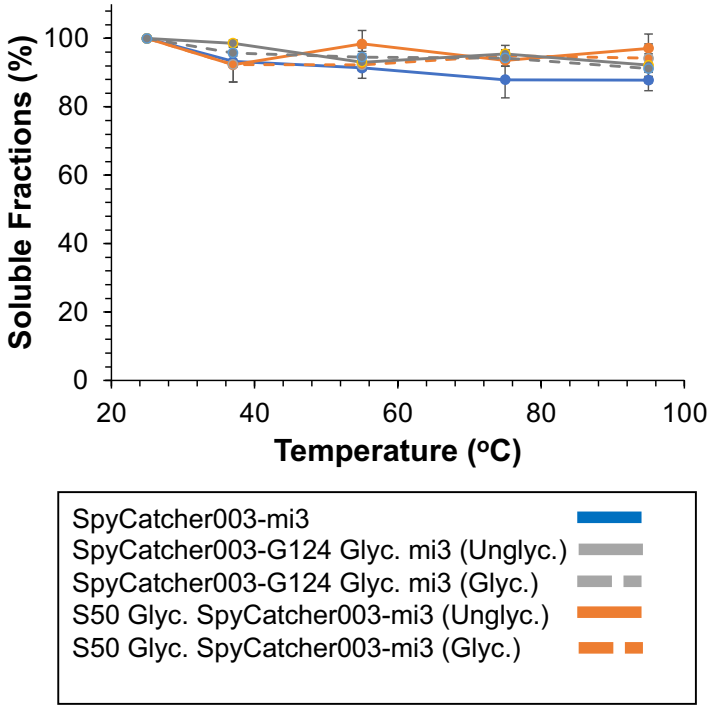
Glyc. SpyCatcher003-mi3 + Kif is marked in light blue; SEC column standard is marked in red with molecular weights denominated in kDa. SEC was run at 0.2 mL/min flow rate. (B) DLS of glycosylated VLPs and HEK293-expressed SpyCatcher003-mi3 at 25 ^{o}C. All hydrodynamic radii (R_h) are represented as mean±1 s.d., n=3. HEK293-expressed SpyCatcher003-mi3 is represented in black; S50 Glyc. SpyCatcher003-mi3 is represented in gray; S50 Glyc. SpyCatcher003-mi3 expressed with Kifunensine is represented in blue, SpyCatcher003-G124 Glyc. mi3 is represented in red. (C) Negative stained TEM images of glycosylated VLPs. Black horizontal bar represents 200 nm. Images were taken by Dr. Niels Wicke.

4.1.6 Heat stability of glycosylated particles

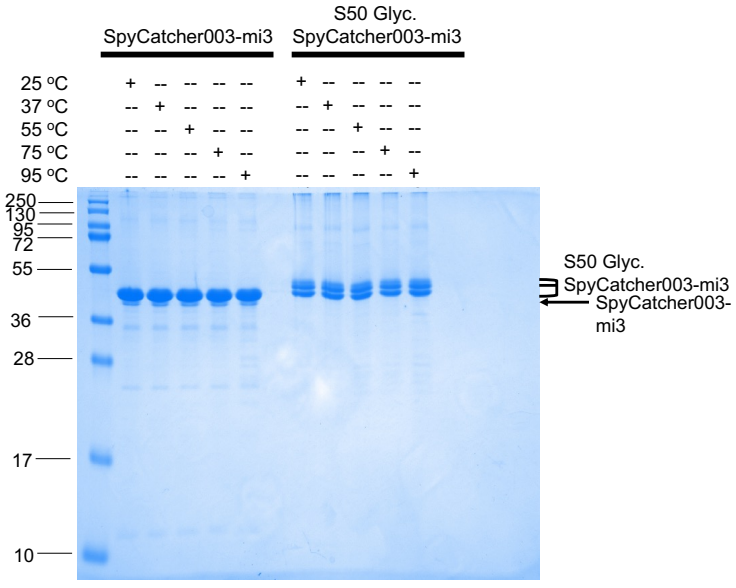
The heat resilient nature of a VLP scaffold has implications for the reliability of a vaccine to be deployed in regions with incomplete cold chains. To assess whether the presence of N-linked glycans on SpyCatcher003 and mi3 impact the heat stability of the particle, I heated 3 μM of S50 Glyc. SpyCatcher003-mi3, SpyCatcher003-G124 Glyc. mi3, and bacterial-expressed SpyCatcher003-mi3 at various temperatures for 1 h, before cooling to 4 ^{o}C for 10 min (Fig 4.11 A).

At the indicated temperatures between 25 ^{o}C and 95 ^{o}C, the glycosylated and unglycosylated subunits of S50 Glyc. SpyCatcher003-mi3 and SpyCatcher003-G124 Glyc. mi3 retained 90% to 100% solubility. This change in percentage solubility is similar to that of bacterial-expressed SpyCatcher003-mi3, which retains an average of 87% to 100% solubility in the same conditions (Fig 4.11 A). Together, this suggests that the presence of these specific N-linked glycans on the loops of SpyCatcher003 and mi3 scaffold do not compromise the heat resilience previously observed in the bacterial-expressed SpyCatcher003-mi3.

A


Soluble Fractions (%)
100
80
60
40
20
0
20
40
60
80
100
Temperature (°C)
SpyCatcher003-mi3
SpyCatcher003-G124 Glyc. mi3 (Unglyc.)
SpyCatcher003-G124 Glyc. mi3 (Glyc.)
S50 Glyc. SpyCatcher003-mi3 (Unglyc.)
S50 Glyc. SpyCatcher003-mi3 (Glyc.)

B


SpyCatcher003-mi3
S50 Glyc.
SpyCatcher003-mi3
25 °C
37 °C
55 °C
75 °C
95 °C
250
130
95
72
55
36
28
17
10
S50 Glyc.
SpyCatcher003-mi3
SpyCatcher003-
mi3

C

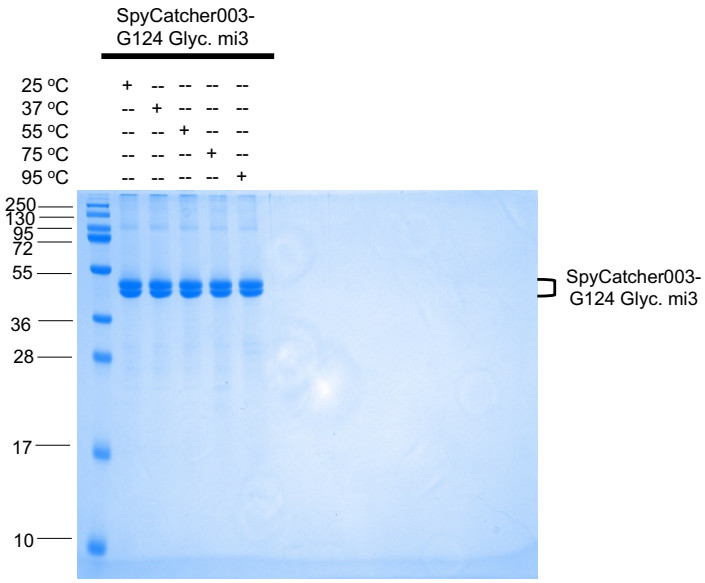


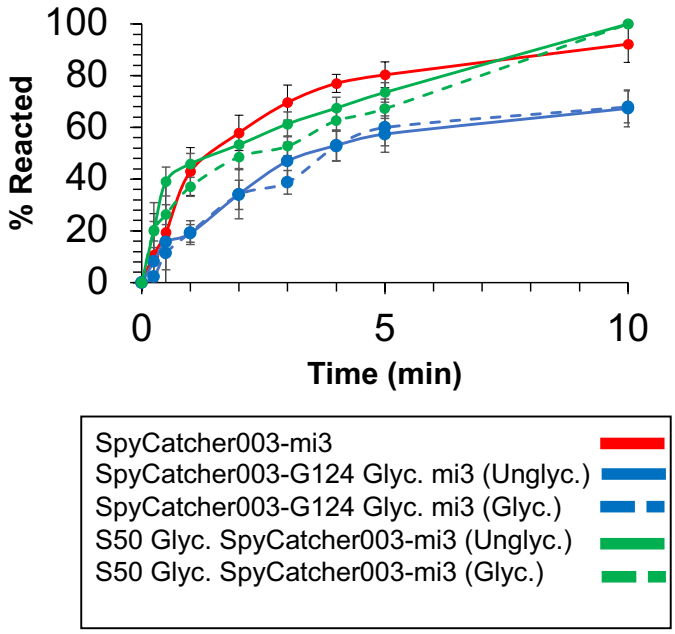
Figure 4. 11. Temperature-dependent solubility assays of glycosylated SpyCatcher003-mi3 compared to bacterial-expressed SpyCatcher003-mi3 VLPs: (A) Graph plot of solubility upon heating to temperatures of 25 ºC - 95 ºC for 1 h, cooling at 4 ºC for 10 min, and centrifuging at 16,000 x g for 30 min. Soluble fractions were calculated based on SDS gel band intensity relative to 25 ºC. These data points and error bars were recorded as mean ± 1 s.d., n=3. Bacterial-expressed SpyCatcher003-mi3 is represented in solid blue; unglycosylated portion of SpyCatcher003-G124 Glyc. mi3 is represented in solid gray; glycosylated portion of SpyCatcher003-G124 Glyc. mi3 is represented in dashed gray; unglycosylated portion of S50 Glyc. SpyCatcher003-mi3 is represented in solid orange; glycosylated portion of S50 Glyc. SpyCatcher003-mi3 is represented in dashed orange. (B) Representative SDS gel of bacterial-expressed SpyCatcher003-mi3 and S50 Glyc. SpyCatcher003-mi3 samples heated to temperatures between 25 ºC and 95 ºC for 1 h and cooled at 4 ºC for 10 min; (C) Representative SDS gel of SpyCatcher003-G124 Glyc. mi3 heated to temperatures between 25 ºC and 95 ºC for 1 h and cooled at 4 ºC for 10 min. The two non-reduced 16% (w/v) SDS gels (Fig 4.11 B and C) were stained with Coomassie.

4.1.7 Time course reactivity of glycosylated particles

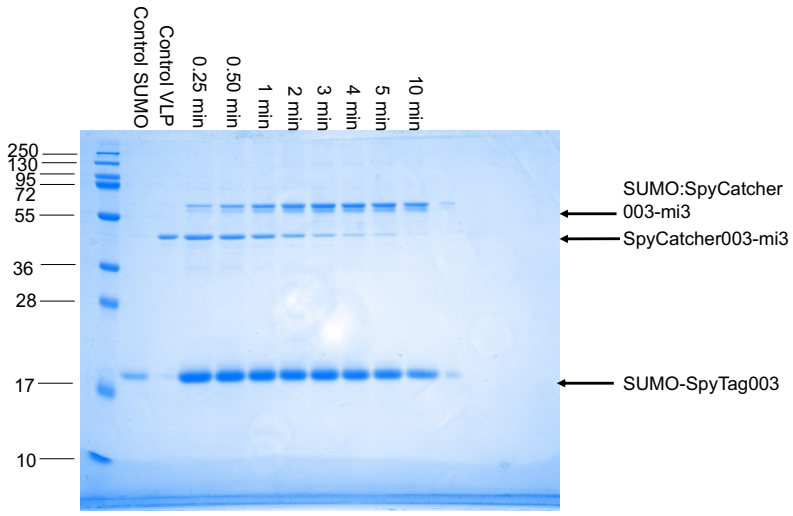
Dr. Anthony Keeble previously determined that 10 nM of SpyCatcher003 and SpyTag003 can react to >90% completion in 20 min at 25 °C (Keeble et al., 2019). There is currently no published literature documenting the coupling efficiency of SpyCatcher003 to SpyTag-antigens when arranged on a three-dimensional scaffold like mi3. By comparing the coupling efficiency of bacterial-expressed SpyCatcher003-mi3 with S50 Glyc. SpyCatcher003-mi3 and SpyCatcher003-G124 Glyc. mi3, it is possible to better understand how including N-linked glycans on flexible loops of SpyCatcher003 and the mi3 scaffold impact the particle's reactivity with SpyTag-antigens.

By reacting subunits of bacterial-expressed SpyCatcher003-mi3, S50 Glyc. SpyCatcher003-mi3 and SpyCatcher003-G124 Glyc. mi3 with excess monomeric SUMO-SpyTag003 antigen in a 1:3 molar ratio, I observed that all three particle variants have different coupling efficiencies after 10 min of incubation at 25 °C. The inclusion of N-linked glycans at the S50 residue on a SpyCatcher003 loop enables the VLP subunits to reach 100% coupling efficiency after 10 minutes, while bacterial-expressed SpyCatcher003-mi3 subunits react only to 80% coupling efficiency in the same time-frame (Fig 4.12 A). The inclusion of N-linked glycans at the G124 residue on an mi3 loop enables the VLP subunits to reach only 60% coupling efficiency in 10 minutes. Both the glycosylated subunits of S50 Glyc. SpyCatcher003-mi3 and SpyCatcher003-G124 Glyc. mi3 VLPs do not substantially deviate from the reaction rate of their non-glycosylated counterparts (Fig 4.12 A). While the presence of N-linked glycans at S50 enhances the reactivity of the VLP subunits, the presence of N-linked glycans at G124 retards the VLP subunits' reactivity. This suggests that some factors such as the position, occupancy, or composition of N-linked glycans impact reactivity of the particles' subunits with antigens.

A


100
80
60
40
20
0
% Reacted
0
5
10
Time (min)
SpyCatcher003-mi3
SpyCatcher003-G124 Glyc. mi3 (Unglyc.)
SpyCatcher003-G124 Glyc. mi3 (Glyc.)
S50 Glyc. SpyCatcher003-mi3 (Unglyc.)
S50 Glyc. SpyCatcher003-mi3 (Glyc.)

B


Control SUMO
Control VLP
0.25 min
0.50 min
1 min
2 min
3 min
4 min
5 min
10 min
250
130
95
72
55
36
28
17
10
SUMO:SpyCatcher 003-mi3
SpyCatcher003-mi3
SUMO-SpyTag003

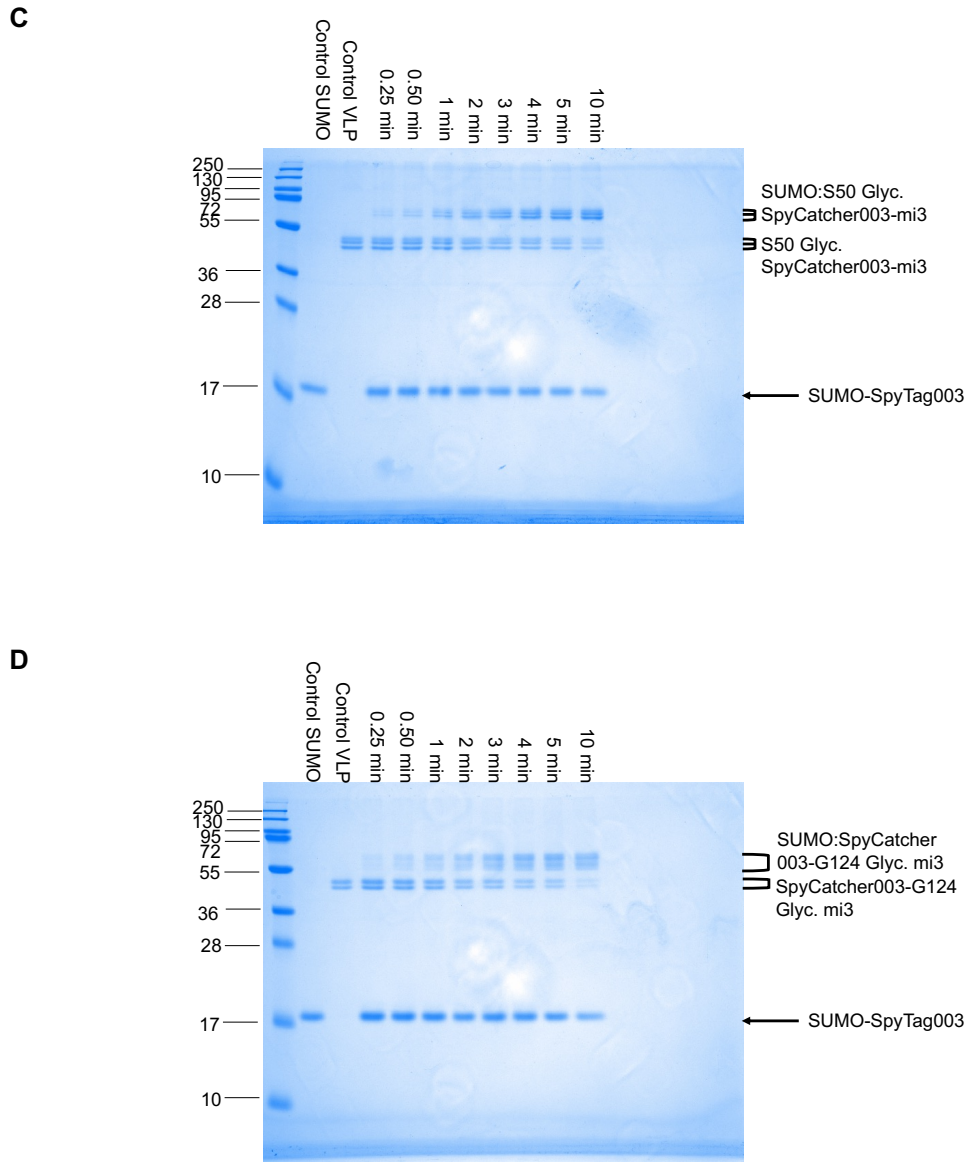


Figure 4. 12. Coupling efficiency of bacterial-expressed SpyCatcher003-mi3 and glycosylated SpyCatcher003-mi3 subunits: (A) Graph showing progression in coupling efficiency for VLPs. Coupling efficiency of bacterial-expressed SpyCatcher003-mi3 is represented in solid red; the unglycosylated portion of SpyCatcher003-G124 Glyc. mi3 is in solid blue; the glycosylated portion of SpyCatcher003-G124 Glyc. mi3 is in dashed blue; the unglycosylated portion of S50 Glyc. SpyCatcher003-mi3 is in solid green; the glycosylated portion of S50 Glyc. SpyCatcher003-mi3 is in dashed green. All data points and error bars were recorded as mean±1 s.d., n=3. (B) Representative SDS gel of

bacterial-expressed SpyCatcher003-mi3 coupling efficiency at 25 °C between 0.25 and 10 minute time-points; (C) Representative SDS gel of S50 Glyc. SpyCatcher003-mi3 coupling efficiency at 25 °C between 0.25 and 10 minute time-points; (D) Representative SDS gel of SpyCatcher003-G124 Glyc. mi3 coupling efficiency at 25 °C between 0.25 and 10 minute time-points. All three non-reducing 16% (w/v) SDS gels (Fig 4.12 B-D) were stained with Coomassie.

4.1.8 N-linked glycan composition and occupancy analysis

It is possible that the occupancy and composition of N-linked glycans impact the purification yield and reactivity of the glycosylated VLPs. Therefore, I processed my samples through glycan mass spectrometry with the help of Dr. Joel Allen and Prof. Max Crispin at the University of Southampton. 0.17 mg S50 Glyc. SpyCatcher003-mi3 and 0.2 mg each of SpyCatcher003-G124 Glyc. mi3 and S50 Glyc. SpyCatcher003-mi3 + Kif were first denatured, reduced, and alkylated. Then, these VLPs were digested overnight with trypsin, chymotrypsin, and alpha-lytic protease. The subsequently dried peptides were separated, fragmented, and quantitated through liquid chromatography electrospray ionization mass spectrometry (LC-ESI-MS).

Dr. Joel Allen found an average of 11% occupancy of complex N-linked glycans on the S50 Glyc. SpyCatcher003-mi3 VLP and 17% complex N-linked glycan occupancy on the S50 Glyc. SpyCatcher003-mi3 + Kif VLP (Fig 4.13 B). He was, however, unable to detect glycan occupancy levels for SpyCatcher003-G124 Glyc. mi3. This was attributed to the lack of peptide coverage around the N-glycan sequon following digestion with trypsin, chymotrypsin, and alpha-lytic protease before LC-based separation. Mass spectrometry had detected an O-linked glycan present at residue T2 with 1% occupancy in S50 Glyc. SpyCatcher003-mi3 and 0.8% occupancy in S50 Glyc. SpyCatcher003-mi3 + Kif (Fig 4.13 A). Mass spectrometry also did not show evidence of any mannosylated glycans, which

further suggests that expressing S50 Glyc. SpyCatcher003-mi3 with 5 nM kifunensine was not effective in producing a mannose-dense VLP variant (Fig 4.13 B). The percentage of glycans detected runs contrary to my PNGase F digestion results, which suggested that ~60% glycosylation was present on the three VLPs.

A

S50 Glyc. O-Linked Glycan Abundance

Glycopeptide	
R.MGSSVtTLSGLSGEQGPSGDMTTEEDSATHIK.F	
Unoccupied	99%
O glycan	1%

S50 Glyc. + Kif O-Linked Glycan Abundance

Glycopeptide	
R.MGSSVTTLSGL.S	
Unoccupied	99.20%
O glycan	0.80%

B

S50	Repeat 1	Repeat 2	Repeat 3	November repeat 4	Average
M9Glc	0	0	0	0	0
M9	0	0	0	0	0
M8	0	0	0	0	0
M7	0	0	0	0	0
M6	0	0	0	0	0
M5	0	0	0	1	0
M4	0	0	0	0	0
M3	0	0	0	0	0
FM	0	0	0	0	0
Hybrid	0	0	0	0	0
Fhybrid	0	0	0	0	0
HexNAc(3)(x)	0	0	0	0	0
HexNAc(3)(F)(x)	1	1	1	1	1
HexNAc(4)(x)	0	0	0	0	0
HexNAc(4)(F)(x)	5	5	6	36	13
HexNAc(5)(x)	0	0	0	0	0
HexNAc(5)(F)(x)	1	1	1	9	3
HexNAc(6+)(x)	0	0	0	0	0
HexNAc(6+)(F)(x)	0	0	0	0	0
Unoccupied	91	90	88	54	81
Core	0	3	3	0	2
EndoH Sensitive	0	0	0	1	0
Complex-type	7	7	8	46	17

S50+ Kif	Repeat 1	Repeat 2	Repeat 3	November repeat 4	Average
M9Glc	0	0	0	0	0
M9	0	0	0	0	0
M8	0	0	0	0	0
M7	0	0	0	0	0
M6	0	0	0	0	0
M5	0	0	0	0	0
M4	0	0	0	0	0
M3	0	0	0	0	0
FM	0	0	0	0	0
Hybrid	0	0	0	0	0
Fhybrid	0	0	0	0	0
HexNAc(3)(x)	0	0	0	0	0
HexNAc(3)(F)(x)	1	0	1	0	1
HexNAc(4)(x)	0	0	0	0	0
HexNAc(4)(F)(x)	4	5	6	16	8
HexNAc(5)(x)	0	0	0	0	0
HexNAc(5)(F)(x)	2	2	1	5	3
HexNAc(6+)(x)	0	0	0	0	0
HexNAc(6+)(F)(x)	0	0	0	0	0
Unoccupied	93	89	91	78	88
Core	0	3	0	0	1
EndoH Sensitive	0	0	0	0	0
Complex-type	7	7	8	21	11

Figure 4. 13. Mass spectrometry glycan analysis of S50 Glyc. SpyCatcher003-mi3 and S50 Glyc. SpyCatcher003-mi3+Kifunensine: (A) Segment of glycopeptide with O-glycan location on T2. Dots (.) mark the start and end of the glycopeptide sequence.

Lowercase (t) represents the T2 residue; the occupancy percentage of O-glycans is documented with corresponding unoccupied percentages; (B) Results from four repeat mass spectrometry runs with the percentage occupancy of each form of glycan detected per run. Oligosaccharide composition is abbreviated as follows: HexNAc(2)Hex(9-5) (M9-M5); HexNAc(2)Hex(10+) (M9Glc); fucosylated oligomannose glycans (FM); HexNAc(3)Hex(5-6)X (Hybrid); hybrid glycans with HexNAc(3)Fuc(1)X (Fhybrid); complex glycans HexNAc(3-6+)(x) are classified based on the number of processed antennae and detected fucosylation patterns (F); truncated glycan structures smaller than M3 (Core). These percentages are then reported as an average, summarized up in the bottom two categories of “EndoH Sensitive” and “Complex-type”. Data generated by Dr. Joel Allen.

4.2 Immunogenicity of SARS-CoV-2 RBD-decorated glycosylated SpyCatcher003-mi3 VLPs

4.2.1 Assessing extent of RBD-focused antibody responses

My next objective was to evaluate how well the glycosylated SpyCatcher003-mi3 VLP variants focused RBD-specific antibody responses and decreased the SpyCatcher003- and mi3-specific antibody responses. I decorated each of the glycosylated VLP variants with SpyTag fused to SARS-CoV-2 RBD (SpyTag-RBD). Dr. Tiong Tan immunized mice with these VLPs and collected sera two weeks post-prime and three weeks post-boost. I then performed endpoint ELISA titering with these sera to evaluate antibody responses against SARS-CoV-2 RBD-His_6Tag, mi3-Ctag, and SpyTag003:SpyCatcher003. Since the SARS-CoV-2 SpyTag-RBD was purified using the Spy&Go resin (Khairil Anuar et al., 2019), it is unlikely that the presence of a His_6-tag would impact the RBD-specific antibody binding observed in an endpoint ELISA. Between the sequences of the 13-residue SpyTag and 16-residue SpyTag003 there is a difference of only six residues (Keeble et al., 2019). The integrity of these three proteins were confirmed on SDS-PAGE before any ELISAs were performed (Fig 4.14).

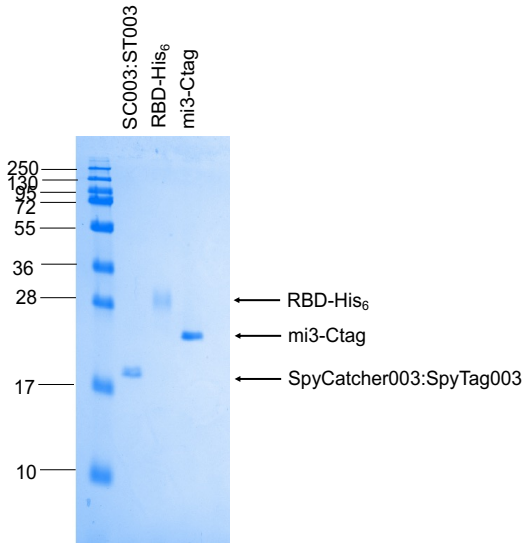
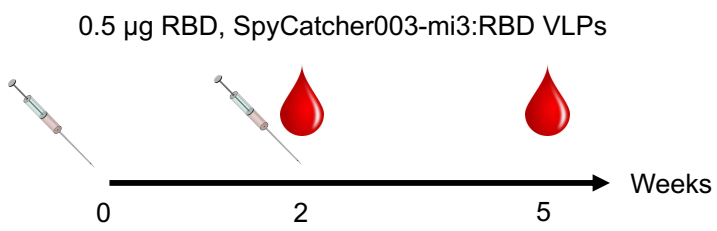


Figure 4. 14. Gel analysis of proteins used for testing ELISA serum binding: 16% (w/v) non-reduced SDS-PAGE showing well-defined bands of affinity-purified RBD-His_6, mi3-Ctag, and SpyCatcher003:SpyTag003 (SC003:ST003). This gel was stained with Coomassie.

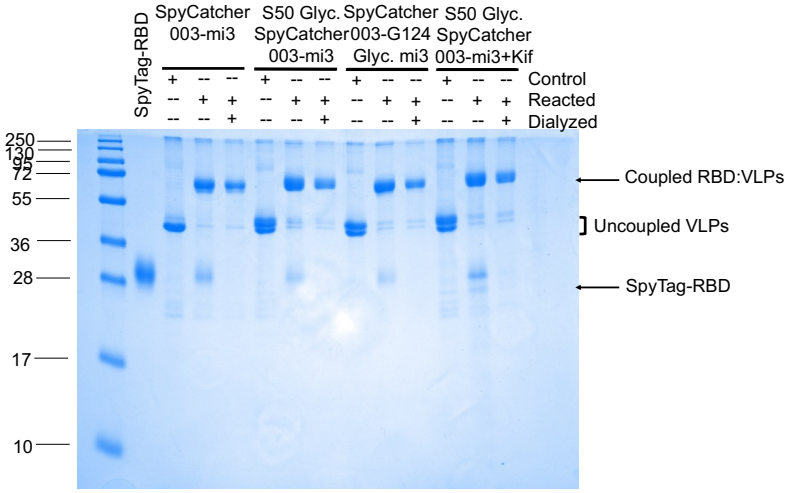
I decorated HEK293-expressed SpyCatcher003-mi3 and the glycosylated VLP variants with RBD-SpyTag, preparing enough for immunization at 0.5 µg RBD/dose, and followed the same immunization schedule as before (Fig 4.15 A and B) (Rahikainen et al., 2021; Tan et al., 2021). At this dose I observed antibody binding titers to RBD, which were distinguishable from the lowest endpoint titer used (1:50), for all the HEK293-expressed VLPs. As previously seen with bacterial-expressed SpyCatcher003-mi3 (Fig 3.11 B), the multimerization of RBD on HEK293-expressed SpyCatcher003-mi3 elicited significantly higher antibody titers against RBD. Furthermore, the inclusion of N-linked glycans on mi3 and SpyCatcher003 loops did not significantly affect RBD-specific antibody response levels relative to the HEK293-expressed SpyCatcher003-mi3 particle (Fig 4.15 C). The inclusion of N-linked glycans on the specific SpyCatcher003 and mi3 loops did not significantly lower mi3-specific or SpyTag003:SpyCatcher003-specific antibody responses.

There was also no difference in RBD-specific, mi3-specific or SpyTag003:SpyCatcher003-specific antibody responses between the S50 Glyc. SpyCatcher003-mi3 and the same VLP expressed with Kifunensine (Fig 4.15 C-E). While incorporation of N-linked glycosylation sites did not significantly lower the RBD-specific antibody response, these sites also did not lower the antibody response to other parts of the scaffold, which the N-linked glycans on SpyCatcher003 and mi3 loops were intended to occlude. This observation could be explained, given the low occupancy of N-linked glycans detected via mass spectrometry.

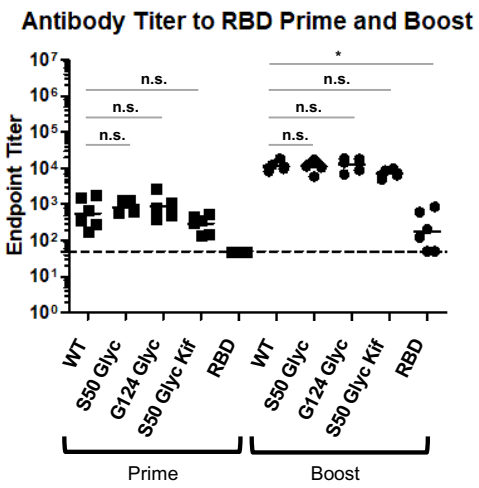
A


0.5 µg RBD, SpyCatcher003-mi3:RBD VLPs
Weeks
0
2
5

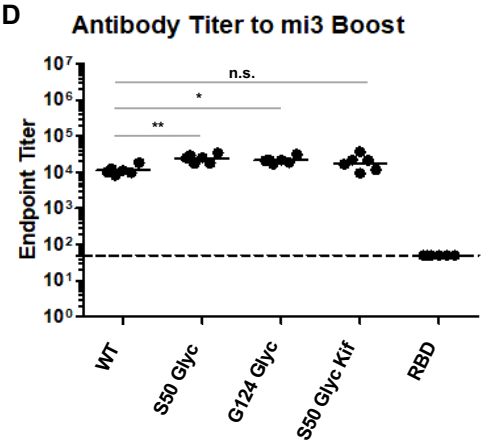
B


SpyTag-RBD
SpyCatcher 003-mi3
S50 Glyc. SpyCatcher 003-mi3
SpyCatcher003-G124 Glyc. mi3
S50 Glyc. SpyCatcher 003-mi3+Kif
Control
Reacted
Dialyzed
250
130
95
72
55
36
28
17
10
Coupled RBD:VLPs
Uncoupled VLPs
SpyTag-RBD

C


Antibody Titer to RBD Prime and Boost
Endpoint Titer
n.s.
*
WT
S50 Glyc
G124 Glyc
S50 Glyc Kif
RBD
Prime
Boost

D


Antibody Titer to mi3 Boost
Endpoint Titer
n.s.
*
**
WT
S50 Glyc
G124 Glyc
S50 Glyc Kif
RBD

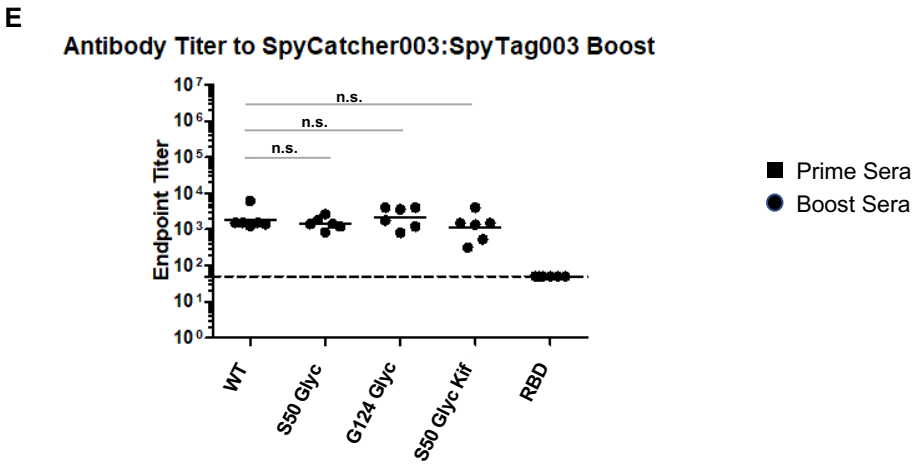


Figure 4. 15. SARS-CoV-2 RBD-, mi3-, and SpyCatcher003:SpyTag003-specific antibody responses: (A) C57BL/6 mice (n=6) received intramuscular immunizations of 0.5 μg RBD/dose of antigen and RBD:SpyCatcher003-mi3 VLPs on this schedule; (B) SDS-PAGE showing glycosylated VLPs coupled to consistent levels with RBD, before and after excess antigen product is dialyzed away. 16% (w/v) non-reduced SDS gel was stained with Coomassie; (C) Prime and boost sera harvested from mice were analyzed in ELISA against RBD. Boost sera harvested from mice were tested for binding against (D) mi3 scaffold and (E) SpyCatcher003:SpyTag003. Black horizontal bar is the mean. One-way ANOVA with Bonferroni correction was used to evaluate $\log_{10}$-transformed endpoint titer differences between two dosing groups, as indicated by gray horizontal bars. HEK293-expressed SpyCatcher003-mi3 is denoted as "WT", S50 Glyc. SpyCatcher003-mi3 as "S50 Glyc", SpyCatcher003-G124 Glyc. mi3 as "G124 Glyc", S50 Glyc. SpyCatcher003-mi3 + Kif as "S50 Glyc Kif" and 0.5 μg RBD as "RBD". Dotted line represents the value of the lowest mouse serum dilution factor tested (50). Prime sera titers are represented by a black square. Boost sera titers are represented by a black circle. Each symbol represents an individual mouse. ** p≤ 0.01; * p≤ 0.05; n.s. p>0.05. Mice immunizations and serum harvesting were performed by Dr. Tiong Tan.

4.2.2 IgG subtyping of glycosylated VLP immune response

I next examined how the presence of glycans on the loops of mi3 and SpyCatcher003 affect the types of IgGs generated. In the context of vaccine design,

understanding the extent of IgG class switching offers insight into how CD4+ T-helper (Th) cells support B cell and CD8+T cell responses through specific cytokine (e.g. interferon-γ or interleukin-4) production. In previous efforts to develop MERS-CoV and SARS-CoV vaccines, Th2 responses following mice immunization have been associated with enhanced eosinophil infiltration and lung immunopathological responses (Agrawal et al., 2016; Dong et al., 2020; Tseng et al., 2012). Patients infected with SARS-CoV-2 have enhanced levels of Th2 cytokines, which may be linked to lung immunopathology (Huang et al., 2020a; Wan et al., 2020). Therefore, it is suggested that SARS-CoV-2 vaccines should ideally induce a Th1 response accompanied by high neutralizing antibodies (Hans-Uwe et al., 2020; Lambert et al., 2020). The commercially available Moderna and Pfizer SARS-CoV-2 mRNA vaccines induce Th1 responses, while trials of Novavax's NVX-CoV2373 VLP candidate show a strong Th1 bias with a weak Th2 response (Li et al., 2021a). Currently, VLP candidates that display the SARS-CoV-2 RBD have exhibited biased or balanced Th1 and Th2 responses, depending on the type and quantity of adjuvants included (Bommireddy et al., 2022; Dalvie et al., 2022; Fougeroux et al., 2021).

The murine IgG subclasses consist of IgG1, IgG2a/c, IgG2b, and IgG3. To examine the extent of Th1 and Th2 responses, I performed endpoint ELISAs against SARS-CoV-2 RBD with mice sera boosted by each RBD-decorated glycosylated VLP (which was adjuvanted with Addavax). A Th1 response against RBD was evaluated based on a goat anti-mouse IgG2a/c horseradish-peroxidase (HRP)-conjugated secondary antibody. A Th2 response against RBD was measured using a goat anti-mouse IgG1 HRP-conjugated secondary antibody. The Th2 response levels of all the glycosylated VLP variants are similar to that of the HEK293-expressed SpyCatcher003-mi3 (Fig 4.16 A). The Th1 response levels of S50 Glyc. SpyCatcher003-mi3 and SpyCatcher003-G124 Glyc. mi3 are similar to that of the HEK293-expressed SpyCatcher003-mi3 (Fig 4.16 B). S50 Glyc.

SpyCatcher003-mi3 + Kif VLP presents a significantly higher Th1 response relative to the HEK293-expressed SpyCatcher003-mi3. This observation is surprising, since there is no evidence that the glycan composition of S50 Glyc. SpyCatcher003-mi3 + Kif differs significantly from that of S50 Glyc. SpyCatcher003-mi3.

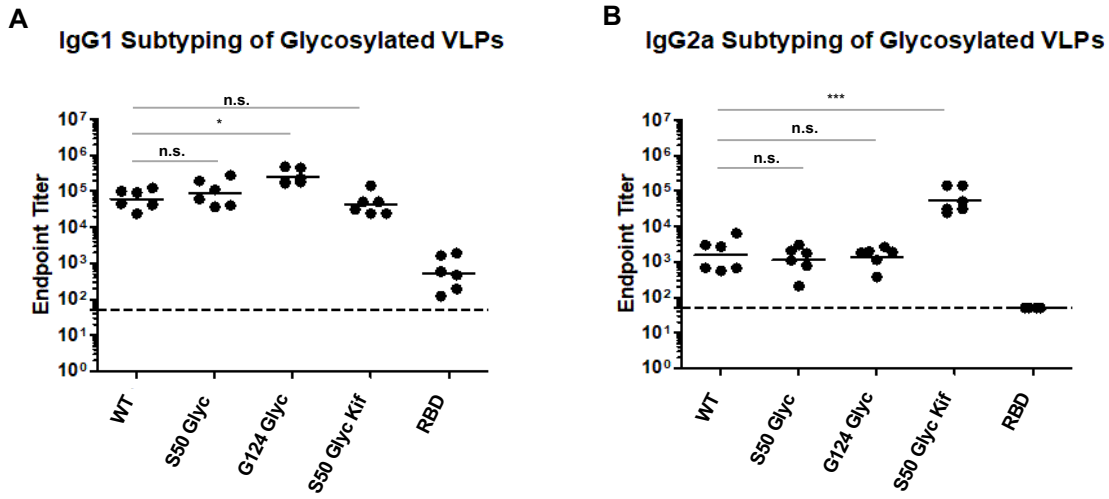


Figure 4. 16. IgG1 and IgG2a subtyping of glycosylated VLPs: Boost sera from C57BL/6 mice (n=6) immunized with 0.5 µg RBD/dose of antigen and RBD:SpyCatcher003-mi3 VLPs were used to measure (A) IgG1 binding, indicative of Th2 cytokine response and (B) IgG2a binding, indicative of Th1 cytokine response. Black horizontal bar is the mean. One-way ANOVA with Bonferroni correction was used to evaluate $\log_{10}$-transformed endpoint titer differences between dosing groups, as indicated by gray horizontal bars. HEK293-expressed SpyCatcher003-mi3 is denoted as “WT”, S50 Glyc. SpyCatcher003-mi3 as “S50 Glyc”, SpyCatcher003-G124 Glyc. mi3 as “G124 Glyc”, S50 Glyc. SpyCatcher003-mi3 + Kif as “S50 Glyc Kif” and 0.5 µg RBD as “RBD”. Dotted line represents the value of the lowest mouse serum dilution factor tested (50). Boost sera titers are represented by a black circle. Each symbol represents an individual mouse. *** means p≤ 0.001; * means p≤ 0.05; n.s. means p>0.05.

4.3 Design of albumin-binding SpyCatcher003-mi3 particles

4.3.1 Expression of SpyCatcher003-mi3 with albumin-binding domain

In previous studies serum albumin has been conjugated to select protein structures by a combination of PEG linkers and maleimide click chemistry (Gulati et al., 2018; Rakhra et al., 2021) or through the strategic insertion of albumin-binding domain peptides on relevant antigens (Gao et al., 2021; Wang et al., 2018). Between these two approaches, the insertion of albumin-binding domain peptides to SpyCatcher003-mi3 would be preferable and least disruptive to scaling up VLP expression. Taking this approach also reduces the possibility of incomplete albumin-VLP coupling and eliminates any regulatory issues that may arise from introducing exogenous albumin to the nanoparticle.

Albumin-binding domains are present on the surface of different bacteria (Johansson et al., 2002; Kronvall et al., 1979; Myhre, 1984). Rational engineering of these domains leads to peptides with higher binding affinities. One research group engineered the 46 residue-long ABD035 albumin-binding domain from G148-GA3 (third albumin-binding domain from streptococcal protein G strain 148) of *Staphylococcus aureus*, which had a binding affinity of 50-500 fM for HSA and 10 pM-10 fM for mouse serum albumin (MSA) (Jonsson et al., 2008). Phage display optimization led to the generation of the 18 residue-long SA21 peptide with a binding affinity of 476 nM for HSA and 7 nM for MSA (Dennis et al., 2002). In addition to ABD035 and SA21, David Schramm also decided to test the *Peptostreptococcus magnus*-derived 53 residue-long Alb8 domain, with 3.1 nM HSA binding affinity and 1.1 μM MSA binding affinity (Johansson et al., 2002), as a possible candidate for fusing to SpyCatcher003-mi3 VLPs. To start off, David Schramm inserted albumin binding sequences at the N-terminus, C-terminus, and in the flexible

GGS_4 linker between SpyCatcher003 and mi3 sequences and expressed them in *E. coli* (Fig 4.17 A).

The placement of ABD035, Alb8, and SA21 at the N-terminal of the SpyCatcher003-mi3 construct did not result in soluble expression (Schramm, 2021; unpublished). Compared to the 14 mg/L yield of purified SpyCatcher003-mi3 obtained following 30% (w/v) ammonium sulfate precipitation and SEC, most of the SpyCatcher003-mi3 VLPs with albumin-binding sequences had lower yields (Schramm, 2021; unpublished). SpyCatcher003-SA21-mi3 and SpyCatcher003-mi3-SA21 had yields of 13 mg/L and 14 mg/L, respectively. SpyCatcher003-Alb8-mi3 and SpyCatcher003-mi3-Alb8 both had yields of 11 mg/L. SpyCatcher003-ABD035-mi3 and SpyCatcher003-mi3-ABD035 had yields of 3.6 mg/L and 7.8 mg/L, respectively.

Albumin-binding SpyCatcher003-mi3 VLPs were then assessed for particle size and uniformity using DLS. VLPs with albumin-binding sites in the GGS_4 linker between the SpyCatcher003 moiety and mi3 scaffold had slightly larger hydrodynamic radii. Relative to SpyCatcher003-mi3, which had a hydrodynamic radius of 18 nm (mean, n=3). SpyCatcher003-SA21-mi3 had a hydrodynamic radius of 25 nm (mean, n=3). SpyCatcher003-Alb8-mi3 and SpyCatcher003-ABD035-mi3 both had hydrodynamic radii of 20 nm (mean, n=3). VLPs with albumin binding sequences fixed to the C-terminus were more similar in size compared to unmodified SpyCatcher003-mi3. SpyCatcher003-mi3-SA21, SpyCatcher003-mi3-Alb8, and SpyCatcher003-mi3-ABD035 had hydrodynamic radii of 17 nm (mean, n=3), 19 nm (mean, n=3) and 18 nm (mean, n=3), respectively (Fig 4.17 B and C).

When coupled to SARS-CoV-2 RBD antigen, VLPs with albumin binding sequences at the C-terminus and between the SpyCatcher003 moiety and mi3 scaffold remained uniform in size. Compared to RBD-coupled SpyCatcher003-mi3, with a

hydrodynamic radius of 22 nm (mean, n=3), RBD-coupled SpyCatcher003-SA21-mi3 had a hydrodynamic radius of 27 nm (mean, n=3). RBD-coupled SpyCatcher003-Alb8-mi3 and SpyCatcher003-ABD035-mi3 had a hydrodynamic radius of 23 nm (mean, n=3) and 22 nm (mean, n=3), respectively. RBD-coupled SpyCatcher003-mi3-SA21, SpyCatcher003-mi3-Alb8, and SpyCatcher003-mi3-ABD035 VLPs had hydrodynamic radii of 22 nm (mean, n=3), 22 nm (mean, n=3) and 20 nm (mean, n=3), respectively (Fig 4.17 D and E).

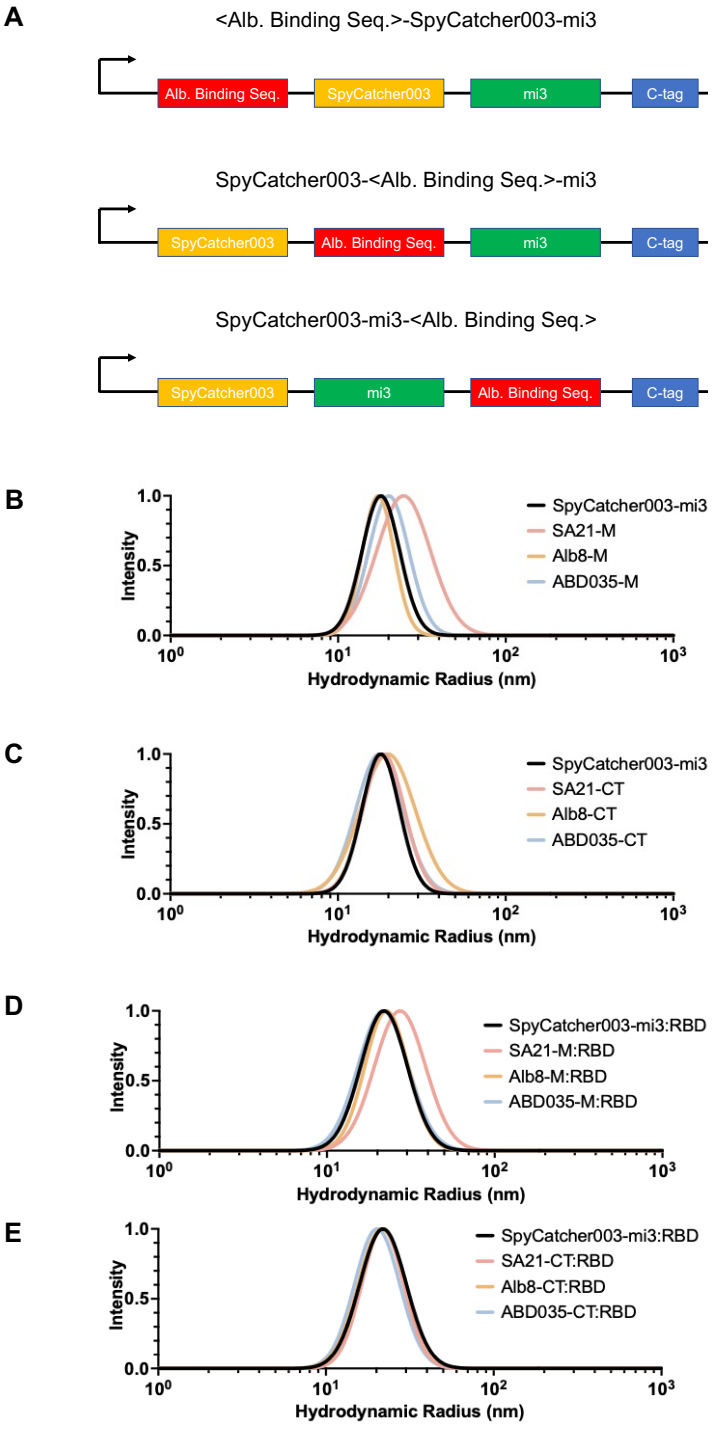

A
<Alb. Binding Seq.>-SpyCatcher003-mi3
Alb. Binding Seq.
SpyCatcher003
mi3
C-tag
SpyCatcher003-<Alb. Binding Seq.>-mi3
SpyCatcher003
Alb. Binding Seq.
mi3
C-tag
SpyCatcher003-mi3-<Alb. Binding Seq.>
SpyCatcher003
mi3
Alb. Binding Seq.
C-tag
B
Intensity
Hydrodynamic Radius (nm)
SpyCatcher003-mi3
SA21-M
Alb8-M
ABD035-M
C
Intensity
Hydrodynamic Radius (nm)
SpyCatcher003-mi3
SA21-CT
Alb8-CT
ABD035-CT
D
Intensity
Hydrodynamic Radius (nm)
SpyCatcher003-mi3:RBD
SA21-M:RBD
Alb8-M:RBD
ABD035-M:RBD
E
Intensity
Hydrodynamic Radius (nm)
SpyCatcher003-mi3:RBD
SA21-CT:RBD
Alb8-CT:RBD
ABD035-CT:RBD

Figure 4. 17. Linear construct schematics and DLS measurements of ABD035 SpyCatcher003-mi3 VLP variants: (A) Albumin-binding VLPs are named according to the configuration of SpyCatcher003, mi3, and albumin-binding sequences <Alb. Binding Seq.> shown in the diagram above. Options for <Alb. Binding Seq.> used in this study include: ABD035, Alb8, and SA21. (B)-(E) DLS intensity curves of uncoupled and RBD-coupled (:RBD) VLPs: in black, are SpyCatcher003-mi3 and the same VLPs coupled to RBD; in pink, are SpyCatcher003-mi3-SA21 (SA21-CT), SpyCatcher003-SA21-mi3 (SA21-M) and the same VLPs coupled to RBD; in gold are SpyCatcher003-mi3-Alb8 (Alb8-CT), SpyCatcher003-Alb8-mi3 (Alb8-M) and the same VLPs coupled to RBD; in light blue are SpyCatcher003-mi3-ABD035 (ABD035-CT), SpyCatcher003-ABD035-mi3 (ABD035-M) and the same VLPs coupled to RBD. All DLS measurements of albumin-binding VLP occurred "at 20 ^{o}C, with 10 scans of 10 seconds, 50% laser intensity, 15% maximum baseline drift, 20% spike tolerance, and 30µL volume." (Schramm, 2021; unpublished). Images/data in 4.17 (B-E) were generated by David Schramm.

4.3.2 Assessing role of albumin-binding domains against antibody binding

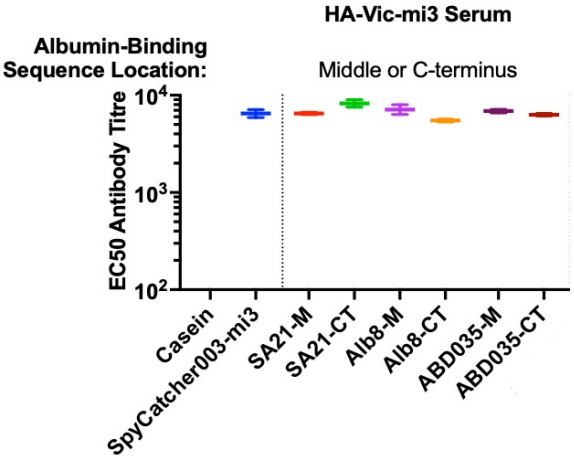
To assess how well SpyCatcher003-ABD035-mi3 and SpyCatcher003-mi3-ABD035 shield against antibodies, David Schramm performed an endpoint ELISA using serum collected from one mouse immunized with influenza antigen HA-Vic-coupled SpyCatcher003-mi3 (SpyCatcher003-mi3:HA-Vic) (Rahikainen et al., 2021), containing polyclonal antibodies against unmodified SpyCatcher003 and the mi3 scaffold. Instead of using skim milk for a blocking buffer, casein was used to keep albumin out of the ELISAs. This ELISA showed that SpyCatcher003-mi3 fused with SA21, Alb8, and ABD035 had similar levels of half-maximal effective concentration (EC50) titers for SpyCatcher003-mi3:HA-Vic compared to SpyCatcher003-mi3 (Fig 4.18 A).

The extent of albumin-dependent shielding to SpyCatcher003-mi3 was evaluated by comparing the serum binding EC50 titer levels of SpyCatcher003-mi3:HA-Vic-immunized mice against SpyCatcher003-mi3 albumin-binding VLPs, in both the absence

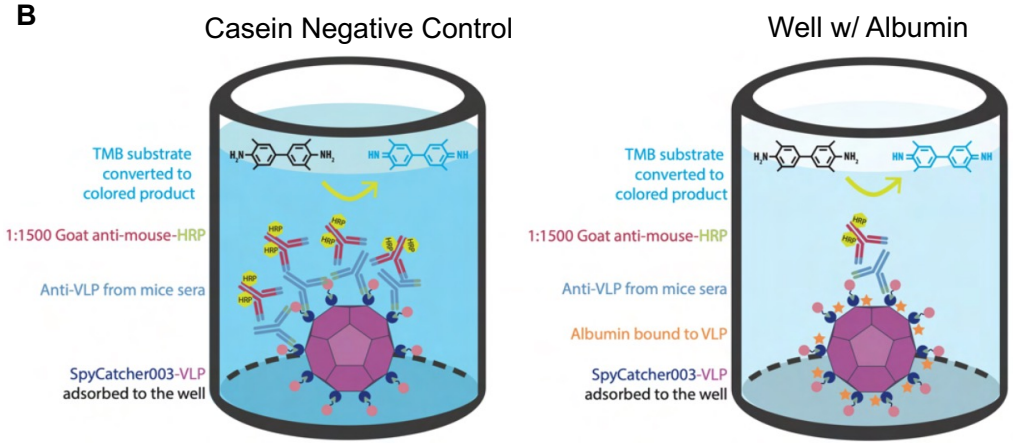
and presence of HSA (Fig 4.18 B). Incubating SpyCatcher003-mi3 albumin-binding VLPs in the presence of HSA closely mimics the state of the VLP when naïve B-cells come into initial contact with it. Potential blocking effects were controlled for by adding an equimolar quantity of N,N-dimethyl casein into negative control wells. There is a significant decrease in serum binding between SpyCatcher003-mi3 and SpyCatcher003-ABD035-mi3 and SpyCatcher003-mi3-ABD035 after just 5 minutes of antibody incubation (Fig 4.18 C). SpyCatcher003-SA21-mi3 exhibited no reduction in serum binding and was therefore eliminated from further characterization (Schramm, 2021; unpublished).

These data encouraged David Schramm to pool the serum samples of six SpyCatcher003-mi3:HA-Vic -immunized mice and another six serum samples from SpyCatcher003-mi3:HA-X31-immunized mice, to quantify the extent of antibody shielding for uncoupled and RBD-coupled SpyCatcher003-ABD035-mi3 and SpyCatcher003-mi3-ABD035 VLPs. A significant decrease was evident in SpyCatcher003-mi3:HA-Vic serum binding between unmodified SpyCatcher003-mi3 and HSA-coated SpyCatcher003-mi3-ABD035. A significant decrease was also apparent in SpyCatcher003-mi3:HA-X31 serum binding between unmodified SpyCatcher003-mi3 and MSA-coated SpyCatcher003-mi3-ABD035. When the VLPs were decorated with RBD, a significant reduction was only observed in SpyCatcher003-mi3:HA-Vic serum binding to HSA-decorated SpyCatcher003-ABD035-mi3 and SpyCatcher003-mi3-ABD035 (Fig 4.18 D).

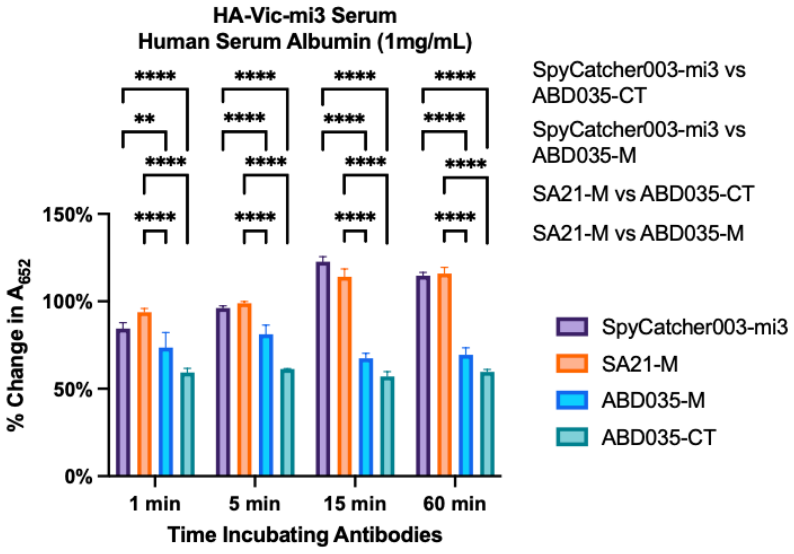
A


HA-Vic-mi3 Serum
Albumin-Binding Sequence Location:
Middle or C-terminus
EC50 Antibody Titre
10^4
10^3
10^2
Casein
SpyCatcher003-mi3
SA21-M
SA21-CT
Alb8-M
Alb8-CT
ABD035-M
ABD035-CT

B


Casein Negative Control
Well w/ Albumin
TMB substrate converted to colored product
1:1500 Goat anti-mouse-HRP
Anti-VLP from mice sera
Albumin bound to VLP
SpyCatcher003-VLP adsorbed to the well
HRP

C


HA-Vic-mi3 Serum
Human Serum Albumin (1mg/mL)
SpyCatcher003-mi3 vs ABD035-CT
SpyCatcher003-mi3 vs ABD035-M
SA21-M vs ABD035-CT
SA21-M vs ABD035-M
****
**
150%
100%
50%
0%
% Change in A_{652}
1 min
5 min
15 min
60 min
Time Incubating Antibodies
SpyCatcher003-mi3
SA21-M
ABD035-M
ABD035-CT

D

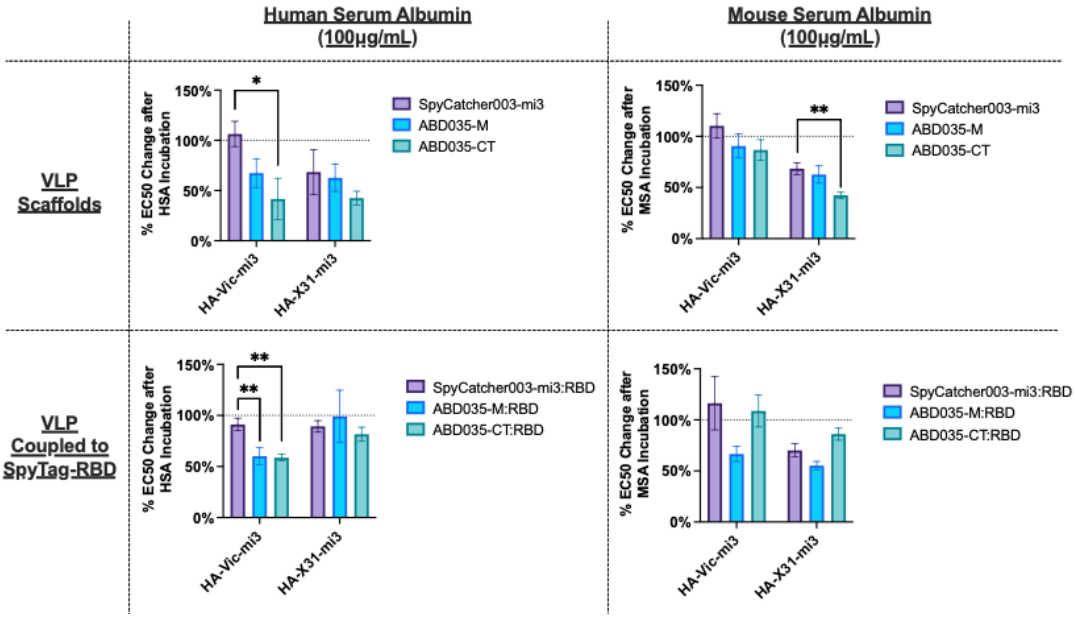


Figure 4. 18. Measuring changes in SpyCatcher003-mi3:HA-Vic serum binding against albumin-bound SpyCatcher003-mi3 VLPs: (A) EC50 titer measurements of SpyCatcher003-mi3:HA-Vic serum binding to albumin-binding VLPs (from left to right): SpyCatcher003-mi3 (blue), SpyCatcher003-SA21-mi3 (SA21-M, red), SpyCatcher003-mi3-SA21 (SA21-CT, green), SpyCatcher003-Alb8-mi3 (Alb8-M, purple), SpyCatcher003-mi3-Alb8 (Alb8-CT, gold), SpyCatcher003-ABD035-mi3 (ABD035-M, brown), and SpyCatcher003-mi3-ABD035 (ABD035-CT, maroon). (B) Schematic of VLPs (purple), albumin (orange star), anti-VLP from mouse sera (light blue), 1:1500 Goat anti-mouse (maroon)-HRP (light green), and TMB substrate (blue) in a plate well; (C) Comparison of SpyCatcher003-mi3:HA-Vic serum binding change between 1 mg/mL HSA-bound VLPs; SpyCatcher003-mi3 (purple), SpyCatcher003-SA21-mi3 (SA21-M, orange), SpyCatcher003-ABD035-mi3 (ABD035-M, light blue), and SpyCatcher003-mi3-ABD035 (ABD035-CT, green) over 1, 5, 15, 60 min antibody incubation period. (D) SpyCatcher003-mi3 (purple), SpyCatcher003-ABD035-mi3 (ABD035-M, light blue), SpyCatcher003-mi3-ABD035 (ABD035-CT, green) are incubated in HSA in uncoupled form (top left) and RBD-coupled form (bottom left). Same VLPs and with corresponding coloring are incubated in MSA in coupled form (top right) and RBD-coupled form (bottom right). For these samples,

n=16 for eight duplicate half-log dilutions. For these samples in (C) and (D), n=3 and error bars indicate standard error of the mean. % Change of in A652= $A_{652+HSA}/A_{652+casein} \times 100$. Two-way ANOVA with Dunnett's post-hoc test was performed to evaluate significance, indicated as ****: p<0.0001, **: p<0.001, and *p<0.05. Images/data generated by David Schramm.

4.4 Immunogenicity of SARS-CoV-2 RBD-decorated albumin-binding SpyCatcher003-mi3 VLPs

4.4.1 Assessing the extent of RBD-focused antibody responses

Following this validation of expression, albumin binding and particle uniformity, I examined whether including the ABD035 domain enhanced antibody responses to RBD-coupled SpyCatcher003-mi3 and shielded antibodies directed at the mi3 scaffold or SpyCatcher003:SpyTag003. I first coupled my SpyCatcher003-mi3 and ABD035 variant VLP subunits with excess RBD, all of which reached 90% coupling efficiency (Fig 4.19). This demonstrates that including ABD035 on SpyCatcher003-mi3 VLPs does not substantially impair the VLP's coupling efficiency to RBD.

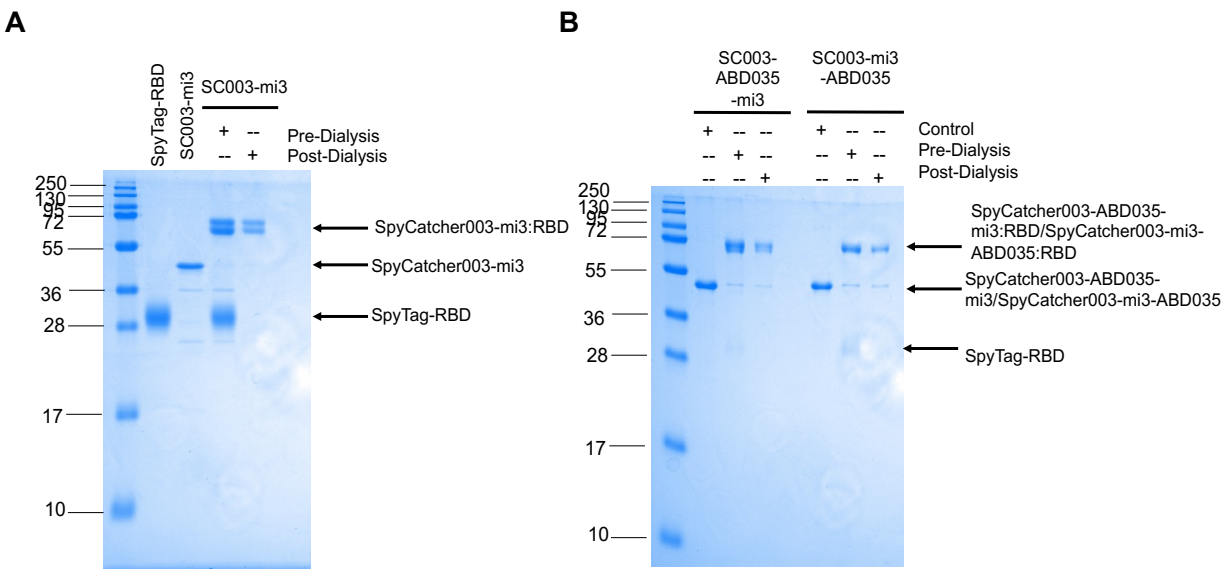


Figure 4. 19. Coupling of SARS-CoV-2 RBD on ABD035 SpyCatcher003-mi3 VLPs: SDS-PAGE showing representative gels of: (A) SpyCatcher003-mi3 (SC003-mi3) and (B) SpyCatcher003-ABD035-mi3 (SC003-ABD035-mi3) and SpyCatcher003-mi3-ABD035 (SC003-mi3-ABD035) VLPs coupled to consistent levels with RBD, before and after excess antigen product is dialyzed away. Both 16% (w/v) non-reduced SDS gels were stained with Coomassie

Dr. Tiong Tan immunized mice according to a similar schedule described previously (Fig 4.20 A). RBD-specific antibody levels induced by both SpyCatcher003-ABD035-mi3 and SpyCatcher003-mi3-ABD035 are similar to that of SpyCatcher003-mi3. However, mi3 scaffold- and SpyCatcher003:SpyTag003-specific antibodies induced by SpyCatcher003-ABD035-mi3 and SpyCatcher003-mi3-ABD035 are also similar to that of SpyCatcher003-mi3 (Fig 4.20 B-D). These results show that including the ABD035 domain does not focus antibody responses to RBD nor shield against the VLP scaffold.

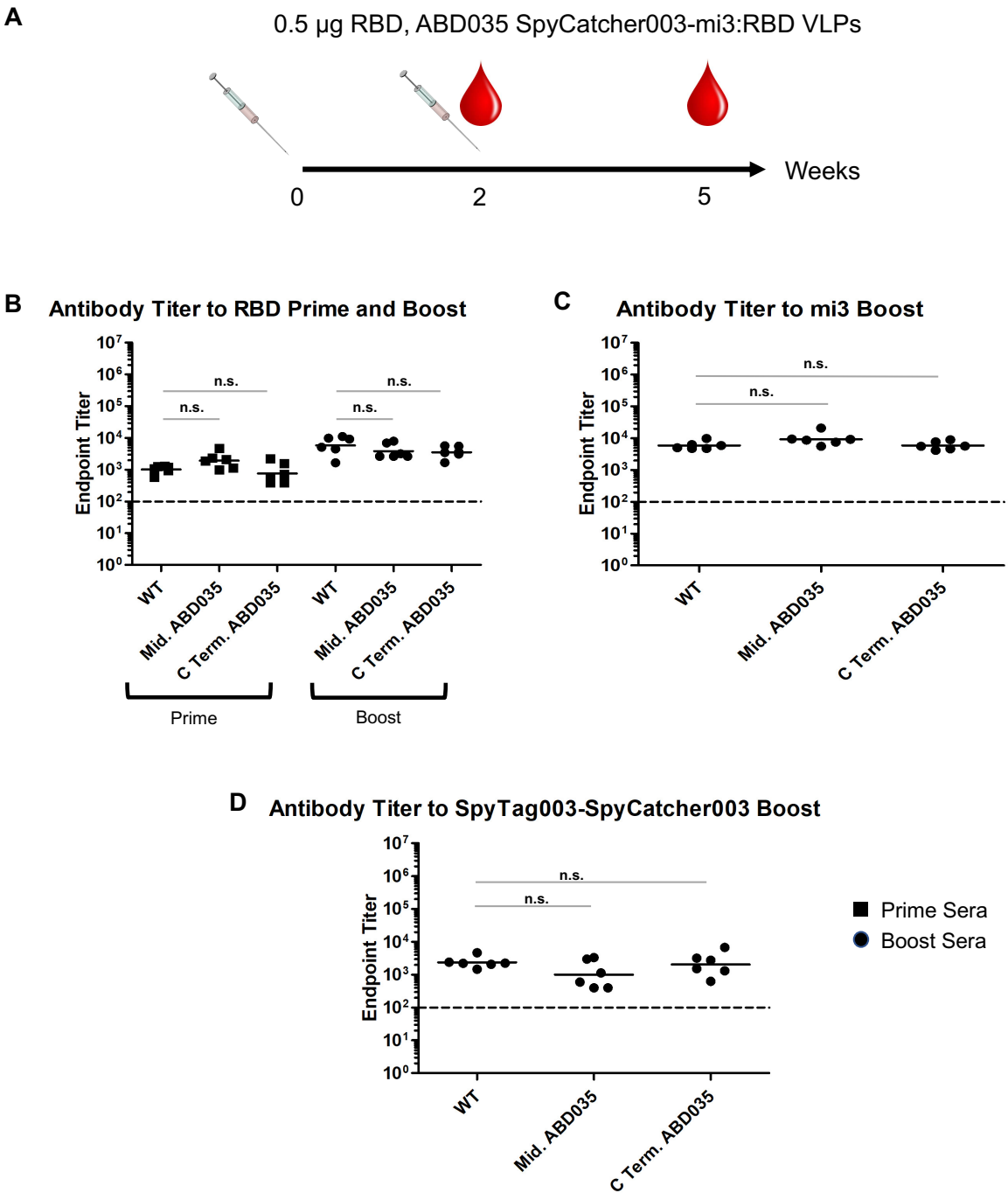


Figure 4. 20. SARS-CoV-2 RBD-, mi3-, and SpyCatcher003:SpyTag003-specific antibody responses: (A) C57BL/6 mice (n=6) received intramuscular immunizations of 0.5 µg RBD/dose of antigen and ABD035 SpyCatcher003-mi3:RBD VLPs on this schedule; (B) Prime and boost sera harvested from mice were analyzed in ELISA against RBD; Boost sera harvested from mice were tested against (C) mi3 scaffold and (D)

SpyCatcher003:SpyTag003. Black horizontal bar is the mean. One-way ANOVA with Bonferroni correction was used to evaluate log_{10}-transformed endpoint titer differences between two dosing groups, as indicated by gray horizontal bars. Groups are denoted as follows: SpyCatcher003-mi3 (WT); SpyCatcher003-ABD035-mi3 (Mid. ABD035), and SpyCatcher003-mi3-ABD035 (C Term. ABD035). Dotted line represents the value of the lowest mouse serum dilution factor tested (100). Prime sera titers are represented by a black square. Boost sera titers are represented by a black circle. Each symbol represents an individual mouse.** $p \leq 0.01$; * $p \leq 0.05$; n.s $p > 0.05$. Mice immunizations and serum harvesting were performed by Dr. Tiong Tan

4.5. Discussion

In the first part of this chapter, I have shown that is possible to solubly express SpyCatcher003-mi3 in HEK293 cells. To my knowledge, mi3 particles have not previously been expressed in a secreted form. Like the bacterial-expressed SpyCatcher003-mi3, the HEK293-expressed SpyCatcher003-mi3 particles are reactive to SpyTag-antigens, exhibit similar overall structure, are just as heat resilient between temperatures of 25 ^{o}C and 95 ^{o}C, and enhance the antibody response to SARS-CoV-2 RBD.

HEK293-expressed SpyCatcher003-mi3 has a lower yield. Having performed some optimization of expression conditions and incubation times, an additional means of increasing yield may be to codon-optimize the construct of SpyCatcher003-mi3. Attempting to express this construct in different eukaryotic cell systems can help improve VLP secretion yield and produce glycans as well. For instance, using the methyltrophic yeast *Pichia pastoris* could be favorable for generating high mannose N-linked glycans (Daly and Hearn, 2005; Yang et al., 2015). The C1 cell line, based on the *Myceliopthora thermophila* fungus, is also capable of expressing human-like N-linked complex glycans (Keresztes et al., 2022).

N-linked glycan sequons were inserted on select loops of SpyCatcher003-mi3, guided by B-factors of the computationally assembled i301 particle (Hsia et al., 2016) and a PyMOL rendering of the SpyCatcher003 parent domain, modified from the crystal structure of the *Streptococcus pyogenes*-derived fibronectin binding protein, Fbab-B (PDB: 2X5P). B-factors can only indicate the regions of a molecule with substantial mobility relative to other atoms in the crystal. Taking this approach will not detect intrinsically flexible loops that are stabilized by crystal packing interactions. Furthermore, both proteins have been considerably mutated in regions proximal to the loops that I selected for inserting N-glycan sequons. Analyzing flexibility on two proteins separately may not reflect the orientation and spacing of SpyCatcher003 relative to mi3 on the actual VLP. A better option may be to select flexible loops based on the the cryo-electron micrograph of RBD coupled to SpyCatcher003-mi3, generated by Dr. Tiong Tan and his collaborators (Tan et al., 2021). This structure was not published at the time I began expressing my glycosylated SpyCatcher003-mi3 variants. However, the increased yield of variants with N-linked glycans, compared to HEK293-expressed SpyCatcher003-mi3, suggests that these glycans may have aided protein folding in the ER, its assembly, and solubility. The presence of these glycans also preserved the thermostable properties previously observed in bacterial-expressed SpyCatcher003-mi3.

The gel shift following PNGase F digestion of my glycosylated SpyCatcher003-mi3 VLP variants offers good evidence that there are glycans present on the mi3 scaffold and the SpyCatcher003 moiety. On each SDS gel, I observed that my glycosylated VLPs had an occupancy of ~60%, while LC-ESI-MS showed only 17% for S50 Glyc. SpyCatcher003-mi3 and 11% for S50 Glyc. SpyCatcher003-mi3 + Kif. Due to this discrepancy, it is less clear how much of each type of glycan there is. Previously, this method and pipeline had only been used to quantitate glycosylation occupancy for antigens (Eldrid et al., 2021). In

using this protocol, it may be possible that glycosylated VLP peptides are not ionized or detected as efficiently as non-glycosylated VLP peptides. One possible cause may be that the hydrophilic nature of glycosylated peptides can affect the desorption from condensed to gas phase, thereby suppressing the signal relative to that of the unglycosylated peptides (Nishikaze, 2017; Yu et al., 2018). Different glycan structures can exist on a glycopeptide with the same amino acid sequence and this may also contribute to the low abundance detected of each type of glycopeptide (Hua et al., 2012; Zhao et al., 2016).

Cleavage with trypsin, chymotrypsin, and alpha-lytic protease was unable to produce N-glycosylated peptide fragments of SpyCatcher003-G124 Glyc. mi3. It is possible that other post-translational modifications may be impeding cleavage, since three lysines, three threonines, and one alanine are within ten residues upstream and downstream of the sequon. It is possible that N-glycans can sterically block the access of trypsin to lysine and arginine residues too close to the glycosylated asparagine (An et al., 2003; Chen et al., 2009; Imre et al., 2005). Tightly folded proteins can also resist trypsin digestion (Saveliev et al., 2013).

Mass spectrometry suggested that S50 Glyc. SpyCatcher003-mi3 had 11% complex glycan occupancy, which is quite low compared to the 60% occupancy estimated from SDS-PAGE densitometry. However, S50 Glyc. SpyCatcher003-mi3 appears to have two N-linked glycosylated bands (Fig 4.5 A), suggesting there may be two distinct sites on S50 Glyc. SpyCatcher003-mi3. One example of an atypical N-glycan sequon includes Asn-X-Cys/Val, where X can be any amino acid except proline. It has been previously observed that N-linked glycans can be bound to aspargines on this sequon for proteins expressed in both HEK293 and CHO cells (Gámez et al., 2021; Gavel and von Heijne, 1990; Sun et al., 2018). In the sequence of S50 Glyc. SpyCatcher003-mi3, an Asn-Ser-Val sequon exists at residues 19-21 of mi3 and an Asn-Val-Cys sequon exists at residues 163-165 of mi3.

While these sequons are present in SpyCatcher003-G124 Glyc. mi3 and SpyCatcher003-mi3, neither VLP exhibits a heavier double-glycosylated band.

Expressing S50 Glyc. SpyCatcher003-mi3 with Kifunensine did not seem to be sufficient to generate a large amount of mannose-rich VLP variant. Mass spectrometry shows no indication of mannosylated glycans and the occupancy level of glycans determined was similar to that of S50 Glyc. SpyCatcher003-mi3. Its likely that 5 nM kifunensine was too low of a dose to effectively inhibit α-mannosidase activity in the ER. In the future, this issue can be improved upon by expressing the VLP in the presence of a higher concentration of Kifunensine, as seen in other studies that express mannose-dense recombinant antigens (Bazzill et al., 2018; Prasanphanich et al., 2014; Saunders et al., 2017; Zhou et al., 2008). Previously I had attempted to express VLPs with 5 μM final concentration of Kifunensine, as done by members of our laboratory (Scheu et al., 2021). However, DLS measurements of these particles showed they were not uniform in size or stable. An alternative method for generating mannose-dense VLPs would be to express these VLPs in *Pichia pastoris* culture.

My endpoint ELISA shows that the antibody responses specific to RBD, mi3, and SpyTag003:SpyCatcher003 for glycosylated VLPs were similar to that of the HEK293-expressed SpyCatcher003-mi3. Without additional data on glycan occupancy and glycan type it is unclear to what extent these specific N-linked glycans shielded SpyCatcher003 or mi3. This ambiguity may suggest that occupancy was low or that the N-linked glycans shielded small surface areas.

It is believed that the accessible surface area of immature N-glycans is often lower than that of mature glycans (Suga et al., 2018). However, this area also depends on the position of the Asn on the protein relative to surrounding tertiary structures, along with the glycan chain's orientation. Using a spherical probe (mimicking a molecule with a 5 Å

radius) to measure the accessible surface area around N-glycosylation sites, Suga and colleagues estimated that a mature $Gal_2Man_3GlcNAc_4Fuc$ glycan on a murine proprotein convertase furin (PDB: 1P8J), has 262 $Å^2$ of accessible surface area, while the mature $Man_3GlcNAc_4$ glycan of human-derived lysosomal integral membrane protein-2 (PDB: 4F7B) has only 3 $Å^2$ of accessible surface area. An immature $Man_9GlcNAc_3$ glycan on a *Trichoderma harzianum*-derived β-mannosidase (PDB: 4CVU) measures 0 $Å^2$ of accessible surface area, while the immature $Man_9GlcNAc_3$ glycan on *S. cerevisiae*-derived exo-1,3- β glucanase (PDB: 1H4P) has 178 $Å^2$ of accessible surface area.

Put in perspective, the glycans on the S-protein from SARS-CoV-2 shields 40% of its surface from antibody recognition (Grant et al., 2020). Furthermore, the N-glycans present on HIV Env trimer can consist of >95% of its surface and account for over half its molecular weight (Depetris et al., 2012; Stewart-Jones et al., 2016; Struwe et al., 2018). SpyCatcher003-mi3 may need to be as heavily glycosylated as the HIV Env or SARS-CoV-2 S protein in order to significantly reduce serum binding to the scaffold.

All my HEK293-expressed VLPs displayed a mixed Th1/Th2 response (based on IgG subtypes). While S50 Glyc. SpyCatcher003-mi3 + Kif displayed a significantly higher Th1 response relative to the HEK293-expressed SpyCatcher003-mi3, this observation may be questionable because no evidence currently suggests that glycans on S50 Glyc. SpyCatcher003-mi3 differ from that of its kifunensine-expressed variant. The way I performed IgG subtyping may have generated variable results. In the future it may be worth repeating IgG subtyping for each of the six mice sera samples corresponding to a VLP, three times, to monitor for consistent titering.

Site-specific N-glycosylation can impact the type and extent of IgG class switching in mice. One study showed that glycans on the C2V3 domain of the HIV envelope protein elicit a Th1-biased response in mice (Heß et al., 2019). Removing these glycans shifted

the IgG subclass to a Th1/2 balanced response (Heß et al., 2019). In another study, removing glycans on the SARS-CoV-2 S protein trimer also induced class switching, from a biased Th2 response to a balanced Th1/2 response in mice (Huang et al., 2021). Separately, immunizing mice with an mRNA vaccine that encodes the S-protein elicited a Th2 response (Wu et al., 2022). Removing the two glycans on RBD maintained this Th2 response, but removing all glycans induced IgG class switching to a Th1 response (Wu et al., 2022).

To my knowledge, not many studies examine how the inclusion of mannose on proteins affects IgG class switching in mice. Mannose-conjugated Qβ nanoparticles can induce inflammatory Th1 cytokines and this is dependent on DC-SIGN binding (Alam et al., 2021). In a separate study, mannose-dense HIV-1 Gag VLPs elicited a Th2-biased response more so than the same VLP with lower mannose density (Mizukoshi et al., 2009).

Incomplete glycan occupancy typically relates to sequon site structural accessibility, interaction with chaperones or other proteins in the ER, and substrate concentrations in the ER (Jenkins et al., 1996). Glycans have greater occupancy near turns and bends between two distinct secondary structures (Petrescu et al., 2003), but positioning N-glycans at these sites may lead to steric clashing. A simpler approach to increase glycan occupancy on SpyCatcher003-mi3 would be to alter the amino acid residues of the sequons itself or those near it. For instance, the Asn-X-Thr sequon is glycosylated two to three times more than Asn-X-Ser (Gavel and von Heijne, 1990). Glycosylation efficiency can be inhibited by glutamic acid and especially proline in the X position, due to its tendency to form an inhibitory loop (Mononen and Karjalainen, 1984). Residues believed to be conducive to glycosylation efficiency include valine and aspartic acid in the X position, arginine one residue upstream of the glycosylated asparagine, and a

serine immediately following the final serine/threonine residue of the N-glycosylation sequon (Mononen and Karjalainen, 1984). My glycosylated SpyCatcher003-mi3 consists of mostly Asn-X-Ser sequons and only one sequon with a Thr as the third residue. In attempting to optimize N-glycan occupancy in the future, it may be worth expressing SpyCatcher003-mi3 with Asn-X-Thr sequons, before attempting to alter additional residues of the N-glycosylation sequon.

My experiments demonstrate proof of concept for SpyCatcher003-mi3 production in mammalian cells. For this to be further considered as a practical vaccine platform, additional work needs to be done to optimize its yield and quantitate its glycan composition. Some evidence of structural discrepancies present in glycosylated VLPs can be seen in the larger standard deviations of HEK293-expressed VLP hydrodynamic radii relative to that of the bacterial-expressed SpyCatcher003-mi3 VLP. Further mass spectrometry studies could be performed on the HEK293-expressed VLPs to understand the extent of other possible post-translational modifications on the particle and its implications for the VLP's immunogenicity.

The second part of this chapter showed that SpyCatcher003-mi3 can be solubly expressed following modification with three different albumin binding sequences, namely: ABD035, Alb8 and SA21. Along with the glycosylated SpyCatcher003-mi3 VLPs, the albumin-binding SpyCatcher003-mi3 VLPs demonstrate that SpyCatcher003-mi3 can remain soluble and functional with multiple amino acid modifications. Inserting the albumin-binding sequences in the GGS_4 linker between the SpyCatcher003 moiety and the mi3 scaffold, along with the C-terminus yielded soluble particles. Taking some inspiration from my glycosylated VLPs, David Schramm has also engineered some albumin-binding sequences onto hydrophilic loops of the mi3 scaffold and SpyCatcher003 moiety (Schramm, 2021; unpublished). Due to observed issues ranging from low albumin binding

to large particle size deviations, these loop-inserted variants were not considered suitable for immunization. Given the availability of RBD-coupled SpyCatcher003-mi3 Cryo-EM data (Tan et al., 2021), it may be worth using this model to select alternate loop positions for inserting albumin binding sequences that will not compromise this VLP's stability. Computational docking of albumin proteins onto this cryo-EM model can also be used to observe the extent of albumin-dependent occlusion of the VLP scaffold and SpyCatcher003 moiety.

The albumin-binding plate assay results conclude that the ABD035 SpyCatcher003-mi3 VLPs bind HSA best, both when it is uncoupled or coupled to RBD. Of the three albumin-binding domains and peptide used in this study, ABD035 has the highest affinity for HSA. In contrast, VLPs with the Alb8 sequence were unable to bind any HSA (Schramm, 2021; unpublished). DLS measurements show that SpyCatcher003-Alb8-mi3 and SpyCatcher003-mi3-Alb8 had hydrodynamic radii of 20 nm and 19 nm, respectively. Since these measurements do not differ greatly from other VLPs with albumin-binding sequences embedded in the GGS_4 linker or unmodified SpyCatcher003-mi3, it is unlikely that VLP unfolding compromised HSA affinity (Schramm, 2021; unpublished). Since SA21 has the lowest binding affinity for HSA, this may explain why SpyCatcher003-SA21-mi3 binds HSA less than both ABD035 SpyCatcher003-mi3 variants.

After establishing that ABD035 was the superior albumin-binder, a second set of plate assays was performed to assess how well albumin-bound SpyCatcher003-ABD035-mi3 and SpyCatcher003-mi3-ABD035 blocked antibody responses from HA:SpyCatcher003-mi3-immunized mice sera. When uncoupled or coupled to RBD, SpyCatcher003-mi3-ABD035 shields antibodies better than SpyCatcher003-ABD035-mi3. With the exception of SpyCatcher003-mi3-ABD035 incubated in MSA, there is no

significant reduction in HA-X31:SpyCatcher003-mi3 serum binding to either of the ABD035 SpyCatcher003-mi3 VLPs. Another key observation here was that ABD035 VLPs shielded less when it was incubated with MSA than HSA. This is expected, given that MSA has a lower binding affinity to ABD035 than HSA (Schramm, 2021; unpublished).

While the RBD-specific antibody responses for both ABD035 VLPs were similar to that of SpyCatcher003-mi3, including the ABD035 domain on SpyCatcher003-mi3 did not significantly decrease antibody titers against the mi3 scaffold or SpyCatcher003:SpyTag003. Since MSA has a lower binding affinity to ABD035 than HSA, this may have decreased the amount of albumin protein bound to the particle. Both the plate assays and the DLS of all albumin-binding VLPs were performed at 20 ^{o}C to 25 ^{o}C. The uncertainty of whether ABD035 VLPs can remain stable at 37 ^{o}C suggests there is a possibility of ABD035-dependent unfolding that might have impacted immunogenicity. Observing protein band density or the VLP's hydrodynamic radius with DLS after heating the particle to 37 ^{o}C can affirm or rule out this possibility.

Crystal structures of HSA show that it has an approximate size of 80 × 80 × 30 Å (Sugio et al., 1999). One study showed that HSA can cover approximately 700 Å^2 at its interface with the 53 residue-long Protein G-related albumin-binding (GA) domain of the anaerobic bacterium *Finegoldia magna* (PDB: 1TF0) (Lejon et al., 2004). I believe the surface area covered by HSA bound to ABD035 is almost the same because GA homologs can be found in the HSA-binding domains of streptococci protein G (Lejon et al., 2004). In comparison, this HSA protein covers more area than what was previously estimated for an N-glycan chitobiose core's (GlcNAc) potential contact area of 500 Å^2 (when rotated in a circle) on *Trichoderma reesei* β-galactosidase (Suga et al., 2018). The low surface coverage by albumin on the VLP may be a reason why mi3- and

SpyCatcher003:SpyTag003-specific antibody titer levels for the bacterial-expressed SpyCatcher003-mi3 and the SpyCatcher003-mi3 ABD035 VLP variants were so similar.

One way to improve albumin shielding of SpyCatcher003-mi3 VLPs would be to use the available Cryo-EM structure of RBD:SpyCatcher003-mi3 (Tan et al., 2021) to select additional flexible loops for inserting multiple ABD035 domains on SpyCatcher003-mi3, thereby increasing the likelihood that more of the VLP's surface area can be occluded by albumin. Another approach may be to perform phage display to select for higher affinity MSA binders for the VLP, then immunizing mice to see if mi3-specific and SpyCatcher003:SpyTag003-specific antibody titers decrease relative to the unmodified bacterial-expressed SpyCatcher003-mi3. If this is effective, a similar approach can be adopted to select for higher affinity HSA binding for the SpyCatcher003-mi3 VLP.

Chapter 5: Summary and Discussion

Chapter 5: Summary and Discussion

By exploiting the human immune system's ability to remember and respond to antigens from previously-encountered pathogens, vaccines have been able to protect populations from deadly diseases. However, as new pathogens continually emerge, there is a need to accelerate the generation of new vaccines. Since 2019, both SpyCatcher and SpyCatcher003 VLPs have enabled different laboratories to design promising vaccine candidates against influenza, HIV, and COVID-19 (Cohen et al., 2021b; Escolano et al., 2019; Rahikainen et al., 2021). Pamela Bjorkman's laboratory has further confirmed that immunizing mice with the mosaic-8 VLP can raise neutralizing antibodies against SARS-CoV-2 variants, such as Omicron (Cohen et al., 2022). Unlike the homotypic SARS-CoV-2 RBD particle, mosaic-8 also conferred protection against SARS-CoV and SARS-CoV-2 challenges in mice and macaques (Cohen et al., 2022). In July 2022, a coalition of laboratories in Oxford and Caltech received financial support from the Coalition for Epidemic Preparedness Innovations (CEPI) that would enable mosaic SpyCatcher003-mi3 VLPs to go in clinical trials (Coalition for Epidemic Preparedness Innovations, 2022). These developments are especially important because COVID-19 variants continue to evolve, threatening lives, economic output, and the return of society to pre-pandemic normality (Murray, 2022; del Rio and Malani, 2022).

In Chapter 3, I first showed that incorporating the SpyCatcher003 protein onto the mi3 scaffold results in a fully assembled VLP. This VLP can be expressed to high yields in bacterial culture and offers enhanced stability relative to its predecessor, SpyCatcher-mi3 (Bruun et al., 2018). Our collaborators have corroborated these findings, while demonstrating that displaying RBD antigens on SpyCatcher003-mi3 significantly increases specific and neutralizing antibody titers compared to uncoupled RBD antigens (Cohen et al., 2021b; Tan et al., 2021).

Since the plug-and-display system of SpyCatcher003-mi3 offers a simple way of assembling antigen-decorated VLPs, it would be interesting to see the range of vaccine candidates that will emerge from displaying diverse antigen combinations on this platform. Our laboratory has demonstrated that SpyCatcher003-mi3 can accommodate antigens of diverse sizes and symmetries (Rahikainen et al., 2021). From a production standpoint, it is worth investigating whether the VLP's purification yield can be increased by varying growth conditions, incorporating fermentation methods (Chen et al., 2016), and applying downstream techniques like ultracentrifugation, which is used in industry to purify VLPs (Effio and Hubbuch, 2015). While SpyCatcher003-mi3 enhances antibody titer levels compared to the uncoupled antigens, it is less clear what antibody subtypes are raised against the bacterial-expressed SpyCatcher003-mi3. This is an important piece of information because vaccines that target different diseases need to elicit different T-helper cell cytokine responses (Morel and Turner, 2010). It would then be interesting to evaluate how different combinations of adjuvants and displayed antigens can modify the antibody subtypes (C. Gomes et al., 2019; Chang et al., 2022; Ko and Kang, 2018; Marrack et al., 2009). This study has not explored in-depth the immune cell dynamics responsible for driving a robust antibody response towards the VLP-displayed antigen. Therefore, it would be worth studying in future work how antigen-decorated SpyCatcher003-mi3 affects B-cell binding and subsequent plasma cell formation in mice, including by following the localization of these VLPs reacted with fluorescent dyes.

In Chapter 4, my initial motivation was to examine whether SpyCatcher003-mi3 could be expressed in mammalian cell culture. SpyCatcher003-mi3 can be expressed solubly in HEK293 cells and efficiently display antigens, much like the bacterial-expressed SpyCatcher003-mi3. I then successfully expressed two partly glycosylated SpyCatcher003-mi3 variants in HEK293 cells, after inserting N-glycan sequons on flexible

loops of the mi3 scaffold and the SpyCatcher003 protein. The inclusion of these glycans enabled the particles to remain stable after being heated to 95 °C for 1 h. Both the glycosylated and non-glycosylated VLPs coupled with RBD at similar rates. However, DLS showed that the HEK293-expressed SpyCatcher003-mi3 particles are larger than bacterial-expressed SpyCatcher003-mi3 particles. After immunizing mice with my glycosylated VLPs, I had observed no significant difference in RBD-, mi3 scaffold-, or SpyCatcher003:SpyTag003-specific endpoint titers relative to that of the HEK293-expressed SpyCatcher003-mi3. Future work would obtain further data on glycan occupancy and glycan type, to clarify to what extent N-linked glycans shielded the SpyCatcher003 protein or the mi3 scaffold. On the other hand, it may be possible to optimize N-linked glycan occupancy of the VLP by inserting Asn-X-Thr sequons onto additional flexible loops on SpyCatcher003 and the mi3 scaffold, or by considering yeast and fungi cell lines for expression.

Encouraged by my work on engineering glycans onto the SpyCatcher003-mi3 VLP, my laboratory's Part II student David Schramm engineered select albumin-binding sequences onto SpyCatcher003-mi3 to test a different method of occluding the VLP scaffold. Of the VLPs inserted with ABD035, Alb8, and SA21 albumin-binding sequences, ABD035 SpyCatcher003-mi3 particles were uniform in size and showed good albumin interactions *in vitro*. After immunizing mice with RBD-coupled ABD035-inserted SpyCatcher003-mi3 VLPs, I did not find significant difference in RBD-, mi3 scaffold-, or SpyCatcher003:SpyTag003-specific endpoint titers relative to that of the bacterial-expressed SpyCatcher003-mi3. A possible cause for this may be because MSA has a lower binding affinity to ABD035 than HSA, which might impact the quantity of albumin bound to SpyCatcher003-mi3. It is also uncertain whether ABD035 VLPs remain stable at 37 °C for the necessary time post-immunization. Monitoring changes in hydrodynamic radii

after these particles are heated to 37 ^{o}C can validate this possibility. It is also possible that because ABD035 was inserted in flexible parts of SpyCatcher003-mi3, ABD035 was unable to consistently shield much of the VLP scaffold. A Cryo-EM structure of RBD-coupled SpyCatcher003-mi3 (Tan et al., 2021) can help guide the insertion of ABD035 onto additional hydrophilic loops that can potentially improve the VLP's serum albumin-dependent shielding capability.

The outlook for VLP vaccines is promising, with extensive research work taking place in this area and many more in different stages of development and approval (Nooraei et al., 2021; Tariq et al., 2022). To date, Novavax's NVX-CoV2373 is the only protein nanoparticle vaccine against COVID-19, based on the pre-fusion stabilized form of the SARS-CoV-2 spike protein (Tian et al., 2021). The U.S. Food and Drug Administration granted NVX-CoV2373 emergency use authorization in July 2022 and since then, studies have demonstrated its ability to neutralize Omicron subvariants BA.1, BA.4, and BA.5, at a comparable level to the BNT162b mRNA vaccine (Bhiman et al., 2022). In my thesis, I have demonstrated how the SpyCatcher003-mi3 platform offers a simple, scalable method of attaching antigens to an immunogenic scaffold. I have also taken the first steps of showing how antibody shielding can be engineered onto this plug-and-display platform and its subsequent performance. However, more work can be performed to better understand the limitations of antibody shielding against the VLP scaffold.

Bibliography

Agrawal, A.S., Tao, X., Algaissi, A., Garron, T., Narayanan, K., Peng, B.-H., Couch, R.B., and Tseng, C.-T.K. (2016). Immunization with inactivated Middle East Respiratory Syndrome coronavirus vaccine leads to lung immunopathology on challenge with live virus. Hum Vaccin Immunother *12*, 2351–2356.

Alam, M.M., Jarvis, C.M., Hincapie, R., McKay, C.S., Schimer, J., Sanhueza, C.A., Xu, K., Diehl, R.C., Finn, M.G., and Kiessling, L.L. (2021). Glycan-modified virus-like particles evoke T helper type 1-like immune responses. ACS Nano *15*, 309–321.

Altgärde, N., Eriksson, C., Peerboom, N., Phan-Xuan, T., Moeller, S., Schnabelrauch, M., Svedhem, S., Trybala, E., Bergström, T., and Bally, M. (2015). Mucin-like region of herpes simplex virus type 1 attachment protein glycoprotein C (GC) modulates the virus-glycosaminoglycan interaction. Journal of Biological Chemistry *290*, 21473–21485.

An, H.J., Peavy, T.R., Hedrick, J.L., and Lebrilla, C.B. (2003). Determination of N-glycosylation sites and site heterogeneity in glycoproteins. Anal Chem *75*, 5628–5637.

Bachmann, M.F., and Jennings, G.T. (2010). Vaccine delivery: a matter of size, geometry, kinetics and molecular patterns. Nat Rev Immunol *10*, 787–796.

Bachmann, M.F., Rohrer, U.H., Kündig, T.M., Bürki, K., Hengartner, H., and Zinkernagel, R.M. (1993). The influence of antigen organization on B cell responsiveness. Science *262*, 1448–1451.

Bahar, M.W., Porta, C., Fox, H., Macadam, A.J., Fry, E.E., and Stuart, D.I. (2021). Mammalian expression of virus-like particles as a proof of principle for next generation polio vaccines. NPJ Vaccines *6*, 5.

Bajic, G., Maron, M.J., Adachi, Y., Onodera, T., McCarthy, K.R., McGee, C.E., Sempowski, G.D., Takahashi, Y., Kelsoe, G., Kuraoka, M., et al. (2019). Influenza Antigen Engineering Focuses Immune Responses to a Subdominant but Broadly Protective Viral Epitope. Cell Host Microbe *25*, 827-835. e6.

Bajic, G., Maron, M.J., Caradonna, T.M., Tian, M., Mermelstein, A., Fera, D., Kelsoe, G., Kuraoka, M., and Schmidt, A.G. (2020). Structure-Guided Molecular Grafting of a Complex Broadly Neutralizing Viral Epitope. ACS Infect Dis *6*, 1182–1191.

Bale, J.B., Gonen, S., Liu, Y., Sheffler, W., Ellis, D., Thomas, C., Cascio, D., Yeates, T.O., Gonen, T., King, N.P., et al. (2016). Accurate design of megadalton-scale two-component icosahedral protein complexes. Science *353*, 389–394.

Balke, I., and Zeltins, A. (2020). Recent Advances in the Use of Plant Virus-Like Particles as Vaccines. Viruses *12*.

Banchereau, J., and Steinman, R.M. (1998). Dendritic cells and the control of immunity. Nature *392*, 245–252.

Bayer, M.E., Blumberg, B.S., and Werner, B. (1968). Particles associated with Australia antigen in the sera of patients with leukaemia, Down's Syndrome and hepatitis. Nature *218*, 1057–1059.

Bazzill, J.D., Ochyl, L.J., Giang, E., Castillo, S., Law, M., and Moon, J.J. (2018). Interrogation of Antigen Display on Individual Vaccine Nanoparticles for Achieving Neutralizing Antibody Responses against Hepatitis C Virus. Nano Lett *18*, 7832–7838.

Bernstein, D.I., Guptill, J., Naficy, A., Nachbagauer, R., Berlanda-Scorza, F., Feser, J., Wilson, P.C., Solórzano, A., van der Wielen, M., Walter, E.B., et al. (2020). Immunogenicity of chimeric haemagglutinin-based, universal influenza virus vaccine candidates: interim results of a randomised, placebo-controlled, phase 1 clinical trial. Lancet Infect Dis *20*, 80–91.

Bhiman, J.N., Richardson, S.I., Lambson, B.E., Kgagudi, P., and Mzindle, N. (2022). Novavax NVX-COV2373 triggers potent neutralization of Omicron sub-lineages. BioRxiv.

Bommireddy, R., Stone, S., Bhatnagar, N., Kumari, P., Munoz, L.E., Oh, J., Kim, K.-H., Berry, J.T.L., Jacobsen, K.M., Jaafar, L., et al. (2022). Influenza virus-like particle-based hybrid vaccine containing RBD induces immunity against influenza and SARS-CoV-2 viruses. Vaccines *10*, 944.

Boyington, J.C., Joyce, M.G., Sastry, M., Stewart-Jones, G.B.E., Chen, M., Kong, W.-P., Ngwuta, J.O., Thomas, P. v., Tsybovsky, Y., Yang, Y., et al. (2016). Structure-based design of head-only fusion glycoprotein immunogens for respiratory syncytial virus. PLoS One *11*, e0159709.

Boylston, A. (2012). The origins of inoculation. J R Soc Med *105*, 309–313.

Boyoglu-Barnum, S., Hutchinson, G.B., Boyington, J.C., Moin, S.M., Gillespie, R.A., Tsybovsky, Y., Stephens, T., Vaile, J.R., Lederhofer, J., Corbett, K.S., et al. (2020). Glycan repositioning of influenza hemagglutinin stem facilitates the elicitation of protective cross-group antibody responses. Nat Commun *11*, 791.

Boyoglu-Barnum, S., Ellis, D., Gillespie, R.A., Hutchinson, G.B., Park, Y.-J., Moin, S.M., Acton, O.J., Ravichandran, R., Murphy, M., Pettie, D., et al. (2021). Quadrivalent influenza nanoparticle vaccines induce broad protection. Nature *592*, 623–628.

Brito, L.A., and Singh, M. (2011). COMMENTARY: Acceptable Levels of Endotoxin in Vaccine Formulations During Preclinical Research. J Pharm Sci *100*, 34–37.

Brouwer, P.J.M., Antanasijevic, A., Berndsen, Z., Yasmeen, A., Fiala, B., Bijl, T.P.L., Bontjer, I., Bale, J.B., Sheffler, W., Allen, J.D., et al. (2019). Enhancing and shaping the immunogenicity of native-like HIV-1 envelope trimers with a two-component protein nanoparticle. Nat Commun *10*, 4272.

Brune, K.D., and Howarth, M. (2018). New routes and opportunities for modular construction of particulate vaccines: stick, click, and glue. Front Immunol *9*.

Brune, K.D., Leneghan, D.B., Brian, I.J., Ishizuka, A.S., Bachmann, M.F., Draper, S.J., Biswas, S., and Howarth, M. (2016). Plug-and-Display: decoration of Virus-Like Particles via isopeptide bonds for modular immunization. Sci Rep *6*, 19234.

Bruun, T.U.J., Andersson, A.-M.C., Draper, S.J., and Howarth, M. (2018). Engineering a rugged nanoscaffold to enhance plug-and-display vaccination. ACS Nano *12*, 8855–8866.

C. Gomes, A., Roesti, E.S., El-Turabi, A., and Bachmann, M.F. (2019). Type of RNA packed in VLPs impacts IgG class switching—implications for an influenza vaccine design. Vaccines *7*, 47.

Caradonna, T.M., and Schmidt, A.G. (2021). Protein engineering strategies for rational immunogen design. NPJ Vaccines 6, 154.

Casalino, L., Gaieb, Z., Goldsmith, J.A., Hjorth, C.K., Dommer, A.C., Harbison, A.M., Fogarty, C.A., Barros, E.P., Taylor, B.C., McLellan, J.S., et al. (2020). Beyond shielding: the roles of glycans in the SARS-CoV-2 spike protein. ACS Central Science *6*, 1722–1734.

Chang, X., Krenger, P., Krueger, C.C., Zha, L., Han, J., Yermanos, A., Roongta, S., Mohsen, M.O., Oxenius, A., Vogel, M., et al. (2022). TLR7 Signaling Shapes and Maintains Antibody Diversity Upon Virus-Like Particle Immunization. Front Immunol *12*.

Chen, R., Jiang, X., Sun, D., Han, G., Wang, F., Ye, M., Wang, L., and Zou, H. (2009). Glycoproteomics analysis of human liver tissue by combination of multiple enzyme digestion and hydrazide chemistry. J Proteome Res *8*, 651–661.

Chen, Y., Liu, Y., Zhang, G., Wang, A., Dong, Z., Qi, Y., Wang, J., Zhao, B., Li, N., and Jiang, M. (2016). Human papillomavirus L1 protein expressed in Escherichia coli self-assembles into virus-like particles that are highly immunogenic. Virus Res *220*, 97–103.

Chin, C.L., Goh, J.B., Srinivasan, H., Liu, K.I., Gowher, A., Shanmugam, R., Lim, H.L., Choo, M., Tang, W.Q., Tan, A.H.-M., et al. (2019). A human expression system based on HEK293 for the stable production of recombinant erythropoietin. Sci Rep *9*, 16768.

Chung, Y.H., Cai, H., and Steinmetz, N.F. (2020). Viral nanoparticles for drug delivery, imaging, immunotherapy, and theranostic applications. Adv Drug Deliv Rev *156*, 214–235.

Coalition for Epidemic Preparedness Innovations (2022). CEPI funds consortium led by CPI to advance Caltech's new all-in-one coronavirus vaccine.

Cohen, A.A., Yang, Z., Gnanapragasam, P.N.P., Ou, S., Dam, K.-M.A., Wang, H., and Bjorkman, P.J. (2021a). Construction, characterization, and immunization of nanoparticles that display a diverse array of influenza HA trimers. PLoS One *16*, e0247963.

Cohen, A.A., Gnanapragasam, P.N.P., Lee, Y.E., Hoffman, P.R., Ou, S., Kakutani, L.M., Keeffe, J.R., Wu, H.-J., Howarth, M., West, A.P., et al. (2021b). Mosaic nanoparticles elicit cross-reactive immune responses to zoonotic coronaviruses in mice. Science *371*, 735–741.

Cohen, A.A., van Doremalen, N., Greaney, A.J., Andersen, H., Sharma, A., Starr, T.N., Keeffe, J.R., Fan, C., Schulz, J.E., Gnanapragasam, P.N.P., et al. (2022). Mosaic RBD nanoparticles protect against multiple sarbecovirus challenges in animal models. BioRxiv

Cook, J.C., Joyce, J.G., George, H.A., Schultz, L.D., Hurni, W.M., Jansen, K.U., Hepler, R.W., Ip, C., Lowe, R.S., Keller, P.M., et al. (1999). Purification of virus-like particles of recombinant human papillomavirus type 11 major capsid protein L1 from saccharomyces cerevisiae. Protein Expression and Purification *17*, 477–484.

Cooper, M.R., Stewart, D.C., Kahl, F.R., Brown, W.M., and Cordell, A.R. (2002). Medicine at the medical center then and now: one hundred years of progress. South Med J *95*, 1113–1121.

Corbett, K.S., Moin, S.M., Yassine, H.M., Cagigi, A., Kanekiyo, M., Boyoglu-Barnum, S., Myers, S.I., Tsybovsky, Y., Wheatley, A.K., Schramm, C.A., et al. (2019). Design of nanoparticulate group 2 influenza virus hemagglutinin stem antigens that activate unmutated ancestor B cell receptors of broadly neutralizing antibody lineages. MBio *10*.

Creytens, S., Pascha, M.N., Ballegeer, M., Saelens, X., and de Haan, C.A.M. (2021). Influenza Neuraminidase Characteristics and Potential as a Vaccine Target. Front Immunol *12*.

Crispin, M., Ward, A.B., and Wilson, I.A. (2018). Structure and Immune Recognition of the HIV Glycan Shield. Annu Rev Biophys *47*, 499–523.

Cristie-David, A.S., Koldewey, P., Meinen, B.A., Bardwell, J.C.A., and Marsh, E.N.G. (2018). Elaborating a coiled-coil-assembled octahedral protein cage with additional protein domains. Protein Science *27*, 1893–1900.

Dalvie, N.C., Tostanoski, L.H., Rodriguez-Aponte, S.A., Kaur, K., Bajoria, S., Kumru, O.S., Martinot, A.J., Chandrashekar, A., McMahan, K., Mercado, N.B., et al. (2022). SARS-CoV-2 receptor binding domain displayed on HBsAg virus–like particles elicits protective immunity in macaques. Sci Adv *8*.

Daly, R., and Hearn, M.T.W. (2005). Expression of heterologous proteins in pichia pastoris: a useful experimental tool in protein engineering and production. Journal of Molecular Recognition *18*, 119–138.

Dash, B., McIntosh, A., Barrett, W., and Daniels, R. (1994). Deletion of a single N-linked glycosylation site from the transmembrane envelope protein of human immunodeficiency virus type 1 stops cleavage and transport of gp160 preventing env-mediated fusion. Journal of General Virology *75*, 1389–1397.

Delany, I., Rappuoli, R., and de Gregorio, E. (2014). Vaccines for the 21st century. EMBO Mol Med *6*, 708–720.

Dennis, M.S., Zhang, M., Meng, Y.G., Kadkhodayan, M., Kirchhofer, D., Combs, D., and Damico, L.A. (2002). Albumin binding as a general strategy for improving the pharmacokinetics of proteins. Journal of Biological Chemistry *277*, 35035–35043.

Depetris, R.S., Julien, J.-P., Khayat, R., Lee, J.H., Pejchal, R., Katpally, U., Cocco, N., Kachare, M., Massi, E., David, K.B., et al. (2012). Partial enzymatic deglycosylation preserves the structure of cleaved recombinant HIV-1 envelope glycoprotein trimers. Journal of Biological Chemistry *287*, 24239–24254.

Dong, Y., Dai, T., Wei, Y., Zhang, L., Zheng, M., and Zhou, F. (2020). A systematic review of SARS-CoV-2 vaccine candidates. Signal Transduct Target Ther *5*, 237.

Duan, H., Chen, X., Boyington, J.C., Cheng, C., Zhang, Y., Jafari, A.J., Stephens, T., Tsybovsky, Y., Kalyuzhniy, O., Zhao, P., et al. (2018). Glycan masking focuses immune responses to the HIV-1 CD4-binding site and enhances elicitation of VRC01-class precursor antibodies. Immunity *49*, 301-311. e5.

Dubrovskaya, V., Tran, K., Ozorowski, G., Guenaga, J., Wilson, R., Bale, S., Cottrell, C.A., Turner, H.L., Seabright, G., O'Dell, S., et al. (2019). Vaccination with glycan-modified HIV NFL envelope trimer-liposomes elicits broadly neutralizing antibodies to multiple sites of vulnerability. Immunity *51*, 915-929. e7.

Dumont, J., Euwart, D., Mei, B., Estes, S., and Kshirsagar, R. (2016). Human cell lines for biopharmaceutical manufacturing: history, status, and future perspectives. Crit Rev Biotechnol *36*, 1110–1122.

Effio, C.L., and Hubbuch, J. (2015). Next generation vaccines and vectors: Designing downstream processes for recombinant protein-based virus-like particles. Biotechnol J *10*, 715–727.

Egesten, A., Frick, I.-M., Mörgelin, M., Olin, A.I., and Björck, L. (2011). Binding of albumin promotes bacterial survival at the epithelial surface. J Biol Chem *286*, 2469–2476.

Elbein, A.D., Tropea, J.E., Mitchell, M., and Kaushal, G.P. (1990). Kifunensine, a potent inhibitor of the glycoprotein processing mannosidase I. Journal of Biological Chemistry *265*, 15599–15605.

Eldrid, C.F.S., Allen, J.D., Newby, M.L., and Crispin, M. (2021). Suppression of O-linked glycosylation of the SARS-CoV-2 spike by quaternary structural restraints. Anal Chem *93*, 14392–14400.

Elzoghby, A.O., Samy, W.M., and Elgindy, N.A. (2012). Albumin-based nanoparticles as potential controlled release drug delivery systems. Journal of Controlled Release *157*, 168–182.

Escolano, A., Gristick, H.B., Abernathy, M.E., Merkenschlager, J., Gautam, R., Oliveira, T.Y., Pai, J., West, A.P., Barnes, C.O., Cohen, A.A., et al. (2019). Immunization expands B cells specific to HIV-1 V3 glycan in mice and macaques. Nature *570*, 468–473.

Fiebiger, E., Meraner, P., Weber, E., Fang, I.-F., Stingl, G., Ploegh, H., and Maurer, D. (2001). Cytokines regulate proteolysis in major histocompatibility complex class II–

dependent antigen presentation by dendritic cells. Journal of Experimental Medicine *193*, 881–892.

Finney, J., Yeh, C.-H., Kelsoe, G., and Kuraoka, M. (2018). Germinal center responses to complex antigens. Immunol Rev *284*, 42–50.

Fliedl, L., Grillari, J., and Grillari-Voglauer, R. (2015). Human cell lines for the production of recombinant proteins: on the horizon. N Biotechnol *32*, 673–679.

Food and Drug Administration (2010). Characterization and qualification of cell substrates and other biological materials used in the production of viral vaccines for infectious disease indications.

Fougeroux, C., Goksøyr, L., Idorn, M., Soroka, V., Myeni, S.K., Dagil, R., Janitzek, C.M., Søgaard, M., Aves, K.-L., Horsted, E.W., et al. (2021). Capsid-like particles decorated with the SARS-CoV-2 receptor-binding domain elicit strong virus neutralization activity. Nat Commun *12*, 324.

Frey, S.J., Varner, C., Arsiwala, A., Currier, M.G., Moore, M.L., and Kane, R.S. (2020). The design of vaccines based on the shielding of antigenic site Ø of a respiratory syncytial virus fusion protein immunogen. Advanced Healthcare Materials *10*, 2000714.

Gámez, G., Hermoso, J.A., Carrasco-López, C., Gómez-Mejia, A., Muskus, C.E., and Hammerschmidt, S. (2021). Atypical N-glycosylation of SARS-CoV-2 impairs the efficient binding of Spike-RBM to the human-host receptor hACE2. BioRxiv.

Gao, Y., Yue, Y., and Xiong, S. (2021). An albumin-binding domain peptide confers enhanced immunoprotection against viral myocarditis by CVB3 VP1 vaccine. Front Immunol *12*, 666594.

Gavel, Y., and von Heijne, G. (1990). Sequence differences between glycosylated and non-glycosylated Asn-X-Thr/Ser acceptor sites: implications for protein engineering. Protein Eng *3*, 433–442.

Ghosh, D.K., and Ranjan, A. (2020). The metastable states of proteins. Protein Science *29*, 1559–1568.

Giurgea, L.T., Morens, D.M., Taubenberger, J.K., and Memoli, M.J. (2020). Influenza neuraminidase: a neglected protein and its potential for a better influenza vaccine. Vaccines *8*, 409.

Gomes, A., Mohsen, M., and Bachmann, M. (2017). Harnessing nanoparticles for immunomodulation and vaccines. Vaccines *5*, 6.

Gradishar, W.J. (2006). Albumin-bound paclitaxel: a next-generation taxane. Expert Opin Pharmacother *7*, 1041–1053.

Gradishar, W.J., Krasnojon, D., Cheporov, S., Makhson, A.N., Manikhas, G.M., Clawson, A., and Bhar, P. (2009). Significantly longer progression-free survival with *nab*-paclitaxel

compared with docetaxel as first-line therapy for metastatic breast cancer. Journal of Clinical Oncology *27*, 3611–3619.

Grant, O.C., Montgomery, D., Ito, K., and Woods, R.J. (2020). Analysis of the SARS-CoV-2 spike protein glycan shield reveals implications for immune recognition. Sci Rep *10*, 14991.

Greenwood, B. (2014). The contribution of vaccination to global health: past, present and future. Philosophical Transactions of the Royal Society of London B: Biological Sciences *369*, 20130433.

Guan, Z.-Z., Li, Q.L., Feng, F., Jiang, Z., Shen, Z., Yu, S., Fen, J., Huang, J., Yao, Z., and Bhar, P. (2009). Superior efficacy of a Cremophor-free albumin-bound paclitaxel compared with solvent-based paclitaxel in Chinese patients with metastatic breast cancer. Asia Pac J Clin Oncol *5*, 165–174.

Gulati, N.M., Pitek, A.S., Czapar, A.E., Stewart, P.L., and Steinmetz, N.F. (2018). The in-vivo fates of plant viral nanoparticles camouflaged using self-proteins: overcoming immune recognition. J Mater Chem B *6*, 2204–2216.

Guthmiller, J.J., Han, J., Li, L., Freyn, A.W., Liu, S.T., Stovicek, O., Stamper, C.T., Dugan, H.L., Tepora, M.E., Utset, H.A., et al. (2021). First exposure to the pandemic H1N1 virus induced broadly neutralizing antibodies targeting hemagglutinin head epitopes. Science Translational Medicine *13*.

Habjan, M., Penski, N., Wagner, V., Spiegel, M., Överby, A.K., Kochs, G., Huiskonen, J.T., and Weber, F. (2009). Efficient production of Rift Valley fever virus-like particles: The antiviral protein Mxa can inhibit primary transcription of Bunyaviruses. Virology *385*, 400–408.

Hai, R., Krammer, F., Tan, G.S., Pica, N., Eggink, D., Maamary, J., Margine, I., Albrecht, R.A., and Palese, P. (2012). Influenza viruses expressing chimeric hemagglutinins: globular head and stalk domains derived from different subtypes. J Virol *86*, 5774–5781.

Hanna, S.L., Pierson, T.C., Sanchez, M.D., Ahmed, A.A., Murtadha, M.M., and Doms, R.W. (2005). N-linked glycosylation of West Nile virus envelope proteins influences particle assembly and infectivity. Journal of Virology *79*, 13262–13274.

Hans-Uwe, S., Karaulov, A.V., and Bachmann, M.F. (2020). Strategies to prevent SARS-CoV-2-mediated eosinophilic disease in association with COVID-19 vaccination and infection. Int Arch Allergy Immunol *181*, 624–628.

Hastie, K.M., Zandonatti, M.A., Kleinfelter, L.M., Heinrich, M.L., Rowland, M.M., Chandran, K., Branco, L.M., Robinson, J.E., Garry, R.F., and Saphire, E.O. (2017). Structural basis for antibody-mediated neutralization of Lassa virus. Science (1979) *356*, 923–928.

Hebert, G.A., Pelham, P.L., and Pittman, B. (1973). Determination of the optimal ammonium sulfate concentration for the fractionation of rabbit, sheep, horse, and goat antisera. Appl Microbiol *25*, 26–36.

Heß, R., Storcksdieck genannt Bonsmann, M., Lapuente, D., Maaske, A., Kirschning, C., Ruland, J., Lepenies, B., Hannaman, D., Tenbusch, M., and Überla, K. (2019). Glycosylation of HIV Env impacts IgG subtype responses to vaccination. Viruses *11*, 153.

Hsia, Y., Bale, J.B., Gonen, S., Shi, D., Sheffler, W., Fong, K.K., Nattermann, U., Xu, C., Huang, P.-S., Ravichandran, R., et al. (2016). Design of a hyperstable 60-subunit protein icosahedron. Nature *535*, 136–139.

Hsieh, C.-L., Goldsmith, J.A., Schaub, J.M., DiVenere, A.M., Kuo, H.-C., Javanmardi, K., Le, K.C., Wrapp, D., Lee, A.G., Liu, Y., et al. (2020). Structure-based design of prefusion-stabilized SARS-CoV-2 spikes. Science *369*, 1501–1505.

Hua, S., Nwosu, C.C., Strum, J.S., Seipert, R.R., An, H.J., Zivkovic, A.M., German, J.B., and Lebrilla, C.B. (2012). Site-specific protein glycosylation analysis with glycan isomer differentiation. Anal Bioanal Chem *403*, 1291–1302.

Huang, C., Wang, Y., Li, X., Ren, L., Zhao, J., Hu, Y., Zhang, L., Fan, G., Xu, J., Gu, X., et al. (2020a). Clinical features of patients infected with 2019 novel coronavirus in Wuhan, China. The Lancet *395*, 497–506.

Huang, D.B., Wu, J.J., and Tyring, S.K. (2004). A review of licensed viral vaccines, some of their safety concerns, and the advances in the development of investigational viral vaccines. J Infect *49*, 179–209.

Huang, H.-Y., Liao, H.-Y., Chen, X., Wang, S.-W., Cheng, C.-W., Shahed-Al-Mahmud, Md., Chen, T.-H., Lo, J.M., Liu, Y.-M., Wu, Y.-M., et al. (2021). Impact of glycosylation on a broad-spectrum vaccine against SARS-CoV-2. BioRxiv.

Huang, H.-Y., Liao, H.-Y., Chen, X., Wang, S.-W., Cheng, C.-W., Shahed-Al-Mahmud, Md., Liu, Y.-M., Mohapatra, A., Chen, T.-H., Lo, J.M., et al. (2022). Vaccination with SARS-CoV-2 spike protein lacking glycan shields elicits enhanced protective responses in animal models. Sci Transl Med *14*.

Huang, Y., Owino, S.O., Crevar, C.J., Carter, D.M., and Ross, T.M. (2020b). N-Linked glycans and K147 residue on hemagglutinin synergize to elicit broadly reactive H1N1 influenza virus antibodies. J Virol *94*.

Hyakumura, M., Walsh, R., Thaysen-Andersen, M., Kingston, N.J., La, M., Lu, L., Lovrecz, G., Packer, N.H., Locarnini, S., and Netter, H.J. (2015). Modification of asparagine-linked glycan density for the design of hepatitis B virus virus-like particles with enhanced immunogenicity. J Virol *89*, 11312–11322.

Imre, T., Schlosser, G., Pocsfalvi, G., Siciliano, R., Molnár-Szöllosi, E., Kremmer, T., Malorni, A., and Vékey, K. (2005). Glycosylation site analysis of human alpha-1-acid glycoprotein (AGP) by capillary liquid chromatography-electrospray mass spectrometry. J Mass Spectrom *40*, 1472–1483.

Iuliano, A.D., Roguski, K.M., Chang, H.H., Muscatello, D.J., Palekar, R., Tempia, S., Cohen, C., Gran, J.M., Schanzer, D., Cowling, B.J., et al. (2018). Estimates of global seasonal influenza-associated respiratory mortality: a modelling study. The Lancet *391*, 1285–1300.

Jardine, J., Julien, J.-P., Menis, S., Ota, T., Kalyuzhniy, O., McGuire, A., Sok, D., Huang, P.-S., MacPherson, S., Jones, M., et al. (2013). Rational HIV immunogen design to target specific germline B cell receptors. Science *340*, 711–716.

Jegerlehner, A., Maurer, P., Bessa, J., Hinton, H.J., Kopf, M., and Bachmann, M.F. (2007). TLR9 signaling in B cells determines class switch recombination to IgG2a. J Immunol *178*, 2415–2420.

Jenkins, N., Parekh, R.B., and James, D.C. (1996). Getting the glycosylation right: Implications for the biotechnology industry. Nat Biotechnol *14*, 975–981.

Jennings, G.T., and Bachmann, M.F. (2008). The coming of age of virus-like particle vaccines. Biol Chem *389*, 521–536.

Jiang, S., Lu, L., Liu, Q., Xu, W., and Du, L. (2012). Receptor-binding domains of spike proteins of emerging or re-emerging viruses as targets for development of antiviral vaccines. Emerg Microbes Infect *1*, e13.

Joe, C.C.D., Chatterjee, S., Lovrecz, G., Adams, T.E., Thaysen-Andersen, M., Walsh, R., Locarnini, S.A., Smooker, P., and Netter, H.J. (2020). Glycoengineered hepatitis B virus-like particles with enhanced immunogenicity. Vaccine *38*, 3892–3901.

Johansson, M.U., Nilsson, H., Evenäs, J., Forsén, S., Drakenberg, T., Björck, L., and Wikström, M. (2002). Differences in backbone dynamics of two homologous bacterial albumin-binding modules: Implications for binding specificity and bacterial adaptation. Journal of Molecular Biology *316*, 1083–1099.

Jonsson, A., Dogan, J., Herne, N., Abrahmsen, L., and Nygren, P.-A. (2008). Engineering of a femtomolar affinity binding protein to human serum albumin. Protein Engineering Design and Selection *21*, 515–527.

Ju, B., Zhang, Q., Ge, J., Wang, R., Sun, J., Ge, X., Yu, J., Shan, S., Zhou, B., Song, S., et al. (2020). Human neutralizing antibodies elicited by SARS-CoV-2 infection. Nature *584*, 115–119.

Kanekiyo, M., Wei, C.-J., Yassine, H.M., McTamney, P.M., Boyington, J.C., Whittle, J.R.R., Rao, S.S., Kong, W.-P., Wang, L., and Nabel, G.J. (2013). Self-assembling influenza nanoparticle vaccines elicit broadly neutralizing H1N1 antibodies. Nature *499*, 102–106.

Kanekiyo, M., Joyce, M.G., Gillespie, R.A., Gallagher, J.R., Andrews, S.F., Yassine, H.M., Wheatley, A.K., Fisher, B.E., Ambrozak, D.R., Creanga, A., et al. (2019). Mosaic nanoparticle display of diverse influenza virus hemagglutinins elicits broad B cell responses. Nat Immunol *20*, 362–372.

Keeble, A.H., Banerjee, A., Ferla, M.P., Reddington, S.C., Anuar, I.N.A.K., and Howarth, M. (2017). Evolving accelerated amidation by SpyTag/SpyCatcher to analyze membrane dynamics. Angewandte Chemie International Edition *56*, 16521–16525.

Keeble, A.H., Turkki, P., Stokes, S., Khairil Anuar, I.N.A., Rahikainen, R., Hytönen, V.P., and Howarth, M. (2019). Approaching infinite affinity through engineering of peptide–protein interaction. Proceedings of the National Academy of Sciences *116*, 26523–26533.

Keeble, A.H., Yadav, V.K., Ferla, M.P., Bauer, C.C., Chuntharpursat-Bon, E., Huang, J., Bon, R.S., and Howarth, M. (2022). DogCatcher allows loop-friendly protein-protein ligation. Cell Chem Biol *29*, 339-350. e10.

Keller, M.W., Glasheen, W., and Kaul, S. (1989). Albunex: A safe and effective commercially produced agent for myocardial contrast echocardiography. Journal of the American Society of Echocardiography *2*, 48–52.

Keresztes, G., Baer, M., Alfenito, M.R., Verwoerd, T.C., Kovalchuk, A., Wiebe, M.G., Andersen, T.K., Saloheimo, M., Tchelet, R., Kensinger, R., et al. (2022). The highly productive Thermothelomyces heterothallica C1 expression system as a host for rapid development of influenza vaccines. Vaccines *10*.

Khairil Anuar, I.N.A., Banerjee, A., Keeble, A.H., Carella, A., Nikov, G.I., and Howarth, M. (2019). Spy&Go purification of SpyTag-proteins using pseudo-SpyCatcher to access an oligomerization toolbox. Nat Commun *10*, 1734.

Ko, E.-J., and Kang, S.-M. (2018). Immunology and efficacy of MF59-adjuvanted vaccines. Hum Vaccin Immunother *14*, 3041–3045.

Koho, T., Mäntylä, T., Laurinmäki, P., Huhti, L., Butcher, S.J., Vesikari, T., Kulomaa, M.S., and Hytönen, V.P. (2012). Purification of norovirus-like particles (vlps) by Ion Exchange Chromatography. Journal of Virological Methods *181*, 6–11.

Krammer, F. (2019). The human antibody response to influenza A virus infection and vaccination. Nature Reviews Immunology *19*, 383–397.

Krammer, F., Fouchier, R.A.M., Eichelberger, M.C., Webby, R.J., Shaw-Saliba, K., Wan, H., Wilson, P.C., Compans, R.W., Skountzou, I., and Monto, A.S. (2018). NAction! How Can Neuraminidase-Based Immunity Contribute to Better Influenza Virus Vaccines? MBio *9*.

Krarup, A., Truan, D., Furmanova-Hollenstein, P., Bogaert, L., Bouchier, P., Bisschop, I.J.M., Widjojoatmodjo, M.N., Zahn, R., Schuitemaker, H., McLellan, J.S., et al. (2015). A highly stable prefusion RSV F vaccine derived from structural analysis of the fusion mechanism. Nat Commun *6*, 8143.

Krieg, A.M. (2006). Therapeutic potential of toll-like receptor 9 activation. Nature Reviews Drug Discovery *5*, 471–484.

Kronvall, G., Simmons, A., Myhre, E.B., and Jonsson, S. (1979). Specific absorption of human serum albumin, immunoglobulin A, and immunoglobulin G with selected strains of group A and G streptococci. Infect Immun *25*, 1–10.

Kuraoka, M., Schmidt, A.G., Nojima, T., Feng, F., Watanabe, A., Kitamura, D., Harrison, S.C., Kepler, T.B., and Kelsoe, G. (2016). Complex antigens drive permissive clonal selection in germinal centers. Immunity *44*, 542–552.

Lai, T., Yang, Y., and Ng, S. (2013). Advances in mammalian cell line development technologies for recombinant protein production. Pharmaceuticals *6*, 579–603.

Lalonde, M.-E., and Durocher, Y. (2017). Therapeutic glycoprotein production in mammalian cells. J Biotechnol *251*, 128–140.

Lambert, P.-H., Ambrosino, D.M., Andersen, S.R., Baric, R.S., Black, S.B., Chen, R.T., Dekker, C.L., Didierlaurent, A.M., Graham, B.S., Martin, S.D., et al. (2020). Consensus summary report for CEPI/BC March 12–13, 2020 meeting: Assessment of risk of disease enhancement with COVID-19 vaccines. Vaccine *38*, 4783–4791.

Lejon, S., Frick, I.-M., Björck, L., Wikström, M., and Svensson, S. (2004). Crystal structure and biological implications of a bacterial albumin binding module in complex with human serum albumin. Journal of Biological Chemistry *279*, 42924–42928.

Leneghan, D.B., Miura, K., Taylor, I.J., Li, Y., Jin, J., Brune, K.D., Bachmann, M.F., Howarth, M., Long, C.A., and Biswas, S. (2017). Nanoassembly routes stimulate conflicting antibody quantity and quality for transmission-blocking malaria vaccines. Sci Rep *7*, 3811.

Letko, M., Marzi, A., and Munster, V. (2020). Functional assessment of cell entry and receptor usage for SARS-CoV-2 and other lineage B betacoronaviruses. Nat Microbiol *5*, 562–569.

Li, Q., Wu, J., Nie, J., Zhang, L., Hao, H., Liu, S., Zhao, C., Zhang, Q., Liu, H., Nie, L., et al. (2020). The impact of mutations in SARS-COV-2 spike on viral infectivity and Antigenicity. Cell *182*.

Li, T., Zhang, T., Gu, Y., Li, S., and Xia, N. (2021a). Current progress and challenges in the design and development of a successful COVID-19 vaccine. Fundamental Research *1*, 139–150.

Li, Y., Liu, D., Wang, Y., Su, W., Liu, G., and Dong, W. (2021b). The importance of glycans of viral and host proteins in enveloped virus infection. Frontiers in Immunology *12*.

Lichty, J.J., Malecki, J.L., Agnew, H.D., Michelson-Horowitz, D.J., and Tan, S. (2005). Comparison of affinity tags for protein purification. Protein Expr Purif *41*, 98–105.

Lin, G., Simmons, G., Pöhlmann, S., Baribaud, F., Ni, H., Leslie, G.J., Haggarty, B.S., Bates, P., Weissman, D., Hoxie, J.A., et al. (2003). Differential N-linked glycosylation of

human immunodeficiency virus and ebola virus envelope glycoproteins modulates interactions with DC-sign and DC-SIGNR. Journal of Virology *77*, 1337–1346.

Liu, W.-C., Jan, J.-T., Huang, Y.-J., Chen, T.-H., and Wu, S.-C. (2016). Unmasking Stem-Specific Neutralizing Epitopes by Abolishing N-Linked Glycosylation Sites of Influenza Virus Hemagglutinin Proteins for Vaccine Design. J Virol *90*, 8496–8508.

López-Macías, C. (2012). Virus-like particle (VLP)-based vaccines for pandemic influenza. Hum Vaccin Immunother *8*, 411–414.

Luo, S., Hu, K., He, S., Wang, P., Zhang, M., Huang, X., Du, T., Zheng, C., Liu, Y., and Hu, Q. (2015). Contribution of N-linked glycans on HSV-2 GB to cell–cell fusion and viral entry. Virology *483*, 72–82.

Lytras, S., Xia, W., Hughes, J., Jiang, X., and Robertson, D.L. (2021). The animal origin of SARS-CoV-2. Science *373*, 968–970.

Maley, F., Trimble, R.B., Tarentino, A.L., and Plummer, T.H. (1989). Characterization of glycoproteins and their associated oligosaccharides through the use of endoglycosidases. Anal Biochem *180*, 195–204.

Marini, A., Zhou, Y., Li, Y., Taylor, I.J., Leneghan, D.B., Jin, J., Zaric, M., Mekhaiel, D., Long, C.A., Miura, K., et al. (2019). A universal plug-and-display vaccine carrier based on HBsAg VLP to maximize effective antibody response. Front Immunol *10*.

Marrack, P., McKee, A.S., and Munks, M.W. (2009). Towards an understanding of the adjuvant action of aluminium. Nat Rev Immunol *9*, 287–293.

McFall-Boegeman, H., and Huang, X. (2022). Mechanisms of cellular and humoral immunity through the lens of VLP-based vaccines. Expert Rev Vaccines *21*, 453–469.

McGinnes, L.W., Gravel, K.A., Finberg, R.W., Kurt-Jones, E.A., Massare, M.J., Smith, G., Schmidt, M.R., and Morrison, T.G. (2011). Assembly and immunological properties of Newcastle disease virus-like particles containing the respiratory syncytial virus F and G proteins. Journal of Virology *85*, 366–377.

Menachery, V.D., Yount, B.L., Debbink, K., Agnihothram, S., Gralinski, L.E., Plante, J.A., Graham, R.L., Scobey, T., Ge, X.-Y., Donaldson, E.F., et al. (2015). A SARS-like cluster of circulating bat coronaviruses shows potential for human emergence. Nat Med *21*, 1508–1513.

Menachery, V.D., Yount, B.L., Sims, A.C., Debbink, K., Agnihothram, S.S., Gralinski, L.E., Graham, R.L., Scobey, T., Plante, J.A., Royal, S.R., et al. (2016). SARS-like WIV1-CoV poised for human emergence. Proceedings of the National Academy of Sciences *113*, 3048–3053.

Merlot, A.M., Kalinowski, D.S., and Richardson, D.R. (2014). Unraveling the mysteries of serum albumin more than just a serum protein. Front Physiol *5*.

Mizukoshi, F., Yamamoto, T., Mitsuki, Y., Terahara, K., Kawana-Tachikawa, A., Kobayashi, K., Iwamoto, A., Morikawa, Y., and Tsunetsugu-Yokota, Y. (2009). Activation of HIV-1 Gag-specific CD8+ T cells by yeast-derived VLP-pulsed dendritic cells is influenced by the level of mannose on the VLP antigen. Microbes and Infection *11*, 191–197.

Mononen, I., and Karjalainen, E. (1984). Structural comparison of protein sequences around potential N-glycosylation sites. Biochimica et Biophysica Acta (BBA) - Protein Structure and Molecular Enzymology *788*, 364–367.

Morel, P.A., and Turner, M.S. (2010). Designing the optimal vaccine: The importance of dytokines and Dendritic Cells. The Open Vaccine Journal *3*, 7–17.

Morens, D.M., Taubenberger, J.K., and Fauci, A.S. (2022). Universal Coronavirus Vaccines — An Urgent Need. New England Journal of Medicine *386*, 297–299.

Morón, V.G., Rueda, P., Sedlik, C., and Leclerc, C. (2003). In vivo, dendritic cells can cross-present virus-like particles using an endosome-to-cytosol pathway. The Journal of Immunology *171*, 2242–2250.

Murray, C.J.L. (2022). COVID-19 will continue but the end of the pandemic is near. The Lancet *399*, 417–419.

Myhre, E.B. (1984). Surface receptors for human serum albumin in Peptococcus Magnus strains. Journal of Medical Microbiology *18*, 189–195.

Nascimento, I.P., and Leite, L.C.C. (2012). Recombinant vaccines and the development of new vaccine strategies. Braz J Med Biol Res *45*, 1102–1111.

Nishikaze, T. (2017). Sensitive and structure-informative N-glycosylation analysis by MALDI-MS; ionization, fragmentation, and derivatization. Mass Spectrometry *6*, A0060.

Nooraei, S., Bahrulolum, H., Hoseini, Z.S., Katalani, C., Hajizade, A., Easton, A.J., and Ahmadian, G. (2021). Virus-like particles: Preparation, immunogenicity and their roles as nanovaccines and drug nanocarriers. Journal of Nanobiotechnology *19*.

Överby, A.K., Popov, V., Neve, E.P., and Pettersson, R.F. (2006). Generation and analysis of infectious virus-like particles of UUKUNIEMI virus (bunyaviridae): A useful system for studying bunyaviral packaging and budding. Journal of Virology *80*, 10428–10435.

Palladini, A., Thrane, S., Janitzek, C.M., Pihl, J., Clemmensen, S.B., de Jongh, W.A., Clausen, T.M., Nicoletti, G., Landuzzi, L., Penichet, M.L., et al. (2018). Virus-like particle display of HER2 induces potent anti-cancer responses. Oncoimmunology *7*, e1408749.

Pallesen, J., Wang, N., Corbett, K.S., Wrapp, D., Kirchdoerfer, R.N., Turner, H.L., Cottrell, C.A., Becker, M.M., Wang, L., Shi, W., et al. (2017). Immunogenicity and structures of a rationally designed prefusion MERS-COV spike antigen. Proceedings of the National Academy of Sciences *114*.

van Panhuis, W.G., Grefenstette, J., Jung, S.Y., Chok, N.S., Cross, A., Eng, H., Lee, B.Y., Zadorozhny, V., Brown, S., Cummings, D., et al. (2013). Contagious diseases in the United States from 1888 to the present. N Engl J Med *369*, 2152–2158.

Parker, D.C. (1993). T cell-dependent B cell activation. Annual Review of Immunology *11*, 331–360.

Patel, K.G., and Swartz, J.R. (2011). Surface functionalization of virus-like particles by direct conjugation using azide−alkyne click chemistry. Bioconjug Chem *22*, 376–387.

Pérez, O., Batista-Duharte, A., González, E., Zayas, C., Balboa, J., Cuello, M., Cabrera, O., Lastre, M., and Schijns, V.E.J.C. (2012). Human prophylactic vaccine adjuvants and their determinant role in new vaccine formulations. Braz J Med Biol Res *45*, 681–692.

Petrescu, A.-J., Milac, A.-L., Petrescu, S.M., Dwek, R.A., and Wormald, M.R. (2003). Statistical analysis of the protein environment of N-glycosylation sites: implications for occupancy, structure, and folding. Glycobiology *14*, 103–114.

Pitek, A. S., Jameson, S. A., Veliz, F. A., Shukla, S., and Steinmetz, N. F. (2016). Serum albumin 'camouflage' of plant virus based nanoparticles prevents their antibody recognition and enhances pharmacokinetics. Biomaterials *89*, 89–97.

Pitek, A.S., Hu, H., Shukla, S., and Steinmetz, N.F. (2018). Cancer Theranostic Applications of Albumin-Coated Tobacco Mosaic Virus Nanoparticles. ACS Appl Mater Interfaces *10*, 39468–39477.

Plotkin, S. (2014). History of vaccination. Proceedings of the National Academy of Sciences *111*, 12283–12287.

Poland, G.A., Ovsyannikova, I.G., and Kennedy, R.B. (2021). The need for broadly protective COVID-19 vaccines: Beyond S-only approaches. Vaccine *39*, 4239–4241.

Pollet, J., Chen, W.-H., and Strych, U. (2021). Recombinant protein vaccines, a proven approach against coronavirus pandemics. Adv Drug Deliv Rev *170*, 71–82.

Pollett, S., Conte, M.A., Sanborn, M., Jarman, R.G., Lidl, G.M., Modjarrad, K., and Maljkovic Berry, I. (2021). A comparative recombination analysis of human coronaviruses and implications for the SARS-CoV-2 pandemic. Sci Rep *11*, 17365.

Powell, T.J., Silk, J.D., Sharps, J., Fodor, E., and Townsend, A.R.M. (2012). Pseudotyped influenza A virus as a vaccine for the induction of heterotypic immunity. J Virol *86*, 13397–13406.

Prasanphanich, N.S., Luyai, A.E., Song, X., Heimburg-Molinaro, J., Mandalasi, M., Mickum, M., Smith, D.F., Nyame, A.K., and Cummings, R.D. (2014). Immunization with recombinantly expressed glycan antigens from Schistosoma mansoni induces glycan-specific antibodies against the parasite. Glycobiology 24, 619–637.

Quan, F.-S., Kim, M.-C., Lee, B.-J., Song, J.-M., Compans, R.W., and Kang, S.-M. (2012). Influenza M1 VLPs containing neuraminidase induce heterosubtypic cross-protection. Virology *430*, 127–135.

Quinlan, B.D., Mou, H., Zhang, L., Guo, Y., He, W., Ojha, A., Parcells, M.S., Luo, G., Li, W., Zhong, G., et al. (2020). The SARS-CoV-2 receptor-binding domain elicits a potent neutralizing response without antibody-dependent enhancement. SSRN Electronic Journal.

Rahikainen, R., Rijal, P., Tan, T.K., Wu, H., Andersson, A.C., Barrett, J.R., Bowden, T.A., Draper, S.J., Townsend, A.R., and Howarth, M. (2021). Overcoming symmetry mismatch in vaccine nanoassembly through spontaneous amidation. Angewandte Chemie International Edition *60*, 321–330.

Rakhra, K., Abraham, W., Wang, C., Moynihan, K.D., Li, N., Donahue, N., Baldeon, A.D., and Irvine, D.J. (2021). Exploiting albumin as a mucosal vaccine chaperone for robust generation of lung-resident memory T cells. Sci Immunol *6*.

Rappuoli, R. (2014). Inner workings: 1885, the first rabies vaccination in humans. Proceedings of the National Academy of Sciences *111*, 12273.

Rappuoli, R., Pizza, M., del Giudice, G., and de Gregorio, E. (2014). Vaccines, new opportunities for a new society. Proceedings of the National Academy of Sciences *111*, 12288–12293.

Read, B.J., Won, L., Kraft, J.C., Sappington, I., Aung, A., Wu, S., Bals, J., Chen, C., Lee, K.K., Lingwood, D., et al. (2022). Mannose-binding lectin and complement mediate follicular localization and enhanced immunogenicity of diverse protein nanoparticle immunogens. Cell Reports *38*, 110217.

Reily, C., Stewart, T.J., Renfrow, M.B., and Novak, J. (2019). Glycosylation in health and disease. Nat Rev Nephrol *15*, 346–366.

Ringe, R.P., Pugach, P., Cottrell, C.A., LaBranche, C.C., Seabright, G.E., Ketas, T.J., Ozorowski, G., Kumar, S., Schorcht, A., van Gils, M.J., et al. (2019). Closing and opening holes in the glycan shield of HIV-1 envelope glycoprotein SOSIP trimers can redirect the neutralizing antibody response to the newly unmasked epitopes. J Virol *93*.

del Rio, C., and Malani, P.N. (2022). COVID-19 in 2022—The beginning of the end or the end of the beginning? JAMA *327*, 2389.

Rogers, T.F., Zhao, F., Huang, D., Beutler, N., Burns, A., He, W., Limbo, O., Smith, C., Song, G., Woehl, J., et al. (2020). Isolation of potent SARS-CoV-2 neutralizing antibodies and protection from disease in a small animal model. Science *369*, 956–963.

Sanders, R.W., and Moore, J.P. (2017). Native-like Env trimers as a platform for HIV-1 vaccine design. Immunol Rev *275*, 161–182.

Sanders, R.W., van Gils, M.J., Derking, R., Sok, D., Ketas, T.J., Burger, J.A., Ozorowski, G., Cupo, A., Simonich, C., Goo, L., et al. (2015). HIV-1 neutralizing antibodies induced by native-like envelope trimers. Science *349*.

Saraswat, S., Athmaram, T.N., Parida, M., Agarwal, A., Saha, A., and Dash, P.K. (2016). Expression and Characterization of yeast derived chikungunya virus like particles (CHIK-VLPs) and its evaluation as a potential vaccine candidate. PLoS Negl Trop Dis *10*, e0004782.

Saunders, K.O., Nicely, N.I., Wiehe, K., Bonsignori, M., Meyerhoff, R.R., Parks, R., Walkowicz, W.E., Aussedat, B., Wu, N.R., Cai, F., et al. (2017). Vaccine elicitation of high mannose-dependent neutralizing antibodies against the V3-glycan broadly neutralizing epitope in nonhuman primates. Cell Rep *18*, 2175–2188.

Saveliev, S., Bratz, M., Zubarev, R., Szapacs, M., Budamgunta, H., and Urh, M. (2013). Trypsin/Lys-C protease mix for enhanced protein mass spectrometry analysis. Nat Methods *10*, i–ii.

Scheu, A.H.A., Lim, S.Y.T., Metzner, F.J., Mohammed, S., and Howarth, M. (2021). NeissLock provides an inducible protein anhydride for covalent targeting of endogenous proteins. Nat Commun *12*, 717.

Schiller, J., and Lowy, D. (2018). Explanations for the high potency of HPV prophylactic vaccines. Vaccine *36*, 4768–4773.

Sesterhenn, F., Galloux, M., Vollers, S.S., Csepregi, L., Yang, C., Descamps, D., Bonet, J., Friedensohn, S., Gainza, P., Corthésy, P., et al. (2019). Boosting subdominant neutralizing antibody responses with a computationally designed epitope-focused immunogen. PLOS Biol *17*, e3000164.

Sesterhenn, F., Yang, C., Bonet, J., Cramer, J.T., Wen, X., Wang, Y., Chiang, C.-I., Abriata, L.A., Kucharska, I., Castoro, G., et al. (2020). De novo protein design enables the precise induction of RSV-neutralizing antibodies. Science *368*.

Sharma, J., Shepardson, K., Johns, L.L., Wellham, J., Avera, J., Schwarz, B., Rynda-Apple, A., and Douglas, T. (2020). A self-adjuvanted, modular, antigenic VLP for rapid response to influenza virus variability. ACS Appl Mater Interfaces *12*, 18211–18224.

Shental-Bechor, D., and Levy, Y. (2008). Effect of glycosylation on protein folding: A close look at thermodynamic stabilization. Proceedings of the National Academy of Sciences *105*, 8256–8261.

Shi, X., Kohl, A., Léonard, V.H., Li, P., McLees, A., and Elliott, R.M. (2006). Requirement of the N-terminal region of orthobunyavirus nonstructural protein NSM for virus assembly and morphogenesis. Journal of Virology *80*, 8089–8099.

Shin, J., Wood, D., Robertson, J., Minor, P., and Peden, K. (2007). WHO informal consultation on the application of molecular methods to assure the quality, safety and efficacy of vaccines, Geneva, Switzerland, 7–8 April 2005. Biologicals *35*, 63–71.

Shinnakasu, R., Sakakibara, S., Yamamoto, H., Wang, P., Moriyama, S., Sax, N., Ono, C., Yamanaka, A., Adachi, Y., Onodera, T., et al. (2021). Glycan engineering of the SARS-CoV-2 receptor-binding domain elicits cross-neutralizing antibodies for SARS-related viruses. Journal of Experimental Medicine *218*.

Smith, G.E., Sun, X., Bai, Y., Liu, Y. v., Massare, M.J., Pearce, M.B., Belser, J.A., Maines, T.R., Creager, H.M., Glenn, G.M., et al. (2017). Neuraminidase-based recombinant virus-like particles protect against lethal avian influenza A(H5N1) virus infection in ferrets. Virology 509, 90–97.

Smith, M.T., Hawes, A.K., and Bundy, B.C. (2013). Reengineering viruses and virus-like particles through chemical functionalization strategies. Curr Opin Biotechnol *24*, 620–626.

Spice, A.J., Aw, R., Bracewell, D.G., and Polizzi, K.M. (2020). Synthesis and Assembly of Hepatitis B Virus-Like Particles in a Pichia pastoris Cell-Free System. Front Bioeng Biotechnol *8*.

Spidel, J.L., Vaessen, B., Chan, Y.Y., Grasso, L., and Kline, J.B. (2016). Rapid high-throughput cloning and stable expression of antibodies in HEK293 cells. J Immunol Methods *439*, 50–58.

Steinmetz, N.F. (2010). Viral nanoparticles as platforms for next-generation therapeutics and imaging devices. Nanomedicine *6*, 634–641.

Stewart-Jones, G.B.E., Soto, C., Lemmin, T., Chuang, G.-Y., Druz, A., Kong, R., Thomas, P. v, Wagh, K., Zhou, T., Behrens, A.-J., et al. (2016). Trimeric HIV-1-Env structures define glycan shields from clades A, B, and G. Cell *165*, 813–826.

Stone, S.R., Heinrich, T., Cunningham, P., Bogdawa, H., Hoffmann, K., Watt, P., and Anastasas, M. (2016). Use of SpyCatcher as a protein scaffold for peptide display; and SpyCatcher/SpyTag cyclised peptides displayed on bacteriophage.

Strecker, T., Eichler, R., Meulen, J.ter, Weissenhorn, W., Dieter Klenk, H., Garten, W., and Lenz, O. (2003). Lassa virus Z protein is a matrix protein sufficient for the release of virus-like particles. Journal of Virology *77*, 10700–10705.

Struwe, W.B., Chertova, E., Allen, J.D., Seabright, G.E., Watanabe, Y., Harvey, D.J., Medina-Ramirez, M., Roser, J.D., Smith, R., Westcott, D., et al. (2018). Site-Specific Glycosylation of Virion-Derived HIV-1 Env Is Mimicked by a Soluble Trimeric Immunogen. Cell Rep *24*, 1958-1966.e5.

Suga, A., Nagae, M., and Yamaguchi, Y. (2018). Analysis of protein landscapes around N-glycosylation sites from the PDB repository for understanding the structural basis of N-glycoprotein processing and maturation. Glycobiology *28*, 774–785.

Sugio, S., Kashima, A., Mochizuki, S., Noda, M., and Kobayashi, K. (1999). Crystal structure of human serum albumin at 2.5 Å resolution. Protein Engineering, Design and Selection *12*, 439–446.

Sultana, I., Yang, K., Getie-Kebtie, M., Couzens, L., Markoff, L., Alterman, M., and Eichelberger, M.C. (2014). Stability of neuraminidase in inactivated influenza vaccines.Vaccine *32*, 2225–2230.

Sun, B., Zhao, X., Wu, Y., Cao, P., Movahedi, F., Liu, J., Wang, J., Xu, Z.P., and Gu, W. (2021). Mannose-functionalized biodegradable nanoparticles efficiently deliver DNA vaccine and promote anti-tumor immunity. ACS Applied Materials; Interfaces *13*, 14015–14027.

Sun, S., Hu, Y., Jia, L., Eshghi, S.T., Liu, Y., Shah, P., and Zhang, H. (2018). Site-specific profiling of serum glycoproteins using N-Linked glycan and glycosite analysis revealing atypical N-glycosylation sites on albumin and α-1B-Glycoprotein. Anal Chem *90*, 6292–6299.

Syomin, B. v, and Ilyin, Y. v (2019). Virus-like particles as an instrument of vaccine production. Mol Biol *53*, 323–334.

Tan, L.L., Hoon, S.S., and Wong, F.T. (2016). Kinetic controlled Tag-Catcher interactions for directed covalent protein assembly. PLoS One *11*, e0165074.

Tan, T.K., Rijal, P., Rahikainen, R., Keeble, A.H., Schimanski, L., Hussain, S., Harvey, R., Hayes, J.W.P., Edwards, J.C., McLean, R.K., et al. (2021). A COVID-19 vaccine candidate using SpyCatcher multimerization of the SARS-CoV-2 spike protein receptor-binding domain induces potent neutralising antibody responses. Nat Commun *12*, 542.

Tang, A.F., Enyindah-Asonye, G., and Hioe, C.E. (2021). Immune Complex Vaccine Strategies to Combat HIV-1 and Other Infectious Diseases. Vaccines *9*. 112.

Tao, Y., and Tong, S. (2019). Complete genome sequence of a severe acute respiratory syndrome-related coronavirus from Kenyan Bats. Microbiology Resource Announcements *8*.

Tariq, H., Batool, S., Asif, S., Ali, M., and Abbasi, B.H. (2021). Virus-like particles: Revolutionary platforms for developing vaccines against emerging infectious diseases. Front Microbiol *12*, 790121.

Tariq, H., Batool, S., Asif, S., Ali, M., and Abbasi, B.H. (2022). Virus-like particles: Revolutionary platforms for developing vaccines against emerging infectious diseases. Frontiers in Microbiology *12*.

Thornlow, D.N., Macintyre, A.N., Oguin, T.H., Karlsson, A.B., Stover, E.L., Lynch, H.E., Sempowski, G.D., and Schmidt, A.G. (2021). Altering the immunogenicity of hemagglutinin immunogens by hyperglycosylation and disulfide stabilization. Frontiers in Immunology *12*.

Thrane, S., Janitzek, C.M., Matondo, S., Resende, M., Gustavsson, T., de Jongh, W.A., Clemmensen, S., Roeffen, W., van de Vegte Bolmer, M., van Gemert, G.J., et al. (2016). Bacterial superglue enables easy development of efficient virus-like particle based vaccines. J Nanobiotechnology *14*, 30.

Thrane, S., Aves, K.-L., Uddbäck, I.E.M., Janitzek, C.M., Han, J., Yang, Y.R., Ward, A.B., Theander, T.G., Nielsen, M.A., Salanti, A., et al. (2020). A vaccine displaying a trimeric influenza-A HA stem protein on capsid-like particles elicits potent and long-lasting protection in mice. Vaccines *8*, 389.

Tian, J.-H., Patel, N., Haupt, R., Zhou, H., Weston, S., Hammond, H., Logue, J., Portnoff, A.D., Norton, J., Guebre-Xabier, M., et al. (2021). SARS-CoV-2 spike glycoprotein vaccine candidate NVX-CoV2373 immunogenicity in baboons and protection in mice. Nat Commun *12*, 372.

Tokatlian, T., Read, B.J., Jones, C.A., Kulp, D.W., Menis, S., Chang, J.Y.H., Steichen, J.M., Kumari, S., Allen, J.D., Dane, E.L., et al. (2019). Innate immune recognition of glycans targets HIV nanoparticle immunogens to germinal centers. Science *363*, 649–654.

Tseng, C.-T., Sbrana, E., Iwata-Yoshikawa, N., Newman, P.C., Garron, T., Atmar, R.L., Peters, C.J., and Couch, R.B. (2012). Immunization with SARS coronavirus vaccines leads to pulmonary immunopathology on challenge with the SARS virus. PLoS One *7*, e35421.

Tsoka, S., Ciniawskyj, O.C., Thomas, O.R.T., Titchener-Hooker, N.J., and Hoare, M. (2000). Selective flocculation and precipitation for the improvement of virus-like particle recovery from yeast homogenate. Biotechnology Progress *16*, 661–667.

Tsouchnikas, G., Zlatkovic, J., Jarmer, J., Strauß, J., Vratskikh, O., Kundi, M., Stiasny, K., and Heinz, F.X. (2015). Immunization with immune complexes modulates the fine specificity of antibody responses to a flavivirus antigen. J Virol *89*, 7970–7978.

U.S. Food and Drug Administration (2022). Coronavirus (COVID-19) update: FDA authorizes emergency use of Novavax COVID-19 vaccine, adjuvanted.

Veggiani, G., Nakamura, T., Brenner, M.D., Gayet, R. v., Yan, J., Robinson, C. v., and Howarth, M. (2016). Programmable polyproteams built using twin peptide superglues. Proceedings of the National Academy of Sciences *113*, 1202–1207.

Walls, A.C., Fiala, B., Schäfer, A., Wrenn, S., Pham, M.N., Murphy, M., Tse, L. v., Shehata, L., O'Connor, M.A., Chen, C., et al. (2020). Elicitation of Potent Neutralizing Antibody Responses by Designed Protein Nanoparticle Vaccines for SARS-CoV-2. Cell *183*, 1367-1382. e17.

Walpita, P., Barr, J., Sherman, M., Basler, C.F., and Wang, L. (2011). Vaccine potential of Nipah virus-like particles. PLoS ONE *6*.

Walsh, G. (2014). Biopharmaceutical benchmarks 2014. Nat Biotechnol *32*, 992–1000.

Wan, S., Yi, Q., Fan, S., Lv, J., Zhang, X., Guo, L., Lang, C., Xiao, Q., Xiao, K., Yi, Z., et al. (2020). Relationships among lymphocyte subsets, cytokines, and the pulmonary inflammation index in coronavirus (COVID-19) infected patients. Br J Haematol *189*, 428–437.

Wang, T.T., and Ravetch, J. v. (2015). Immune complexes: Not just an innocent bystander in chronic viral infection. Immunity *42*, 213–215.

Wang, H., Chen, X., Wang, D., Yao, C., Wang, Q., Xie, J., Shi, X., Xiang, Y., Liu, W., and Zhang, L. (2018a). Epitope-focused immunogens against the CD4-binding site of HIV-1 envelope protein induce neutralizing antibodies against auto- and heterologous viruses. J Biol Chem *293*, 830–846.

Wang, N., Li, S.-Y., Yang, X.-L., Huang, H.-M., Zhang, Y.-J., Guo, H., Luo, C.-M., Miller, M., Zhu, G., Chmura, A.A., et al. (2018b). Serological evidence of bat SARS-related coronavirus infection in humans, China. Virol Sin *33*, 104–107.

Wang, P., Zhao, P., Dong, S., Xu, T., He, X., and Chen, M. (2018). An albumin-binding polypeptide both targets cytotoxic T lymphocyte vaccines to lymph nodes and boosts vaccine presentation by dendritic cells. Theranostics *8*, 223–236.

Wei, X., Decker, J.M., Wang, S., Hui, H., Kappes, J.C., Wu, X., Salazar-Gonzalez, J.F., Salazar, M.G., Kilby, J.M., Saag, M.S., et al. (2003). Antibody neutralization and escape by HIV-1. Nature *422*, 307–312.

Weldon, W.C., Wang, B.-Z., Martin, M.P., Koutsonanos, D.G., Skountzou, I., and Compans, R.W. (2010). Enhanced Immunogenicity of Stabilized Trimeric Soluble Influenza Hemagglutinin. PLoS One 5, e12466.

Willey, R.L., Shibata, R., Freed, E.O., Cho, M.W., and Martin, M.A. (1996). Differential glycosylation, virion incorporation, and sensitivity to neutralizing antibodies of human immunodeficiency virus type 1 envelope produced from infected primary T-lymphocyte and macrophage cultures. Journal of Virology *70*, 6431–6436.

Wingfield, P. (2001). Protein precipitation using ammonium sulfate. Curr Protoc Protein Sci Appendix 3, Appendix 3F.

de Wit, E., van Doremalen, N., Falzarano, D., and Munster, V.J. (2016). SARS and MERS: recent insights into emerging coronaviruses. Nat Rev Microbiol *14*, 523–534.

World Health Organization. (2014). Guidelines on the quality, safety and efficacy of recombinant malaria vaccines targeting the pre-erythrocytic and blood stages of Plasmodium falciparum.

World Health Organization (2021). Vaccine inequity undermining global economic recovery.

Wu, C.-Y., Cheng, C.-W., Kung, C.-C., Liao, K.-S., Jan, J.-T., Ma, C., and Wong, C.-H. (2022). Glycosite-deleted mRNA of SARS-CoV-2 spike protein as a broad-spectrum vaccine. Proceedings of the National Academy of Sciences *119*.

Yang, J., Wang, W., Chen, Z., Lu, S., Yang, F., Bi, Z., Bao, L., Mo, F., Li, X., Huang, Y., et al. (2020). A vaccine targeting the RBD of the S protein of SARS-CoV-2 induces protective immunity. Nature *586*, 572–577.

Yang, M., Yu, X.-W., Zheng, H., Sha, C., Zhao, C., Qian, M., and Xu, Y. (2015). Role of N-linked glycosylation in the secretion and enzymatic properties of Rhizopus chinensis lipase expressed in Pichia pastoris. Microb Cell Fact *14*, 40.

Yao, Q., Zhang, R., Guo, L., Li, M., and Chen, C. (2004). Th cell-independent immune responses to chimeric hemagglutinin/Simian human immunodeficiency virus-like particles vaccine. The Journal of Immunology *173*, 1951–1958.

Yu, A., Zhao, J., Peng, W., Banazadeh, A., Williamson, S.D., Goli, M., Huang, Y., and Mechref, Y. (2018). Advances in mass spectrometry-based glycoproteomics. Electrophoresis *39*, 3104–3122.

Zakeri, B., Fierer, J.O., Celik, E., Chittock, E.C., Schwarz-Linek, U., Moy, V.T., and Howarth, M. (2012). Peptide tag forming a rapid covalent bond to a protein, through engineering a bacterial adhesin. Proceedings of the National Academy of Sciences *109*.

Zarnitsyna, V.I., Ellebedy, A.H., Davis, C., Jacob, J., Ahmed, R., and Antia, R. (2015). Masking of antigenic epitopes by antibodies shapes the humoral immune response to influenza. Philosophical Transactions of the Royal Society B: Biological Sciences *370*. 20140248

Zhang, B., Chao, C.W., Tsybovsky, Y., Abiona, O.M., Hutchinson, G.B., Moliva, J.I., Olia, A.S., Pegu, A., Phung, E., Stewart-Jones, G.B.E., et al. (2020). A platform incorporating trimeric antigens into self-assembling nanoparticles reveals SARS-CoV-2-spike nanoparticles to elicit substantially higher neutralizing responses than spike alone. Sci Rep *10*, 18149.

Zhao, J., Song, E., Zhu, R., and Mechref, Y. (2016). Parallel data acquisition of in-source fragmented glycopeptides to sequence the glycosylation sites of proteins. Electrophoresis 37, 1420–1430.

Zhao, M., Vandersluis, M., Stout, J., Haupts, U., Sanders, M., and Jacquemart, R. (2019). Affinity chromatography for vaccines manufacturing: Finally ready for prime time? Vaccine *37*, 5491–5503.

Zhao, X., Li, G., and Liang, S. (2013). Several affinity tags commonly used in chromatographic purification. J Anal Methods Chem *2013*, 1–8.

Zhou, Q., and Qiu, H. (2019). The mechanistic impact of N-Glycosylation on stability, pharmacokinetics, and immunogenicity of therapeutic proteins. J Pharm Sci *108*, 1366–1377.

Zhou, Q., Shankara, S., Roy, A., Qiu, H., Estes, S., McVie-Wylie, A., Culm-Merdek, K., Park, A., Pan, C., and Edmunds, T. (2008). Development of a simple and rapid method for producing non-fucosylated oligomannose containing antibodies with increased effector function. Biotechnol Bioeng *99*, 652–665.

Zhou, Y., Jiang, S., and Du, L. (2018). Prospects for a MERS-CoV spike vaccine. Expert Rev Vaccines *17*, 677–686.